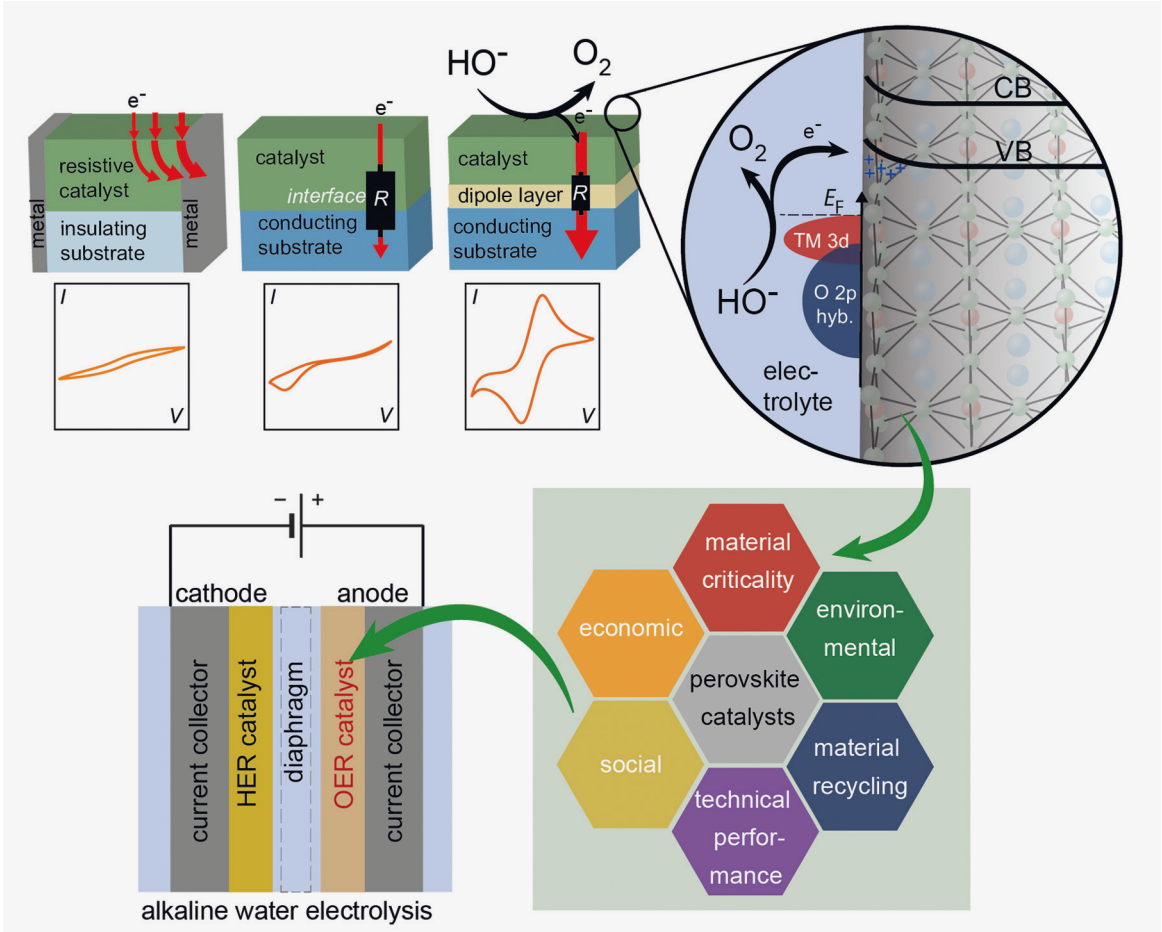

Model Perovskite Oxide Electrocatalysts for the Oxygen Evolution Reaction and their Material Sustainability Evaluation

Lisa Manja Katrin Heymann

Energie & Umwelt / Energy & Environment
Band / Volume 688
ISBN 978-3-95806-878-0

Mitglied der Helmholtz-Gemeinschaft

JÜLICH
Forschungszentrum

Schriften des Forschungszentrums Jülich
Reihe Energie & Umwelt / Energy & Environment Band / Volume 688

Forschungszentrum Jülich GmbH
Peter Grünberg Institut (PGI)
Elektronische Materialien (PGI-7)

Model Perovskite Oxide Electrocatalysts for the Oxygen Evolution Reaction and their Material Sustainability Evaluation

Lisa Manja Katrin Heymann

Schriften des Forschungszentrums Jülich
Reihe Energie & Umwelt / Energy & Environment Band / Volume 688

ISSN 1866-1793 ISBN 978-3-95806-878-0

Bibliografische Information der Deutschen Nationalbibliothek.
Die Deutsche Nationalbibliothek verzeichnet diese Publikation in der
Deutschen Nationalbibliografie; detaillierte Bibliografische Daten
sind im Internet über http://dnb.d-nb.de abrufbar.

Herausgeber und Vertrieb:	Forschungszentrum Jülich GmbH Zentralbibliothek, Verlag 52425 Jülich Tel.: +49 2461 61-5368 Fax: +49 2461 61-6103 zb-publikation@fz-juelich.de www.fz-juelich.de/zb
Umschlaggestaltung:	Grafische Medien, Forschungszentrum Jülich GmbH
Druck:	Grafische Medien, Forschungszentrum Jülich GmbH
Copyright:	Forschungszentrum Jülich 2026

Schriften des Forschungszentrums Jülich
Reihe Energie & Umwelt / Energy & Environment, Band / Volume 688

ISSN 1866-1793
ISBN 978-3-95806-878-0

Vollständig frei verfügbar über das Publikationsportal des Forschungszentrums Jülich (JuSER)
unter www.fz-juelich.de/zb/openaccess.

Abstract

Green hydrogen, produced by water electrolysis from renewable electricity, is a highly recommended energy carrier in the energy transition. However, the oxygen evolution reaction (OER) on the anode suffers from sluggish kinetics, rendering the process inefficient. Thus, there is a strong need for efficient OER catalysts and to uncover their structure-property relationships for a predictable OER catalyst design. Furthermore, a sustainable material choice for catalysts is urgently needed due to the drastically increasing materials demand of the energy transition.
Perovskites are promising catalysts to decrease the OER overpotentials. However, revealing the intrinsic catalytic activity independent of their large conductivity differences is a big challenge, and several electronic structure properties are discussed to determine their OER performance. In this thesis, the influence of the large conductivity differences is systematically disentangled from the intrinsic catalytic properties for the here investigated $ABO_{3-\delta}$ (A = La, Sr, Ca; B = Mn, Fe, Co, Ni) perovskites based on a model catalyst approach of epitaxial thin films. The revealed intrinsic OER activity trend is then correlated to their electronic structure properties to uncover structure-property relationships for the OER. We found that the highly resistive ferrates have similar intrinsic OER activity compared to the highly conductive cobaltates and nickelates. Interestingly, the O 2*p* band center, as the energetic distance from the oxygen states in the valence band to the Fermi level, revealed a volcano-shaped OER activity trend. Hence, neither too high nor too low O 2*p* band center leads to a high OER activity, which may advance predictions of efficient catalysts based on the valence band electronic structure.
Besides the catalytic efficiency, the perovskite oxide elemental diversity implies large sustainability differences often not considered in technical performance studies. However, determining sustainability parameters in early-stage research for those electrocatalysts is challenging, as final process and supply chains are not known at this stage. Therefore, this thesis determines sustainability parameters for the electrocatalysts in early-stage research to uncover material hotspots for the energy transition. For this, a process chain for the perovskite catalysts is projected, and their precursor materials are identified to evaluate their material criticality, economic, environmental, and social impact, in addition to their thin film OER activity. $La_{0.6}Sr_{0.4}CoO_{3-\delta}$ is compared to the A- and B-site substituted $La_{0.6}Ca_{0.4}FeO_{3-\delta}$ electrocatalyst as an exemplary case study. The exchange of Co to Fe and Sr to Ca results in a lower raw material criticality, lower economic, environmental, and social impact. However, the La-precursor has a high material criticality and environmental impact, which is a disadvantage for both perovskites.

Together, the revelation of intrinsic properties of OER catalysts independent of their resistivity, the revelation of electronic structure-property relationships, as well as the evaluation of sustainability parameters enables one to identify efficient, and sustainable material compositions that can be feasible for the energy transition. Further feedback loops between electrocatalyst performance and sustainability evaluation in early-stage research can guide the path for holistic material design concepts from the onset.

Kurzfassung

Grüner Wasserstoff, der in der Wasserelektrolyse mit erneuerbarem Strom hergestellt wird, ist ein sehr empfehlenswerter Energieträger für die Energiewende. Allerdings leidet die Sauerstoffentwicklungsreaktion (OER) an der Anode unter einer schleppenden Kinetik, was den Prozess ineffizient macht. Daher besteht ein dringender Bedarf an effizienten OER-Katalysatoren und an der Aufdeckung ihrer Struktur-Eigenschafts-Beziehungen für ein prädiktives OER Katalysatordesign. Darüber hinaus ist eine nachhaltige Materialauswahl für Katalysatoren dringend erforderlich, da der gesamte Materialbedarf in der Energiewende drastisch ansteigt.
Perowskite sind vielversprechende Katalysatoren zur Verringerung der OER-Überpotenziale. Jedoch ist die Aufdeckung der intrinsischen katalytischen Aktivität unabhängig von ihren großen Leitfähigkeitsunterschieden eine große Herausforderung, und es werden mehrere Eigenschaften der elektronischen Struktur diskutiert, die ihre intrinsische Aktivität beeinflussen können. In dieser Arbeit wird der Einfluss der großen Leitfähigkeitsunterschiede von den intrinsischen katalytischen Eigenschaften der Perowskite systematisch entkoppelt. Dies wird mittels eines Modellkatalysator-Ansatzes umgesetzt, der auf epitaktischen Dünnschichten der untersuchten Perowskite $ABO_{3-\delta}$ (A = La, Sr, Ca; B = Mn, Fe, Co, Ni) basiert. Der aufgezeigte intrinsische OER-Aktivitätstrend wird dann mit den elektronischen Struktureigenschaften korreliert, um Struktur-Eigenschafts-Beziehungen für die OER aufzudecken. Es zeigte sich, dass die wenig leitfähigen Ferrate eine ähnliche intrinsische OER-Aktivität aufweisen wie die hochleitfähigen Cobaltate und Nickelate. Interessanterweise zeigte das O 2*p*-Bandzentrum, definiert als energetischer Abstand der Sauerstoffzustände im Valenzband zum Fermi-Niveau, einen vulkan-förmigen OER-Aktivitätstrend. Daher führt weder ein zu hohes noch ein zu niedriges O 2*p*-Bandzentrum zu einer hohen OER-Aktivität. Das könnte die Vorhersage für effiziente OER-Katalysatoren basierend auf der elektronischen Struktur der Valenzbänder erleichtern.
Darüber hinaus impliziert die Elementvielfalt der Perowskitoxide große Unterschiede in der Nachhaltigkeit, die in technischen Performance-Studien oft nicht berücksichtigt werden. Die Bestimmung von relevanten Nachhaltigkeitsparametern für diese Elektrokatalysatoren ist jedoch schwierig gerade in der frühen Forschungsphase, da die endgültigen Prozess- und Lieferketten in dieser Phase noch nicht bekannt sind. Daher werden in dieser Arbeit entscheidende Nachhaltigkeitsparameter für die Elektrokatalysatoren in der frühen Forschungsphase ermittelt, um mögliche Material-Hotspots für die Energiewende aufzudecken. Dafür wird eine mögliche Prozesskette für die Perowskit-Katalysatoren entworfen, und daraus ihre Ausgangsstoffe identifiziert, um neben der OER-Aktivität der Dünnschichten auch ihre Materialkritikalität sowie ihre wirtschaftlichen, ökologischen und sozialen Auswirkungen zu bewerten. $La_{0.6}Sr_{0.4}CoO_{3-\delta}$ wird in einer exemplarischen Fallstudie mit dem die A- und B-Seiten substituierten Elektrokatalysator $La_{0.6}Ca_{0.4}FeO_{3-\delta}$ verglichen. Der Austausch von Co durch Fe und Sr durch Ca führt zu einer geringeren Materialkritikalität sowie geringeren wirtschaftlichen, ökologischen und sozialen Auswirkungen. Der La-Vorläufer weist jedoch eine hohe Materialkritikalität und Umweltbelas-

tung auf, was für beide Perowskite von Nachteil ist.
Insgesamt ermöglicht die Entkopplung von intrinsischen Eigenschaften der OER-Katalysatoren und ihrer Leitfähigkeit, die Aufdeckung von Beziehungen zwischen elektronischer Struktur und katalytischen Eigenschaften sowie die Bewertung von Nachhaltigkeitsparametern die Identifizierung effizienter und nachhaltiger Material-zusammensetzungen. Kontinuirliche Feedback-Schleifen zwischen der technischen Bewertung der Elektrokatalysatoren und deren Nachhaltigkeit können den Weg für ganzheitliche Materialdesignkonzepte schon in der frühen Forschungsphase ebnen.

Acknowledgments

During the journey of my PhD, several people supported me in various fields, and I want to express my deepest gratitude here. First, I want to thank you, Professor Rainer Waser, Professor Regina Dittmann, Professor Felix Gunkel, and Professor Christoph Bäumer for giving me the opportunity to do my PhD at the Peter Grünberg Institute 7 at the Forschungszentrum Jülich. I am very thankful to Professor Rainer Waser and Professor Christoph Bäumer for examining my thesis.

I want to express my greatest gratitude to both my supervisors, Professor Felix Gunkel and Professor Christoph Bäumer, for the supportive mentoring, fruitful scientific discussions, their detailed feedback, and encouragement during challenging times. I am especially grateful for the fact that the three of us appreciated the interdisciplinary work spanning materials science, chemistry, physics, and sustainability sciences from various perspectives as a team. Here, I would also like to say a big thank you to Dr. Andrea Schreiber (Institute for Climate and Energy Systems 2, Forschungszentrum Jülich), who provided me insight into life cycle assessment and supported me patiently in this.

I was pleased about the opportunity to collaborate with Christoph Bäumer's group at the University of Twente, especially with Iris van den Bosch, Emma van der Minne, and Ellen Kiens. Their responsiveness and effort to include me, even remotely, was heartwarming. Furthermore, I am grateful for learning about COMSOL simulations taught by Dr. Daan Wielens, Daniel Schön, and Dr. Stephan Menzel. Moreover, I am very thankful for Marcel Gerst's and Malte Decker's support for immediate help and always great ideas around IT software and hardware issues. I am also very thankful for the support in the lab by Cerstin Makovicka, Grigory Potemkin, Professor Christian Pithan, Georg Pickartz, Stephan Masberg, and Sylvia van de Waals. Their reliability and great help are outstanding. Besides this, I enjoyed the discussions with Professor Pithan about large-scale perovskite oxide synthesis.

For great scientific discussions and good times in the lab or after work, I would like to thank my best office mates, Anton Kaus and Dr. Suqin He, as well as Professor Moritz Weber, Kapil Nayak, Marcus Wohlgemuth, Sebastian Siegel, Johannes Hellwig, Max Buczek, Judith Knabe, and the rest of the members in the PGI 7. I was happy and honored to work and grow together with my two master students, Ole Kurbjeweit and Linda Joseph.

And in the end, I am deeply thankful for my husband Dr. Mauricio Gago constant emotional support, joking around, and encouragement in all facets of my life. The same gratitude I would like to express to my family, Margret Heymann, Heinrich Heymann, Manuel Heymann, Andrea Schönfeld, and Hermann Vatter. Many thanks also to the physiotherapy specialists Ili M. and Dana Q., who were very creative in developing solutions for my working needs.

The support of all these great people made this work possible. Thank you all.

Contents

1 Introduction

The global economy is attempting to reduce greenhouse gas emissions to limit global warming. For that, the economy shifts from a fossil fuel-intensive to a material-intensive economy as renewable energy, energy storage, and conversion systems must be installed and maintained [1, 2]. It is estimated that to fulfill the Paris climate agreement, the mineral requirements will quadruple by 2040 compared to today's mineral needs in the energy sector [3, 4]. The shift to material-intensive large-scale applications leads to new criticalities of raw materials, and technological, scientific, economic, environmental, and social challenges [5, 6].
Energy conversion technologies are crucial for capping supply and demand gaps in the energy grid from variable renewable energy technologies, and they are crucial for defossilizing the mobility as well as the industrial sector. Green hydrogen is a promising energy carrier that can tackle these challenges as it can be stored long-term, reconverted into electricity in fuel cells, and applied as a chemical agent or fuel. Green hydrogen is produced by electrochemical water splitting in water electrolyzers from renewable energy sources [7–9].
In water electrolysis, there are, however, still efficiency drawbacks that limit today's green hydrogen supply. Especially at the anode, where the oxygen evolution reaction (OER) takes place, the 4-electron transfer step from water to oxygen suffers from sluggish kinetics, lowering the overall performance of the hydrogen production [10, 11]. Moreover, high-performance catalysts can consist of elements such as Ir, Ru, or Pt that have several sustainability drawbacks and might suffer from limited supply in the close future [12].
Hence, materials scientists aim to develop anode catalyst materials that decrease the kinetic barriers and improve the sustainability compared to today's state-of-the-art OER catalyst materials [13–22]. However, determining the intrinsic catalytic performance to achieve a quantifiable material comparison is hard, as various parameters can influence the observed performance in the electrochemical cell. Especially, the low conductivity of catalyst materials and high interface resistances often lead to a decreased observed catalytic performance [15, 17, 23]. Some electrocatalysts have even been discarded because of their limited conductivity [24, 25], although it is not verified if they can have a high intrinsic catalytic activity. Furthermore, uncovering possible catalyst structure-property relationships that may allow scientists to predict OER catalyst design rules for highly efficient catalysts would facilitate the research, but it remains a key discipline up to today. This is because catalytic efficiency relies on the Gibbs free energies (ΔG) of the adsorbates on the catalyst surface during the catalytic cycle, which are experimentally hard to address. Hence, experimentally accessible alternatives to ΔG for determining structure-property relationships of OER catalysts are investigated and highly discussed.
Moreover, evaluating material sustainability in early-stage research, as a further crucial criterion for a holistic elemental choice for the energy transition, is a big challenge. Although several studies highly recommend to evaluate possible threats of material shortages, economic, environmental and social impact for technologies in the energy transition already in early stages

of materials research [26–30], it is seldomly conducted until today, because final process and supply chains are not known at this stage, so that assumptions have to be made.
In this thesis, a method is first established to reveal and quantify intrinsic OER activity trends, disentangled from low catalyst conductivity and occurring interface resistances. Based on this, the intrinsic OER activity trend is correlated to different electronic structure properties of the catalysts. Then, a concept for material sustainability evaluation of the investigated OER electrocatalysts in early-stage research is introduced. These three points tackle the open questions:

- How do the catalyst conductivity and interface resistances influence the OER activity, and can this be disentangled from intrinsic catalytic properties?
- How does the electronic structure influence the observed intrinsic OER activity trend?
- Which crucial sustainability parameters can already be evaluated and quantified for a holistic material choice of electrocatalysts in early-stage research to uncover possible hotspots of their usage for the energy transition?

Here, perovskite oxides are investigated as promising OER catalysts. The perovskite oxide structure $ABO_{3-\delta}$ offers high flexibility for testing various elemental and stoichiometric compositions to reduce the high overpotentials of the OER. However, their composition can drastically influence the conductivity from quasi metallic to insulating behavior. Moreover, the perovskite elemental diversity implies large sustainability differences that are often not addressed in technical performance studies [26, 28, 31, 32].
A high comparability of OER catalytic activity and material properties is achieved with the design of model thin film catalysts. They are grown as epitaxial thin films by pulsed laser deposition (PLD), enabling one to precisely control the catalyst thickness, surface morphology, and crystallinity [33]. A sophisticated thin film design enables us to decouple the intrinsic OER activity from poor electrical conductivity in the catalyst bulk by the substrate choice and the intentional design of dipole interlayers. Based on the intrinsic OER activity trend, we correlate valence band electronic structure properties measured by X-ray photoelectron spectroscopy to uncover possible OER descriptors of the investigated perovskites.
We compare the OER activity of several A- and B-site varied perovskite oxides with the structure $A_{1-x}A'_xBO_{3-\delta}$ where A = La, A' = Ca, Sr, and B = Mn, Fe, Co, Ni. For one, $La_{0.6}Sr_{0.4}CoO_{3-\delta}$, $LaNiO_{3-\delta}$, and $La_{0.67}Sr_{0.33}MnO_{3-\delta}$ are investigated as they are known as OER active catalysts. $La_{0.6}Sr_{0.4}CoO_{3-\delta}$ and $LaNiO_{3-\delta}$ are known in the literature for their high OER performance and are often used as benchmark catalysts for single B-site perovskites [19, 21, 34, 35]. $La_{0.67}Sr_{0.33}MnO_{3-\delta}$ is known for its high oxygen reduction reaction (ORR) activity, which is the reverse reaction of the OER in fuel cells, and is hence often discussed as a bifunctional ORR and OER catalyst [36, 37]. However, especially Co, Mn, and Sr might already face short- and medium-term depletion of known reserves [38]. Sr and Mn depletion of known reserves is expected to be in the next 20-50 years, and Co reserves in the next 50-100 years. Hence, the

depletion of known reserves was taken as the first orientation and easily- available decision criteria toward a holistic elemental choice. We exchange Sr to Ca on the A-site and Co to Ni and Fe on the B-site as Ca and Ni as well as Fe are available from larger reserves [26, 38, 39]. The substituted perovskites $La_{0.6}Ca_{0.4}CoO_{3-\delta}$, $La_{0.6}Ca_{0.4}NiO_{3-\delta}$, $La_{0.6}Sr_{0.4}FeO_{3-\delta}$ and $La_{0.6}Ca_{0.4}FeO_{3-\delta}$ were compared to the benchmark $LaNiO_{3-\delta}$, $La_{0.67}Sr_{0.33}MnO_{3-\delta}$ and $La_{0.6}Sr_{0.4}CoO_{3-\delta}$ catalysts' OER activity.
To address crucial sustainability aspects that are relevant for the high material demand of the energy transition, a concept for a material sustainability evaluation for the OER catalysts is established in the frame of early-stage materials research. The benchmark catalyst $La_{0.6}Sr_{0.4}CoO_{3-\delta}$ is compared to the A- and B-site exchanged $La_{0.6}Ca_{0.4}FeO_{3-\delta}$ as an exemplary case study for this holistic material evaluation for the raw material criticality, economic, environmental and social impact.
Hence, this thesis introduces a model catalyst approach that enables us to differentiate the influence of intrinsic catalytic properties and conductivity as well as contact resistances in the electrode stack and to the electrolyte. It delivers insights into the valence band electronic structure properties of those seven perovskites and their role in OER catalytic activity. It tackles the need to develop a concept for material sustainability evaluation in early-stage research for those model system thin films. This opens up the opportunity to uncover if there are elemental compositions with promising intrinsic catalytic activity and if there are elemental compositions of concern for the energy transition, so that the composition can be reevaluated in terms of their sustainability and technical performance.

Outline: In the background chapter **2**, the working principle of water electrolysis and the role of OER electrocatalysts are introduced in detail. Then, the structural and electronic structure properties, including the conductivity of perovskite oxides, are explained. Based on this, the current state of the literature is given on the influence of conductivity and electronic structure properties on the OER. Then the role of the energy transition's material shortages, economic, environmental, and social impact are reviewed, and its challenges to analyze those in early-stage research are pointed out. Chapter **3** comprises the experimental methods used for the epitaxial growth, thin film characterization, electrochemical tests, and considered methods for the material sustainability evaluation.
In chapter **4**, the epitaxial growth results of the perovskite oxides $La_{0.6}Sr_{0.4}CoO_{3-\delta}$, $La_{0.6}Sr_{0.4}FeO_{3-\delta}$, $La_{0.6}Ca_{0.4}FeO_{3-\delta}$, $La_{0.6}Ca_{0.4}CoO_{3-\delta}$, and $La_{0.6}Ca_{0.4}NiO_{3-\delta}$ are shown. Their lattice constants, surface morphology, resistivity and valence band electronic structure are compared. In chapter **5**, the electrochemical performance results of all seven perovskites are shown. In chapter **6**, the valence band electronic structure properties are correlated to the intrinsic OER trend. In chapter **7**, the material sustainability evaluation results of the two catalysts $La_{0.6}Sr_{0.4}CoO_{3-\delta}$ and $La_{0.6}Ca_{0.4}FeO_{3-\delta}$ are presented. Based on this, the observed chances and limitations of sustainability evaluations in early-stage research are discussed. Chapter **8** comprises the conclusions of the thesis.

2 Background

In this chapter, the working principle of water electrolyzers is explained first. Then, the role of OER catalysts is described, including the two important metrics, overpotential and Tafel slope, which are commonly used to evaluate electrocatalyst activity. Afterwards, the structural and electronic properties of the perovskite oxide family are introduced, including the basics of the transition metal (TM) and oxygen (O) band structures in the valence and conduction band, that are influencing e.g. electrical conductivity, TM-O covalency, and charge transfer energies. Furthermore, as interface resistances to the catalyst support or electrolyte can significantly influence the OER activity, relevant interface resistance properties in electrochemical systems are explained. Based on this, the influence of conductivity and electronic structure on the OER activity is briefly reviewed, pointing out which open questions remain in the literature that this thesis will approach.
In addition to the technical performance of OER catalysts, a sustainable material choice is crucial in the context of the increasing material demand for the energy transition. This includes the sustainability parameters from earth abundance to raw material criticality, as well as the economic, environmental, and social impacts of raw material extraction and processing. These aspects will be reviewed with an emphasis on the relevance for materials scientists in early-stage research.

2.1 Water electrolysis and the role of electrocatalysts

In water electrolysis, water is split into H_2 and O_2 gas in a redox reaction initiated by an applied electrical potential. Water electrolyzers contain a cathode and an anode that are typically separated by a Zirfon diaphragm or polymer membrane [10, 40] (figure 1a). The anode and cathode consist of a current collector and catalyst layer that lowers the overpotential of the half-cell reaction. The electrolyte is an acidic or alkaline water solution that ensures ionic conductivity between the two electrodes and serves as the reactant. The acidic or alkaline environment is decisive about the applicability of the different materials of the separator, current collectors, and catalysts [12, 40]. The highly corrosive surrounding of acidic electrolyte solutions narrows catalyst material choices to noble metals, such as Pt on the cathode and Ir- or Ru-based catalysts on the anode in commercial systems. The alkaline environment is less harsh and allows the application of a broader variety of non-noble catalyst materials, such as the 3*d*-transition metals (TM) Fe, Co, and Ni, also in the form of (complex) metal oxides like the perovskites [10, 12, 40].

This thesis focuses on alkaline water electrolysis (AWE) at room temperature. In AWE, H_2O is reduced to H_2 on the cathode, and hydroxyl ions OH^- are oxidized to O_2 on the anode, following the chemical equations of the hydrogen evolution reaction (HER):

$$2\,H_2O + 2\,e^- \longrightarrow H_2 + 2\,OH^- \tag{1}$$

and OER:

$$4\,OH^- \longrightarrow O_2 + 2\,H_2O + 4\,e^- \tag{2}$$

In the HER, only two electrons are transferred to produce H_2. In the OER, the oxidation of hydroxyl ions to O_2 requires a transfer of 4 electrons and protons in a multistep reaction. This catalytic cycle is highly discussed to date.

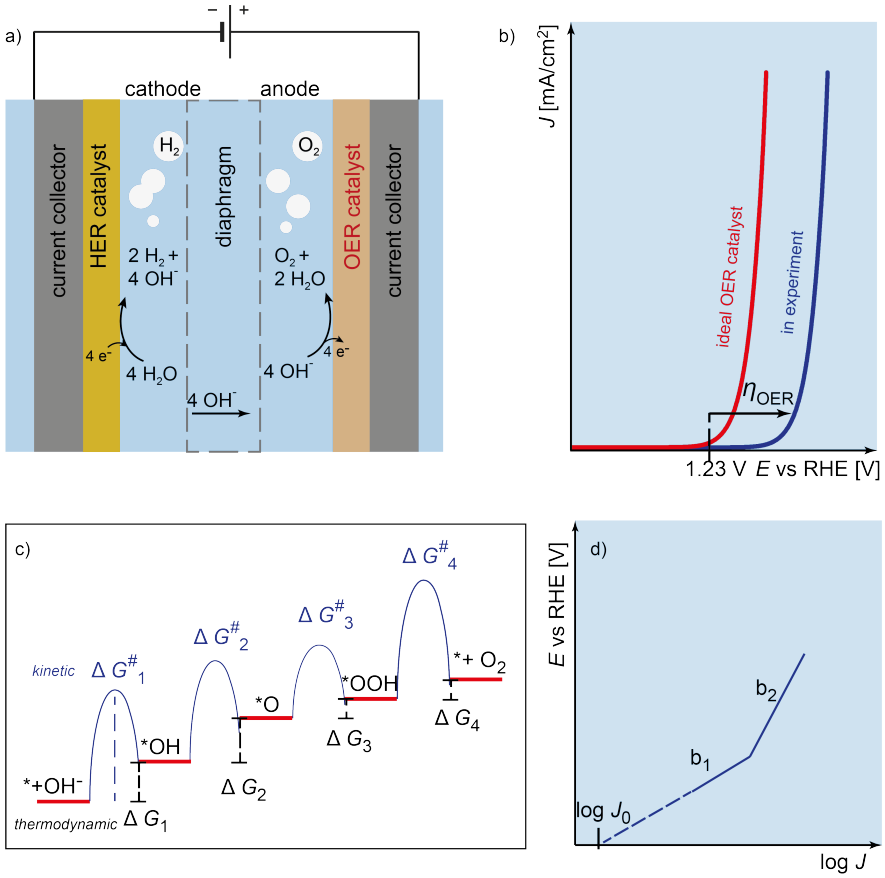

Figure 1: a) Sketch of an alkaline water electrolyzer. b) Cyclic voltammetry example of an ideal OER catalyst and catalyst in experiment, where an additional overpotential η_{OER} has to be applied to drive the reaction. c) Sketch of a Gibbs free energy diagram of the four electron transfer steps in the OER adapted from [41–43]. ΔG_n is the thermodynamic energy difference from one reaction intermediate (*OH, *O, *OOH, * + O_2) to another. $\Delta G_n^{\#}$ is the kinetic energy of each step that has to be overcome to form the subsequent reaction intermediate. d) Illustration of the Tafel plot with two different Tafel slopes b_1 and b_2.

In the simplest case, the four steps are:

$$OH^- + * \longrightarrow *OH + e^- \tag{3}$$

$$OH^- + *OH \longrightarrow H_2O + *O + e^- \tag{4}$$

$$OH^- + *O \longrightarrow *OOH + e^- \tag{5}$$

$$OH^- + *OOH \longrightarrow O_2 + H_2O + e^- + * \tag{6}$$

where the * denotes the active site of the OER catalyst [42]. In the first step, OH^- is adsorbed on the surface and the first electron is released into the electrode. In the second step, the binding *OH is deprotonized and further oxidized, forming *O. Then, another OH^- reacts with the oxygen intermediate to *OOH undergoing further oxidation. In the last step, *OOH is deprotonated and oxidized to O_2 gas. This multistep reaction is the bottleneck in water electrolysis. The thermodynamically required potential E^0 for the OER reaction is 1.23 V versus the reversible hydrogen electrode (vs RHE) [42]. In water electrolysis experiments, however, higher potentials need to be applied (E^{applied}) to drive the reaction, leading to the higher overpotentials η (figure 1b):

$$\eta = E^{\text{applied}} - E^0 \tag{7}$$

These required overpotentials originate from the thermodynamic and kinetic barriers between each reaction intermediate in the OER. As illustrated in figure 1c the Gibbs free energy difference ΔG_n (with n = 1, 2, 3, 4 for each step) between each reaction intermediate has to be overcome by the applied potential [41–44]. For an ideal catalyst, the adsorption of all intermediate steps is perfectly aligned, and the adsorbates bond neither too weakly nor too strongly in each step, leading to the smallest ΔG_n possible for each reaction intermediate. This catalyst follows the so-called Sabatier principle and can catalyze the reaction without any thermodynamic overpotential. If the adsorbates bind too strongly or too weakly, the catalyst can only react by applying an η because some ΔG_n is higher than under perfect conditions. The balance between weak and strong binding leads to volcano shaped activity trends, where the ideal catalyst is located at the top, catalyzing the reaction with η_{OER} close to 0 V [13, 41, 43, 44].
However, an ideal catalyst with $\eta \approx 0\,\text{V}$ can only count for a redox process that includes a maximum of 2 reaction intermediates [41, 45]. In the OER as a multistep reaction, the single adsorbates can only be optimal for some intermediates. Therefore, another reaction intermediate automatically has a non-optimized adsorbate bonding condition [41, 45]. Since the Gibbs free energy ΔG_n of each intermediate step in the OER scales linearly with the others, it has to lead to a higher overpotential *per se*, called the scaling relations. The scaling relations are estimated to cause an overpotential of $\eta \approx 0.37\,\text{V}$ in the OER [10, 45, 46]. Thus, for the perovskites investigated in this thesis, the potential required to drive the OER is expected to be around 1.6 V vs RHE.

Besides the role of thermodynamic energy differences of the reaction intermediates, the kinetic barriers from one step to another play an important role. They are illustrated in figure 1c as parabolas between each step with their activation energy barriers of $\Delta G_n^{\#}$ (with n = 1, 2, 3, 4). The rate-determining step ($\Delta G_{\mathsf{rds}}^{\#}$) of those four steps controls the potential inclination for a certain amount of generated current. In other words, it dictates the ratio of $\frac{\Delta E}{\Delta \log J}$. This is called the Tafel slope b which is illustrated in figure 1d in the Tafel plot where log J vs E is plotted. The Tafel slope is derived from the Butler-Volmer equation:

$$J = J_0[exp(\frac{\alpha e\eta}{k_{\mathsf{B}}T}) - exp(-\frac{(1-\alpha)e\eta}{k_{\mathsf{B}}T})] \tag{8}$$

where J_0 is the exchange current density, that is the extrapolated *x*-axis intercept in figure 1d. α is the transfer coefficient of the anodic oxidation reaction, $(1-\alpha)$ is the transfer coefficient of the cathodic reduction reaction, and e is the elementary charge. η is normalized by the thermal activity, which is the product of the Boltzmann constant k_{B} and the temperature T. When the anodic overpotential is high enough, the term of the cathodic reaction is negligible. The remaining term of the anodic reaction can be expressed with the decadic logarithm:

$$\log J = \log J_0 + \frac{\eta}{b} \tag{9}$$

as the Tafel equation. Depending on the current density interval, the Tafel slope b can change as a function of the current density as illustrated by b_1 and b_2 in figure 1d. The value of the Tafel slope is determined by its rate limiting step, and depends on how many electrons n_{b} have already been transferred before the rate determining step follows, and how many electrons n_{d} are transferred during the rate determining step [47]:

$$b = \left(\frac{\delta E}{\delta log J}\right) = \frac{2.303RT}{F}\frac{1}{n_{\mathsf{b}} + \alpha n_{\mathsf{d}}} \approx \frac{59\,\mathrm{mV\,dec^{-1}}}{n_{\mathsf{b}} + \alpha n_{\mathsf{d}}} \tag{10}$$

When the first reaction step in the OER catalytic cycle is rate determining, n_{b} and n_{d} are both one, resulting in a Tafel slope around 120 mV dec^{-1} in the OER. When subsequent steps are rate limiting, the Tafel slope gets smaller [47, 48] which is favorable for an efficient catalyst. In this thesis, the overpotentials and Tafel slopes are determined to evaluate which perovskite catalysts most effectively decrease the kinetic and potential barriers. Typically, the potential determining step ΔG_{pds} is linked via the Bronsted-Evans-Polanyi principle to the rate-limiting step $\Delta G_{\mathsf{rds}}^{\#}$, so that the pds and rds are the same. Exner and Koper have shown that this is likely the case, but not always [43, 49].
As the ΔG_n and $\Delta G_n^{\#}$ are experimentally hard to access, scientists aim to find experimentally measurable structure-property relationships that dictate the OER activity of a catalyst [11]. For one, the electronic conductivity is discussed to play a big role, as electrocatalytic reactions always require electron transfer [17]. Furthermore, the OER activity of an electrocatalyst strongly

relates to its structural and valence and conduction band electronic material properties [11, 13, 14, 19, 42]. Those properties can be the number of 3*d*-electrons of the transition metal (TM), the e_g electron filling, the TM-O covalency, the location of the oxygen states to the Fermi level, or charge transfer energy, which are discussed to date as possible OER descriptors [13, 14, 16, 18]. To understand their role, the following chapter describes the structural properties and valence and conduction band electronic structure of the here used perovskite oxide catalysts.

2.2 Perovskite crystal structure and their epitaxial thin films

Perovskite oxides crystallize in the $ABO_{3-\delta}$ structure as shown in figure 2a. The A-site cation is 12-fold coordinated, and the B-site is 6-fold coordinated by oxygen anions. The A-site has a

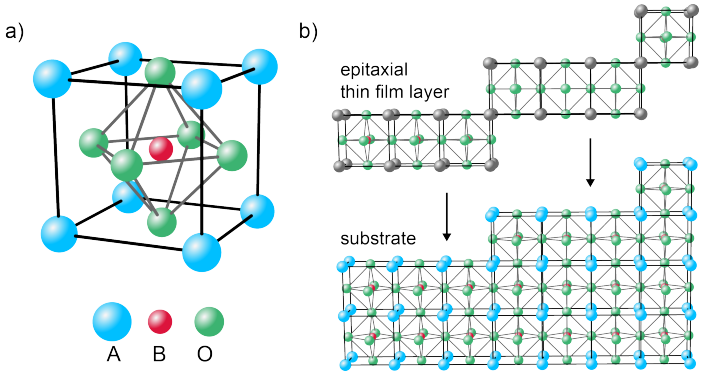

Figure 2: a) One perovskite oxide unit cell. b) Single crystalline substrate in the bottom and epitaxial thin film monolayer at the top, illustration is inspired by Weber *et al*. [33].

larger ionic radius with values typically above 90 pm, and the B-site ionic radius is typically above 50 pm [50]. The ionic radius of O^{2-} is the largest with a value of 140 pm. The structure opens up the opportunity to insert 90 % of elements in the periodic table. Until today, more than 1000 compositions have been identified [18]. Often, 3*d* transition metals occupy the B-site, which is typically considered as catalytically active site in the OER [17, 18]. Also noble metals, such as Ru or Ir, can occupy the B-site and have been reported to be highly active in the OER [31, 32]. Rare earth elements and alkaline earth elements typically occupy the A-site. In this thesis, La, Sr, and Ca were used on the A-site, and Mn, Fe, Co, and Ni on the B-site. The final composition determines the crystal system and lattice parameter, and relies on several factors such as ionic radii, octahedral tilting, cation (off-)stoichiometry, or oxygen vacancy content [51]. For example, the crystal system can be cubic, tetragonal, rhombohedral, or orthorhombic.
Here, the perovskites are grown as epitaxial thin films on single-crystalline substrates (figure 2b). The epitaxial thin films serve as model catalyst systems as they have several advantages compared to common powder catalysts, facilitating the revelation of intrinsic catalytic properties and

structure-functional properties relevant for the OER [33, 52]. They exhibit smooth surface morphologies with single crystal facet orientation, are free of catalyst binder and conductive carbon, and allows one to determine catalytic properties also free of grain boundary effects [20, 33, 52]. For a successful epitaxial growth, the substrate has to exhibit similar lattice parameters as the perovskites of interest. It can grow with a strain (ϵ_{strain}) on the substrate which is defined as:

$$\epsilon_{\text{strain}} = \frac{a_{\text{substrate}} - a_{\text{bulk}}}{a_{\text{bulk}}} \tag{11}$$

where $a_{\text{substrate}}$ is the in-plane lattice parameter of the substrate, and a_{bulk} the in-plane lattice parameter of the perovskite bulk. In this thesis, $LaAlO_3$, $NdGdO_3$ and $SrTiO_3$ substrates were used which exhibit an increasing lattice parameter of 3.788 Å (pseudocubic), 3.865 Å (pseudocubic) and 3.905 Å (cubic), respectively. For example, $La_{0.6}Sr_{0.4}CoO_{3-\delta}$ as powder shows a rhombohedral structure which gives a pseudocubic lattice parameter of 3.844 Å [53]. On a $SrTiO_3$ substrate, this leads to a lattice mismatch of 1.6% in tensile strain. For the epitaxial growth, PLD is used, which is explained in section 3.1.

2.3 Conductivity and electronic structure in perovskite oxides

Perovskite oxides can exhibit vastly different electrical conductivity depending on the conduction and valence band structure, the band gap itself, possible different conduction mechanisms, and carrier mobility. Those parameters depend on the repulsive and attractive forces of the transition metal (TM) 3*d* states and the oxygen (O) 2*p* states in the octahedral field, resulting from different electronnegativities, ionic radii and octahedral tilting [54]. The d_{z^2} and $d_{x^2-y^2}$ orbitals of the 3*d* TM states directly overlap with the neighboring O 2*p* orbitals, leading to a repulsion. This increases the energy level of those states compared to d_{xy} d_{xz} and d_{yz} orbitals, which is called the crystal field splitting. The upper states are the e_g states and the lower ones t_{2g} states [54]. $SrTiO_3$ for example, is a wide band gap insulator and the Ti 3*d*-O 2*p* bond is rather ionic. The perovskites used in this thesis have smaller band gaps and more covalent TM-O bonds due to a larger hybridization of the TM and O bands.
In the Zaanen, Sawatzky and Allen model [55, 56] so-called charge transfer and Mott-Hubbard metal-to-insulator transitions are defined. These models are based on the energetic distances between the filled O 2*p* states (blue), the highest occupied, and lowest unoccupied (transition) metal states (red) as illustrated in figure 3. In a charge transfer metal, also called semi-metal, the filled O 2*p* states strongly overlap with the highest filled metal states (figure 3 left side), and the Fermi level is located within those states. The charge transfer energy is the distance between the center of weight of those states, and is denoted with a Δ. Newer findings also describe that especially in high oxidation state TM oxides, the TM band can be lower than the O 2*p* band, which is denoted as negative charge transfer in correlated compounds [57].
When the O 2*p* states and the metal states separate and Δ increases, a band gap evolves, and the metal oxide becomes a charge transfer insulator (second sketch of figure 3). Here, the

distance between the highest filled and lowest unfilled metal states is smaller than the distance between the O 2*p* states and the lowest unfilled TM states (Δ). Tis energetic difference is defined as *U*'. When *U*' becomes smaller than Δ the notation changes to a Mott-Hubbard insulator. When the filled and unfilled TM states move closer and partly overlap (fourth sketch of figure 3), the TM oxide is denoted as low *U*'-metal, and typically exhibits high conductivity.

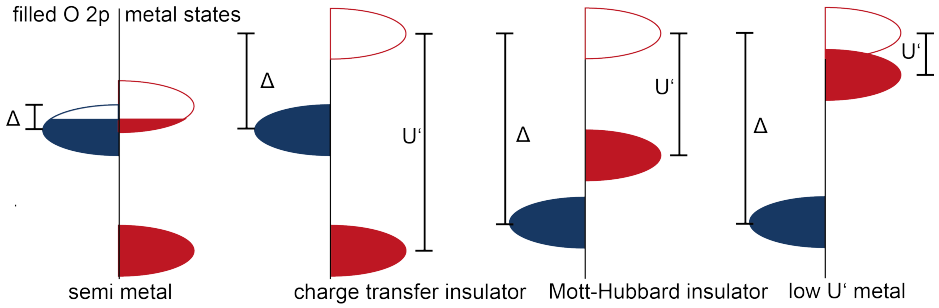

Figure 3: Metal to insulator transition of the charge transfer and Mott-Hubbard type adapted from [55, 56].

Many $ABO_{3-\delta}$ perovskites such as $LaMnO_{3-\delta}$, $LaFeO_{3-\delta}$ and $LaCoO_{3-\delta}$ have a band gap and show only very limited conductivity, being discussed as semiconductors or insulators of the Mott-Hubbard or charge transfer type [58]. In contrast, $LaNiO_{3-\delta}$ shows quasi-metallic behavior. Its Fermi level is located in the valence band. Corresponding sketches of $LaMnO_{3-\delta}$, $LaFeO_{3-\delta}$, $LaCoO_{3-\delta}$, and $LaNiO_{3-\delta}$ valence and conduction band structure are shown in figure 4 on the left side of each panel.
A-site doping in the $A_{1-x}A'_xBO_{3-\delta}$ perovskite with a bivalent cation such as the alkaline metals A' = Sr or Ca, induces nominally *p*-type doping as the B-site oxidation state increases. The hole carrier density increases in principle with the acceptor concentration N_a of the doping material. However, A-site doping alone does not always predict the conductivity and final hole carrier density in these systems well, as other phenomena, such as the carrier mobility and defect formation, can influence the conductivity significantly [54].

$LaCoO_{3-\delta}$ has a small band gap of 0.6 eV and is denoted as semiconductor [59, 60]. The sketch in figure 4a shows that the Fermi level is located between the filled O 2*p*, Co 3*d* and unfilled Co 3*d* states [16]. The filled Co 3*d* states comprise the e_g and t_{2g} states. Upon Sr doping in the solid solution series of $La_{1-x}Sr_xCoO_{3-\delta}$, the valence band shifts to lower binding energies close to the Fermi level. Already above $x \geq 0.2$, the valence band states shift into the Fermi level, leading to semi-metallic behavior and high conductivity [61–63] (figure 4a). Moreover, with increased A-site doping, the filled O 2*p* and Co 3*d* states move closer to each other, leading to increased Co-O covalency [16, 34].
$LaFeO_{3-\delta}$ is a wide band gap insulator with a value of $2 - 2.2\,\mathrm{eV}$. Upon Sr doping, the O 2*p*

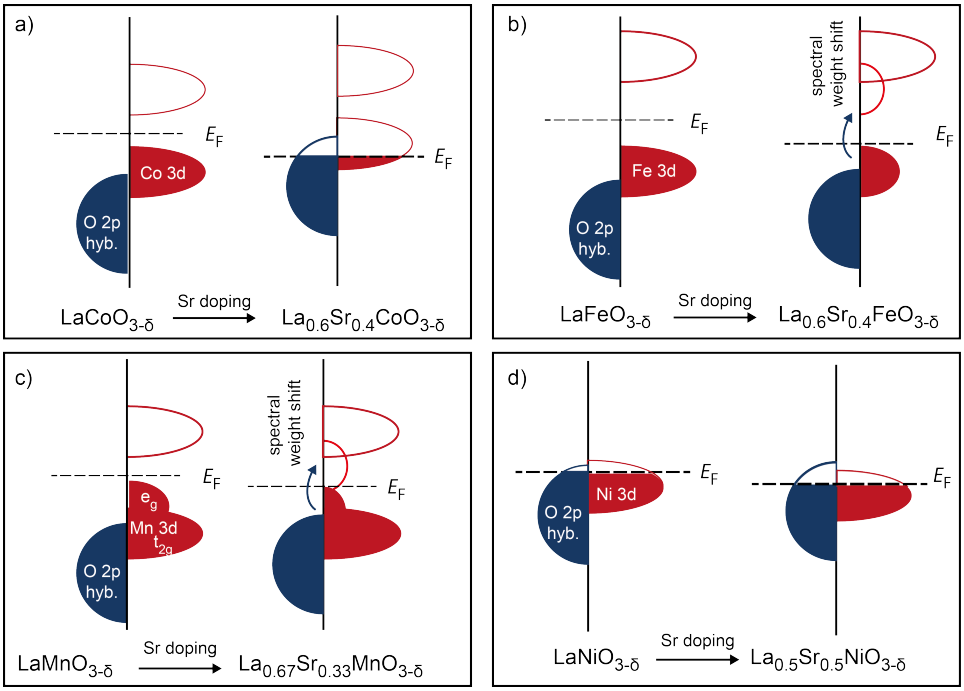

Figure 4: Band structure of $LMO_{3-\delta}$ (M = Mn, Fe, Co, Ni) and doped $La_{1-x}Sr_xMO_{3-\delta}$. Sketches of the a) manganates are drawn from [64–66], b) for the ferrates from [35, 65, 67, 68], c) for the cobaltates from [16], and d) for the nickelates taken from [65, 69]. O 2*p* states are partially hybrid states with the TM 3*d* states as described by Hong *et al*. [14, 65].

and Fe 3*d* states shift toward the Fermi level, the Fe 3*d* and O 2*p* states move closer to each other, and the occupation of the available Fe 3*d* state decreases [35, 65, 67]. At the same time, a new electronic state evolves above the Fermi level, reducing the band gap to 1 eV [67, 70] for $x = 0.4$. Such decrease of the filled Fe 3*d* states coupled to the evolution of the new and empty state in the conduction band is called spectral weight shift. In contrast to $La_{0.6}Sr_{0.4}CoO_{3-\delta}$, the induced hole states cannot fill the band gap and hence, $La_{0.6}Sr_{0.4}FeO_{3-\delta}$ shows lower conductivity, and is denoted as a semiconductor. Furthermore, Wadati *et al*. observe strongly localized states in $La_{0.6}Sr_{0.4}FeO_{3-\delta}$, suggesting a polaron formation, leading to lower carrier mobility than in $La_{0.6}Sr_{0.4}CoO_{3-\delta}$, where no polaron formation is observed. The carrier mobility is a crucial factor determining the observed conductivity, in addition to the carrier concentration [67]. Moreover, $La_{0.6}Sr_{0.4}FeO_{3-\delta}$ shows a typical semiconductor conductivity-temperature curve, indicating the significantly different behavior compared to the doped cobaltates [67].
$LaMnO_{3-\delta}$ is in the d^4 high spin configuration and has nominally one electron in the e_g states. In

the sketch of figure 4c, its intensity is relatively low. The t_{2g} states are differentiable from the e_g states because the crystal field splitting in the manganate is the highest among Mn, Fe, Co, and Ni based perovskites [64, 66, 71]. The $LaMnO_{3-\delta}$ band gap is estimated between 1.2 eV and 1.7 eV [64, 72]. Upon Sr doping, the valence band edge shifts toward the Fermi level, and the Mn 3*d* e_g density of states decreases while the corresponding unfilled e_g state evolves in the band gap above the Fermi level. This spectral weight shift closes the band gap for $0.3 \leq x \geq 0.6$, leading to the metallic behavior of Sr-doped $LaMnO_{3-\delta}$. Note, that the density of states around the Fermi level remains small [64].

$LaNiO_{3-\delta}$, as mentioned before, exhibits metallic behavior. Typically, strong electron-electron interactions within one orbital in the octahedral space of the $LaMO_{3-\delta}$ (M = Mn, Fe, Co) lead to an electrostatic repulsion. As a result, the octahedral field splitting is further split, forming a band gap. For $LaNiO_{3-\delta}$, however, the repulsion is not significant, hence it is a correlated metal [54]. Liu *et al*. observe that with Sr doping ($0 < x < 0.5$), the conductivity decreases consecutively, however, only within one order of magnitude. They describe that Sr doping increases the Ni 3*d* and O 2*p* overlap, which they link to increased Ni-O covalency. Note, that the solid-solution series of $(La,Sr)NiO_{3-\delta}$ has not been extensively studied yet, as such substitutions often result in K_2NiF_4 phase [73, 74]. The K_2NiF_4 is the first member of the Ruddlesden-Popper phase with the formula: $A_{n+1}B_nO_{3n+1}$.

Green and Sawatzky made an extensive literature review on the charge transfer energy Δ of such 3*d* TM complex oxides. They found that with increasing atomic number of the 3*d* transition metals Δ decreases. Further, Δ decreases with increasing oxidation state of the TM. For the perovskites studied in this thesis, Δ might decrease from Mn to Ni. For the A-site doped cobaltates and nickelates, the oxidation state is nominally between 3+ and 4+, and is expected to be at the border to a negative Δ [57].

To summarize, the undoped $LaMnO_{3-\delta}$, $LaFeO_{3-\delta}$, and $LaCoO_{3-\delta}$ perovskites have a low conductivity and are rather semiconducting or insulating. A-site doping of those perovskites increases the conductivity, leading to metallic behavior in the cobaltates and manganates for certain doping concentrations. For the ferrates, A-site doping increases the conductivity only modestly compared to the manganates and cobaltates up to x = 0.4, owing to the persistence of a band gap and polaron formation. Consequently, they remain semiconducting within this doping range. In contrast, $LaNiO_{3-\delta}$ is a correlated metal, and A-site doping reduces its conductivity only slightly, so the doped nickelates retain their predominantly metallic character.

2.3.1 Role of conductivity in OER electrocatalysts

In the literature, it is often addressed that a high electrical conductivity is a crucial necessity for a good electrocatalyst [17, 25]. The high electrical conductivity ensures an unhindered electron transport through the material bulk. Therefore, perovskites with high resistivity are often described to be poor electrocatalysts such as $LaFeO_{3-\delta}$, $LaCoO_{3-\delta}$ or $LaMnO_{3-\delta}$ [14, 15] and low-conductivity perovskites have been discarded from catalyst research in some cases, due

to the difficulty to run sufficiently high current [24]. However, it is hard to disentangle whether low electrochemical activity stems from high bulk resistivity or poor intrinsic catalytic properties [75, 76]. The intrinsic catalytic properties reflect the ability to lower the kinetic barriers for the electrochemical reaction at the electrolyte/catalyst interface, independent of their resistivity and additional stack resistances. For example, substituting Ni into the solid-solution series of $La_{0.7}Sr_{0.3}Fe_{1-x}Ni_xO_{3-\delta}$ induces a phase transition and increased oxygen vacancy content, leading to an overall lower resistivity that correlates with the OER performance [77]. Furthermore, $LaCoO_3$ shows comparably low OER activity in experiment, but lowering its resistivity through compressive lattice strain and introducing conductive support layers increases the OER activity [78, 79]. Additionally, contact resistances (induced e.g. through space charge layers) at the interface to the substrate or support layer can dilute the determination of intrinsic catalytic properties [32, 34, 80–82]. This will be detailed in section 2.4. These examples indicate a correlation between electrical and electrochemical properties, yet it remains often unclear if a varied electrical resistivity directly affects the intrinsic catalytic activity of the OER catalyst. Further, the relations between electron transport pathways, bulk and interface resistances remain unclear and pathway-dependent current density losses are not quantified.
In chapter 5, the influence of electrical resistivity and contact resistances are systematically decoupled from the intrinsic catalytic activity in the OER for all perovskite oxides that cover a resistivity range of three orders of magnitude. The epitaxial model systems allow precise tuning of the electron transport pathways to the current collectors, enabling such differentiation of intrinsic OER activity and current losses through material resistance.

2.3.2 Electronic structure OER descriptors

The electronic structure of perovskite oxides is discussed to have a crucial influence on the catalytic activity [14, 16, 17, 69, 83]. As described in section 2.1, a catalyst decreases the Gibbs free energy ΔG_n and kinetic energy barrier $\Delta G_\mathrm{n}^{\#}$ between each reaction intermediate, leading to a lower η. To which extent these energy barriers can be decreased by a catalyst may depend on their electronic structure, as it e.g. influences the adsorption strength of the reaction intermediates in the OER. Therefore, different properties of the electronic structure are correlated to their OER activity to uncover possible relationships between them. Those electronic structure properties are called OER descriptors.
e_g electron filling: One electronic structure property that is discussed to influence the OER activity is the e_g electron filling. The e_g orbitals often determine the electronic nature of the available electronic states close to the Fermi level (section 2.3), and the e_g orbitals directly overlap with the orbitals of the OH^- adsorbates. The e_g orbitals of the catalyst and the OH^- adsorbates form a σ-bond [84], where the electrons fill the antibonding states. The e_g electron filling itself depends on the number of electrons of the TM cation and on the spin configuration in the octahedral surrounding. In figure 5a this is sketched for $LaMnO_{3-\delta}$, $LaFeO_{3-\delta}$, $LaCoO_{3-\delta}$ and $LaNiO_{3-\delta}$. $LaMnO_{3-\delta}$ has d^4-electrons that are distributed in a high spin (hs) configuration.

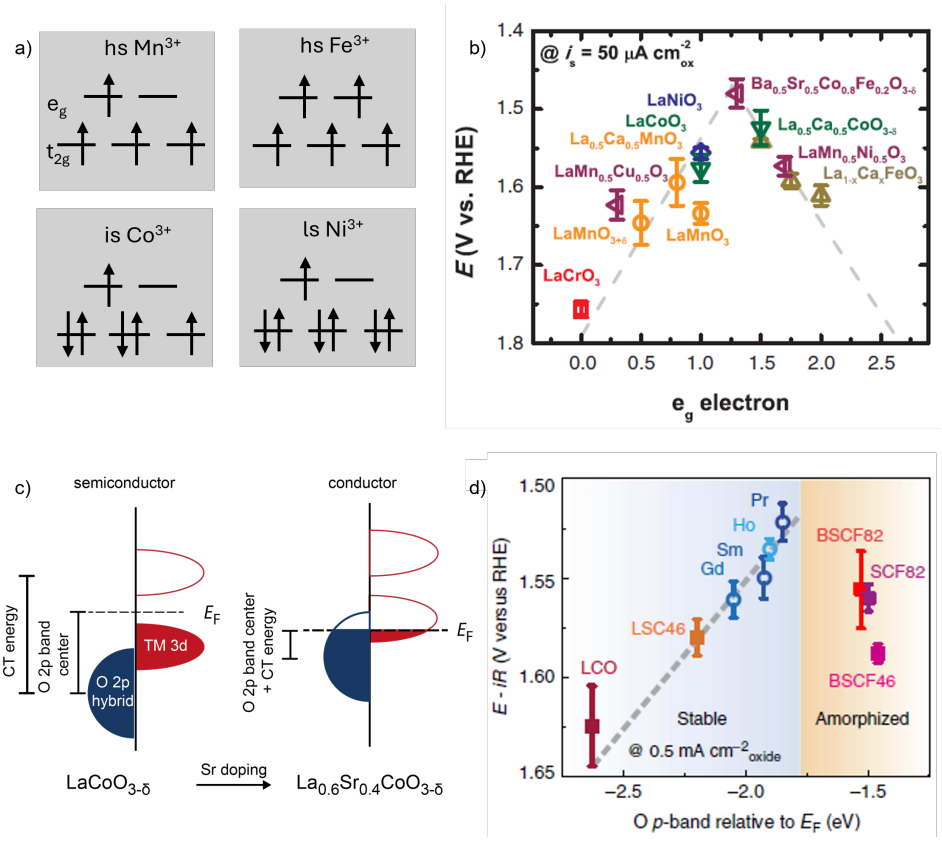

Figure 5: a) Spin configuration and e_g filling of $LaMnO_{3-\delta}$, $LaFeO_{3-\delta}$, $LaCoO_{3-\delta}$ and $LaNiO_{3-\delta}$ in line with ref. [13]. b) Volcano trend of the OER potential at 50 µA cm^{-2} in dependence of the catalyst e_g filling published by Suntivich *et al*. from [13]. Reprinted with permission from AAAS. c) Band structure of a semiconductor and semi-metal, where the O 2*p* band center and charge transfer (CT) energy are drawn in. d) Volcano trend of the OER potential at 500 µA cm^{-2} in dependence of the catalyst O 2*p* band center published by Grimaud *et al*. [83]. Reproduced with permission from Springer Nature.

The resulting e_g filling is one. $LaFeO_{3-\delta}$ has one additional *d*-electron, yielding an e_g filling of two in the hs configuration. For $LaCoO_{3-\delta}$, the spin configuration is discussed to date. Here, the intermediate spin configuration (is) configuration is assumed according to ref. [13], resulting in an e_g filling of one. $LaNiO_3$ is typically observed in a low spin (ls) configuration, yielding an e_g filling of one.

Suntivich *et al*. found that perovskite oxides with an e_g filling close to one exhibit the highest OER activity. Figure 5b shows their correlation plot between the e_g electron filling of the per-

ovskite catalysts and the OER potential recorded at 50 µA cm^{-2}. Perovskites with significantly higher or lower e_g filling than one exhibit lower OER activity, leading to a volcano-shaped trend of the OER activity. For those perovskites that exhibit the same e_g filling close to one, the TM-O covalency additionally enhances the OER activity. This trend they observed for the three perovskites $LaMO_3$ with M = Mn, Co, Ni that all have an e_g filling of one but their covalency and OER accordingly increases with $LaMnO_{3-\delta}$ <$LaCoO_{3-\delta}$ <$LaNiO_{3-\delta}$. Other studies have also observed the important role of TM-O covalency [16, 17, 69]. For example, a higher covalency in the (La,Sr)$CoO_{3-\delta}$ solid solution series can induce a change in OER mechanism from the absorption evolution mechanism to the lattice oxygen mechanism, reducing the thermodynamic barriers in the catalytic cycle [16, 85].

O 2*p* band center: Another electronic structure parameter that is discussed to influence the OER catalytic activity is the energetic distance between the O 2*p* states in the valence band and the Fermi level (figure 5c) [14, 18, 83]. The energetic distance of the centroid of the O 2p bands and the Fermi level is called the O 2*p* band center. When OH^- binds/adsorbs at the dangling bond of a surface transition metal, its energy might align to the O 2*p* states of the perovskite. Hence, the adsorbed oxygen species would align to the energetic level of the O 2*p* bands that have a defined distance to the Fermi level, which influences how strongly or weakly the oxygen species is bound to the catalyst surface. Grimaud *et al*. studied the OER activity trend of double perovskites and their energetic distance between the O 2*p* band center and Fermi level. The correlation shows a volcano-shaped trend as seen in figure 5d. Catalysts with higher O 2*p* band center are located on the left side. When the O 2*p* band center is located too close to the Fermi level, catalysts amorphize rapidly, decreasing the OER performance and forming the volcano trend. Therefore, an intermediate O 2*p* band center should lead to the highest OER activity [83].

Charge transfer energy: Hong *et al*. describe that the O 2*p* band center correlates with the OER activity well, when the perovskites are semi-metallic. However, they claim that for semiconducting perovskite catalysts, the O 2*p* band center does not correlate to the OER activity. Instead, the charge-transfer energy, which is the energy difference of the O 2*p* band center to the first unoccupied state, correlates with the OER activity of both, metallic and semiconductor perovskite catalysts. For the semi-metallic perovskite, the charge-transfer energy is related to the O 2*p* band center as can be seen in figure 5c on the right side. For semiconductors, the charge-transfer energy is larger, as the unoccupied states are above the band gap (figure 5c on the left side) [14].

In this thesis, the four OER descriptors e_g filling, energetic distance between the filled TM 3*d* and O 2*p* states (ΔTM 3*d*-O 2*p*), O 2*p* band center and charge-transfer energy will be addressed. For that, the perovskite oxide valence band is recorded with X-ray photoelectron spectroscopy. Details on this methodology and their results are shown in section 3.4 and 4.4.3.

2.4 Substrate/catalyst/electrolyte interface resistances

Besides low electrical conductivity, interface resistances between the catalyst and substrate, or the catalyst and electrolyte can significantly decrease the OER activity [23, 34]. At the catalyst/electrolyte interface, the adsorption of ions and polar molecules, such as OH^- and H_2O, induces an electrode polarization and consequently a potential drop across the interface. This interface charge distribution leads to the formation of a capacitor, also called the electrochemical double layer [86]. In addition to the adsorption of polar species, the Fermi level of the catalyst and electrolyte equilibrate and can form a space charge layer, leading to a contact resistance. The same also counts for the substrate/catalyst interface.
Figure 6a shows the case of a *p*-type OER catalyst with ohmic contacts at both interfaces between the catalyst to the substrate and the electrolyte. The conduction and valence bands are bent upward, which allows the holes to travel to the electrolyte, where they can recombine with the incoming electrons from the OH^- oxidation process. These electrons are then transferred into the electrode. In the case of figure 6b a space charge barrier exists between the substrate

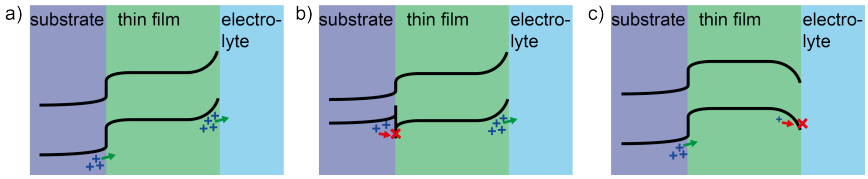

Figure 6: Band bending at the substrate/thin film interface and thin film/electrolyte interface. Holes need to move toward the electrolyte in order to receive the incoming electrons from the OER. a) Upward band bending is beneficial for the hole transport at both interfaces. b) At the substrate/thin film interface the bands are bent downward, hindering sufficient hole transport. c) At the thin film/electrolyte interface, hole transport to the electrolyte is hindered due to downward band bending. This illustration is inspired by [23].

and the catalyst layer which hampers the hole transport to the catalyst layer. This is a disadvantage for catalyzing the OER [23]. In the case of figure 6c, the bands of the catalyst are bent downward to the electrolyte, leading to a hampered electron transfer at this interface for the OER.
The band bending and space charge barrier at the electrolyte/catalyst interface is an unavoidable property of the chosen catalyst material due to its individual electronic band structure and energetic distance to the Fermi level of the electrolyte. However, the band bending and space charge barrier at the catalyst/substrate interface can be tuned by the choice of the substrate and by interface engineering. For epitaxial perovskite thin films, typically Nb-doped $SrTiO_3$ (Nb:$SrTiO_3$) is used as a conductive substrate to ensure electrical contact for the catalyst layer, which was also applied in this thesis. However, Nb:$SrTiO_3$ is an *n*-type conductor, and it was already reported that large contact resistances can form at the interface of Nb:$SrTiO_3$ and *p*-type perovskite oxide thin films [32, 34, 80–82]. Therefore, this thesis investigates the influence

of the substrate/catalyst contact resistance on the overall performance. The interface resistances are systematically studied with impedance spectroscopy (more details in section 5), and a dipole interlayer approach is used to decrease the contact resistances between Nb:$SrTiO_3$ and *p*-type thin films. The decoupling of high electrical resistivity and high interface resistances of the perovskite epitaxial thin films enable us to reveal their intrinsic OER catalytic activity. This builds the basis for a fair comparison of the catalysts in the sustainability evaluation.

2.5 Sustainability evaluation of energy conversion technologies in early-stage research

Besides a fundamental understanding of catalyst performances and physical descriptors, this thesis assesses the sustainability of the proposed OER catalysts. The sustainability of such catalysts is crucial in an industrial roll-out where large amounts of minerals are required for their production [2–4]. Therefore, the early-stage materials science community makes large efforts to shed light on the chemical and physical properties of energy materials that are “less scarce”, “more earth abundant” and “less costly” than state-of-the-art electrolyzer, fuel cell and battery materials [10, 87–92]. However, different terms such as “shortage”, “scarcity”, or “earth abundance” and the price are often not clearly defined and not quantified for the investigated materials. Moreover, the environmental, geopolitical, or social impacts are seldomly considered, although they are of high importance for the prevention of potential supply chain disruptions, ecosystem damage or social disparities.
For this reason, there are growing efforts by governmental and scientific institutions to quantify potential risks for material supply, ecological, economic and social aspects as well as technological requirements for new electrolyzers, fuel cells and batteries [26–29, 93–98]. Recently, the effort for holistic material choice evaluation in early-stage material development was recommended by Klemenz *et al*. who explain that a “second-best” performance material can be more sustainable in a holistic evaluation than the material with the higher performance [26]. Helbig *et al*. recommend evaluating material sustainability in basic research to estimate possible supply risks and environmental impacts using the example of yttrium manganese oxide ($YMnO_3$) for electronic applications [27]. Porzio and Scown recommend comparing new battery technology performances and their potential environmental impact to push sustainable battery development [29]. Eikeng *et al*. provide an extensive study on the future availability of critical raw materials for commercial hydrogen electrolyzers and fuel cell technologies. They point out the potential supply lacks of, for example, Ni for AWE or platinum group metals for proton exchange membrane electrolyzers [12]. Yet, this study includes neither an estimate of new or alternative materials that are in early-stage development nor a full sustainability evaluation. However, conducting a more holistic material evaluation in early-stage materials research is extremely challenging because the observed material’s functionality as well as physical and chemical properties in laboratory scale model systems - such as applied also in this thesis for

perovskite-based OER catalysts - need to be projected to global material supply chains and industrial application standards.
In this thesis, the epitaxial thin film model catalyst $La_{0.6}Sr_{0.4}CoO_{3-\delta}$ is compared to the A- and B-site exchanged $La_{0.6}Ca_{0.4}FeO_{3-\delta}$ in a sustainability evaluation that is exemplary for materials research in such early stages. The evaluation comprises the material criticality, economic, environmental, and social impacts, and the role of material recycling as illustrated in figure 7. In

Figure 7: Relevant sustainability parameters for a holistic materials evaluation of perovskite oxide OER catalysts.

this way, this thesis provides a guideline to translate fundamental material insights into realistic roll-out scenarios. The relevance of the sustainability parameters from earth abundance to material criticality, economic, environmental, and social impacts for the energy transition is briefly introduced in the following. The methodologies used to characterize the different parameters are introduced in section 3.7. The case study results of $La_{0.6}Sr_{0.4}CoO_{3-\delta}$ and $La_{0.6}Ca_{0.4}FeO_{3-\delta}$ electrocatalysts are shown in section 7.

2.5.1 Earth abundance, mineral resources, and material criticality

As mentioned above and in the introduction of the thesis, the energy transition dramatically increases the raw materials demand. Several scientific studies discuss whether the materials' earth abundance, resources, reserves, and current extraction rates are high enough to meet this increasing demand, including the materials demand for electrocatalysts [3, 4, 12, 99–101]. As the terms such as earth abundance and resources are often not defined and differentiated in research articles for energy conversion performance studies, a definition of those is given first. The earth abundance is the mass concentration of the elements in the earth's crust and is a purely geological term. Resources are defined as economically viable extractable minerals,

possibly today and in the closer future [102]. Reserves are a part of the resources that are today economically extractable because the minerals of the reserve meet the physical requirements to be extracted by existing technologies [102]. Current extraction rates refer to the current yearly amount of mined minerals available on the market for further processing.
It is estimated that sufficiently large material resources exist for most of the currently used energy materials that are required for the full energy transition [3, 4, 99–101]. It thus implies that the minerals' earth abundance is high enough for the energy transition. Nevertheless, the current extraction rates and market supplies of some crucial materials are predicted to be too low to meet the extraordinarily increasing demand in material supply for the energy transition and other industries in the near future [3, 4, 99–101]. Additionally, the vastly increasing geopolitical tensions might challenge the reliability of global material supply chains.
Hence, the material supply for the energy transition depends on the expansion of the mining industry and reliable supply chains within a network of geopolitical interdependencies, rather than on the general abundance of elements in the Earth's crust as a purely geological concept. Reviewing the current extraction and production rates [103] also in dependence of the depletion of known reserves [38] might give an overview of possible short-term material shortages, but neglects for example low supply chain diversifications, political instabilities of supplying countries, import reliance on other countries, export prohibitions, material recycling rates, or possible material substitution options in applications [38, 93, 97].
To evaluate these aspects, so-called material criticality assessments are used. The strongest economies USA [97, 104], China [105], the EU [93] and Japan [106] periodically conduct criticality assessments for raw materials [107] to estimate material supply risks in their economy, and to assess which impact a potential material shortage can have on their industrial sectors. Here, the material criticality assessment of the European Commission is considered for the material sustainability evaluation and further explained in the methodology section 3.7.1. Because material criticality is a quantified and periodically updated parameter from the governmental institutions, the material criticality can serve as an instructive input to compare possible material shortages for energy materials in the early stages of energy materials research [28].

2.5.2 Economic impact

Beyond ensuring a reliable material supply, green energy technologies must achieve economic viability to sustain long-term profitability in the energy and industrial sectors. To predict the possible profitability of, for example, batteries, fuel cells or electrolyzers, including their required materials, the investment and operational costs need to be related to the final market price. To calculate the full costs, typically the CapEx (Capital Expenditure) and OpEx (Operational Expenditure) methods are used [26, 108, 109]. To render the full life cycle costs of a technology the life cycle costing (LCC) method is a strong tool that can also include externalized costs of environmental impacts [26, 110]. During early-stage materials research, the projected industrial CapEx and OpEx, as well as the market price, are hardly known. However, there are possible

options to estimate different costs. For example, the price of necessary precursor materials or the energy costs for material fabrication can be estimated if the (scalable) production process is projected. In this thesis, the precursor prices of the perovskites were collected to identify possible economic threats to the catalyst production.

2.5.3 Environmental impact

Despite being envisioned as environment-friendly technologies, the production, operation, and end-of-life of electrolyzers, fuel cells, and batteries can have a severe impact on the environment, particularly given the high material demand [99]. Therefore, the minimization of environmental impacts must be considered over the entire life cycle of the technologies [3]. Especially, the mining and processing industries are extremely energy and resource-intensive and largely influence the environment [111]. This would also include the mineral extraction required for the perovskite fabrication, such as the rare earth minerals for the lanthanum supply or the cobalt ores for the cobalt supply. For example, up to 2000 m^3 of water are required to extract one ton of Co metal, which even increases up to 1.2 Mio. m^3 of water for Pt group metals [112]. Besides potential water scarcities, other factors such as high greenhouse gas (GHG) emissions, extensive land transformation, and toxification are crucial factors that are for example, endanger living space, biodiversity, and agricultural land [112]. To adress this, Life cycle assessment (LCA) is a strong tool, which quantifies and evaluates such environmental impacts [113], and is implemented in well-defined ISO standards [114, 115]. A description of the major steps in the LCA methodology can be found in the references [116, 117] and is explained in section 3.7.3. In this thesis, the environmental footprint for the different precursors of the perovskites is calculated for several factors from LCA, to uncover whether some materials production might impact the environment.

2.5.4 Social impact

Material supply chains for renewable energy and energy conversion technologies have recently been intensively discussed regarding their social impact, especially on workers and local communities of raw material extraction [95, 118]. Such social impacts that may arise e.g from the material extraction and processing are often not considered in early-stage materials research, and specifically not when suggesting new catalyst materials based on performance matrices. In general, these aspects are underexplored concerning the majority of materials relevant to the energy transition [6]. For those cases, the UN has published human rights guidelines for enterprises and governments [119] (implemented in the social responsibility standard SA8000), tracking child labor, forced work, health and safety, discrimination of employees and much more [120, 121]. Moreover, the EU just recently passed the law for social responsibility throughout the whole supply chain [122]. For energy materials such as noble metals or transition metals, the often-mentioned hazardous conditions in artisanal mining are criticized [118]. The hazardous

working conditions are even more dramatic when child labor is involved [95]. These aspects are analysed for a projected roll-out scenario of perovskite-based OER catalysts in the case study, and the methodological approach is explained in section 3.7.4.

3 Methodology

3.1 Pulsed laser deposition (PLD)

PLD is a physical vapor deposition technique to grow complex metal oxides as dense thin films on a substrate in the stoichiometry of the desired ceramic target material. Depending on the substrate used and the applied growth conditions, the growth can take place in an epitaxial manner, leading to single-crystal layers, textured, or polycrystalline films. Even multilayer structures of different target materials can be achieved with unit cell precision by switching the target in between [123, 124]. Here, the perovskite oxide thin films were epitaxially grown on single-crystal substrates.
The design of the used PLD system is shown in figure 8. The target and heater with the glued substrate are placed with parallelized surfaces in the vacuum chamber. Initially, the laser hits the spinning target and the plasma plume (purple) propagates to the substrate. The growth can be controlled via a defined gas atmosphere, typically oxygen gas for metal oxides, heater temperature, laser fluence, laser pulse frequency, and substrate choice.

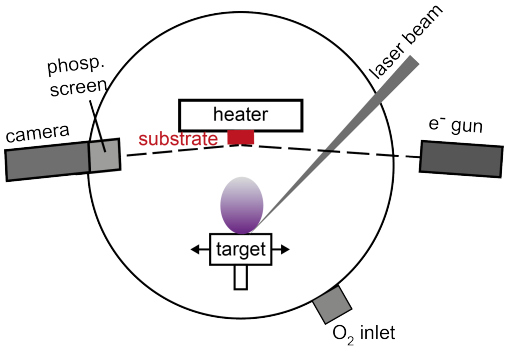

Figure 8: Design of the here used PLD system; scetch inspired by [123]. The UV laser hits the moving target. The plasma plume (purple) evolves and propagates to the substrate, which is glued to the heater. For *in-situ* growth detection a reflective high energy electron diffraction (RHEED) system is installed, with the electron gun focused in an incident angle on the substrate surface, and reflected to the phosphorous screen. The screen is filmed by a CCD camera (more details in section 3.2).

Here, a nano-second pulsed UV excimer laser (248 nm KrF) is used to ablate the ceramic metal oxide from the target. When the laser hits the target, its electrons are photo-excited to non-bonding states in the first picoseconds, leading to the formation of the plasma plume. The plasma plume consists of atoms, electrons, ions, and small molecules that further react with the laser pulse, inducing additional ionization processes [123, 125]. While the laser fluence has to be sufficiently high to ablate all elements of the ternary or quaternary oxide in the desired stoichiometry, the fluence also influences the kinetic energy of the emerging plasma particles [124].

This can directly affect the plume expansion speed and length, and the kinetic impact of particles arriving on the substrate surface. As it was found that the oxygen content of the plasma particles is often lower than in the target, oxygen is typically inserted in the vacuum chamber as background gas in the pressure range of 1×10^{-5} mbar-1×10^{-1} mbar [126, 127]. The oxygen gas collides and reacts with the plasma, forming oxidized species propagating towards the substrate. The inserted oxygen gas not only ensures a desired oxygen stoichiometry but also reduces the kinetic energy of arriving particles at the surface. Especially light species are scattered more than heavy species, which directly influences the final cation stoichiometry [124].
When the plasma plume hits the substrate, backside heating of the substrate ensures sufficient atomic mobility to form smooth unit-cell thin layers on the substrate surface. The mobility of particles on the substrate surface is individual for many perovskite oxides. The substrate temperature and the chemical affinity to the substrate can substantially influence the final surface morphology. Moreover, highly kinetic particles might bombard the already attached layers leading to undesired side effects such as off-stoichiometries [124]. In summary, the laser fluence, oxygen partial pressure, substrate temperature, and substrate type play a crucial role in achieving stoichiometric-, crystallographic-, and surface morphology-defined thin films, and are the most common parameters to optimize the growth of the desired material.

Experimental procedure and PLD parameters: In this thesis, electrically insulating $LaAlO_3$, $NdGaO_3$, $SrTiO_3$ substrates in the size of 10x10 mm^2x0.5 mm are used for the epitaxial growth of the perovskite oxides by PLD. Since the cobaltates $La_{0.6}Sr_{0.4}CoO_{3-\delta}$ and $La_{0.6}Ca_{0.4}CoO_{3-\delta}$ have a smaller lattice parameter, they were grown on the $NdGaO_3$ and $LaAlO_3$ substrates, as they have a smaller lattice parameter than $SrTiO_3$. Growing thin films on substrates with similar lattice parameters is beneficial to avoid possible thin film cracking due to a higher tensile strain [128]. Additionally, the thin films are also deposited on 0.5 wt% Nb-doped $SrTiO_3$ (Nb:$SrTiO_3$) substrates to ensure direct electrical backside contact in the electrochemical measurements. Annealing and etching procedures are shown in table 1. Note, that the decreased annealing time and temperature used for Nb:$SrTiO_3$ were decisive in reducing the amount of step bunching.

The substrate is glued with Ag-paste onto the electrical heater and pre-heated for 15 min outside the chamber to evaporate the solvent in the Ag-paste. Then the target and heater are

Table 1: Annealing procedure of the substrates. Nb:$SrTiO_3$ was etched beforehand in buffered FH solution for 90 seconds.

substrate	temp °C	ramp time h	hold time h
$LaAlO_3$	1000	2	2
$NdGaO_3$	1000	2	2
$SrTiO_3$	950	2	2
Nb:$SrTiO_3$	930	1.5	1.5

mounted into the vacuum chamber of the *Twente Solid State Technology* (*Demcom TSST), B.V., Netherlands*) PLD system. Inside, the target and substrate surface are aligned parallel with a distance of 55 mm. The desired growth temperature and O_2 pressure are set. The laser energy is set with an adjustable beam splitter. Typically, thin films of 20 nm thickness are deposited with a pulse repetition rate of 5 Hz. To compensate for the contact resistance between Nb:$SrTiO_3$ and the thin films, a 2-4 unit cell thick $LaAlO_3$ layer, as a dipole layer, was grown first on Nb:$SrTiO_3$, where noted. For this, the repetition rate was decreased to 1 Hz.
The deposition parameters of the previously reported $La_{0.6}Sr_{0.4}CoO_{3-\delta}$ thin films [34, 129] are also successfully applied to $La_{0.6}Sr_{0.4}FeO_{3-\delta}$ and $La_{0.6}Ca_{0.4}FeO_{3-\delta}$. $La_{0.6}Ca_{0.4}CoO_{3-\delta}$ and $La_{0.6}Ca_{0.4}NiO_{3-\delta}$ growth is tested under different conditions with fluences varying between 1.8 J cm^{-2} and 3.5 J cm^{-2} temperature ranges between 450 °C and 800 °C, and O_2 partial pressures between 4×10^{-3} mbar and 1.5×10^{-1} mbar. The final growth parameters of each perovskite thin film are listed in table 2.

Table 2: Final growth parameters. * $La_{0.6}Sr_{0.4}CoO_{3-\delta}$ was grown on $NdGaO_3$ with a fluence of 2.2 J cm^{-2} and on $SrTiO_3$ with the higher fluence, ** $La_{0.6}Ca_{0.4}NiO_{3-\delta}$ target was inserted one night before sample growth as the target degases over a longer period.

perovskite	fluence J cm^{-2}	temperature °C	O_2 partial pressure mbar	frequency Hz
$La_{0.6}Sr_{0.4}CoO_{3-\delta}$	2.2-2.6*	650	0.05	5
$La_{0.6}Ca_{0.4}CoO_{3-\delta}$	2.2	700	0.05	5
$La_{0.6}Ca_{0.4}NiO_{3-\delta}$ **	2.2	550	0.05	5
$La_{0.6}Sr_{0.4}FeO_{3-\delta}$	2.2	650	0.05	5
$La_{0.6}Ca_{0.4}FeO_{3-\delta}$	2.2	650	0.05	5
$LaAlO_3$	1.8	700	0.0001	1

The cobaltates and ferrates are also deposited on platinized silicon stacks of the layered structure Si/Ti 5 nm/Pt 50 nm, to compare the OER current densities without any contact resistance to the substrate. For that, Si (100) substrates (size: 10x10 mm^2 and 0.5 mm) were first treated with a high-temperature process to form a SiO_2 amorphous top layer. Then a 5 nm thick adhesive layer of Ti was sputtered with the Univex sputter tool (*Siemens*). Subsequently, 50 nm of Pt is sputtered on top of the Ti layer. Those stacks are denoted as Si/Ti 5 nm/Pt 50 nm or Si/Ti/Pt in the following.

3.2 Reflective High Energy Electron Diffraction (RHEED)

To control the film thickness during PLD and to reveal two- or three-dimensional growth modes, Reflection High Energy Electron Diffraction (RHEED) is an established scattering technique tracing *in-situ* the growth of epitaxial thin films. In this thesis, a *TorrRHEED^{TM}* from *STAIB Instruments GmbH* (*Germany*) is used.
In RHEED, an electron beam of 10-50 keV is directed along the substrate crystallographic plane,

striking the surface at a grazing angle of 0.1-5°. On the two-dimensional surface of the single-crystal substrate, the electrons are reflected and visualized on an oppositely placed phosphorus screen. Figure 9a, shows an exemplary RHEED pattern of a $SrTiO_3$ surface where the incoming electron beam is denoted with 1, the specular spot as a result of the electron surface reflection with 2, and two more diffraction spots from 2-dimensional surface scattering, denoted with 3 [130]. A CCD camera tracks the intensity changes on the phosphorous screen during growth. To analyse the reflectivity changes, a frame is placed around the specular spot in the RHEED software, and the varied intensity is traced over time as illustrated in figure 9b.

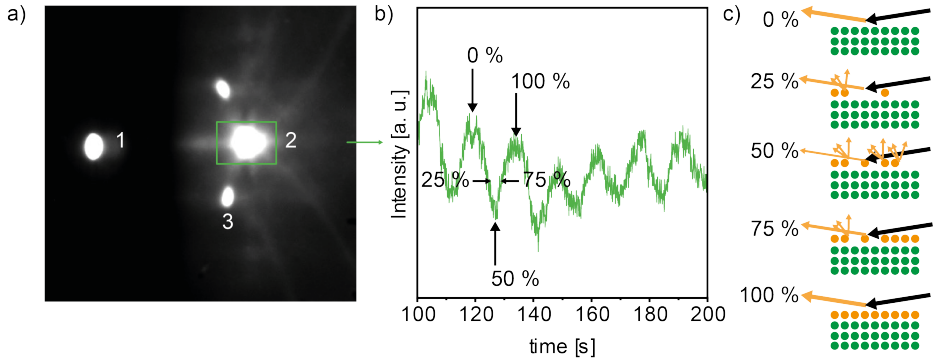

Figure 9: a) RHEED pattern of a $SrTiO_3$ surface. No.1 is the primary electron beam, no. 2 is the specular spot, no.3 are the diffractive spots (bottom and top). The green square indicates the area where intensity changes are tracked. b) This results in the oscillations for layer-by-layer growth over time. The percentages represent the progress of one growing monolayer. c) Schematic of the roughening and subsequent smoothing of the surface during the growth of one monolayer. The black arrow represents the incoming electron beam, the orange beam represents the reflected electron beam, and the smaller orange arrows represent the scattered electrons, reducing the intensity of the specular spot.

There are different growth modes possible on single-crystal substrates such as layer-by-layer growth, island growth, or step flow growth. The thin film can grow layer-by-layer on the substrate when the growth parameters are sufficiently chosen and the surface energy of the thin film is lower than of the substrate [130]. Such growth is illustrated in figure 9b and c. When the 2D surface is smooth and a monolayer is fully established, the electron beam reflection is high, appearing as a local maximum of one RHEED oscillation (here the 0 %). Further incoming particles start to nucleate on the surface, and the electrons scatter at the roughened surface, yielding a lower intensity of the specular spot (25 %). When the surface coverage is around 50 % of one monolayer a local minimum forms in the intensity plot (figure 9b). As the coverage gets higher, electrons scatter less and the specular spot intensity increases again, reaching another local maximum with the accomplishment of one monolayer (100 %). With the periodic distance of the local maxima, the growth rate and deposition time for a specific film thickness

can be determined.
The step flow growth might be observed on substrates, where a monoatomic step edge terrace structure is present through the miscut angle along the crystallographic plane. Here, the mobility of the initially nucleated particles is so high that they quickly move to the step edges before the next pulse arrives. Subsequently, they continue to grow along the step terrace plane. Although this is also a monolayer growth, no oscillations can be seen. A constant specular spot intensity indicates the step flow growth mode [123]. When the growth conditions are not optimized, or for example the affinity of the deposited material to the substrate is not high [123], island growth can occur. Then a three-dimensional RHEED pattern is visible, often linked to a large intensity drop of the specular spot.

3.3 X-ray diffraction (XRD) techniques

X-ray diffraction (XRD) and X-ray reflectivity (XRR) yield a multitude of information, such as crystal lattice parameters from constructive interference at the crystallographic planes or thin film thicknesses of multilayer structures through reflection at their interfaces [131]. In this thesis, XRD is used in 2θ–ω geometry to determine the crystallinity, lattice parameter, and strain of the thin films on single-crystal substrates. For the Si/Ti 5 nm/Pt 50 nm/perovskite stacks, also grazing incident XRD (GIXRD) is applied, enabling us to characterize the stack crystallinity of polycrystalline thin films. X-ray reflectivity (XRR) is applied to compare thin film layer thicknesses. A Bruker *D8 Discover*, (*Bruker AXS GmbH*) is used, equipped with a Cu K_α source ($\lambda = 1.54$ Å).

XRD: In the symmetric 2θ–ω configuration between X-ray source, detector, and sample, ω represents the angle between the sample surface to the incoming X-ray beam (figure 10a). 2θ is the angle along the extension of the X-ray beam to the detector. In XRD, diffraction reflexes are seen when the X-rays scatter at the periodic crystallographic planes and constructively interfere. Following the Bragg equation $2d \sin\theta = \lambda n$, constructive interference only occurs when the X-ray beam is at the angle θ where the distance of the planes d is an integer multiple n of the X-ray wavelength λ.
For epitaxial thin films that are in perfect registry to the substrate, only this one orientation can be detected in 2θ–ω geometry as illustrated in figure 10b (top). For example, epitaxial growth of the perovskites on (001) $SrTiO_3$ substrates will show the reflexes from (001) to (004) for $2\theta = 10 - 120°$. As the penetration depths of X-rays are typically between 10-100 µm, the high intensity signal shown in grey stems from the substrate and the lower intensity signals from the thin film. Laue oscillations around the thin film reflexes can be obtained when the interface to the substrate and air is sharp. Their presence is an indicator of high thin film quality [133]. To determine if the epitaxial thin films grow fully strained on the substrate, the (130) plane is aligned in grazing exit geometry, and 1D detection is applied. This XRD method is called reciprocal space mapping (RSM), enabling one to disentangle in-plane and out-of-plane lattice

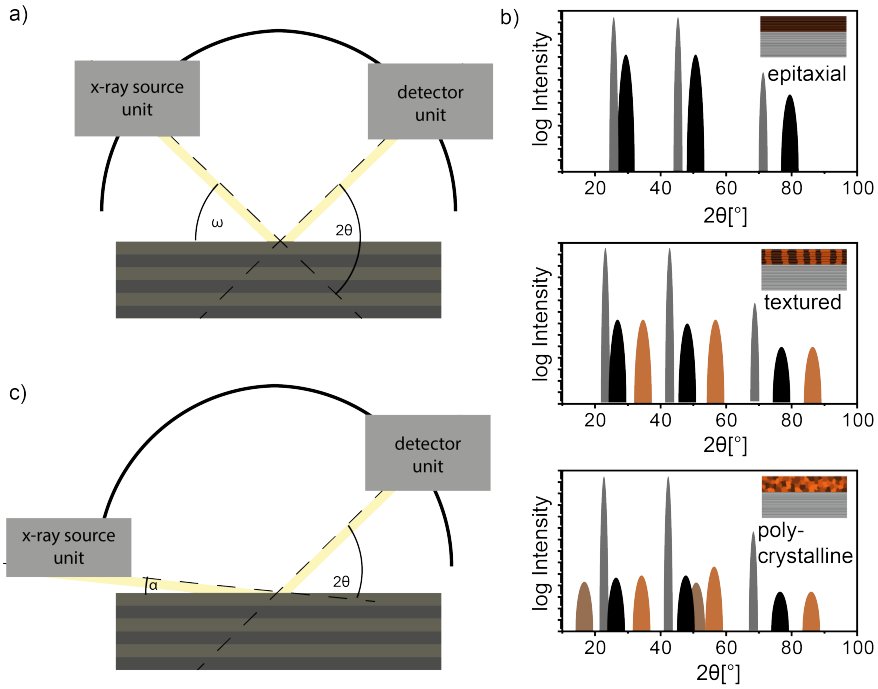

Figure 10: a) Sketch of XRD setup in 2θ–ω geometry. b) Sketch of a 2θ–ω XRD pattern of an epitaxial thin film (top), textured thin film (center) and polycrystalline thin film (bottom) inspired by [132]. Partly reproduced with permission from Springer Nature. c) GIXRD setup geometry.

parameters.

Depending on the thin film quality and properties of the chosen substrate or stack, for example, the Si/Ti/Pt stacks, perovskite growth might be less defined and does not grow as a single crystalline layer. As illustrated in figure 10b (center), the film might grow in a textured manner, yielding partly oriented growth but with domains of different tilts or partly different oriented grains. In the diffractogram of the 2θ-ω scan, the overall intensity of the thin film signals decreases, and the partly differently oriented domains appear as additional signals. As sketched in figure 10b (bottom), thin films of randomly oriented grain structures will reveal all possible Bragg peaks like in a powder diffraction pattern, however, with even further reduced signal intensity.

GIXRD: As many thin films are much thinner than the penetration depth of the X-rays, the diffraction signals of randomly oriented polycrstalline films are very low or not even visible. Here, GIXRD is a strong alternative technique to record a higher diffraction intensity of polycrystalline thin film layers [132]. In GIXRD (figure 10c), the incoming X-ray beam is fixed and aligned with

an incident angle α to the surface of only some degrees, typically between 0.1-3°. The detector is then moved along the 2θ plane. The advantage of GIXRD is that the X-ray penetration depth is much smaller, and hence, the signal from buried layers or substrate decreases, while the penetration length of the X-rays along the upper layers is extended. With this technique, randomly oriented polycrystalline thin films also yield the 2θ Bragg-peaks as in powder diffraction. However, this technique can also suffer from limited signal detection, especially if thin films are not thick enough, or grains are tilted in specific configurations to each other and not randomly [132, 134]. Note that the grazing incident angle α has to be chosen above the so-called critical angle, as the total reflection of the X-rays occurs below.

In **XRR**, a 2θ–ω scan is recorded at incident angles. Interfering reflections at the interface of the thin film to the substrate and air result in the so-called Kiessig fringes, where their periodicity contains information on the layer thickness t. Multilayer structures create an overlapping pattern from the interfering reflections of the interfaces [133]. To quantify the film thickness the adapted Bragg equation can be applied, $\sin^2\theta_i = \theta_c^2 + \frac{(n_i+\Delta n^2)\lambda^2}{4t^2}$ where θ_i denotes a local fringe maximum, θ_c the critical angle, n_i the index of the fringe, n the refraction index and λ the wavelength. For a thickness estimation the equation:

$$t = \frac{\lambda}{\Delta 2\theta} \tag{12}$$

can be used. To obtain the thickness of the different layers in the Si/Ti 5 nm/Pt 50 nm/perovskite stacks, the GenX 3 software is used to fit the graphs.

3.4 X-ray photo electron spectroscopy (XPS)

X-ray photoelectron spectroscopy is a surface-sensitive technique and provides insights into the chemical states of the elements in the sample [135]. Here, it was used to determine different chemical phases of Ca compounds and the valence band electronic structure of the catalyst surface. In XPS, the X-rays ionize the sample based on the photoelectric effect (figure 11). Only electrons located close to the sample surface within a distance of a few nanometers are ejected to the surrounding ultra-high vacuum, as electrons situated deeper in the sample are scattered, losing their kinetic energy drastically. The electrons located close to the surface are ejected with defined kinetic energy (*KE*) depending on their binding strength to the nuclei. Therefore, released core level electrons of e.g. the Ca 2*p* orbital have a lower kinetic energy than those from the valence band where the O 2*p* and TM 3*d* electrons are located. The *KE* can be calculated from the equation:

$$KE = E_{h\nu} - \phi_{\text{sample}} - BE \tag{13}$$

where $E_{h\nu}$ is the energy of the X-rays, ϕ_{sample} is the work function of the investigated material, and *BE* is the binding energy of the ejected electron. The electrons are focused with extraction

lenses on the analyzer, which consists of an outer and inner hemisphere (figure 11). An applied electric field at these hemispheres directs the electrons to the detector. Faster electrons fly on the outer trajectories and the slower ones on the inner trajectories [135], and only electrons of a specific kinetic energy window (spherical trajectory) reach the detector unit. In this XPS setup, the electric field of the extraction lens is successively varied, so that electrons of defined kinetic energies are detected one by another with 0D detection. Incoming electrons with higher or lower kinetic energy eventually hit the hemispheres and are not counted. To increase the resolution of the spectra, the pass energy can be reduced, which spreads the trajectories of the ejected electrons further. This achieves more distinct peaks with a smaller full width at half maximum (FWHM), and can, for example, facilitate the determination of different chemical phases, seen in a core level.

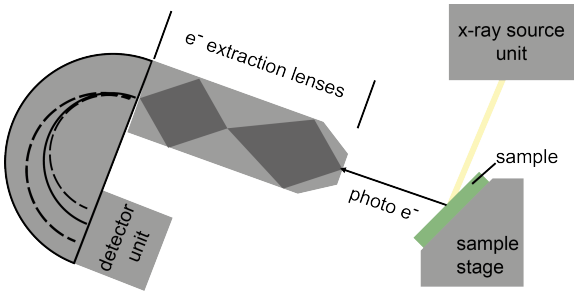

Figure 11: X-ray photo electron spectroscopy working principle. Sketch is inspired by [135].

The XPS data were recorded with a Phi 5000 VersaProbe II system (*ULVAC Phi, Physical electronics Inc*., *USA*) with Al K_α X-ray illumination without charge neutralization. This refers to a photon energy of 1.49 keV. The vacuum was held in the range of 10^{-6} mbar with a titanium sublimation pump. The pass energy was 23.5 e V and the step width was set to 0.1 e V. The photoemission angle θ was set to 15°.
The spectra were analyzed with the casaXPS software. The core level and valence band spectra were aligned to the aliphatic C 1s peak at 284.8 e V. The valence band spectra of the ferrates, cobaltates and nickelates were fit with three to four components. Gauss-Lorentz shape with a ratio of 40:60 was used to fit the single components. According to ref. [34], no constraints are set, as the peaks might undergo a broadening unrelated to the instrumental broadening. Further explanations are given in the results section of the valence band spectra 4.4.3.

3.5 Electrical characterization

To determine the resistivity of the different perovskite oxides, the sheet resistance R_S was measured in van-der-Pauw geometry in a four-point probe station. For this, the thin films were deposited on insulating substrates and connected with an Al wire to the contact pads of the

setup. The bond connections were wedged by ultrasound with a HB16 wire bonder from *TPT Wire Bonder GmbH & Co. KG* (Germany). As contact resistances occur between the Al wire and the thin films, the samples were sputtered with Pt on the edges. For measurements on $NdGaO_3$, the force of the bonding needle had to be reduced compared to the bonding process on $SrTiO_3$ substrates to avoid damaging the substrate.

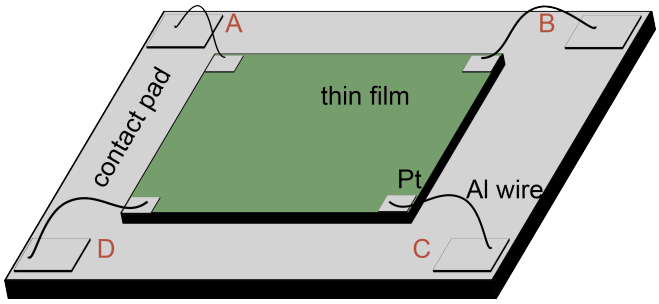

Figure 12: Sketch of the sample sputtered with Pt contacts on the edges. From there, the sample is contacted with four Al wire bonds to the contact pad.

To determine R_S, a current is applied between C and D, and the voltage is measured from A to B in the LakeShore 8400 series setup (*Lake Shore Cryotronics, Inc.*, USA). Then, the current is applied between A and D, and the voltage is measured from B to C. The resistance is then calculated from both measurements:

$$R_\mathrm{AB,CD} = \frac{U_\mathrm{AB}}{I_\mathrm{CD}} \tag{14}$$

$$R_\mathrm{BC,AD} = \frac{U_\mathrm{BC}}{I_\mathrm{AD}} \tag{15}$$

With the equation:

$$R_\mathrm{S} = \frac{1}{\rho t} = \frac{\pi}{\ln(2)} \frac{R_\mathrm{AB,CD} + R_\mathrm{BC,AD}}{2} f\left(\frac{R_\mathrm{AB,CD}}{R_\mathrm{BC,AD}}\right) \tag{16}$$

the two values are averaged and corrected with the factor f. With given thickness t and the measured R_S, the resistivity ρ can be calculated [136, 137]. The factor f is calculated by the software via the equation:

$$\cosh\left(\frac{R_\mathrm{AB,CD}/R_\mathrm{BC,AD} - 1}{R_\mathrm{AB,CD}/R_\mathrm{BC,AD} + 1} \frac{\ln(2)}{f}\right) = 0.5\exp\left(\frac{\ln(2)}{f}\right) \tag{17}$$

3.6 Electrochemical characterization

To determine the OER activity of the perovskite oxide thin film catalysts, electrochemical measurements were performed in alkaline media. To identify possible resistances in the electrochemical cell, potentiostatic electrochemical impedance spectroscopy (PEIS) was measured. To obtain the catalyst overpotential η and Tafel slopes b, cyclic voltammetry (CV) was conducted. The electrochemical measurements were conducted in a 3-electrode configuration where a rotating disk electrode (RDE, *Pine Research*, USA) served as the working electrode, as illustrated in figure 13a.

The thin films are mounted on the rotating shaft, which facilitates the removal of evolving oxygen

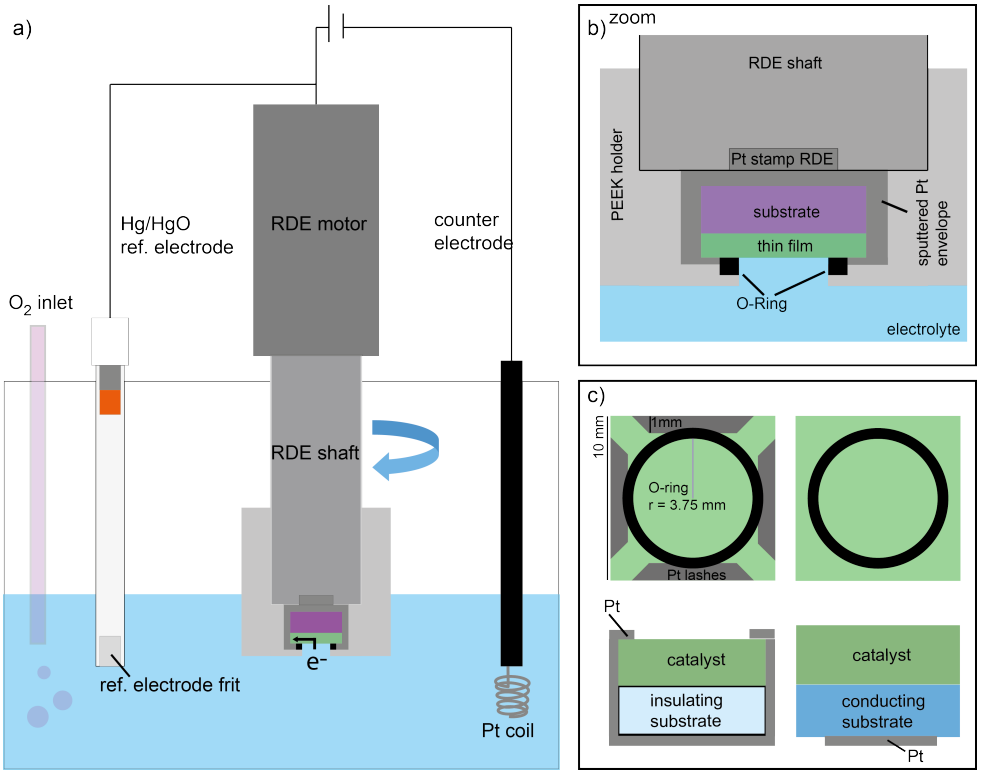

Figure 13: a) 3-electrode RDE setup. The Hg/HgO reference electrode, Pt counter electrode, and RDE with attached thin film are immersed in the electrolyte. The electrolyte is purged with O_2 gas. b) Zoom to the RDE shaft where the sample is mounted. The sample is placed in a custom-made PEEK holder. The backside and edges are sealed with an O-ring from the electrolyte. c) Pt contacts sputtered for insulating substrates (left) and for Nb:$SrTiO_3$ substrates (right).

gas during the OER. The rotation of the RDE was set to 1600 rpm (rounds per minute). The electrodes are connected to a VSP-300 potentiostat (*Bio-Logic Science Instruments*, *France*). The operation and analysis software was EC-Lab 50.11 from *Bio-Logic*. The measurements were conducted in a Teflon beaker in 0.1 M KOH solution made from KOH pellets (Sigma-Aldrich, purity 99.99%) that were dissolved in deionized water (Milli-Q, >18.2 MΩ cm). The Hg/HgO reference electrode (CH152 by *CH Instruments*, USA) was protected with a Teflon tube, which was filled with 1 M KOH solution (figure 13a). A Pt coil served as the counter electrode. To saturate the electrolyte, O_2 gas was purged at least 30 minutes before and during the experiment.
Figure 13b shows a zoom of the thin film sample mounted to the RDE. An O-ring (*ERIKS Deutschland GmbH*) is placed in the custom-made PEEK holder where the sample is placed on top with the catalyst facing the opening to the electrolyte. The sample is then mounted to the RDE shaft and brought into contact with the Pt disk. To ensure electrical contact to the catalyst deposited on insulating substrates, the backside, edges, and front edges were sputtered with 50 nm Pt (UNIVEX sputter tool) as illustrated in figure 13c on the left. Thin films deposited on Nb:$SrTiO_3$ were only sputtered on the back side (as sketched in)figure 13c on the right).
Moreover, electrochemical measurements were conducted in 0.1 M KOH solution with the hexacyanoferrate (II)/(III) $K_4[Fe(CN)_6]/K_3[Fe(CN)_6]$ in 0.003 M concentration. This was done to gain insight into electrical resistances and possible space charge barriers independent of the sluggish OER kinetics. For this, the RDE rotation is turned off.
A typical measurement protocol starts with a 10 minute long open circuit potential (OCP) equilibration phase, followed by a PEIS measurement at OCP. Then CV scans are recorded from small to larger potential ranges. To determine the evolution of interface space charge barriers, staircase PEIS (SPEIS) was measured.

3.6.1 Cyclic voltammetry (CV)

CV is a widely used technique to test the electrochemical properties of catalysts. Typically, CV is used to obtain the potential required to trigger an electrochemical redox reaction of the electrolyte species or the catalyst itself. Positive currents stem from an oxidation reaction and negative currents from a reduction reaction. Here, CV was used in different potential ranges to determine the double layer capacitance C_{DLC}, redox reactions of the catalyst material in the pre-OER voltage regime, and OER activity. To obtain possible overpotentials caused by resistances, CV was conducted with an electrolyte mix of 0.1 M KOH and 0.003 M $K_4[Fe(CN)_6]/K_3[Fe(CN)_6]$ (in the following denoted as hexacyanoferrate (II)/(III)). The recorded potential-current ($E-I$) curves were normalized to the exposed surface area of 0.44 cm^2 to plot the current density. The recorded potential against the Hg/HgO reference electrode was scaled to the reversible hydrogen electrode (RHE, *Hydroflex*, USA). For that, the RHE is equilibrated against the Hg/HgO reference electrode, and the resulting value is added to the measured potentials as shown in

the equation 18. Additionally, the potentials are *iR* corrected with the uncompensated resistance R_u obtained from PEIS, which is introduced in the next section.

$$E = E_{Hg/HgO} - iR_u + E_{RHE} \tag{18}$$

For the double layer capacitance determination CV was applied in a potential range, where predominantly non-farradaic currents occur. First a steep incline of the current is observed, as the catalyst/electrolyte interface charges like a capacitor. Once a current density plateau is reached, capacitive charging is completed. The observed current plateau scales with the applied sweep rate ν:

$$\frac{i/A}{\nu} = C_{DLC}/A \tag{19}$$

where A is the electrode surface area. From that the double layer capacitance C_{DLC}/A can be determined. For that, CV cycles were recorded from 0.1-0.2 V vs Hg/HgO with increasing sweep rates from 10 mV s^{-1} to 500 mV s^{-1} in 12 steps. As $La_{0.6}Ca_{0.4}FeO_{3-\delta}$ undergoes a reduction reaction in the potential window, the C_{DLC} was obtained from 0.2-0.3 V vs Hg/HgO. Furthermore, to intentionally obtain information on redox-reactions taking place under applied potential in the pre-OER voltage regime, CV was recorded between 0.0, 0.1, 0.2 to 0.7 V vs Hg/HgO with increasing sweep rates from 10 mV s^{-1} to 500 mV s^{-1} in 12 steps.

The OER activity was finally addressed with a forward and backward sweep to reach at least 0.1 mA cm^{-2}. The maximum applied potential was 1.15 V vs Hg/HgO. For this, the applied sweep rate was 10 mV/s. To avoid further contributions from capacitive charging and discharg-

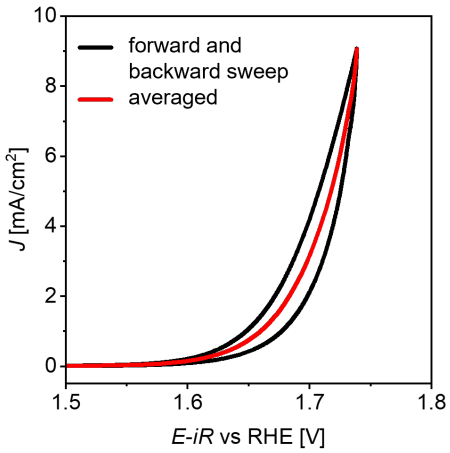

Figure 14: Example of the averaged forward and backward sweep.

ing in the CV, the forward and backward sweeps are averaged as sketched in figure 14. To determine the Tafel slopes, the E and J-axis of the CV scan were switched to a log*J* vs *E* plot, which we denote here as "Tafel-like" plots. To determine the Tafel slope at each current density, the first derivative of the Tafel-like plots was calculated and is plotted as the "Tafel slope plots" with the first derivative as a function of the current density. In hexacyanoferrate (II)/(III) containing electrolyte, CV scans were recorded between 0 V and 0.6 V vs Hg/HgO. The sweep rate was 30 mV s^{-1}.

3.6.2 Potentiostatic electrochemical impedance spectroscopy (PEIS)

PEIS is a powerful technique to obtain and quantify serial resistances from the electrolyte and catalyst, as well as capacitances and resistances at the catalyst/substrate or catalyst/electrolyte interface in the electrochemical cell. In PEIS, a sinusodial voltage $U(t)$ from high to low frequencies ω (e.g. 1 MHz to 0.1 Hz) is applied between the working electrode and reference electrode, and the resulting current $I(t)$ is recorded:

$$U(t) = U\mathrm{exp}(i\omega) \tag{20}$$

$$I(t) = I\mathrm{exp}(i\omega t + i\phi) \tag{21}$$

ϕ is the phase shift of the current and i is the imaginary number. The alternating voltage can resonate with electrons and ions from high to low frequencies. This enables one to probe and distinguish the fast motion of mobile carriers at (semi-)conductor interfaces from slow ionic motion at the catalyst/electrolyte interface.
The ratio of the applied voltage and measured current gives the impedance Z, which can be split into a real $Z'(\omega)$ and an imaginary part $Z''(\omega)$:

$$Z(\omega) = \frac{U}{I}\mathrm{exp}(i\phi) = Z'(\omega) + iZ''(\omega) \tag{22}$$

Typically, $Z''(\omega)$ is plotted against $Z'(\omega)$, yielding the so-called Nyquist plot. In equivalent electric circuits, the presence of serial resistances results in an offset on the real axis $Z'(\omega)$. Each present interface represents a capacitor and resistor in parallel (RC), yielding a semicircle in the Nyquist plot. A semicircle is observed because at high perturbation frequencies, interfacial capacitor plates are charged and discharged quickly, dominantly contributing to the imaginary part of the impedance $Z''(\omega)$. Toward lower frequencies, the capacitor plates become fully charged, and the resistance at the interface starts to dominate, increasing the values of the real part of the impedance $Z'(\omega)$. This imitates almost direct currents (DC).

Experimental parameters, equivalent electric circuits, and data analysis: PEIS was recorded at the OCP before any performance tests were conducted. The applied frequency was varied from 7 MHz to 0.1 Hz with an automatic current range setting to avoid noisy data

over such large frequency ranges. It is very important to analyse the spectra carefully and assign the observed impedance features to the correct interfaces in the electrochemical cell for meaningful physical interpretations. To distinguish impedance features, that stem from the electrochemical cell, and not from the catalyst stack and its catalyst/electrolyte interface, a Pt sample was chosen as a simple metallic electrode, and the OCP impedance was recorded. Figure 15a shows an exemplary impedance spectrum of a Pt thin film in 0.1 M KOH recorded from 7 MHz to 0.1 Hz. Two impedance features are distinguishable. For one, the initial part of a large semicircle is seen toward lower frequencies, which is attributed to the Pt/electrolyte interface. Slow ionic motions are resonating at lower frequencies. Such a large interface resistance indicates that no meaningful faradaic currents flow across this interface, as a redox reaction between the electrolyte and Pt film is not triggered at OCP. A second semicircle is seen in the zoom to the

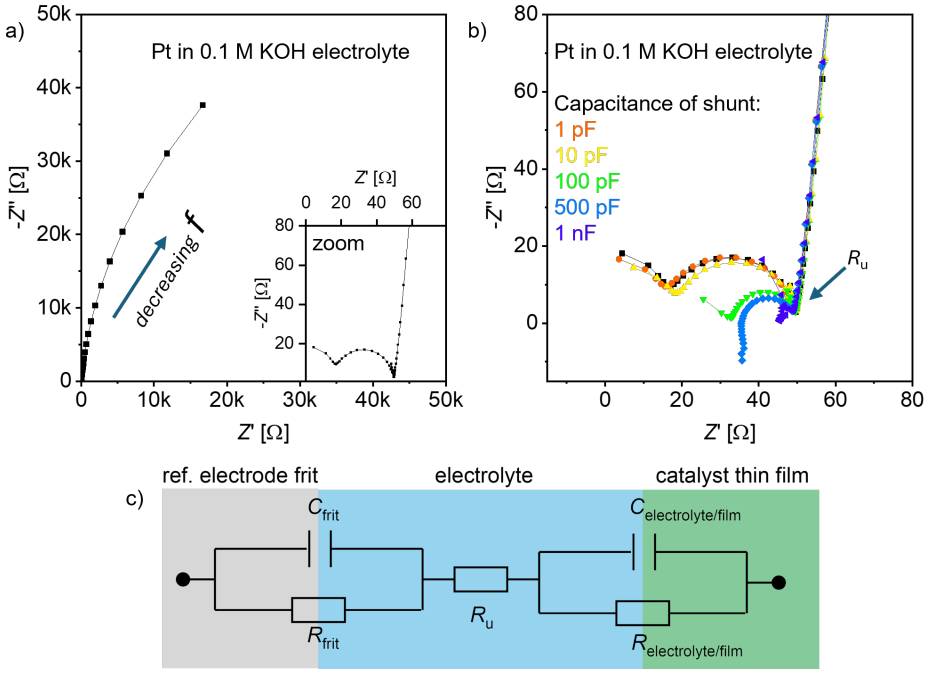

Figure 15: a) PEIS at OCP for a 50 nm thick Pt sample in 0.1 M KOH electrolyte. The initial part of a large semicircle is seen, which is attributed to the Pt thin film/electrolyte interface $RC_{film/electrolyte}$. The graph inset shows the zoom to the high-frequency region. A small semicircle is observed. b) The same Pt sample is tested in 0.1 M KOH electrolyte, where a shunt is connected in parallel to the reference electrode. The shunt was tested with various capacitor sizes from 1 pF to 1 nF. The size of the capacitor directly influences the small semicircle.

high-frequency region, close to the origin of the plot. As literature suggests [138], at high perturbation frequencies, the reference electrode frit might show an impedance. This was confirmed by the implementation of a shunt that was connected in parallel to the reference electrode. The shunt consists of a Pt wire attached to a capacitor and is connected to the same contact as the reference electrode and immersed in the electrolyte. Figure 15b shows that the impedance signal at high frequencies scales with the inserted shunt capacitor. This yields an equivalent electric circuit as shown in figure 15c. The RC_{frit} element from the reference electrode frit is in series with the uncompensated resistance R_{u} from the electrolyte and the $RC_{\text{electrolyte/film}}$ element from the Pt/electrolyte interface. Therefore, the semicircle in the high frequency range was not further considered in the electrochemical characterization of chapter 5. After correction for the frit signature, the serial resistance of the electrolyte R_{u} can be determined as the x-axis offset. Thus, R_{u} was determined with a linear interpolation to the x-axis of the large semicircle in the region marked with an arrow in figure 15b. This was used to iR_{u} correct the applied potential in the CV scans, as mentioned above.

Depending on the substrate choice, contacting geometry, and thin film material, the impedance features can vary. Figure 16a shows an exemplary impedance spectrum of $La_{0.6}Sr_{0.4}FeO_{3-\delta}$ on the conductive Nb:$SrTiO_3$ substrate. Toward lower frequencies, the initial part of a large semicircle is seen, representing the $La_{0.6}Sr_{0.4}FeO_{3-\delta}$/electrolyte interface, similar to the Pt thin film impedance. In the equivalent electric circuit, this is represented by a $RC_{\text{film/electrolyte}}$ element. A zoom to the higher frequency region (graph inset) shows a second semicircle, which is attributed to the substrate/thin film interface represented by the $RC_{\text{film/substrate}}$ element in the equivalent electric circuit. The data points of the reference electrode frit are removed here. This yields an equivalent electric circuit shown at the bottom of the figure.

To fit the impedance data, the capacitor is replaced by a constant phase element Q. Constant phase elements represent a capacitor with an ideality factor a. Constant phase elements are often necessary to consider, as in real systems the interface represents rather a "dispersion of capacitors" due to e.g. differing local surface reactivities or inhomogenieties [139]. In the literature, this is described as the local impedance of a single surface state, while the global impedance of the entire interface is represented by a constant phase element Q that accounts for the sum of all surface states in parallel [140].

A further important equivalent electric circuit element is the Warburg impedance stemming from semi-infinite diffusion. When the electrochemical reaction is partially or fully controlled by mass transport diffusion of reactants to the catalyst surface, this is observed in the impedance as a Q with an ideality factor of 0.5 [141]. It results in a linear impedance feature that is 45° to the x-axis. This is illustrated in figure 16b with the corresponding equivalent electric circuit below. The uncompensated resistance R_{u} is seen as offset on the Z' axis, followed by an interfacial resistance $R_{\text{interface}}$ and the Warburg impedance.

For determining the OER activity, the surface reactants OH^- and the products O_2 are removed by the fast rotation of the RDE, therefore, mass transport is not a limiting factor for the OER in

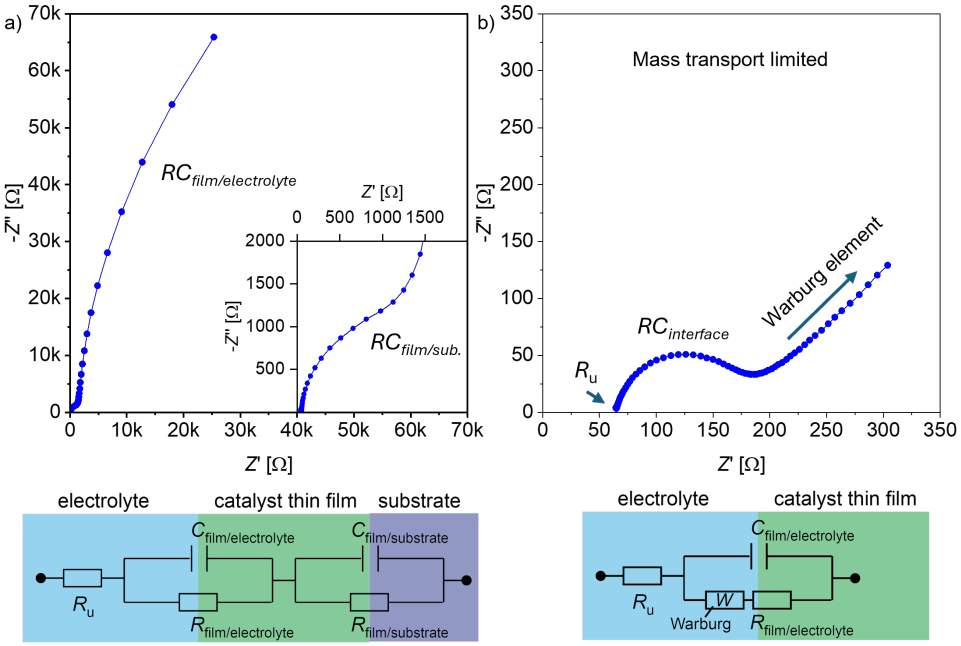

Figure 16: a) PEIS at OCP for a perovskite oxide catalyst thin film deposited on Nb:$SrTiO_3$. The $RC_{film/electrolyte}$ is here also seen toward lower frequencies. The semicircle seen in the graph inset stems from the $RC_{film/substrate}$ interface. The signal of the reference electrode is cut off. b) PEIS at OCP in hexacyanoferrate (II)/(III) electrolyte. A charge transfer resistance from an interface is seen and a 45° incline towards low frequencies, which stems from a Warburg impedance.

this case. However, for the experiments containing the hexacyanoferrate redox couple (II)/(III), the rotation was turned off to observe the distinct overpotential peaks of the redox reaction; therefore, the Warburg element was considered.
To quantify those capacitor and resistance values from an impedance spectrum, the EC lab software was used. It provides the *z*-fit tool, where the fit was made by the randomize+simplex method.

3.6.3 Staircase PEIS and Mott-Schottky analysis

Staircase PEIS was applied to determine the space charge capacitance and resistance at the catalyst/electrolyte interface as well as at the catalyst/substrate interface in dependence on the applied voltage. The space charge capacitance at the catalyst/electrolyte interface was then used to create a Mott-Schottky (MS) plot, which can reveal several interface properties such as

the flatband potential and band bending profile of the semiconductors at this interface. This enables one to determine whether a space charge barrier at the solid/liquid interface might cause a higher observed overpotential of an OER catalyst. Depending on the band bending profile under applied potential, the electron transfer from the electrolyte to the thin film might be hampered or even facilitated [15, 23]. For the OER, upward band bending is beneficial because incoming electrons can be recombined with the accumulated holes below the surface.
In staircase PEIS, the impedance is measured at subsequent DC voltage steps. The DC bias was increased from low potentials (close to OCP) to the OER voltage regime in 50 mV steps. The applied sinusoidal voltage was 20 mV, and the frequency was measured until 0.1 Hz at each voltage step. Depending on the reference electrode signal, the first considered high-frequency point was without reference electrode signal (typically 10 kHz). To determine the flatband potential and the band bending direction at the catalyst/electrolyte interface, the MS analysis was conducted.
To introduce the course of an exemplary MS plot characteristic, the here investigated *p*-type conductors are chosen. The *p*-type conductor is immersed in the electrolyte, and their Fermi levels equilibrate. In this case, the Fermi level of the electrolyte is higher than that of the electrode, so that electrons transfer to the electrode. This results in a hole-depleted space charge zone, where the valence and conduction bands are bent downward and the space charge voltage V_{sc} drops across the interface. Increasing the applied voltage V_{applied} towards the OER voltage regime lowers the bulk valence and conduction band levels. When V_{applied} reaches V_{sc}, the bands are flat and the C_{sc} is minimized. This potential is called the flatband potential V_{fb}. The behavior of the C_{sc} is described by the MS equation:

$$\frac{1}{C_{\mathrm{sc}}^2} = \frac{2}{\epsilon\epsilon_0 q A^2 N_{\mathrm{A}}} \left(V_{\mathrm{applied}} - V_{\mathrm{sc}} \frac{k_{\mathrm{B}} T}{q} \right) \tag{23}$$

where ϵ is the material permittivity, ϵ_0 the vacuum permittivity, q the elementary charge, A the surface area, N_{A} the acceptor concentration of the material, k_{B} the Boltzman constant, and T the temperature. The behavior of the hole-depleted space charge capacitance shows in the MS plot a negative sign and decreases linearly with V_{applied}, as the $1/C_{\mathrm{sc}}^2$ decreases successively [86]. As the interface at low frequencies represents the catalyst/electrolyte interface, the C_{sc} of the interface was calculated from Z'' in the low frequency range, i.e. 0.1 Hz via the equation:

$$C_{\mathrm{sc}} = -\frac{1}{\omega Z''} \tag{24}$$

where ω is the angular frequency. The MS plot is then established as a function of the voltage on the x-axis and A^2/C_{sc}^2 on the y-axis. The plot maximum was normalized to 1. A linear fit in the regime of the decreasing MS plot was used to determine the V_{fb}.

3.7 Material sustainability evaluation

After the thorough analysis of the OER catalytic activity of the perovskite oxides, the materials sustainability evaluation is conducted with the exemplary case study of the benchmark catalyst $La_{0.6}Sr_{0.4}CoO_{3-\delta}$ and the less studied catalyst $La_{0.6}Ca_{0.4}FeO_{3-\delta}$. First, the catalyst mass activity in the OER is determined for the two perovskites by CV to define the underlying catalyst performance per mass rather than per surface area for the sustainability evaluation. Based on these results, a catalyst mass of 1 kg is chosen for a quantitative comparison between the two perovskites to determine their economic and environmental impacts. In life cycle assessments (LCA), such a comparison unit is referred to as the functional unit (FU), which is explained in detail in section 3.7.3. Then, we elaborate potential industrial synthesis routes to find common precursor materials that can be used for the fabrication of $La_{0.6}Sr_{0.4}CoO_{3-\delta}$ and $La_{0.6}Ca_{0.4}FeO_{3-\delta}$ on a large scale. For this, recycled materials are considered when the secondary supply is sufficiently abundant and compatible with perovskite fabrication. Based on the catalytic activity and identification of the catalyst precursor materials, we determine the different sustainability parameters of material criticality, economic, environmental, and social impact. The evaluation was conducted in collaboration with Dr. Andrea Schreiber, based at the Institute of Climate and Energy Systems, Jülicher Systemanalyse 2 (ICE-2, Forschungszentrum Jülich GmbH). The methodologies used for each parameter are listed in table 3, and are introduced in the following.

Table 3: Methods and resources used in the case study for the sustainability evaluation.

Sustainability parameters	Methodology and resources
Matearial criticality	European Commission critical raw materials (EC-CRM 2023)
Economic	Precursor price comparison
Environmental	Precursor environmental impact based on LCA
Social	Qualitative indicators from literature
Technical performance	CV with perovskite oxide model catalysts
Material recycling	End-of-life recycling input rate (EOL RIR)

3.7.1 Material criticality assessments

As explained in section 2.5.1, the material supply for green energy technologies will rely on diversified and functioning material supply chains that minimize the risk of possible supply chain disruption. So-called material criticality assessments quantify those risks and can point out possible material hotspots for the energy transition. In this thesis, the material criticality is assessed for the perovskite oxide raw materials based on the European Commission critical raw material assessment (EC-CRM 2023). The EC-CRM 2023 assessment quantifies the EU material supply risk (SR) and economic importance (EI) in the most relevant industrial sectors [142]. Above a certain threshold of both parameters, the material is defined as critical [93]. Both parameters

are unitless numbers. The threshold for the EI is 2.8, and for the SR 1. It should be noted that the EC-CRM 2023 method is not a forecasting tool but uses recent data in its current CRM report. The EI of a raw material is determined by the share of an end-use application's value added to the EU economy. It decreases when the material can be substituted by an alternative in the final application. The supply risk is calculated from the supplying country concentration, weighted with the world governance indicators, and also weighted with the import reliance of the EU. The supply risk is reduced by the end-of-life recycling input rate (EOL-RIR) and is also reduced when the raw material can be substituted by other materials in an end-application. The underlying calculations for the economic importance and the supply risk are shown and explained in detail in the appendix D and were taken from ref. [142]. Moreover, we projected the possible demand of perovskite oxide precursors in AWE (based on our experimental results) in 2050 to estimate if supply bottlenecks might occur for the EU economy.

3.7.2 Economic impact - precursor price determination

To project the economic impact of $La_{0.6}Sr_{0.4}CoO_{3-\delta}$ and $La_{0.6}Ca_{0.4}FeO_{3-\delta}$ catalysts, their precursor prices were considered. This is because in an early-stage of catalyst research, where the catalyst performances are screened, it is not feasible to estimate the CapEx and OpEx, as well as the final market price of a commercial electrolyzer. For precursor materials that are traded globally and have global market prices, the prices were taken from the Institute of Rare Earth Elements and Strategic Metals (ISE - Institut für Seltene Erden und Metalle) (appendix table C.1). For domestically traded precursor materials, price estimates were taken or requested from German suppliers. A cumulative price of the precursor materials for 1 kg of stoichiometric $La_{0.6}Sr_{0.4}CoO_{3-\delta}$ and $La_{0.6}Ca_{0.4}FeO_{3-\delta}$ was calculated based on the required masses of the precursors shown in Table 4.

Table 4: Required precursor masses for 1 kg perovskite. The molar content of 1 kg perovskite was calculated for $La_{0.6}Sr_{0.4}CoO_{3-\delta}$ (4.4 mol) and $La_{0.6}Ca_{0.4}FeO_{3-\delta}$ (4.9 mol). The required stoichiometric amounts for each cation were calculated accordingly and related to the required mass of the precursor material. The oxygen content was not stoichiometrically balanced here, as it originates from precursor anions such as the nitrates or acetates in the later stage of fabrication as well as from oxygen in the air in the calcination step.

$La_{0.6}Sr_{0.4}CoO_{3-\delta}$ precursor	precursor mass required for 1 kg [g]	**$La_{0.6}Ca_{0.4}FeO_{3-\delta}$** precursor	precursor mass required for 1 kg [g]
La_2O_3	434	La_2O_3	481
$SrCO_3$	262	$CaCO_3$	197
Co_3O_4	356	Fe	275

3.7.3 Environmental impact - Life cycle assessment

We identified the environmental impacts of $La_{0.6}Sr_{0.4}CoO_{3-\delta}$ and $La_{0.6}Ca_{0.4}FeO_{3-\delta}$ precursors serving as catalysts at the anode of AWE based on the LCA approach. There are different LCA methodologies established today, where the environmental footprint method (EF) 3.1 is chosen in this thesis as it is recommended by the European Commission [116, 117]. The data were aggregated and provided by Dr. Andrea Schreiber (ICE-2, Forschungszentrum Jülich GmbH). The EF methods were developed by the European Commission in 2013 and updated in 2021 (EF 3.1) [143, 144]. The EF methods include the Product Environmental Footprint (PEF) and the Organization Environmental Footprint (OEF). They provide detailed guidelines for modeling, calculating and reporting the environmental impacts of products and organizations over their entire life cycle, based on established international practices and standards such as ISO 14040/44 [114, 115]. This fosters transparency, provides access to credible environmental information and supports informed decision-making by companies and consumers, making it a crucial enabler on the path towards a more sustainable economy.

The LCA EF 3.1 methodology: LCA consists of 4 major steps: the system boundary definition, the life cycle inventory, the life cycle impact assessment, and interpretation of the results [116]. For the system boundary definition, it is determined and described which life cycle stages of the investigated product are included into the life cycle assessment. These steps are typically raw material extraction, material processing, assembly to the final product, product operation time including necessary maintenance, and the end-of-life stage, considering recycling or disposal. The transport and distribution of materials and products is also considered between the different stages. Furthermore, in this step, the functional unit (FU) is defined so that a comparison can be made between products/materials that serve the same purpose.
In the second step, the material and energy inputs and outputs are identified and quantified for all targeted life cycle stages, which is called life cycle inventory. The inputs and outputs, such as the energy mix of a country or basic chemicals, are modelled from the investigated processes. Either those in- and outputs can be directly obtained from established databases such as ecoinvent [145], or they have to be self-modelled. In the third step, the inputs and outputs of the Life Cycle Inventory are assigned to the environmental impact categories such as global warming potential, land use, water use, acidification potential of soil and water, ozone depletion, human and environmental toxicity [116, 117, 146]. Finally, in the fourth step, the assessment results are interpreted.

System boundary and functional unit in the case study: The system boundary for the LCA covers the entire precursor fabrication process of $La_{0.6}Sr_{0.4}CoO_{3-\delta}$ and $La_{0.6}Ca_{0.4}FeO_{3-\delta}$, including raw material extraction and processing with all necessary transportation steps (see also figure 54). In this study, 1 kg catalyst load of the two perovskites serves as FU. The choice of the functional unit is based on the CV results of $La_{0.6}Sr_{0.4}CoO_{3-\delta}$ and $La_{0.6}Ca_{0.4}FeO_{3-\delta}$ thin films, which are further elaborated in section 5.9 and 7.1.

This FU is a simplified approach compared to FUs used in LCAs of more mature hydrogen technologies, where typically the catalyst mass per kW or per kg H_2 over the lifespan of the electrolyzer is chosen [147]. However, the choice of mass as FU is useful for comparing initial impact differences and identifying possible hotspots of the precursor materials. Here, the FU is hence chosen based on the initial activity obtained in rotating disk electrode (RDE) studies, but has to neglect aspects of load optimization, integration and final stack lifetime. A similar approach was chosen by Mori *et al*. for their hydrogen technology LCA study where the FU is also set to the mass of the relevant material [148].

Life cycle inventory and life cycle impact assessment in the case study: The life cycle inventory data and their resulting environmental impacts were taken from the ecoinvent3.9 database for the $La_{0.6}Sr_{0.4}CoO_{3-\delta}$ and $La_{0.6}Ca_{0.4}FeO_{3-\delta}$ precursors, based on the precursor masses in table 4. The ecoinvent datasets used for the different precursors can be found in the table 5. While the La-, Sr-, Ca-, and Co-precursors stem from primary material extraction,

Table 5: Precursor life cycle impact assessment datasets taken from ecoinvent3.9. GLO stands for an average global supply, and RER for supply in Europe.

precursor	database entry ecoinvent3.9
La_2O_3	GLO: market for lanthanum oxide
$SrCO_3$	GLO: strontium carbonate production
Co_3O_4	GLO: market for cobalt oxide
$CaCO_3$	RER: calcium carbonate production
Fe	modelled by Dr. A. Schreiber

the Fe-precursor comes from secondary material sources. This is because higher Fe-scrap amounts are available on the market, and it is compatible with the perovskite fabrication. A detailed discussion on this is provided in section 7.2 and 7.7. Therefore, the result for the Fe-precursor was self-modelled. For the supply of those iron filings, the process chain includes the following single processes from the ecoinvent3.9 database: collecting of new and old iron scrap, transport to the scrap-yard, sorting and pressing to blocks, and an iron milling process to obtain iron filings. The impact categories evaluated here for the life cycle impact assessment are climate change, water use, land use, acidification, human ecotoxicity, freshwater ecotoxicity, resource use - minerals and metals, eutrophication marine and freshwater, ozone depletion, photochemical ozone formation and ionizing radiation. Table 6 shows the impact category indicators and units of the evaluated categories.

Table 6: Considered impact categories and the corresponding units [116, 117].

Impact category	Explanation and unit
climate change	global warming potential in kg CO_2 equivalents (eq.)
water use	deprivation weighted water consumption in m^3 world equivalents (eq.)
land use	soil quality index in points (Pt)
acidification potential	accumulated exceedance of acids in the exposed area in mol of H^+ eq.
human toxicity, cancer	comparative toxic unit for humans in CTUh
ecotoxicity, freshwater	comparative toxic unit for ecosystems in CTUe (comparative toxic unit for aquatic ecotoxicity impacts)
resource use - minerals and metals	abiotic resource use of minerals and metals in kg antimony (Sb) eq.
eutrophication, freshwater	fraction of nutrients reaching fresh water endcompartment in kg P eq. (impacts of nutrients relative to P phosphorous containing nutrients)
eutrophication, marine	fraction of nutrients reaching marine end compartment in kg N eq. (impacts of nutrients relative to N nitrogen containing nutrients)
ionizing radiation human health	human exposure efficiency relative to U235 in kBq U235 eq. (Becquerel)
ozone depletion	ozone depletion potential in kg CFC-11 eq. (chlorofluorocarbon-11)
photochemical ozone formation, human health	tropospheric ozone concentration increase in kg NMVOC eq. (non-methane volatile organic compounds)

3.7.4 Social impact - qualitative indicators

Qualitative and (semi-)quantitative tools for a social life cycle assessment (sLCA) have been developed [149, 150] and applied to energy technologies [151–153]. However, social impact assessment methodologies have a lower stage of maturity than environmental LCA [150]. Typically, sLCA requires extensive data collection, often inaccessible on the level of early-stage research. Hence, this study considers existing literature for a qualitative identification of hazardous working conditions and the existence of child labor for the raw material extraction of the precursors for $La_{0.6}Sr_{0.4}CoO_{3-\delta}$ and $La_{0.6}Ca_{0.4}FeO_{3-\delta}$.

3.7.5 Material recycling

Recycling and substitution of critical materials are risk-minimizing factors as they directly reduce the dependency of the raw material supplying countries and companies [93, 154]. This is re-

flected in the calculation of the supply risk in the EC-CRM 2023 [93]. However, today's recycling rates and secondary material usage are relatively low for many relevant materials [93, 154]. For example, the "End-of-life Recycling Input Rate" (EOL-RIR) [154] of the platinum group metals and the rare earth metals is only 12% and 1%, respectively [93]. Here, the current EOL-RIR was considered as a separate indicator [93] to identify if sufficient secondary material supply exists for the relevant precursor materials of $La_{0.6}Sr_{0.4}CoO_{3-\delta}$ and $La_{0.6}Ca_{0.4}FeO_{3-\delta}$. Then, we assess if the available recycled materials are suitable for the projected perovskite synthesis (see sectionsection 7.2 and 7.7). Based on this, recycled precursor materials are considered for the sustainability evaluation.

4 Thin film fabrication and characterization

This chapter contains the fabrication and characterization of the perovskite epitaxial thin films $La_{0.6}Sr_{0.4}CoO_{3-\delta}$, $La_{0.6}Ca_{0.4}CoO_{3-\delta}$, $La_{0.6}Sr_{0.4}FeO_{3-\delta}$, $La_{0.6}Ca_{0.4}FeO_{3-\delta}$ and $La_{0.6}Ca_{0.4}NiO_{3-\delta}$ by PLD on single-crystalline substrates as well as on platinized silicon. The perovskites were grown on $SrTiO_3$, $NdGaO_3$ or $LaAlO_3$ to achieve the best lattice match. To ensure electrical contact to the potentiostat for electrochemical measurements Pt side contacts were sputtered at the front edges of the thin films on the insulating substrates. For a direct backside contact, Nb:$SrTiO_3$ was used as substrate whereas a 2-4 unit cells of $LaAlO_3$ were grown as interlayer to counteract contact resistances between Nb:$SrTiO_3$ and the catalyst layer. While $La_{0.6}Sr_{0.4}CoO_{3-\delta}$, $La_{0.6}Sr_{0.4}FeO_{3-\delta}$ and $La_{0.6}Ca_{0.4}FeO_{3-\delta}$ were grown under the same conditions, $La_{0.6}Ca_{0.4}CoO_{3-\delta}$ and $La_{0.6}Ca_{0.4}NiO_{3-\delta}$ epitaxial thin films required growth optimization as detailed in sections 4.2 and 4.3. Additionally, $La_{0.67}Sr_{0.33}MnO_{3-\delta}$ as well as $LaNiO_{3-\delta}$ thin films, used for a comparative study of electrocatalytic performances, were fabricated by Iris van den Bosch, Emma van der Minne and Ellen Kiens at the University of Twente (Netherlands). Corresponding sample characterization is summarized in the appendix figure A.1. The growth optimized crystal structure, resistivity as well as valence band electronic structure of all perovskites are compared in the final section 4.4 of this chapter.

4.1 $La_{0.6}Sr_{0.4}CoO_{3-\delta}$, $La_{0.6}Sr_{0.4}FeO_{3-\delta}$ and $La_{0.6}Ca_{0.4}FeO_{3-\delta}$ growth

$La_{0.6}Sr_{0.4}CoO_{3-\delta}$ as benchmark material was grown at 650 °C, with 0.05 mbar oxygen partial pressure, 5 Hz pulse frequency and 2.2 J cm^{-2} laser fluence on (110) orthorhombic $NdGaO_3$ [34, 129]. The lattice parameter of the pseudo-cubic notation of (100) $La_{0.6}Sr_{0.4}CoO_{3-\delta}$ is similar to that of the pseudo-cubic $NdGaO_3$ [129]. The orthorhombic lattice parameters of $NdGaO_3$ are $a = 5.431$ Å, $b = 5.499$ Å, $c = 7.710$ Å, which corresponds to a pseudo-cubic unit cell lattice parameter of $a = 3.865$ Å.

The growth was tracked *in situ* with RHEED as illustrated in figure 17a. Initially, clear intensity oscillations can be obtained while the overall intensity of the specular spot increased continuously, reaching a plateau after 200 s. In the RHEED pattern after deposition (figure 17a inset), the specular and diffractive spots exhibit a streaky shape, indicating a slightly roughened surface. The corresponding AFM shows a clear step terrace structure and smooth surface morphology. For $La_{0.6}Sr_{0.4}FeO_{3-\delta}$, as a potentially more sustainable catalyst material, the same growth parameters were applied, except that (100) $SrTiO_3$ was selected as the substrate. The lattice mismatch between $La_{0.6}Sr_{0.4}FeO_{3-\delta}$ and $SrTiO_3$ is smaller than on $NdGaO_3$ (see also table 8). The initial RHEED intensity (figure 17b) decreases in the first few seconds and shows layer-by-layer growth up to 250 s. The RHEED intensity partly recovers while the oscillations fade out. The final RHEED pattern is similar to that of $La_{0.6}Sr_{0.4}CoO_{3-\delta}$, showing streaks of the specular and diffractive spots. Also, the AFM scan shows a smooth surface morphology with a clear step terrace structure.

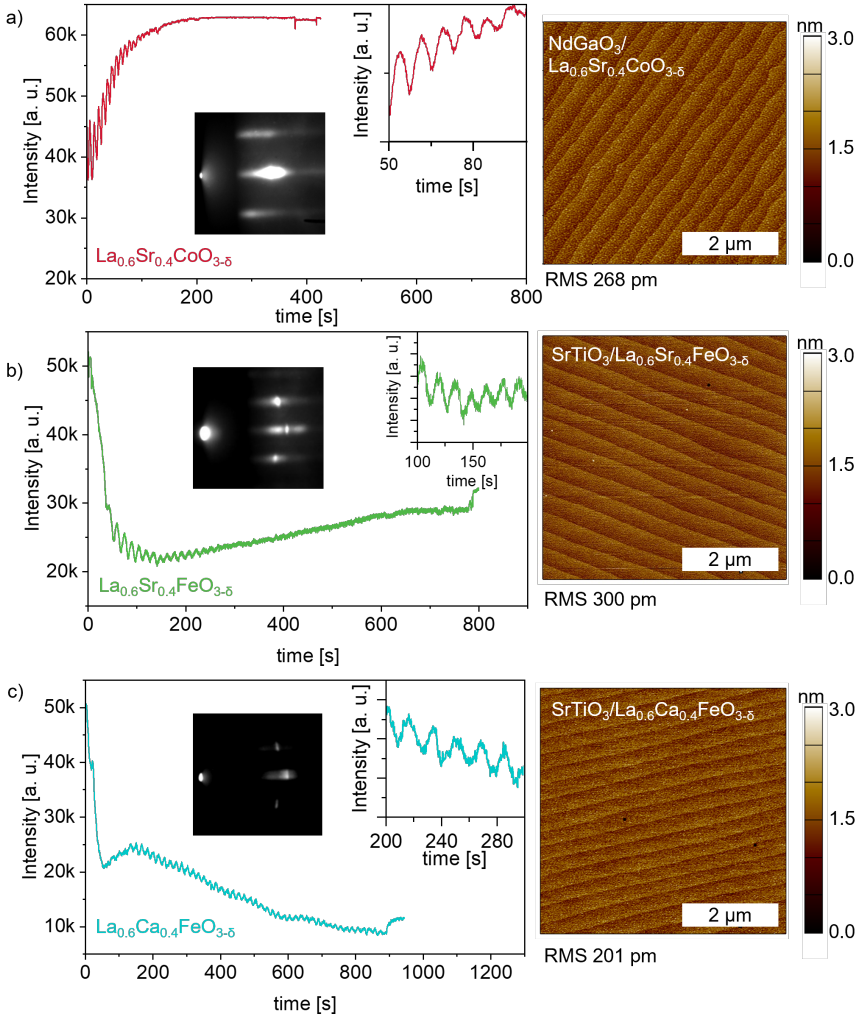

Figure 17: PLD deposition of a) $La_{0.6}Sr_{0.4}CoO_{3-\delta}$ on $NdGaO_3$ b) $La_{0.6}Sr_{0.4}FeO_{3-\delta}$ on $SrTiO_3$ and c) $La_{0.6}Ca_{0.4}FeO_{3-\delta}$ on $SrTiO_3$. The RHEED oscillations are shown on the left, the RHEED pattern after deposition of 20 nm in the inset, and the surface morphology on the right.

Furthermore, $La_{0.6}Ca_{0.4}FeO_{3-\delta}$, in which Sr was substituted for Ca due to its potentially greater sustainability (cf. chapter 7), was successfully grown under the same conditions on (100) $SrTiO_3$ (figure 17c). The RHEED signal initially decreases. However, RHEED oscillations indicative of layer-by-layer growth are observed for all 52 unit cells (uc). A final 2D streaky RHEED pattern and a smooth surface morphology of $La_{0.6}Ca_{0.4}FeO_{3-\delta}$ in the AFM scan is observed.
Overall, no further parameter optimization was necessary to synthesize single-crystalline films of these three materials. While all the above listed perovskites are tested for electrochemical OER activity, $La_{0.6}Sr_{0.4}CoO_{3-\delta}$and $La_{0.6}Ca_{0.4}FeO_{3-\delta}$ later play a major role in the material sustainability evaluation. There, they are used as case study examples to determine which impact the A- and B-site substitution from $La_{0.6}Sr_{0.4}CoO_{3-\delta}$ to $La_{0.6}Ca_{0.4}FeO_{3-\delta}$ makes from a holistic material choice point of view. The crystallographic characterization and conductivity can be viewed in the section 4.4.

4.2 $La_{0.6}Ca_{0.4}CoO_{3-\delta}$ growth

$La_{0.6}Ca_{0.4}CoO_{3-\delta}$ exhibits a cubic lattice parameter of $c = 3.817$ Å [155] (see also table 8). Therefore, 20 nm of $La_{0.6}Ca_{0.4}CoO_{3-\delta}$ were initially grown on $NdGaO_3$ as the lattice mismatch is relatively small (1.3 %) compared to $SrTiO_3$ (2.3 %). Initial growth parameters were chosen according to previous $La_{0.6}Sr_{0.4}CoO_{3-\delta}$ parameters of 0.05 mbar O_2 pressure, 650 °C growth temperature, and the fluence was varied between 1.8-3.5 J cm^{-2}. The fluence can influence, for example, the final plasma plume stoichiometry and the kinetic energy of arriving particles at the substrate surface.
Fluence variation: Independent of the varied fluence, the $La_{0.6}Ca_{0.4}CoO_{3-\delta}$ thin films show in the XRD scan in 2θ-ω geometry a distinct thin film peak at 48.14° of the (002) orientation (figure 18a). This corresponds to a c-lattice parameter of $c = 3.78$ Å in the pseudo-cubic notation. The c-lattice parameter is smaller than the literature bulk value, because it grows in a tensile strain on the substrate. The thickness fringes indicate a defined and sharp interface to the substrate and air. However, the AFM scans in figure 18b show that particles form on the surface. From 1.8 J/cm^2 to 2.4 J/cm^2, the RMS decreases from 1 nm to 709 pm. From there, a higher fluence increases the surface roughness. Up to 3.0 J/cm^2 the surface particles preferably sit on the step edges whereas at 3.5 mJ/cm^2 the particles seem to be randomly distributed.
Temperature variation: With the aim of decreasing particle formation, the growth temperature was varied between 550 °C and 800 °C. The growth temperature influences the mobility of adatoms on the surface and, with that, the agglomeration of particles. Further, a higher temperature can induce particle segregation from the bulk. Figure 19a illustrates the XRD of the as-grown films where the (002) peak and thickness fringes can be obtained for all samples in the tested temperature range. Also here, the lattice parameter remains around $c = 3.78$ Å. As can be seen from the AFM scans in figure 19b, at a growth temperature of 550 °C the RMS is 1.4 nm. Hence, the surface roughness increases compared to the initial growth temperature of

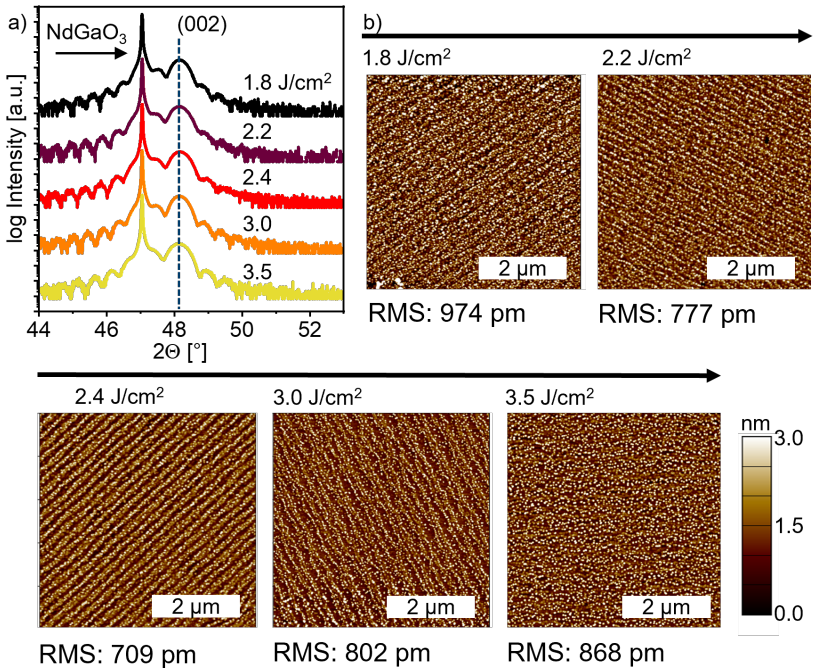

Figure 18: a) XRD scans recorded in the range of the (002) peak of 20 nm thick $La_{0.6}Ca_{0.4}CoO_{3-\delta}$ epitaxial thin films grown on $NdGaO_3$ substrates with increasing laser fluence as listed accordingly. b) Corresponding AFM scans with increasing laser fluence as listed along the arrows. Particles are seen on every surface. THE RMS is the lowest at a laser fluence of 2.4 J cm^{-2}.

650 °C. At 700 °C and 750 °C, the RMS decreases to approx. 500 pm, but as the step terrace width of the sample grown at 750 °C is much wider, the decreased RMS might not be solely related to the increased growth temperature. At a growth temperature of 800 °C, large particles form on the surface, resulting in a RMS of 6.1 nm. While the surface particles on the thin films grown between 550 °C and 750 °C are within the color bar range of 3 nm, the particles of the sample grown at 800 °C are much larger with a height of 15-20 nm.

To obtain the possible nature of the particles on the surface, XPS was conducted where the Ca 2*p* core level is shown in figure 19. The Ca 2*p* 1/2 and 3/2 peaks exhibit at least two different Ca species, represented by the peaks of at least two doublets. The signal at higher binding energies might be a Ca-containing compound at the surface, as also described and observed for $La_{0.6}Ca_{0.4}CoO_{3-\delta}$ thin films in the literature [156]. As described by Weber et al. [21], a Sr surface component of $La_{0.6}Sr_{0.4}CoO_{3-\delta}$ thin films can be dissolved when the thin film is soaked in a 0.1 M KOH solution, which is the electrolyte later on used in the electrochemical mea-

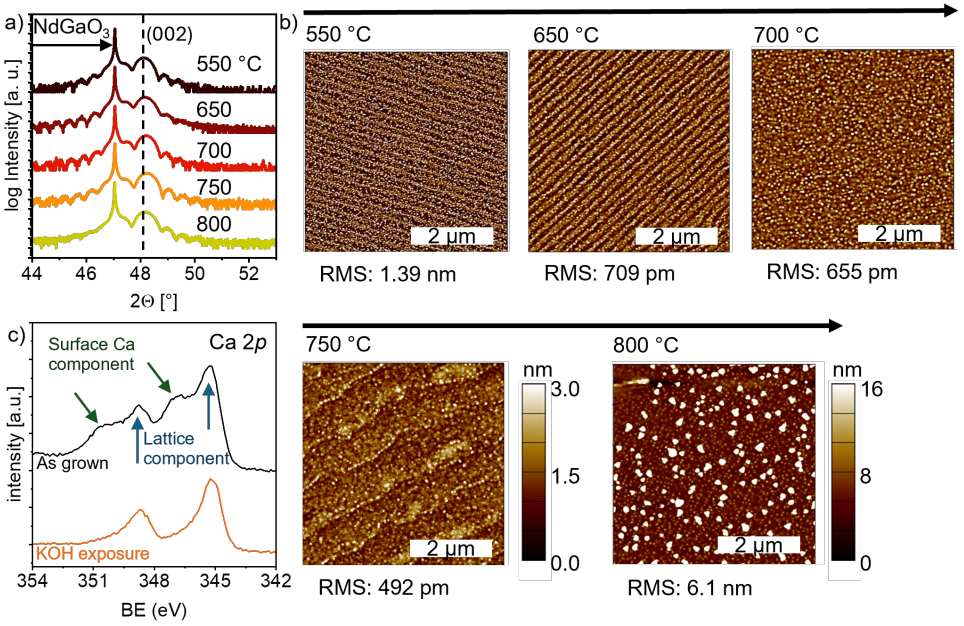

Figure 19: XRD scans recorded in the range of the (002) peak of 20 nm thick $La_{0.6}Ca_{0.4}CoO_{3-\delta}$ thin films that were grown on $NdGaO_3$ substrates with increasing temperature. b) AFM of corresponding thin films with increasing temperature as listed along the arrows. c) $La_{0.6}Ca_{0.4}CoO_{3-\delta}$ thin film XPS data of the Ca 2*p* core level are shown in the as-prepared state and after exposure to 0.1 M KOH solution.

surements. When the $La_{0.6}Ca_{0.4}CoO_{3-\delta}$ sample is exposed to 0.1 M KOH for 45 min, the Ca species at higher binding energies is indeed strongly decreased as indicated in the spectrum at the bottom of figure 19. Hence, the surface Ca-species may be dissolved in the electrochemical experiments. Note, that the surface morphology did not change significantly after the film was exposed to the KOH solution.

Oxygen partial pressure variation: To investigate the particle formation upon different oxygen pressures, 0.004 mbar, 0.05 mbar, and 0.15 mbar were applied. The fluence was fixed at 2.4 J cm^{-2} and the temperature was fixed at 750 °C. As in the presence of oxygen gas, lighter plasma particles scatter more strongly than heavier particles [124], excessive Ca in the plasma might be decreased at higher O_2 partial pressures ($m_{Ca} = 40$ Da $< m_{Co} = 59$ Da $< m_{La} = 138$ Da). Additionally, different metal oxide species can form in the plasma plume, leading to different oxygen and cation stoichiometries. As seen in figure 20, the oxygen pressure significantly influences the c-lattice parameter of the thin film. At a partial pressure of 0.004 mbar the (200) XRD peak shifts close to the one of $NdGaO_3$, where some thickness fringes can be obtained at higher 2θ angles. Supposedly, oxygen vacancies are formed, leading to a lattice

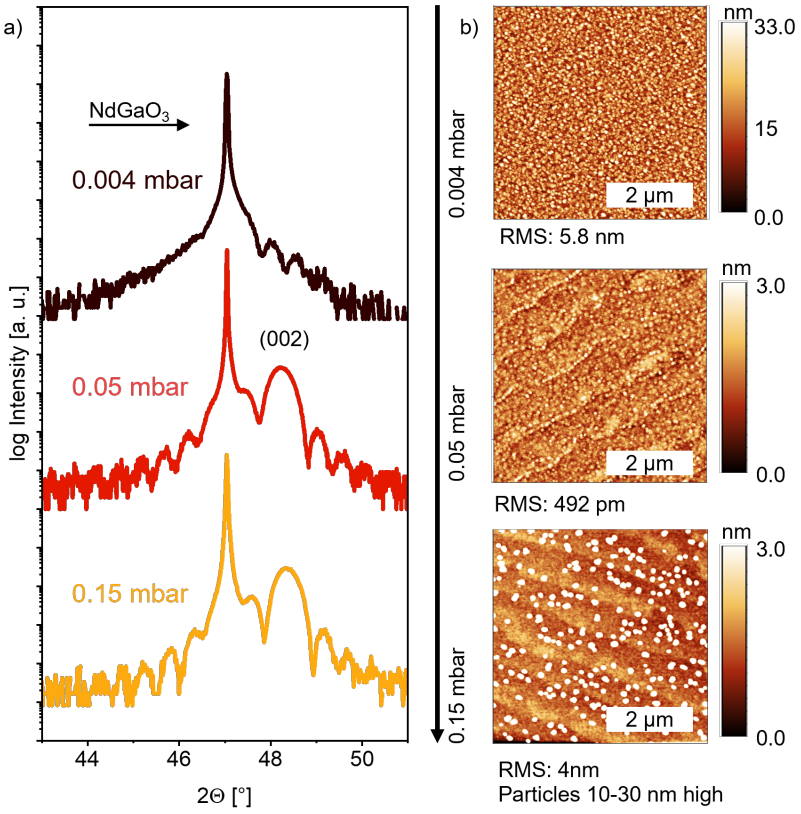

Figure 20: a) XRD b) AFM of 20 nm thick $La_{0.6}Ca_{0.4}CoO_{3-\delta}$ thin films grown on $NdGaO_3$ substrates with increasing O_2 partial pressure.

expansion. Similarly, a lattice expansion of $La_{0.6}Sr_{0.4}CoO_{3-\delta}$ thin films was observed by oxygen vacancy formation under reducing conditions by He *et al*. [157].
At a deposition pressure of 0.15 mbar the c-lattice constant slightly decreases which might stem from a change in cation or oxygen stoichiometry. For the samples grown with an oxygen partial pressure of 0.004 mbar and 0.15 mbar the surface roughnesses are high with a RMS of 5.8 nm and 4 nm, respectively. Note, that the particle distribution differs between those two samples. The film grown at 0.004 mbar is shown with a big color range bar of 33 nm, and the 15-20 nm high

particles are closely packed next to each other, referring more to islands. The thin film grown at 0.15 mbar still exhibits a step terraced surface morphology with large particles of 10-30 nm but in a much lower density. Hence, the initially chosen oxygen partial pressure of 0.05 mbar remains the most advantageous. The observed surface particles that potentially stem from a Ca-component as indicated by the XPS results, might occur due to cation segregation effects. The driving forces of cation segregation in solid solutions are elastic and electrostatic interactions of the dopant with the host lattice [158].

Strain variation: As the strain (ϵ) of the epitaxial thin films can influence the segregation of different cations [159], $La_{0.6}Ca_{0.4}CoO_{3-\delta}$ was grown on $LaAlO_3$ ($\epsilon = -0.8$ %), $NdGaO_3$ ($\epsilon = 1.3$ %) and $SrTiO_3$ (2.3 %) substrates with a lattice constant of 3.788 Å, 3.865 Å and 3.905 Å, respectively. The XRD in figure 21 shows that in all three strain states the (002) peaks are clearly

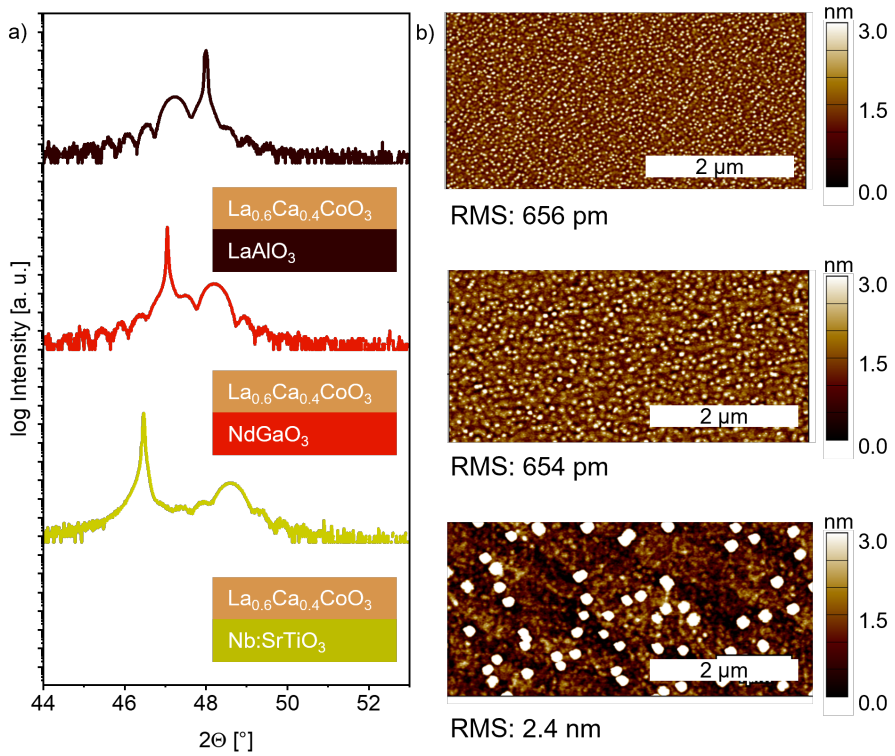

Figure 21: $La_{0.6}Ca_{0.4}CoO_{3-\delta}$ grown on the different substrates $LaAlO_3$, $NdGaO_3$ and $SrTiO_3$ to induce compressive and tensile strain. a) shows the XRD and b) the AFM.

visible, $LaAlO_3$ inducing a compressive strain, $NdGaO_3$ and $SrTiO_3$ inducing increasing tensile strain. The AFM scans in figure 21b indicate that going from tensile to compressive strain does not influence the surface roughness. On $LaAlO_3$ as well as on $NdGaO_3$, the RMS is around 650 pm. Hence, the Ca surface species could not be suppressed by inducing the opposite strain. However, when $La_{0.6}Ca_{0.4}CoO_{3-\delta}$ is grown on $SrTiO_3$, the further increased tensile strain induces the formation of large particles (RMS 2.4 nm), that are approx. between 8-20 nm high.
Overall, $La_{0.6}Ca_{0.4}CoO_{3-\delta}$ shows high crystallinity over a wide laser fluence (1.8 J cm^{-2}-3.5 J cm^{-2}), temperature (550 °C-800 °C) and oxygen partial pressure range (0.004 mbar-0.15 mbar). However, the upper and lower limits of those ranges increase the surface roughness and particle formation. Within the scope of this parameter variation, the formation of small surface particles was hence unavoidable, apparently related to a tendency for Ca surface segregation. Hence, the intermediate regime of the growth parameters was chosen for the use of the epitaxial thin films in the electrochemical characterization; the final growth parameters are listed in table 2.

Insertion of $LaAlO_3$ interlayer: As described in section 3.6, Nb:$SrTiO_3$ is used as a conducting single-crystalline substrate to reduce electron transport pathways through the thin film to the electrical contact of the RDE. Nevertheless, it can lead to contact resistances at the thin film interface, and hence, $LaAlO_3$ as a dipole layer is inserted (see section 2.4). In the case of $La_{0.6}Ca_{0.4}CoO_{3-\delta}$, 4 uc of $LaAlO_3$ were grown on the etched and annealed Nb:$SrTiO_3$ substrate, where the four local maxima of the RHEED intensity oscillations can be seen in figure 22a. The RHEED intensity decreases with the growth of the 4 uc as can be seen from the initial and final RHEED patterns. For the subsequent $La_{0.6}Ca_{0.4}CoO_{3-\delta}$ deposition, the RHEED intensity was manually increased. $La_{0.6}Ca_{0.4}CoO_{3-\delta}$ growth starts with a RHEED intensity drop (figure 22b) and partly recovers the intensity over time, initially exhibiting layer-by-layer growth. The observed oscillations fade out, and the intensity continuously decreases. A streaky, 2D RHEED pattern can be observed after the deposition (see in the top right corner). In the bottom panel of figure 22b, the RHEED intensity and pattern of an $La_{0.6}Ca_{0.4}CoO_{3-\delta}$ thin film directly grown on $SrTiO_3$ are shown for comparison. Here, the initial intensity drop does not recover leading to a very weak RHEED intensity signal in the RHEED pattern after deposition.

Surprisingly, the AFM shows a much smoother surface compared to the $La_{0.6}Ca_{0.4}CoO_{3-\delta}$ thin film directly deposited on Nb:$SrTiO_3$, and step terraces are clearly visible. The RMS of the $La_{0.6}Ca_{0.4}CoO_{3-\delta}$ thin film with the $LaAlO_3$ interlayer is only 430 pm, whereas on Nb:$SrTiO_3$ it is 2.4 nm (compare with figure 21). However, the thin film surface shows straight lines, which might suggest a cracking of the thin film due to the high strain. Such crack formation was observed on thicker $La_{0.6}Sr_{0.4}CoO_{3-\delta}$ thin films on $SrTiO_3$ [128], where such stripes were also observed on the thin film surface. In figure 22d, the corresponding XRD is shown for $La_{0.6}Ca_{0.4}CoO_{3-\delta}$ with and without $LaAlO_3$ interlayer on $SrTiO_3$. The tensile strain is only slightly smaller, when the interlayer is present. Thus, the large particle formation of the $La_{0.6}Ca_{0.4}CoO_{3-\delta}$ thin film directly

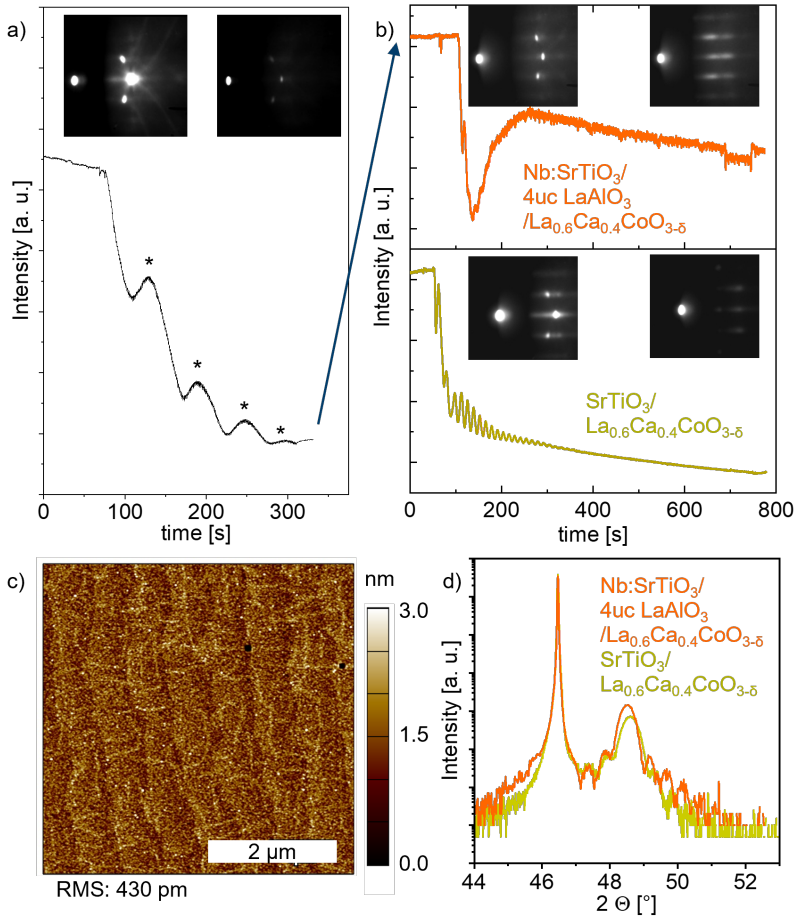

Figure 22: a) Growth of 4 unit cells $LaAlO_3$ on Nb:$SrTiO_3$. The * mark the four local RHEED intensity maxima of the $LaAlO_3$ growth. b) Top graph: subsequent $La_{0.6}Ca_{0.4}CoO_{3-\delta}$ deposition with the RHEED patterns before and after growth. Bottom graph $La_{0.6}Ca_{0.4}CoO_{3-\delta}$ deposition directly on $SrTiO_3$ without $LaAlO_3$ layer. c) AFM of the $La_{0.6}Ca_{0.4}CoO_{3-\delta}$ surface where $LaAlO_3$ layer is buried. d) XRD comparison of the (002) $La_{0.6}Ca_{0.4}CoO_{3-\delta}$ peak grown on Nb:$SrTiO_3$ with a 4 uc thick $LaAlO_3$ interlayer, and directly deposited on a $SrTiO_3$ substrate.

deposited on $SrTiO_3$ seems to be strongly suppressed by the $LaAlO_3$ interlayer. Hence, the tensile strain might not significantly influence particle formation, but other phenomena could influence the particle formation, such as the octahedral tilt differences of the underlying layer [160]. For the electrochemical characterization, $La_{0.6}Ca_{0.4}CoO_{3-\delta}$ was grown on the $LaAlO_3$ substrate

to receive the smallest lattice mismatch on the substrate. Additionally, to ensure backside contact, the Nb:$SrTiO_3$/4 uc $LaAlO_3$/$La_{0.6}Ca_{0.4}CoO_{3-\delta}$ stack was used.

4.3 $La_{0.6}Ca_{0.4}NiO_{3-\delta}$ growth

To obtain favorable growth conditions for epitaxial $La_{0.6}Ca_{0.4}NiO_{3-\delta}$, a temperature series from 450 °C to 750 °C was conducted on orthorombic $NdGaO_3$ (110) substrates inspired by previous work on $LaNiO_{3-\delta}$ [19]. The pseudo-cubic lattice parameter of $LaNiO_{3-\delta}$ $c = 3.853$ Å [161] is similar to the one of $NdGaO_3$ ($c = 3.865$ Å). The fluence was 2.2 J cm^{-2}, the O_2 partial pressure was 0.05 mbar. As shown in figure 23a, for all depositions the RHEED intensity initially drops drastically. RHEED oscillations can be observed within the first 100 seconds of the deposition and fade out over time. For all samples, the whole RHEED pattern was not observable anymore, after a deposition time equivalent to the growth of 52 uc. For the sample grown at 550 °C, most local maxima for a layer-by-layer growth were observed.
To confirm the targeted layer thickness of 20 nm, XRR scans were conducted and are shown in figure 23c. As can be seen from the periodicity of the Kiessig fringes, the thickness is comparable for all samples. However, for the samples grown at 650 °C and 750 °C, the Kiessig fringes are not clearly seen above $2\theta = 2°$. The thin film thickness t of the different samples was estimated with the equation 12 yielding a result of 20-23 nm.
The AFM scans show that the surface roughness increases with the growth temperature (figure 23c). The samples grown at 450 °C and 550 °C exhibit a surface roughness below 500 pm. The sample grown at 550 °C shows fewer particles on the surface compared to the one grown at 450 °C, but a stripe pattern along the step terraces from light brown to dark brown is observed. This might be related to the $NdGaO_3$ substrate, which showed kinks along the step edges. The samples grown at 650 °C and 750 °C have an increased surface roughness and exhibit small needle-like structures, where small holes occur in between. This increased roughness might suppress the observation of Kiessig fringes in the XRR at higher angles. The thin film roughness directly influences the obtainable Kiessig fringes [132].
The XRD pattern of the sample grown at 450 °C (figure 24a and b) does not show a clear peak across the whole scanning range from 10-120°. The sharp, lower intensity peaks seen at 11.4°, 34.8°, 59.4° and 88.7° stem from other reflexes of the $NdGaO_3$ substrate as the XRD of a bare $NdGaO_3$ substrate reference (yellow) shows. The sample grown at 550 °C shows clear thin film reflections from the (002) and (004) planes (figure 24a and b). For the sample grown at 650 °C, there is also no thin film peak observed over the whole scanning range.
From the RHEED, XRR and XRD data it is to conclude that the film thickness is achieved at all investigated growth temperatures, however only at 550 °C an epitaxial thin film with the defined (001) orientation was obtainable. It might be that randomly oriented crystallization takes place above 550 °C. Additionally, if the thin film peak is located at the same diffraction angle of the $NdGaO_3$ substrate, the substrate covers its signal.

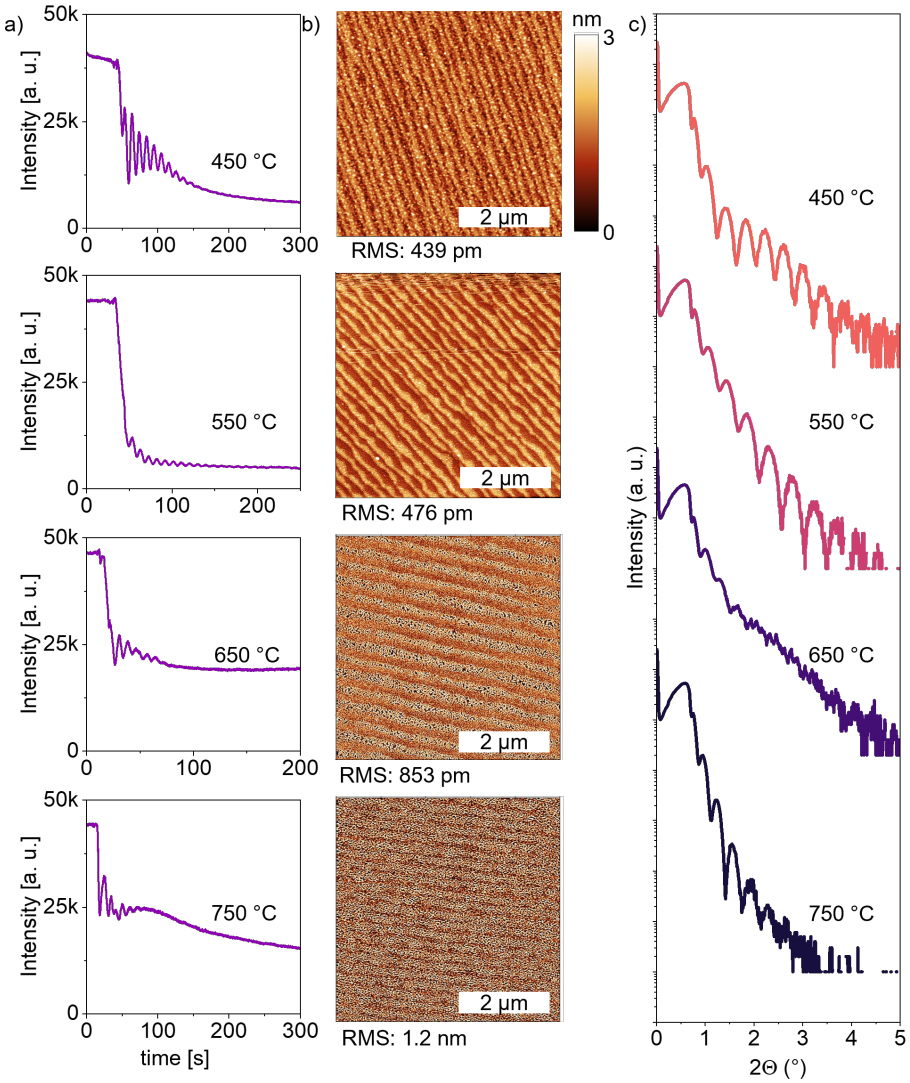

Figure 23: $La_{0.6}Ca_{0.4}NiO_{3-\delta}$ thin films grown on $NdGaO_3$ with increasing temperature a) *In-situ* RHEED tracking of the growth. b) Corresponding AFM scans and c) XRR scans.

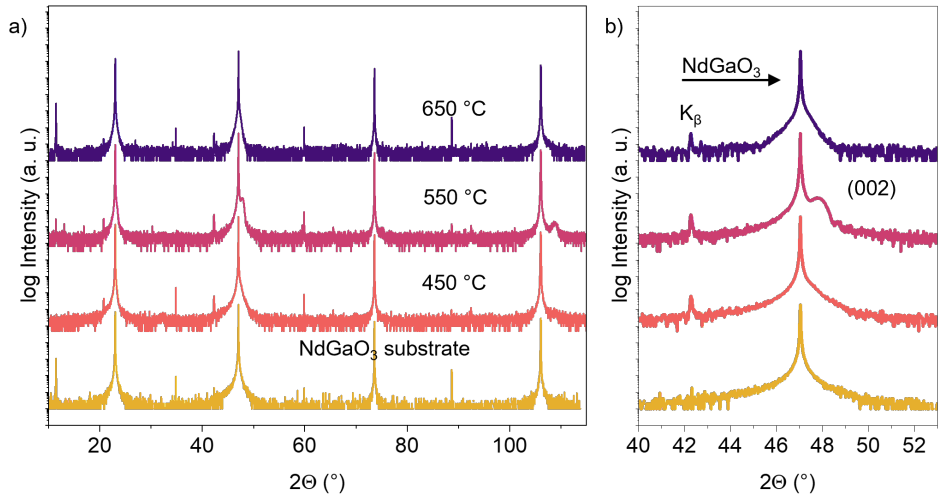

Figure 24: Temperature series of $La_{0.6}Ca_{0.4}NiO_{3-\delta}$ a) XRD from 10°-120° in 2θ-ω geometry. The yellow graph shows the $NdGaO_3$ substrate as reference. b) Zoom to the (002) peak.

To avoid a possible overlap of diffraction peaks with the $NdGaO_3$ substrate and enable electrical backside contact on Nb:$SrTiO_3$, $La_{0.6}Ca_{0.4}NiO_{3-\delta}$ was grown at 550 °C on $SrTiO_3$ and Nb:$SrTiO_3$. The AFM scan and XRD scan of the sample grown on $SrTiO_3$ are shown in figure 25a and b (top). The surface morphology is smooth with a RMS of only 187 pm which is lower compared to the RMS under the same growth conditions on $NdGaO_3$. The XRD scan shows a clear (002) peak and Laue oscillations towards higher and lower 2θ angles (figure 25b (top)). However, at around 2θ =43-44°, the Laue oscillations overlap with a smaller peak (see blue arrow) which might be attributed to an additional crystal phase in the thin film. For example, NiO is likely to form with a peak at 43.3° [162, 163]. Also, a $Ca(CO_3)_2$ species might form in air exhibiting a peak at 43.5° in the calcit phase [164]. Further, the peak might stem from the Ruddlesden-Popper phase, which was observed in a solid solution series of Ca-doped lanthanum nickelates. For example, $La_{1.6}Ca_{0.4}NiO_{4-\delta}$ shows the (006) reflex at 43.1° [73, 74]. Note, that the additional peak might also stem from remaining silver paste. However, since the signal repeatedly occurred only under these growth conditions for $La_{0.6}Ca_{0.4}NiO_{3-\delta}$ and not for any other sample measured, it would be unlikely that the XRD signal stems from remaining silver paste.

A repeated AFM scan was recorded 6 weeks after the thin film growth (figure 25 middle). Upon prolonged air exposure, the surface morphology changes drastically. Large needle structures form and are randomly distributed on the surface. The corresponding XRD scan, however, does not show significant differences compared to the XRD recorded only some days after growth.

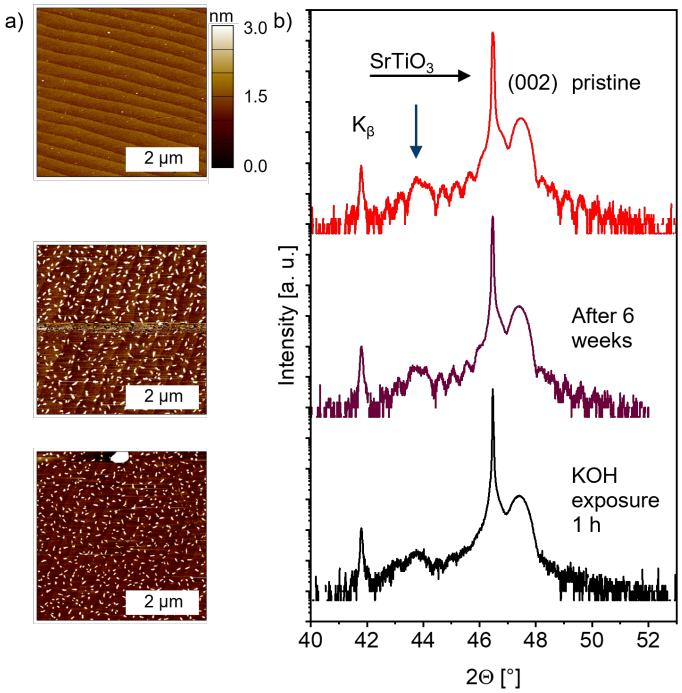

Figure 25: a) AFM scans and b) XRD of a 20 nm thick $La_{0.6}Ca_{0.4}NiO_{3-\delta}$ film grown on $SrTiO_3$. Data of the pristine film are in the top, six weeks of air exposure in the middle and subsequent exposure to 0.1 M KOH solution for 1 h in the bottom.

Hence, mainly the surface morphology is affected by the aging effect when storing the sample for extended periods in air, but not the crystallinity. When the sample is exposed to 0.1 M KOH solution, this needle structure remains, which is shown in the AFM scan at the bottom of figure 25a. As the corresponding XRD indicates, the additional crystalline phase remains intact, and only the Laue oscillations fade upon exposure to the KOH solution. As the surface morphology changes drastically in air, electrochemical measurements were conducted within 6 days (including XPS measurements in vacuum) after the sample fabrication.

4.4 Crystal structure, resistivity and valence band structure of the perovskites

This section starts with the crystal structure characterization of the perovskites $La_{0.6}Sr_{0.4}CoO_{3-\delta}$, $La_{0.6}Ca_{0.4}CoO_{3-\delta}$, $La_{0.6}Ca_{0.4}NiO_{3-\delta}$, $La_{0.6}Sr_{0.4}FeO_{3-\delta}$, and $La_{0.6}Ca_{0.4}FeO_{3-\delta}$ grown on $SrTiO_3$. This is because the conducting Nb:$SrTiO_3$ was necessary for an electronic backside contact in the electrochemical experiments for all perovskites. Then the crystal structure is compared to the growth on substrates with their best lattice match to asses the electrochemical activity without backside contact influence (see also section 3.6) and strong influence on the strain. The electrical resistivity is then compared for all perovskites, including $La_{0.67}Sr_{0.33}MnO_{3-\delta}$ and $LaNiO_{3-\delta}$ produced by Emma van der Minne, Ellen Kiens and Iris van den Bosch in the University of Twente. The valence band electronic structure is characterized for $La_{0.6}Sr_{0.4}CoO_{3-\delta}$, $La_{0.6}Ca_{0.4}CoO_{3-\delta}$, $La_{0.6}Ca_{0.4}NiO_{3-\delta}$, $La_{0.6}Sr_{0.4}FeO_{3-\delta}$ and $La_{0.6}Ca_{0.4}FeO_{3-\delta}$ enabling us to obtain OER descriptors derived from the relative contribution of the TM 3*d* states and O 2*p* states in the valence band. $La_{0.67}Sr_{0.33}MnO_{3-\delta}$ and $LaNiO_{3-\delta}$ valence band electronic structure is discussed in the appendix A. A table of the final growth conditions of each material is shown in table 2.

4.4.1 Crystal structure characterization

The crystal structure of the 20 nm thick epitaxial thin films grown on (001) $SrTiO_3$ is compared in figure 26a. The ferrates, $La_{0.6}Sr_{0.4}FeO_{3-\delta}$ and $La_{0.6}Ca_{0.4}FeO_{3-\delta}$, exhibit the largest *c*-lattice parameter, followed by $La_{0.6}Ca_{0.4}NiO_{3-\delta}$ and the cobaltates, $La_{0.6}Sr_{0.4}CoO_{3-\delta}$ and $La_{0.6}Ca_{0.4}CoO_{3-\delta}$. The cation B-site variation seems to have the strongest impact on the lattice parameter here (view table 7 for the *c*-lattice parameters). From $La_{0.6}Ca_{0.4}FeO_{3-\delta}$ to $La_{0.6}Ca_{0.4}NiO_{3-\delta}$ the lattice parameter decreases by 0.044 Å, and to $La_{0.6}Ca_{0.4}CoO_{3-\delta}$ by 0.127 Å. In contrast, the *c*-lattice parameters decrease upon Ca-substitution on the A-site for the ferrates from $La_{0.6}Sr_{0.4}FeO_{3-\delta}$ to $La_{0.6}Ca_{0.4}FeO_{3-\delta}$ only by 0.012 Å, and for the cobaltates from $La_{0.6}Sr_{0.4}CoO_{3-\delta}$ to $La_{0.6}Ca_{0.4}CoO_{3-\delta}$ by 0.028 Å.

Table 7: *c*- and *a*-lattice parameters of the perovskite oxides on $SrTiO_3$.

perovskite thin film	c [Å]	a [Å]
$La_{0.6}Sr_{0.4}FeO_{3-\delta}$	3.886	3.905
$La_{0.6}Ca_{0.4}FeO_{3-\delta}$	3.874	3.905
$La_{0.6}Ca_{0.4}NiO_{3-\delta}$	3.830	3.905
$La_{0.6}Sr_{0.4}CoO_{3-\delta}$	3.775	3.905
$La_{0.6}Ca_{0.4}CoO_{3-\delta}$	3.747	≈3.905

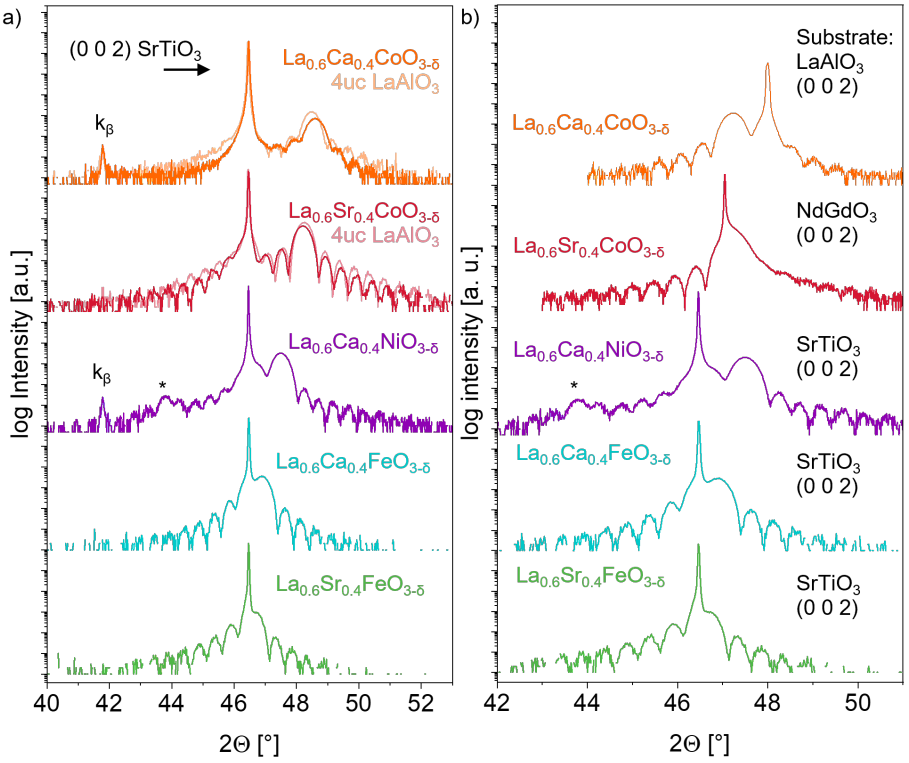

Figure 26: a) (002) reflex of perovskite oxides grown on (001) $SrTiO_3$. b) Grown on least strain for the cobaltates; $La_{0.6}Ca_{0.4}CoO_{3-\delta}$ on a $LaAlO_3$ substrate and $La_{0.6}Sr_{0.4}CoO_{3-\delta}$ on a $NdGaO_3$ substrate.

As RSM data show in figure 27, $La_{0.6}Sr_{0.4}FeO_{3-\delta}$ has a very similar in- and out-of-plane lattice parameter (*a*- and *c*-lattice parameter) as the $SrTiO_3$ substrate, because the $La_{0.6}Sr_{0.4}FeO_{3-\delta}$ peak is hard to distinguish from the substrate peak. $La_{0.6}Ca_{0.4}FeO_{3-\delta}$ grows fully strained on the $SrTiO_3$ substrate with a distinguishable *c*-lattice parameter. $La_{0.6}Ca_{0.4}NiO_{3-\delta}$ grows accordingly in a larger tensile strain on $SrTiO_3$. $La_{0.6}Sr_{0.4}CoO_{3-\delta}$ grows in an even stronger tensile strain on the $SrTiO_3$ substrate. $La_{0.6}Ca_{0.4}CoO_{3-\delta}$ shows the largest tensile strain, and already to a small extent relaxes as the $La_{0.6}Ca_{0.4}CoO_{3-\delta}$ signal is broadly distributed towards smaller *a*-lattice spacings. Since the large tensile strain can lead to a partial strain relaxation in the cobaltate thin films [128] and to a conductivity loss as discussed in the following section 4.4.2, the $La_{0.6}Sr_{0.4}CoO_{3-\delta}$ and $La_{0.6}Ca_{0.4}CoO_{3-\delta}$ thin films were electrochemically tested on the Nb:$SrTiO_3$ substrate with a 4 uc thick $LaAlO_3$ interlayer, as well as on their

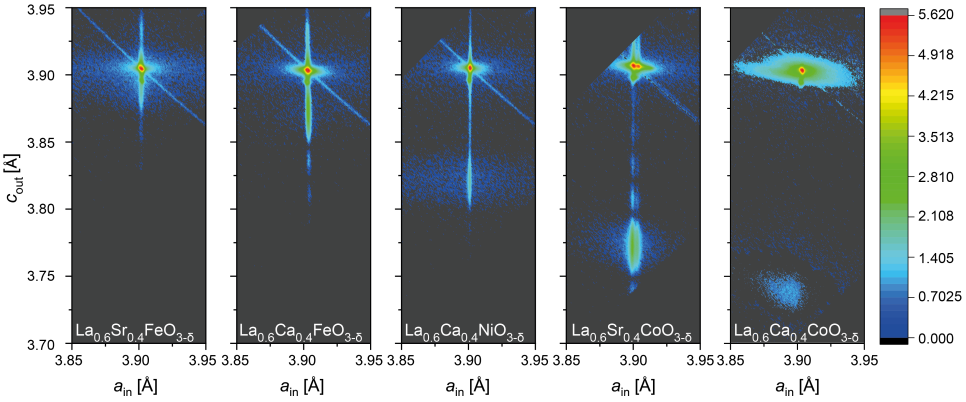

Figure 27: RSM of the perovskites on $SrTiO_3$. The strain increases from the ferrates to the cobaltates.

best lattice matched substrates $NdGaO_3$ and $LaAlO_3$. The corresponding XRD scans can be seen in figure 26a and b.
To compare the lattice parameters of those with the literature values for perovskites powders (and partly also thin films), the previously reported crystal structures and pseudo-cubic lattice parameters are listed in table 8. Due to the strain, the *c*-lattice parameters of the thin films cannot be directly compared to the pseudo-cubic lattice parameters from literature on perovskite powders. Under a tensile strain from the single crystalline substrate, their a- and b-lattice parameters expand while the c-lattice parameters contract, compared to powder perovskites, which are not attached to any substrate. This is related to the Poisson effect. Such elastic deformation may result in a different unit cell volume, especially when the strain is large. Nevertheless, when the strain is not too large, the lattice parameter trend should be the same. The powder perovskite pseudo-cubic lattice parameters confirm that the ferrates exhibit the largest values, followed by the nickelate and cobaltates (table 8).

Song *et al*. observe for $La_{0.6}Sr_{0.4}FeO_{3-\delta}$ a rhombohedral structure yielding in a calculated pseudo-cubic lattice parameter of 3.905 Å which is the same as the cubic lattice constant of our $SrTiO_3$ substrates and similar to our $La_{0.6}Sr_{0.4}FeO_{3-\delta}$ thin film. Wadati *et al*. also produced $La_{0.6}Sr_{0.4}FeO_{3-\delta}$ epitaxial thin films where the *c*-lattice parameter is similar to what we observe for $La_{0.6}Sr_{0.4}FeO_{3-\delta}$. As determined by ref. [165, 166], $La_{0.6}Ca_{0.4}FeO_{3-\delta}$ occurs in an orthorhombic structure with only a slightly smaller pseudo-cubic lattice parameter than $La_{0.6}Sr_{0.4}FeO_{3-\delta}$, which agrees with our experimental observations.
The two cobaltates as powders, $La_{0.6}Sr_{0.4}CoO_{3-\delta}$ and $La_{0.6}Ca_{0.4}CoO_{3-\delta}$, also exhibit smaller pseudo-cubic lattice parameters [53, 155] compared to the ferrates, where the Ca-doped system also has a smaller lattice constant. Ca-doped nickelates, so far, are reported in literature as a tetragonal systems crystallizing in the Ruddlesden-Popper phase as $La_{1-x}Ca_xNiO_{4+\delta}$ [73,

Table 8: Crystal structure of the perovskite oxides in the literature. The last column shows the pseudo-cubic lattice parameter calculated from the orthorhombic or rhombohedral structures. The lattice parameters are given from powder literature values. Additionally, the lattice parameter of $La_{0.6}Sr_{0.4}FeO_{3-\delta}$ is given on an $SrTiO_3$ substrate taken from Wadati *et al*..

perovskite	literature	crystal structure	*a*	*b*	*c*	pseudo cubic
			Å	Å	Å	Å
$La_{0.6}Sr_{0.4}FeO_{3-\delta}$	Song [165]	rhombohedral	5.5226	5.5226	13.4462	3.905
$La_{0.6}Sr_{0.4}FeO_{3-\delta}$	Wadati[67]	pseudo-cubic	3.905	3.905	3.883	
$La_{0.6}Ca_{0.4}FeO_{3-\delta}$	Song[165]	orthorhombic	5.5138	7.7574	5.4896	3.879
$La_{0.6}Ca_{0.4}FeO_{3-\delta}$	Sankan.[166]	orthorhombic	5.4845	7.7558	5.5039	3.885
$LaNiO_{3-\delta}$	Park[161]	rhombohedral	5.4534	5.4534	13.1369	3.853
$La_{0.6}Sr_{0.4}CoO_{3-\delta}$	Chen[53]	rhombohedral	5.4367	5.4367	13.2142	3.844
$La_{0.6}Ca_{0.4}CoO_{3-\delta}$	Weidenk.[155]	cubic	3.817	3.817	3.817	3.817

74]. Undoped $LaNiO_{3-\delta}$, however, crystallizes in the rhombohedral phase with a pseudo-cubic lattice parameter of 3.853 Å [161]. As La^{3+} and Ca^{2+} have similar ionic radii, $La_{0.6}Ca_{0.4}NiO_{3-\delta}$ might be compared to the lattice parameter of $LaNiO_{3-\delta}$. It exhibits a pseudo-cubic lattice parameter smaller than those of the ferrates but larger than those of the cobaltates. This agrees with our observation of the here grown thin films.

As mentioned above, the cell volume of thin film perovskites may change compared that one of the perovskite powders, especially with larger strain. As shown in table 9, the cell volume decreases for the powder and thin film pervoskites in the same manner, $La_{0.6}Sr_{0.4}FeO_{3-\delta} < La_{0.6}Ca_{0.4}FeO_{3-\delta} <$ $LaNiO_{3-\delta}/La_{0.6}Ca_{0.4}NiO_{3-\delta} < La_{0.6}Sr_{0.4}CoO_{3-\delta} < La_{0.6}Ca_{0.4}CoO_{3-\delta}$. The cell volume of the ferrates deviates insignifi-

Table 9: Pseudo-cubic unit cell volume of the here synthesized perovskite thin films (V_{film}) compared to perovskite powders (V_{powder}) calculated from literature lattice parameters. The fourth column shows the thin film-to-powder cell volume deviation $\left(\frac{V_{\text{film}}}{V_{\text{powder}}} - 1\right) * 100$.

perovskite	V_{film} thesis [Å^3]	V_{powder} lit. [Å^3]	lit.	thin film-to-powder cell volume deviation %
$La_{0.6}Sr_{0.4}FeO_{3-\delta}$	59.26	59.21	Wadati	0.08
$La_{0.6}Ca_{0.4}FeO_{3-\delta}$	59.07	58.64	Sankan.	0.74
$La_{0.6}Ca_{0.4}NiO_{3-\delta}/LaNiO_{3-\delta}$	58.40	57.20	Park	2.1
$La_{0.6}Sr_{0.4}CoO_{3-\delta}$	57.57	56.80	Chen	1.35
$La_{0.6}Ca_{0.4}CoO_{3-\delta}$	57.15	55.61	Weidenk.	2.76

cantly from that of the powder catalysts, whereas the nickelate and the cobaltates cell volumes deviate by up to 2.8%. Possibly, the larger strain on $SrTiO_3$ of the cobaltates and nickelate, leads to a lightly increased unit cell volume as compared to the ferrates. This leads to a larger

cell volume deviation of the cobaltate and nickelate thin films compared to the powders. Summarizing, all perovskites can be grown as epitaxial thin films by PLD. $La_{0.6}Ca_{0.4}NiO_{3-\delta}$ is the only material that exhibits the presence of a small contribution of an undesired secondary phase. The ferrates have a larger lattice parameter compared to the nickelates and cobaltates, which also agrees with the literature. Absolute values may vary due to other oxygen stoichiometry, defect structures, and the strain on the substrate. Decreasing the tensile strain for the cobaltates is important to avoid possible strain relaxation.

In figure 28, the AFM scans of the corresponding, growth-optimized thin films with their best lattice-matched substrate are summarized. Those were used for the electrochemical characterization. Corresponding thin films on $Nb:SrTiO_3$ with $LaAlO_3$ interlayer are shown in the appendix B. For all thin films, the RMS is below 700 pm and step terraces from the substrate can be seen. $La_{0.6}Ca_{0.4}CoO_{3-\delta}$ exhibits small particles along the step edges, and $La_{0.6}Ca_{0.4}NiO_{3-\delta}$ exhibits small particles in a very low density. The surface area of the thin films measured by AFM is deviating only by 0.4 % from the geometric surface area. Hence, the epitaxial thin films deliver a highly comparable surface area for the electrochemical characterization which is not the case for powder catalysts where it can deviate by orders of magnitude. As mentioned before, $La_{0.6}Ca_{0.4}NiO_{3-\delta}$ surface morphology changed through air exposure, and therefore, the electrochemical characterization was conducted within 6 days.

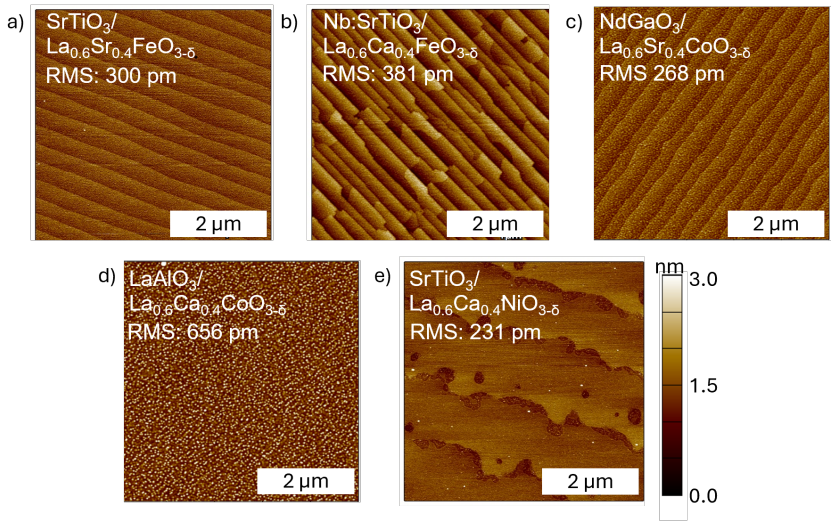

Figure 28: AFM scans of the perovskites oxide grown on the substrates with the best lattice match to the substrate a) $La_{0.6}Sr_{0.4}FeO_{3-\delta}$ b) $La_{0.6}Ca_{0.4}FeO_{3-\delta}$ c) $La_{0.6}Sr_{0.4}CoO_{3-\delta}$ d) $La_{0.6}Ca_{0.4}CoO_{3-\delta}$ e) $La_{0.6}Ca_{0.4}NiO_{3-\delta}$.

4.4.2 Resistivity

The sheet resistance was measured at room temperature in van-der-Pauw geometry and multiplied by the film thickness to obtain the resistivity. Figure 29 illustrates the resistivity trend of the here investigated perovskite oxides for 20 nm thick films. The two cobaltates, $La_{0.6}Sr_{0.4}CoO_{3-\delta}$ and $La_{0.6}Ca_{0.4}CoO_{3-\delta}$, show very low resistivity on the respective best lattice-matched substrates ($La_{0.6}Sr_{0.4}CoO_{3-\delta}$ on $NdGaO_3$ $2.5 \times 10^{-4}\,\Omega\,cm$ and $La_{0.6}Ca_{0.4}CoO_{3-\delta}$ on $LaAlO_3$ $4.1 \times 10^{-4}\,\Omega\,cm$). With a larger tensile strain, their resistivity increases. For $La_{0.6}Sr_{0.4}CoO_{3-\delta}$, the resistivity increases to $4.1 \times 10^{-4}\,\Omega\,cm$ when grown on $SrTiO_3$. For $La_{0.6}Ca_{0.4}CoO_{3-\delta}$, the resistivity increases to $5.4 \times 10^{-4}\,\Omega\,cm$ when grown in $NdGaO_3$. $La_{0.6}Ca_{0.4}CoO_{3-\delta}$ exhibits a very high resistivity of $0.2\,\Omega\,cm$ when grown on $SrTiO_3$. In the figure 29, this is marked with the orange *. This might be related to a partially grainy structure as seen in figure 21. Such a jump in resistivity could also be related to the partial strain relaxation that was seen in the

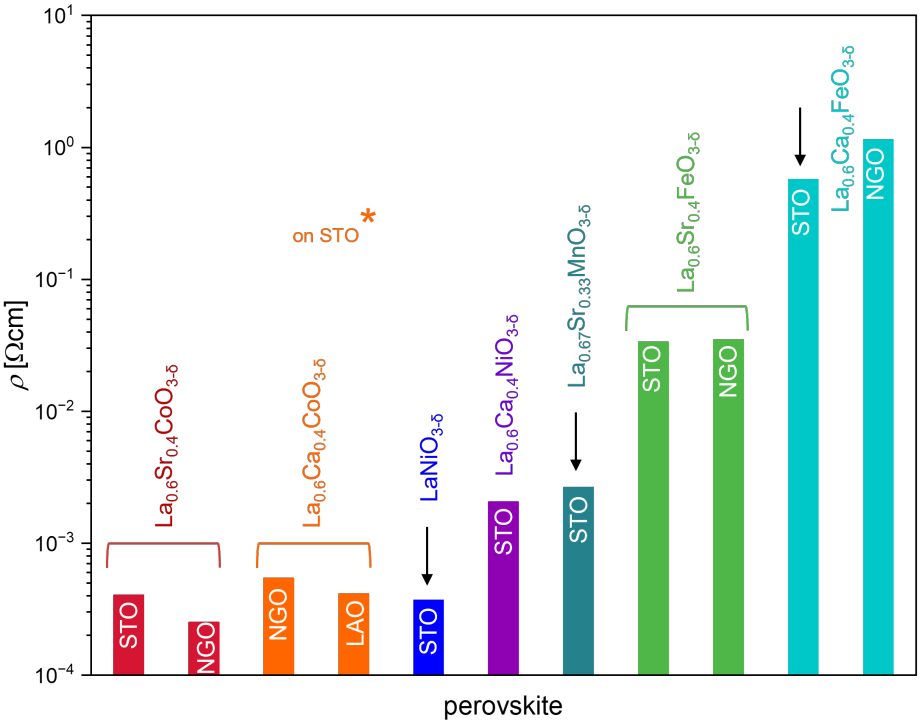

Figure 29: Resistivity trend of the here investigated perovskite oxides: on different insulating substrates, inducing different strain states. $La_{0.6}Ca_{0.4}CoO_{3-\delta}$ showed high resistivity grwon on $SrTiO_3$. As its origin could be related to some other effects it is only marked with a star.

RSM of $La_{0.6}Ca_{0.4}CoO_{3-\delta}$ on $SrTiO_3$ substrate in figure 27. $LaNiO_{3-\delta}$ shows a low resistivity of $3.7 \times 10^{-4}\,\Omega\,cm$ which is comparable to the two cobaltates. The Ca-doping in the nickelate increases the resistivity by one order of magnitude to $2 \times 10^{-3}\,\Omega\,cm$ for $La_{0.6}Ca_{0.4}NiO_{3-\delta}$. $La_{0.67}Sr_{0.33}MnO_{3-\delta}$ shows a comparable resistivity to $La_{0.6}Ca_{0.4}NiO_{3-\delta}$. $La_{0.6}Sr_{0.4}FeO_{3-\delta}$ shows one order of magnitude higher resistivity compared to $La_{0.67}Sr_{0.33}MnO_{3-\delta}$ and $La_{0.6}Ca_{0.4}NiO_{3-\delta}$ on both substrates $SrTiO_3$ and $NdGaO_3$. $La_{0.6}Ca_{0.4}FeO_{3-\delta}$ shows an additional order of magnitude higher resistivity ($0.57\,\Omega\,cm$) compared to the other ferrate $La_{0.6}Sr_{0.4}FeO_{3-\delta}$. For $La_{0.6}Ca_{0.4}FeO_{3-\delta}$, the resistivity is higher on $NdGaO_3$ than on $SrTiO_3$. Here, the tensile strain on $SrTiO_3$ is lower than the compressive strain on $NdGaO_3$.

Principally, this observed resistivity trend of all perovskites is consistent with the literature (table 10), while single values can vary in a certain range. The two cobaltates, $La_{0.6}Sr_{0.4}CoO_{3-\delta}$ and $La_{0.6}Ca_{0.4}CoO_{3-\delta}$ as well as the $LaNiO_{3-\delta}$ show very low resistivity in the order of magnitude $10^{-4}\,\Omega\,cm$, which is comparable to our obtained resistivity values. As a resistivity value for $La_{0.6}Ca_{0.4}NiO_{3-\delta}$ was not available in the literature, $La_{0.5}Sr_{0.5}NiO_{3-\delta}$ is compared instead from Liu *et al*. [69]. It also shows increased resistivity compared to $LaNiO_{3-\delta}$, however, it shows a four-fold increase and not like in our case, an order of magnitude increase from $LaNiO_{3-\delta}$ to $La_{0.6}Ca_{0.4}NiO_{3-\delta}$. $La_{0.67}Sr_{0.33}MnO_{3-\delta}$ resistivity determined by Boschker *et al*. [168] is comparable to our observed resistivity. An $La_{0.6}Sr_{0.4}FeO_{3-\delta}$ thin film, fabricated by Wadati *et al*. [67], shows one order of magnitude higher resistivity than our thin films. $La_{0.6}Ca_{0.4}FeO_{3-\delta}$ in the form of pressed powder also shows one order of magnitude higher resistivity compared to our $La_{0.6}Ca_{0.4}FeO_{3-\delta}$ thin films. Hence, conductivity losses through, grain boundary effects, or crystal facet-dependent resistivity in powders could be successfully suppressed with the epitaxial thin films, allowing one to assess electrochemical performance results from intrinsic catalyst properties.

Table 10: Resistivity literature values of comparable perovskite oxides.

perovskite	resistivity Ωcm	sample type
$La_{0.6}Sr_{0.4}CoO_{3-\delta}$	$2x10^{-4}$	powder [62]
$La_{0.6}Ca_{0.4}CoO_{3-\delta}$	$1x10^{-4}$	powder [167]
$LaNiO_{3-\delta}$	$1x10^{-4}$	thin film [69]
$La_{0.5}Sr_{0.5}NiO_{3-\delta}$	$4x10^{-4}$	thin film [69]
$La_{0.67}Sr_{0.33}MnO_{3-\delta}$	$1x10^{-3}$	thin film [168]
$La_{0.6}Sr_{0.4}FeO_{3-\delta}$	1.1	thin film [67]
$La_{0.6}Ca_{0.4}FeO_{3-\delta}$	29	powder [169]

Overall, the perovskite thin films under investigation span a wide resistivity range, varying over four orders of magnitude. The trend is that the cobaltates and $LaNiO_{3-\delta}$ show quasi metallic behavior, $La_{0.67}Sr_{0.33}MnO_{3-\delta}$ and $La_{0.6}Ca_{0.4}NiO_{3-\delta}$ are still relatively conductive, however, they exhibit one order of magnitude higher resistivity compared to the cobaltates and $LaNiO_{3-\delta}$. The

ferrates exhibit the highest resistivity with an additional one and two orders of magnitude difference for $La_{0.6}Sr_{0.4}FeO_{3-\delta}$ and $La_{0.6}Ca_{0.4}FeO_{3-\delta}$, respectively. The three perovskites marked with an arrow in figure 29 are later used as exemplary perovskites to test the influence of the resistivity on the electrochemical activity.

4.4.3 Electronic structure derived by valence band spectroscopy

The valence band spectra of $La_{0.6}Sr_{0.4}FeO_{3-\delta}$, $La_{0.6}Ca_{0.4}FeO_{3-\delta}$, $La_{0.6}Sr_{0.4}CoO_{3-\delta}$, $La_{0.6}Ca_{0.4}CoO_{3-\delta}$ and $La_{0.6}Ca_{0.4}NiO_{3-\delta}$ were obtained by XPS to determine the energetic distance between the TM 3*d* and O 2*p* states (ΔTM 3*d*-O 2*p*) as one descriptor to attain TM-O covalency, the O 2*p* band center, and charge transfer energy. For this, the valence band main components need to be identified and assigned to the different A- and B-site as well as O bands. These electronic structure parameters will be then correlated to the OER activity of the epitaxial thin films in section 6.2. $LaNiO_{3-\delta}$ was taken from and measured by Kante *et al*. [170]. $La_{0.67}Sr_{0.33}MnO_{3-\delta}$ was measured in a different XPS by Emma van der Minne at the University of Twente (Netherlands). Their valence band spectra are shown in the appendix in figure A.2.

Fitting and assigning the peaks in the valence band to TM 3*d* and O 2*p* states, and determining ΔTM 3*d*-O 2*p*, O 2*p* band center and charge transfer energy: As known from the previous section 2.3, the valence band consists mainly of O 2*p* and TM 3*d* states of such perovskites. The states partially overlap and can form hybrid states of TM and O character [42]. In the case of highly covalent perovskite oxides, the hybridization effects of the TM and O states are stronger, especially for those with a negative charge transfer energy (see also section 2.3) [16, 57]. Furthermore, a small partial density of states (PDOS) of the A-site La 5*p* bands is located in the valence band region [171]. Although the cross section of the La 5*p* bands is moderately bigger than the cross section of the O 2*p* bands when soft X-rays are used, the PDOS of the O 2*p* bands is much larger than the PDOS of the La 5*p* bands [171]. Hence, we assume that the La 5*p* states do not significantly contribute to the valence band spectrum.

Figure 30 shows the exemplary valence band spectrum of $La_{0.6}Sr_{0.4}CoO_{3-\delta}$ where three main components A, B and C can be identified [14, 34]. A Gauss-Lorentz shape with a ratio of 40:60 was used to fit the A-C components. According to our previous study [34], no constraints are set, because peak broadening can arise from mechanisms unrelated to instrumental effects, for instance through hybridization effects. For the shown $La_{0.6}Sr_{0.4}CoO_{3-\delta}$ valence band, the peak A refers to the Co 3*d* peak. This includes the e_g and t_{2g} states, as the crystal field splitting is calculated to be rather small [172] for those perovskites, and two separate e_g and t_{2g} states would be located within the area of peak A. The peak B has a stronger oxygen character (O 2*p* states), and the higher binding energy peak C is a TM-O hybridized state, according to Hong *et al*. [65]. The peaks A-C were assigned to the TM 3*d*, O 2*p*, and TM-O hybrid states accordingly, also for the other perovskites in this thesis. This is because the studies of Hong *et al*. indicate that peak A is also of strong 3*d* transition metal character for the perovskites with varied

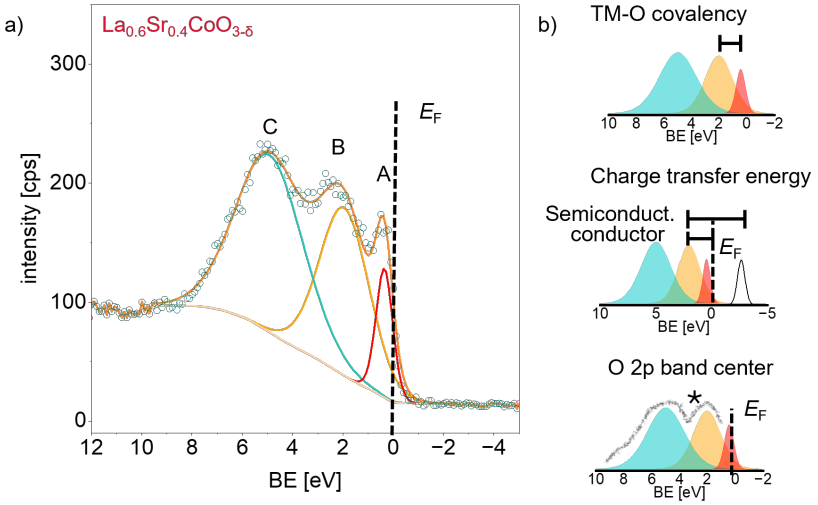

Figure 30: a) XPS valence band spectrum of $La_{0.6}Sr_{0.4}CoO_{3-\delta}$ fitted with three components. b) Illustration of the approaches to determine the electronic structure descriptors. ΔTM 3*d*-O 2*p* is the distance between peak A and B, referring to predominantly TM 3*d* and O 2*p* states. The charge transfer energy is the distance from peak B to the Fermi level for highly conducting perovskites, and for semiconducting material the peak B to the first unoccupied state. The O 2*p* band center is the centroid of peak B and C in distance to the Fermi level.

A- and B-site $La_{1-x}Sr_xMO_{3-\delta}$ (M = Cr, Mn, Fe, Co, and Ni), and peak B of strong O 2*p* character. Peak C refers to hybrid states [14, 65]. Based on this, the three parameters ΔTM 3*d*-O 2*p*, charge transfer energy, and O 2*p* center were addressed as sketched in figure 30b. **ΔTM 3*d*-O 2*p*** was determined as the distance between Peak A (TM 3*d*) and B (O 2*p*) as one descriptor to attain TM-O covalency. The **O 2*p* band center** was determined as the centroid of the peaks B and C. It reflects the center of mass for the O 2*p* and TM-O hybrid states as inspired by [65]. Note, that a final PDOS of the different elements cannot be assigned in the XPS spectra. The photoionisation cross section is lower for the O 2*p* states than for the transition metal states, which leads to the fact that O 2*p* states underproportionally contribute to the spectrum compared to the TM states. The **charge transfer energy** is determined as the distance of peak B (O 2*p*) to the Fermi level for highly conducting perovskites (the cobaltates, nickelates, and manganate), in line with ref. [14]. For the semiconducting $La_{0.6}Sr_{0.4}FeO_{3-\delta}$, the charge transfer energy is determined as the distance of peak B to the Fermi level plus its band gap [14, 68].

Valence band spectra results: Figure 31 shows the valence band spectra by increasing TM atomic number from the bottom to the top of the two ferrates $La_{0.6}Sr_{0.4}FeO_{3-\delta}$ and

$La_{0.6}Ca_{0.4}FeO_{3-\delta}$, the cobaltates $La_{0.6}Sr_{0.4}CoO_{3-\delta}$ and $La_{0.6}Ca_{0.4}CoO_{3-\delta}$, and $La_{0.6}Ca_{0.4}NiO_{3-\delta}$ with the three fitted components A-C. Note that the particles observed on the $La_{0.6}Ca_{0.4}CoO_{3-\delta}$ surface, stemming from a Ca species, can decrease the XPS measurement's overall inten-

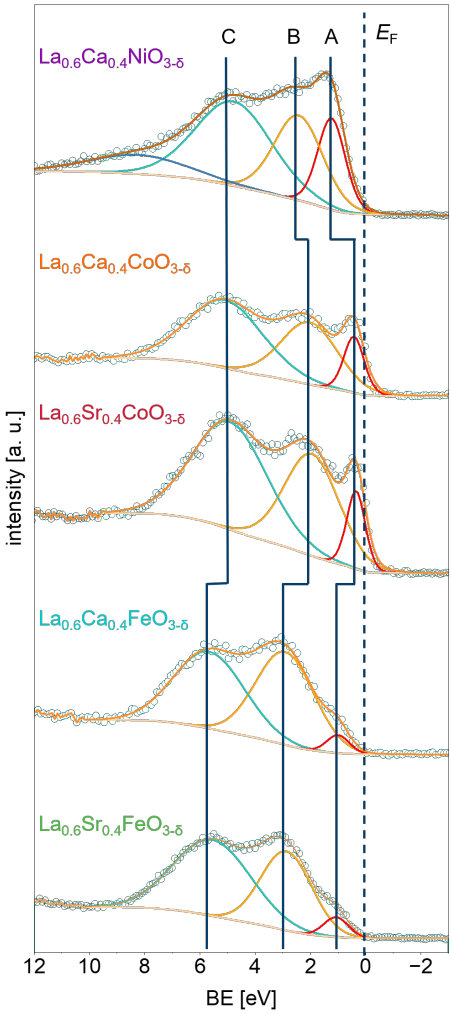

Figure 31: XPS Valence band spectra with increasing atomic number from bottom to top, $La_{0.6}Sr_{0.4}FeO_{3-\delta}$, $La_{0.6}Ca_{0.4}FeO_{3-\delta}$, $La_{0.6}Sr_{0.4}CoO_{3-\delta}$, $La_{0.6}Ca_{0.4}CoO_{3-\delta}$, and $La_{0.6}Ca_{0.4}NiO_{3-\delta}$; recorded in a 15° photoemission angle. Red: transition metal 3*d* peak, yellow: O 2*p* peak, blue: hybrid states.

sity in the valence band region. The valence band spectra of the ferrates $La_{0.6}Sr_{0.4}FeO_{3-\delta}$ and $La_{0.6}Ca_{0.4}FeO_{3-\delta}$ have a comparable shape, which is also the case for the two cobaltates $La_{0.6}Sr_{0.4}CoO_{3-\delta}$ and $La_{0.6}Ca_{0.4}CoO_{3-\delta}$. This suggests that the A-site substitution from Sr to Ca has only a small influence on the spectral shape of the ferrates and cobaltates. In contrast, the B-site substitution from Fe to Co to Ni has a high impact. From the ferrates to the cobaltates, peaks A-C shift closer to the Fermi level, as can be seen by the guide-to-the-eye dark blue lines. For $La_{0.6}Ca_{0.4}NiO_{3-\delta}$, the O 2*p* state peak B and TM 3*d* state peak A, are located a bit further away from the Fermi level compared to the cobaltate peak A and B. Thus, peaks A-C are located the narrowest to each other in the $La_{0.6}Ca_{0.4}NiO_{3-\delta}$ valence band compared to the other shown valence bands. The $La_{0.6}Ca_{0.4}NiO_{3-\delta}$ valence band fit requires a fourth species to be inserted at a binding energy above 8 eV. The origin of this peak is not clarified, but it may be related to the additional phase that was observed in the XRD. Elsewhere, a peak around 8 eV of NiO is reported to stem from the Ni 4*s* [173]. Moreover, with increasing TM atomic number (Fe to Co, to Ni), the TM 3*d* state intensity increases, which might be attributed to the larger number of electrons in the *d*-orbitals.

The descriptors ΔTM 3*d*-O 2*p*, O 2*p* band center, and charge transfer energy including $LaNiO_{3-\delta}$ and $La_{0.67}Sr_{0.33}MnO_{3-\delta}$ from the appendix figure A.2 are illustrated in figure 32 and are listed in table 11.

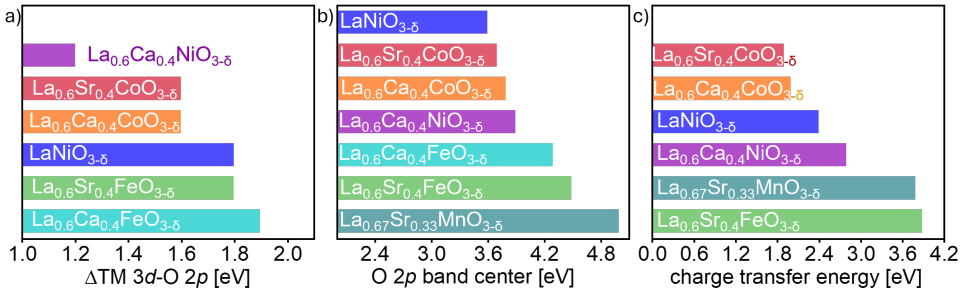

Figure 32: ΔTM 3*d*-O 2*p*, O 2*p* band center and charge transfer energy of the perovskite oxides sorted by decreasing energy values from bottom to top.

Figure 32a shows the energetic distance ΔTM 3*d*-O 2*p* sorted by decreasing value from the bottom to the top. The two ferrates and $LaNiO_{3-\delta}$ exhibit the highest values, followed by the two cobaltates. $La_{0.6}Ca_{0.4}NiO_{3-\delta}$ shows the lowest ΔTM 3*d*-O 2*p*. This suggests that the covalency in the Ca/Sr substituted perovskites might be the highest in the Ni-O bond, followed by the Co-O and Fe-O bond. $La_{0.67}Sr_{0.33}MnO_{3-\delta}$ was not considered here, as the larger e_g-t_{2g} splitting challenges the determination of ΔTM 3*d*-O 2*p* (see appendix in figure A.2).
The O 2*p* band center is shown in figure 32b. $La_{0.67}Sr_{0.33}MnO_{3-\delta}$ shows the highest value (5 eV), followed by the two ferrates with a 0.5-0.7 eV lower O 2*p* band center. The nickelates

Table 11: A-C peak position relative to the Fermi level of the valence band spectra; fourth column: relative distance between peak A and B, denoted as $\triangle$TM 3*d*-O 2*p*; fifth column: O 2*p* band center is represented as O 2*p* centroid from peak B and C. sixth column: Charge transfer (CT) energy represented by the BE distance from peak B to the Fermi level in the case of all conductors. $La_{0.6}Sr_{0.4}FeO_{3-\delta}$ as a semiconductor shows a band gap of 1 eV [68] which was added to the BE distance from peak B to the Fermi level.

perovskite	red peak A (TM 3*d*) eV	yellow peak B (O 2*p*) eV	blue peak C (hybrid) eV	TM-O distance (A-B) eV	O 2*p* center eV	CT energy eV
$La_{0.6}Ca_{0.4}NiO_{3-\delta}$	1.2	2.4	4.8	1.2	3.9	2.4
$LaNiO_{3-\delta}$	1.0	2.8	5.1	1.8	3.6	2.8
$La_{0.6}Ca_{0.4}CoO_{3-\delta}$	0.4	2	5.1	1.6	3.8	2
$La_{0.6}Sr_{0.4}CoO_{3-\delta}$	0.4	1.9	4.9	1.6	3.7	1.9
$La_{0.6}Ca_{0.4}FeO_{3-\delta}$	1	2.9	5.7	1.9	4.3	
$La_{0.6}Sr_{0.4}FeO_{3-\delta}$	1.1	2.9	5.6	1.8	4.5	3.9
$La_{0.67}Sr_{0.33}MnO_{3-\delta}$	0.4	3.8	5.8	3.3	5.0	3.8
$La_{0.67}Sr_{0.33}MnO_{3-\delta}$	2.1 (t_{2g})					

and cobaltates exhibit at least 0.4 eV lower O 2*p* band center values compared to the ferrates. In figure 32c the charge transfer energy is plotted with decreasing value, from the bottom to the top. The charge transfer energy is the highest for $La_{0.67}Sr_{0.33}MnO_{3-\delta}$ and $La_{0.6}Sr_{0.4}FeO_{3-\delta}$, followed by a ca. 1 eV smaller charge transfer energy of the nickelates. The cobaltates exhibit the smallest charge transfer energy, close to the nickelates. As $La_{0.6}Sr_{0.4}FeO_{3-\delta}$ is a semiconductor (explained in section 2.3), the band gap of 1 eV [68] adds to the energetic difference of the O 2*p* state to the Fermi level, leading to a similar charge transfer energy as $La_{0.67}Sr_{0.33}MnO_{3-\delta}$, while the charge transfer energy of the conducting $La_{0.67}Sr_{0.33}MnO_{3-\delta}$ results from the larger distance of the peak B (O 2*p* state) from the Fermi level. For the highly resistive $La_{0.6}Ca_{0.4}FeO_{3-\delta}$, no band gap value was found in the literature, and is therefore not considered here.

Summarizing, the major differences of the valence band electronic structure occur for the TM-site exchange, where the ferrates, cobaltates, nickelates and manganate show a significantly different spectral shape. The A-site substitution from Sr to Ca does not strongly influence the valence band's spectral shape and peak distances. The ferrates show the largest energetic distance $\triangle$TM 3*d*-O 2*p*, followed by the cobaltates. The Ca-doped nickelate has the lowest $\triangle$TM 3*d*-O 2*p*. The O 2*p* band center is the smallest for $LaNiO_{3-\delta}$ and the cobaltates, followed by $La_{0.6}Ca_{0.4}NiO_{3-\delta}$, the ferrates, and the manganate. The charge transfer energy significantly increases for the semiconductor $La_{0.6}Sr_{0.4}FeO_{3-\delta}$, compared to the other conductive perovskites.

4.5 Morphology, crystal and electronic structure characterization of perovskites grown on platinized silicon

$La_{0.6}Sr_{0.4}FeO_{3-\delta}$, $La_{0.6}Ca_{0.4}FeO_{3-\delta}$, $La_{0.6}Sr_{0.4}CoO_{3-\delta}$, and $La_{0.6}Ca_{0.4}CoO_{3-\delta}$ thin films were also grown on platinized silicon substrates to have a metallic contact for the catalyst layers in the electrochemical characterization. This facilitates the generation of higher current densities in the OER, which is relevant to larger-scale applications. The power-to-mass ratio at high current densities will be then used for the sustainability evaluation in section 7. The advantage is, that on the platinized silicon stack the contact to the perovskite catalyst layer is free of interfacial resistances, which is not the case for the conducting $Nb:SrTiO_3$ as will be discussed in the sections 5.4 and 5.9. Moreover, the advantage of using the noble metal for the PLD growth process is, that it does not oxidize at 650 °C in a high-pressure PLD oxygen atmosphere (0.05 mbar). Such thin films reflect less defined structural model systems, but allow closer-to-application analysis.

A sketch of the platinized silicon stack is shown in figure 33a. The silicon substrate is treated first with a high-temperature process, to achieve an amorphous SiO_2 layer. Then 5 nm of Ti are sputtered on the Si substrate to achieve an adhesive layer for the subsequent Pt sputter deposition of about 50 nm. Figure 33b shows an AFM scan of the Pt surface exhibiting only small particles on the surface with a RMS of 658 pm. The perovskite thin films were grown on the

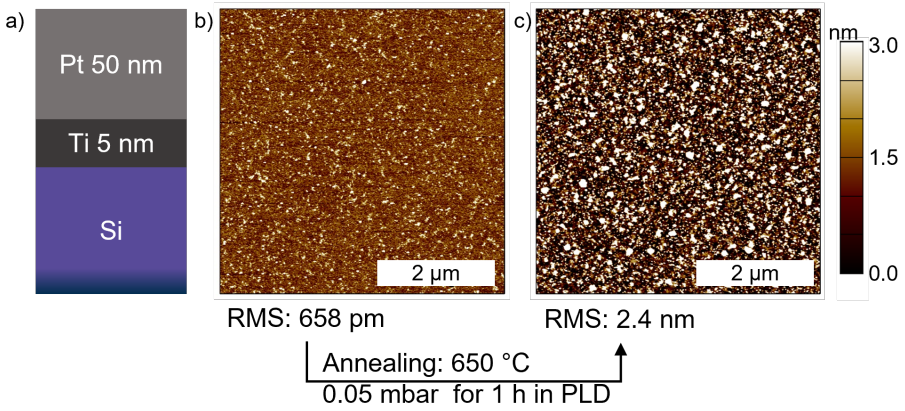

Figure 33: a) Platinized silicon stack: Si substrate, 5 nm Ti adhesive layer and 50 nm Pt. b) Surface morphology of Pt layer. c) Surface morphology of Pt after annealing for 1 h.

Pt layer under the same growth conditions as on the single crystalline metal oxide substrates (except the $La_{0.6}Ca_{0.4}CoO_{3-\delta}$ growth, here the temperature was also kept at 650 °C and thus below the optimized temperature for the epitaxial growth of 700 °C to avoid a further surface roughening of the Pt layer).

To check if the Pt surface roughens under these conditions, the stack was annealed for 1 h at 650 °C and 0.05 mbar O_2 pressure. As seen in figure 33c, this leads to a strong roughening of the surface resulting in an RMS of 2.4 nm. Some particles can be around 35 nm high. Hence, the buried Pt layer will also influence the final morphology of the grown perovskite thin film. Therefore, the deposition was conducted for all thin films at 650 °C. Since no RHEED pattern was observed for the polycrystalline Pt layer, the deposition time was determined based on growth on single-crystalline substrates.

Surface morphology: Figure 34 shows the AFM scans of $La_{0.6}Sr_{0.4}FeO_{3-\delta}$, $La_{0.6}Ca_{0.4}FeO_{3-\delta}$, $La_{0.6}Sr_{0.4}CoO_{3-\delta}$, and $La_{0.6}Ca_{0.4}CoO_{3-\delta}$, where all thin films show a higher roughness and larger particle formation than the thin films on the single crystalline substrates. The ferrates and $La_{0.6}Sr_{0.4}CoO_{3-\delta}$ exhibit an RMS of 3-5 nm. $La_{0.6}Ca_{0.4}CoO_{3-\delta}$ forms larger particles, leading to an RMS of 11.2 nm, where a height of 70 nm can be observed for some particles. We can estimate the total surface area of the thin films by the integration

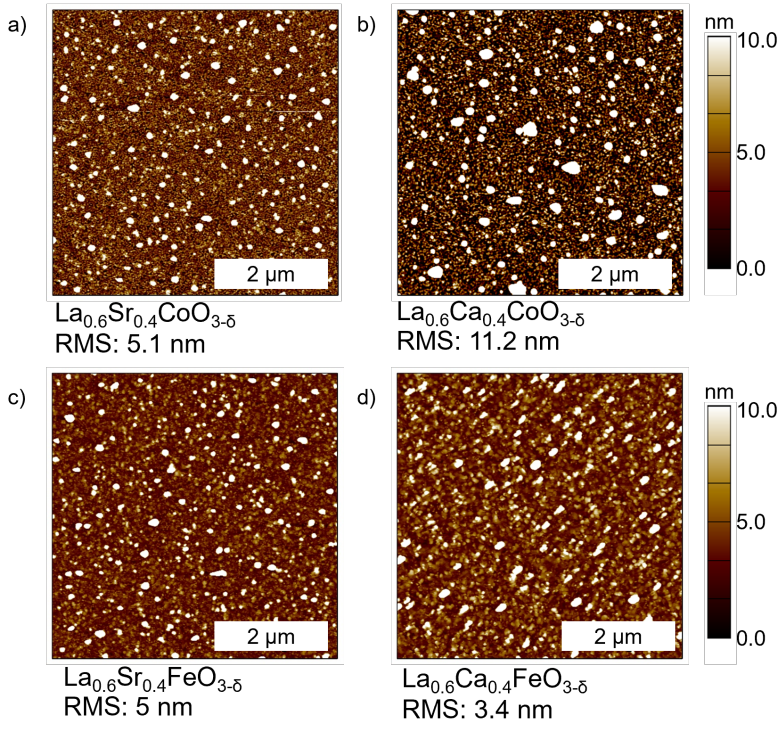

Figure 34: AFM of a) $La_{0.6}Sr_{0.4}CoO_{3-\delta}$ b) $La_{0.6}Ca_{0.4}CoO_{3-\delta}$ c) $La_{0.6}Sr_{0.4}FeO_{3-\delta}$ d) $La_{0.6}Ca_{0.4}FeO_{3-\delta}$ grown on Si/Ti 5 nm/Pt 50 nm.

over the height profile. As a result, the overall surface area only increases by a maximum of 6 % in the case of $La_{0.6}Ca_{0.4}CoO_{3-\delta}$ compared to the geometric surface area. Hence, the catalyst surface area deviates by a maximum of 6 % compared to the geometric surface area, justifying a fair comparison of the catalyst layers by their geometric surface area in the electrochemical activity tests. This is a major advantage compared to powder or micro-structured catalysts, where the effective surface area deviates from the geometric surface area by orders of magnitude.

Layer thickness estimation: To determine if the desired 20 nm thick perovskite layer was deposited on the Pt stack by using the same deposition time as for the single crystal substrates, XRR was recorded. In figure 35a the experimental and fitted XRR scans are shown for the Si/Ti 5 nm/Pt 50 nm reference stack. The fit overlaps well with the recorded scan, resulting in a

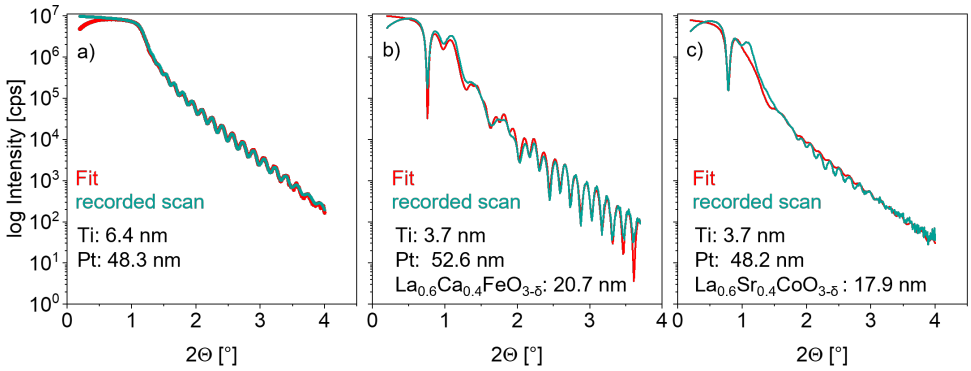

Figure 35: Recorded XRR scan and fit of a) Si/Ti/Pt, b) Si/Ti/Pt/$La_{0.6}Ca_{0.4}FeO_{3-\delta}$, and c) Si/Ti/Pt/$La_{0.6}Sr_{0.4}CoO_{3-\delta}$ stacks. The calculated layer thicknesses are given for each scan.

thickness of 6.4 nm for the Ti layer and 48.3 nm for the Pt layer. In figure 35b the experimental and fitted XRR scan of a Si/Ti 5 nm/Pt 50 nm/$La_{0.6}Ca_{0.4}FeO_{3-\delta}$ sample are shown. Also here, recorded and fitted reflectivity overlap well, resulting in a calculated thickness of 3.7 nm for the Ti layer, 52.6 nm for the Pt layer and 20.7 nm for the $La_{0.6}Ca_{0.4}FeO_{3-\delta}$ perovskite layer. This confirms that the used deposition time led to the desired perovskite layer thickness. To include the material density in the GenX 3 software and refractive index, CIF data from the ICSD database are used for the initial fitting ($La_{0.6}Ca_{0.4}FeO_{3-\delta}$: ICSD_CollCode16096).

The fitted XRR scan of the Si/Ti 5 nm/Pt 50 nm/$La_{0.6}Sr_{0.4}CoO_{3-\delta}$ sample (figure 35c) overlaps less well with the recorded XRR scan ($La_{0.6}Sr_{0.4}CoO_{3-\delta}$: ICSD_CollCode159136)). However, the periodicity is similar, only the local minima are less pronounced in the fit. The XRR fit might have a too high roughness parameter, as this causes damping of the oscillations. Here, the Ti layer results in 3.7 nm thickness, the Pt layer is 48.2 nm thick, and the $La_{0.6}Sr_{0.4}CoO_{3-\delta}$ layer

is 17.9 nm thick. The small discrepancy might stem indeed from a too short deposition time, or from the small deviations of the fit compared to the recorded XRR scan. As the AFM scan showed that $La_{0.6}Sr_{0.4}CoO_{3-\delta}$ had a higher surface roughness than $La_{0.6}Ca_{0.4}FeO_{3-\delta}$, the XRR scan might not be as accurate as for the $La_{0.6}Ca_{0.4}FeO_{3-\delta}$ film.

Surface coverage of perovskite oxides on Pt and electronic structure: To assess the surface coverage of the perovskite layers on Pt, XPS was conducted. Figure 36 shows the Pt 4*d* core level spectrum of a platinized silicon substrate as a reference. The XPS spectra recorded for the Si/Ti/Pt/$La_{0.6}Sr_{0.4}CoO_{3-\delta}$ and Si/Ti/Pt/$La_{0.6}Ca_{0.4}FeO_{3-\delta}$ stacks (below) show no signal of the Pt 4*d* peak. This indicates that the perovskites sufficiently cover the Pt layer. This ensures that only the perovskite catalyst layer will contribute to the electrochemical

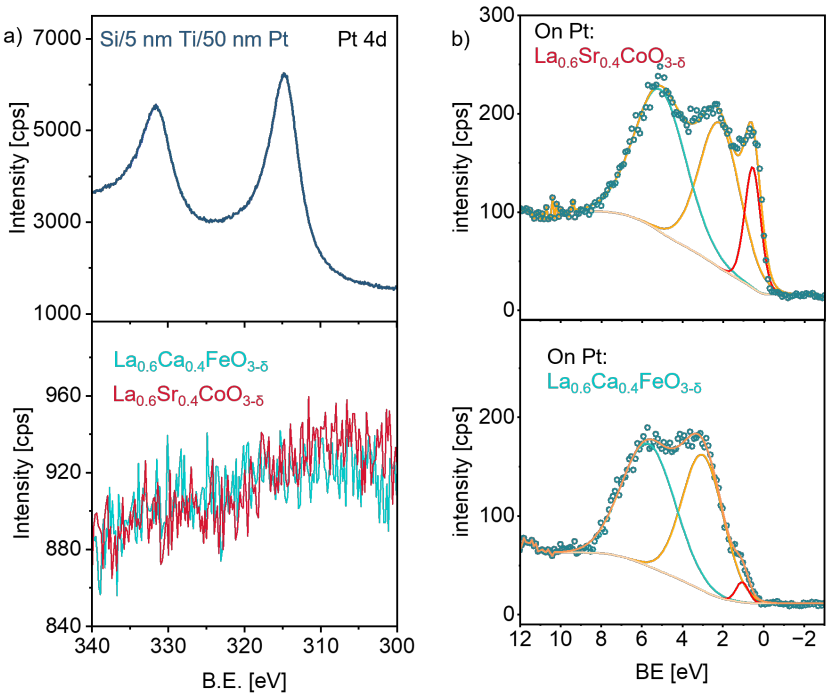

Figure 36: a) XPS of the Pt 4*d* core level recorded for the Si/Ti/Pt stack shown in the top panel, and of the Si/Ti/Pt/$La_{0.6}Ca_{0.4}FeO_{3-\delta}$ and Si/Ti/Pt/$La_{0.6}Sr_{0.4}CoO_{3-\delta}$ stacks in the bottom panel. b) XPS valence band spectra of the two peovskites grown on Pt.

performance in the OER, despite the roughened surface of the buried Pt layer. The Pt 4*f* peak was not recorded for this purpose as it can overlap with the Fe or Co transition metal 3*p* core level. Moreover, the valence band spectra of $La_{0.6}Sr_{0.4}CoO_{3-\delta}$ and $La_{0.6}Ca_{0.4}FeO_{3-\delta}$ on the Pt layer were recorded and are shown in 36b. The spectral shape of the valence band is very similar to that of the $La_{0.6}Sr_{0.4}CoO_{3-\delta}$ and $La_{0.6}Ca_{0.4}FeO_{3-\delta}$ thin films on the single crystal substrates, hence similar electronic structure properties were achieved.

Crystallographic characterization of Pt/perovskite stacks: For the crystallographic characterization of the Si/Ti/Pt/perovskite stacks, $La_{0.6}Sr_{0.4}CoO_{3-\delta}$ as benchmark catalyst and $La_{0.6}Ca_{0.4}FeO_{3-\delta}$ as A-and B-site exchanged catalyst were analyzed with GIXRD as exemplary scans. These two perovskites are also the focus of the sustainability evaluation (as detailed in chapter 7). GIXRD (figure 37) was conducted to achieve higher intensity signals from the perovskite thin film and less from the underlying Pt layer. In the bottom panel, the GIXRD is shown for a bare platinized Si substrate. The (111), (200), (220) and (11-3) reflexes can be observed, matching with the cubic platinum structure from the ICSD database (collCode 243678). For the $Pt/La_{0.6}Sr_{0.4}CoO_{3-\delta}$ stack (red graph), mainly the (220) Pt peak is prominent. At slightly higher 2θ angles of the Pt (220) peak, there is a shoulder which might stem from the $La_{0.6}Sr_{0.4}CoO_{3-\delta}$ (220) peak. As the lattice parameter of cubic Pt ($a = 3.923$ Å) is similar to the ones from the perovskites, their reflexes might overlap.

Figure 37b shows a zoom to the lower intensity region of the GIXRD in a). Here, an additional peak at 58.9° can be observed, which is attributed to the (11-2) peak of pseudo-cubic $La_{0.6}Sr_{0.4}CoO_{3-\delta}$ with a lattice parameter of 3.840 Å (ICSD collcode 86943). The (11-2) peak of $La_{0.6}Ca_{0.4}FeO_{3-\delta}$ is located at 57.91°, which gives in the pseudo-cubic notation a lattice parameter of 3.903 Å and is similar to the literature (table 8). Note, that only a tetragonal system of $La_{0.6}Ca_{0.4}FeO_{3-\delta}$ was available from the ICSD database (collCode 16096). The $La_{0.6}Ca_{0.4}FeO_{3-\delta}$ lattice parameter is larger than the $La_{0.6}Sr_{0.4}CoO_{3-\delta}$ lattice parameter which agrees with the parameters of the two perovskites grown on the single crystalline substrates.

Typically, the (110) signal has the highest intensity in powder perovskite XRD (located around 2θ = 33° [174]), which is less pronounced here. One reason for the differently weighted reflexes could be that the Pt deposits in a partially preferred orientation [175] on the Ti layer. Hence, the perovskite might also grow partly textured on the Pt layer. When the thin film is partly oriented to the sample surface, the grazing incident beam in GIXRD can be almost parallel to the crystal facets so that the parallel oriented facets cannot create a diffraction signal [132].

Therefore, to determine if the Pt and perovskite layers grow in a textured manner, symmetric 2θ-ω scans were recorded and are shown in figure 38. The XRD of the Pt-thin film Si/Ti/Pt reference (bottom XRD scan) shows only reflexes of the (111) orientation, suggesting that the Pt layer partially deposits in a textured manner on the Ti layer. The calculated lattice parameter is listed in table 12. Another reference spectrum of a Si/Ti/Pt stack shown in the overlaying spectrum in dark green exhibits a peak at 31.91°. For one, this peak was not always present in the Si/Ti/Pt stacks, and when the 2θ-ω scan was recorded in a different region of the sample, it

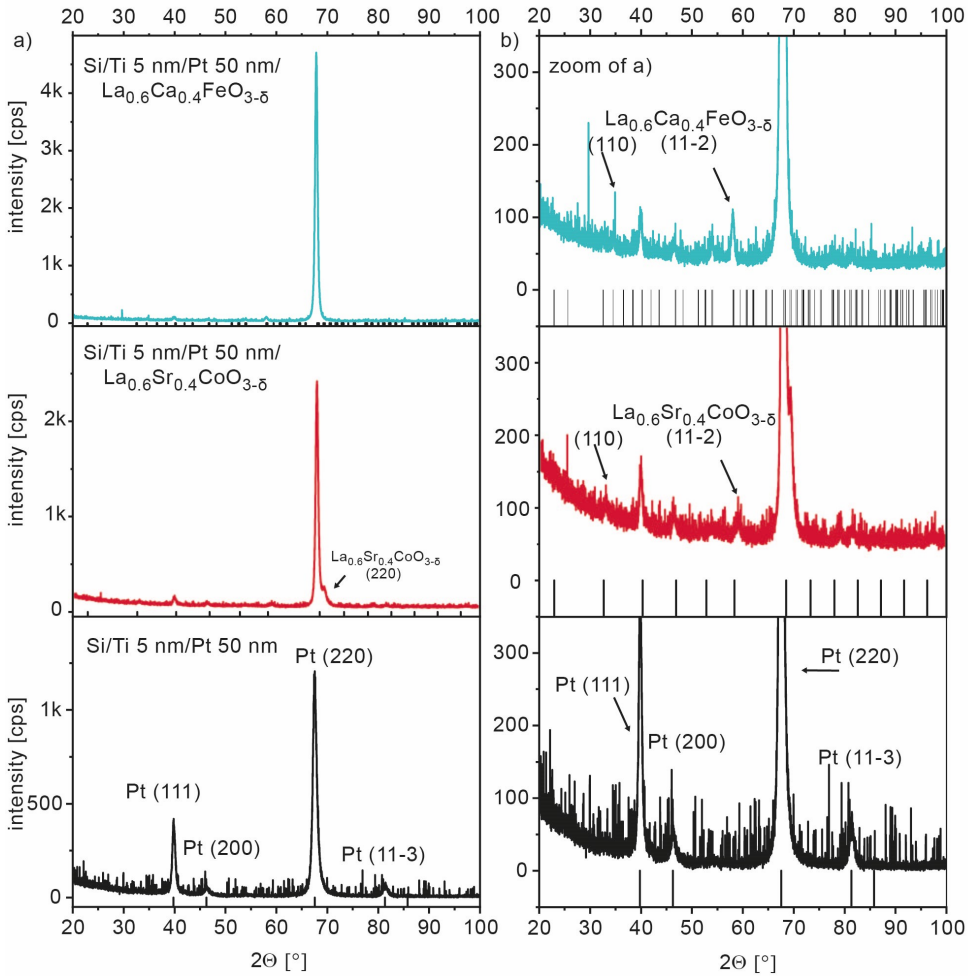

Figure 37: a) GIXRD of $La_{0.6}Sr_{0.4}CoO_{3-\delta}$, $La_{0.6}Ca_{0.4}FeO_{3-\delta}$ grown on Pt thin films, the bottom scan stems from a Pt thin film sample as a reference. b) Zoom of a) to the lower intensity regime.

was also not always present. For now, it remains unclear where the reflex is coming from. The spectra of the two ferrates $La_{0.6}Sr_{0.4}FeO_{3-\delta}$ and $La_{0.6}Ca_{0.4}FeO_{3-\delta}$ show reflexes in the region of their cubic (110) peak which was relatively unpronounced in the GIXRD scans. The calculated lattice parameters from those reflexes are similar to the lattice parameters of the thin films on $SrTiO_3$ (table 12). However, it cannot be fully excluded that the reflex stems from

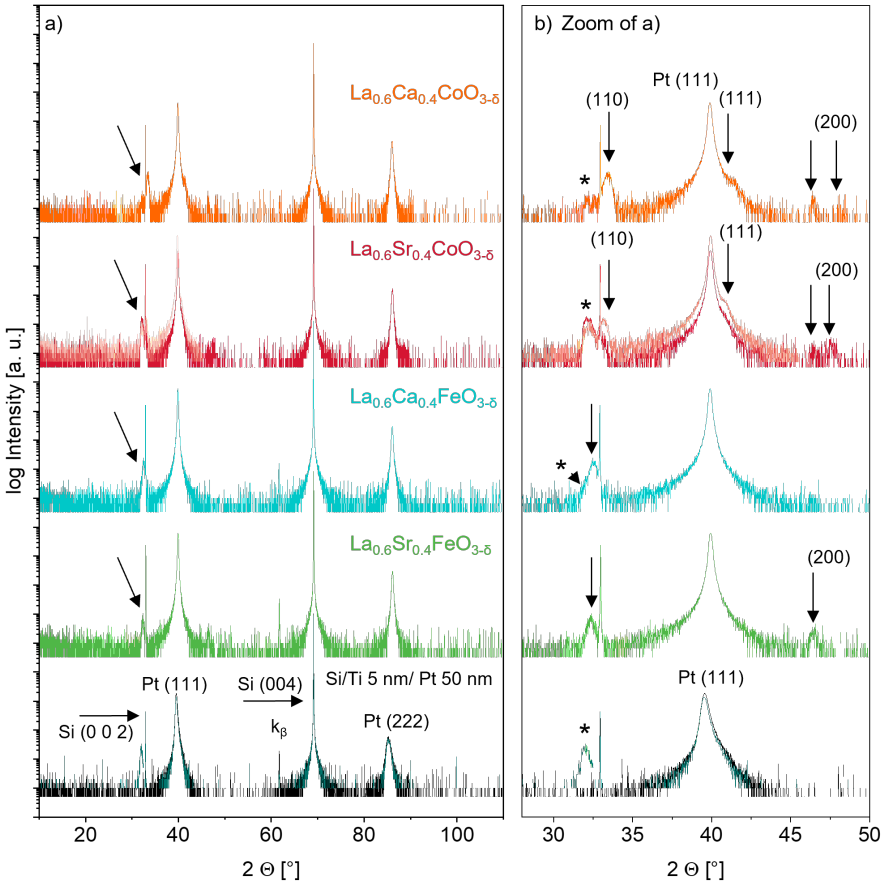

Figure 38: 2θ-ω scan of Pt stack reference, $La_{0.6}Ca_{0.4}CoO_{3-\delta}$, $La_{0.6}Sr_{0.4}CoO_{3-\delta}$, $La_{0.6}Ca_{0.4}FeO_{3-\delta}$, $La_{0.6}Sr_{0.4}FeO_{3-\delta}$ grown on Pt stack. a) full scan. b) In the region from 25°-50°. As the scans varied from sample to sample, scans of two different samples are plotted when needed for further explanation. The peaks marked with * remain unidentified.

a Pt-related species, or as indicated for the $La_{0.6}Ca_{0.4}FeO_{3-\delta}$ XRD, partly overlaps with the peak also seen in the Si/Ti/Pt-reference stack.

For $La_{0.6}Sr_{0.4}CoO_{3-\delta}$, the reflexes seen in the range of 31° to 35° can vary from sample to sample. The reflex marked with a star ($2\theta = 32$°) can be attributed to the peak also seen in the XRD of the Pt-reference stack. A second peak is observed at higher 2θ-ω angles (33°), which is

similar to the expected $La_{0.6}Sr_{0.4}CoO_{3-\delta}$ (110) cubic lattice parameter. Moreover, a light shoulder of the (111) Pt reflex is seen (marked with the arrow), which can be attributed to the (111) orientation of $La_{0.6}Sr_{0.4}CoO_{3-\delta}$. Very weak signals of the (200) Pt and $La_{0.6}Sr_{0.4}CoO_{3-\delta}$ can be seen at around 46-47°. Those reflexes can also be observed for the Si/Ti/Pt/$La_{0.6}Ca_{0.4}CoO_{3-\delta}$ stack with a similar intensity distribution. In the XRD scan of the Si/Ti/Pt/$La_{0.6}Ca_{0.4}CoO_{3-\delta}$ stack, the reflex at 33.39° can be attributed to the (110) orientation with a lattice parameter of 3.797 Å. A low-intensity signal of the (111) and (200) orientation can also be attributed to the $La_{0.6}Ca_{0.4}CoO_{3-\delta}$ layer.
In conclusion, the unexpectedly low intensity of the (110) reflection in the GIXRD patterns of $La_{0.6}Sr_{0.4}CoO_{3-\delta}$ and $La_{0.6}Ca_{0.4}FeO_{3-\delta}$ contrasts with its pronounced appearance in their symmetric XRD scans. Hence, the perovskite thin films grow in a partly textured manner on the Pt layer, which is surprising for the growth of perovskite layers on a less-defined sputtered Pt layer compared to a single crystalline substrate.

Table 12: Diffraction angles of the peaks in figure 38 and calculated cubic lattice parameters. The unidentified peak has a similar value in all scans.

Sample	Angle °	hkl	Lattice parameter Å
$La_{0.6}Ca_{0.4}CoO_{3-\delta}$	32.13		unidentified
$La_{0.6}Ca_{0.4}CoO_{3-\delta}$	33.39	110	**3.797**
Pt ($La_{0.6}Ca_{0.4}CoO_{3-\delta}$)	39.87	111	3.919
Pt ($La_{0.6}Ca_{0.4}CoO_{3-\delta}$)	46.36	200	3.919
$La_{0.6}Ca_{0.4}CoO_{3-\delta}$	47.95	200	**3.797**
$La_{0.6}Sr_{0.4}CoO_{3-\delta}$ 1	32.09		unidentified
$La_{0.6}Sr_{0.4}CoO_{3-\delta}$ 1	33.11	110	**3.829**
Pt ($La_{0.6}Sr_{0.4}CoO_{3-\delta}$ 1)	39.94	111	3.912
$La_{0.6}Sr_{0.4}CoO_{3-\delta}$ 2	32.06		unidentified
Pt ($La_{0.6}Sr_{0.4}CoO_{3-\delta}$ 2)	39.92	111	3.914
Pt ($La_{0.6}Sr_{0.4}CoO_{3-\delta}$ 2)	46.39	200	3.917
$La_{0.6}Sr_{0.4}CoO_{3-\delta}$ 2	47.6	200	**3.823**
$La_{0.6}Ca_{0.4}FeO_{3-\delta}$	32.43	110	**3.907**
Pt ($La_{0.6}Ca_{0.4}FeO_{3-\delta}$)	39.9	111	3.916
$La_{0.6}Sr_{0.4}FeO_{3-\delta}$	32.34	110	**3.917**
Pt ($La_{0.6}Sr_{0.4}FeO_{3-\delta}$)	39.92	111	3.914
$La_{0.6}Sr_{0.4}FeO_{3-\delta}$	46.41	200	**3.915**
Pt	31.92		unidentified
Pt	39.54	111	3.950

5 Revealing intrinsic catalytic properties of perovskites across conductivity ranges

First, the alkaline OER catalytic activity of the seven perovskites is tested with CV on the insulating substrates. Then, the influence of the large conductivity range of the perovskites on the OER activity is systematically investigated. For this, the CV and impedance were compared in hexacyanoferrate(II)/(III) ($K_4[Fe(CN)_6]$ / $K_3[Fe(CN)_6]$) containing electrolyte. The results of the hexacyanoferrate (II)/(III) experiments are based on the publication by Heymann *et al*. [176]. Based on this, a dedicated sample design is chosen on the conducting Nb:$SrTiO_3$ substrate to reveal the intrinsic OER catalytic activity independent of the perovskite resistivity. The influence of occurring interface resistances to the substrate is carefully decoupled, and minimized by interface engineering between the substrate and perovskite thin films. Then, interface barriers at the perovskite catalyst/electrolyte interface that might hamper the OER activity are determined via a Mott-Schottky analysis.
The intrinsically driven OER overpotential and Tafel slope of the seven perovskite thin films are then summarized to observe a possible trend in the OER activity in dependence of the chemical and stoichiometric composition. After that, these values are compared to the literature OER activity trends to uncover if intrinsic- or conductivity-driven OER overpotentials are distinguished in these literature studies. The polycrystalline ferrates and cobaltates grown on Pt thin films were tested additionally to attain higher current densities in the OER than on single-crystalline substrates. The OER activity results of $La_{0.6}Sr_{0.4}CoO_{3-\delta}$ and $La_{0.6}Ca_{0.4}FeO_{3-\delta}$ thin films on Pt are later used for the sustainability evaluation.

5.1 OER activity of perovskite catalysts on insulating substrates

Initially, the electrochemical performance of the seven perovskites was tested with CV on insulating substrates with the best lattice-matching. The sample details are listed in table 13 and the corresponding CV scans are shown in figure 39a.

Table 13: Sample details with choice of substrate and layer thickness for figure 39.

perovskite	substrate	layer thickness nm
$La_{0.67}Sr_{0.33}MnO_{3-\delta}$	$SrTiO_3$	25
$La_{0.6}Sr_{0.4}FeO_{3-\delta}$	$SrTiO_3$	20
$La_{0.6}Ca_{0.4}FeO_{3-\delta}$	$SrTiO_3$	25
$La_{0.6}Sr_{0.4}CoO_{3-\delta}$	$NdGaO_3$	20
$La_{0.6}Ca_{0.4}CoO_{3-\delta}$	$LaAlO_3$	20
$LaNiO_{3-\delta}$	$SrTiO_3$	10
$La_{0.6}Ca_{0.4}NiO_{3-\delta}$	$SrTiO_3$	20

The electrolyte is a 0.1 M KOH solution, and an RDE rotation speed of 1600 rpm is applied to remove the evolving oxygen gas. The CV sweep rate was 10 mV/s. The second OER CV scan was averaged from the forward and backward sweep (see also section 3.6), and the applied potential was corrected with the uncompensated resistance R_u of the OCP impedance (figure 39). The R_{uu} was determined by a linear extrapolation of the high-frequency region to the x-axis. Note, that the iR_u correction was applied to the CV curve after the electrochemical testing, as recommended [52] for a 100 % *iR* correction. The potential range was chosen to achieve at least 0.1 mA cm^{-2}, whereas the higher current densities of some CV scans are cut off at 1 mA cm^{-2} to facilitate the comparability.
The two cobaltates $La_{0.6}Sr_{0.4}CoO_{3-\delta}$ and $La_{0.6}Ca_{0.4}CoO_{3-\delta}$ show very similar high OER activity in the CV (red and orange curves in figure 39a). $LaNiO_{3-\delta}$ shows a comparably high activity, whereas the Ca-doped nickelate $La_{0.6}Ca_{0.4}NiO_{3-\delta}$ shows a slightly increased OER activity compared to the cobaltates and $LaNiO_{3-\delta}$. The overpotentials recorded at 0.1 mA cm^{-2} are listed in table 14. $La_{0.6}Sr_{0.4}FeO_{3-\delta}$ requires a slightly higher potential to reach 0.1 mA cm^{-2} compared to the nickelates and cobaltates, whereas $La_{0.67}Sr_{0.33}MnO_{3-\delta}$ shows an even higher overpotential at 0.1 mA cm^{-2}. $La_{0.6}Ca_{0.4}FeO_{3-\delta}$ exhibits by far the highest overpotential of all here-tested perovskites at 0.1 mA cm^{-2}.
Both ferrates show a rather linear slope of the current density, whereas all other catalyst layers show the expected exponential inclination of an electrochemical reaction. This different behavior can also be observed in the Tafel-like plot with a logarithmic current density axis in figure 39b. Here, the ferrates drastically change in slope above 0.01 and 0.1 mA cm^{-2}, respectively, whereas the other OER catalysts exhibit a rather linear behavior. Therefore, the $La_{0.6}Sr_{0.4}FeO_{3-\delta}$ CV scan crosses that of $La_{0.67}Sr_{0.33}MnO_{3-\delta}$ eventually, resulting in a higher overpotential for $La_{0.6}Sr_{0.4}FeO_{3-\delta}$ above 0.5 mA cm^{-2}.
This indicates that, especially for the two ferrates, a high ohmic resistance or limiting OER kinetics strongly suppress the OER activity in this current density range. The presence of such resistances can be observed in the impedance at OCP, which is shown for the perovskites in figure 39c. In the high frequency range, the spectra exhibit an *Z*'-axis offset which is attributed to the uncompensated resistance R_u. For the cobaltates, nickelates, and manganate R_u is between 65-93 Ω. For the ferrates $La_{0.6}Sr_{0.4}FeO_{3-\delta}$ and $La_{0.6}Ca_{0.4}FeO_{3-\delta}$, R_u is significantly higher with a value of 217 Ω and 724 Ω, respectively. Furthermore, the ferrates exhibit an offset on the -*Z*"-axis as well.
Note, that typically the imaginary part of the impedance -*Z*" is expected to be around zero at high frequencies because ohmic resistances only give an offset in the real part of the impedance. The ferrates show here an offset in -*Z*" because the perturbation frequency overlaps with the impedance of the reference electrode frit [82, 138], leading to an additional semi-circle as seen in the appendix figure E.1. The semi-circle was removed for clarity in figure 39c. The cobaltates, nickelates, and manganate exhibit the initial part of a large semi-circle, representing the catalyst/electrolyte interface (see also section 3.6.2). For $La_{0.6}Sr_{0.4}FeO_{3-\delta}$ there are two impedance

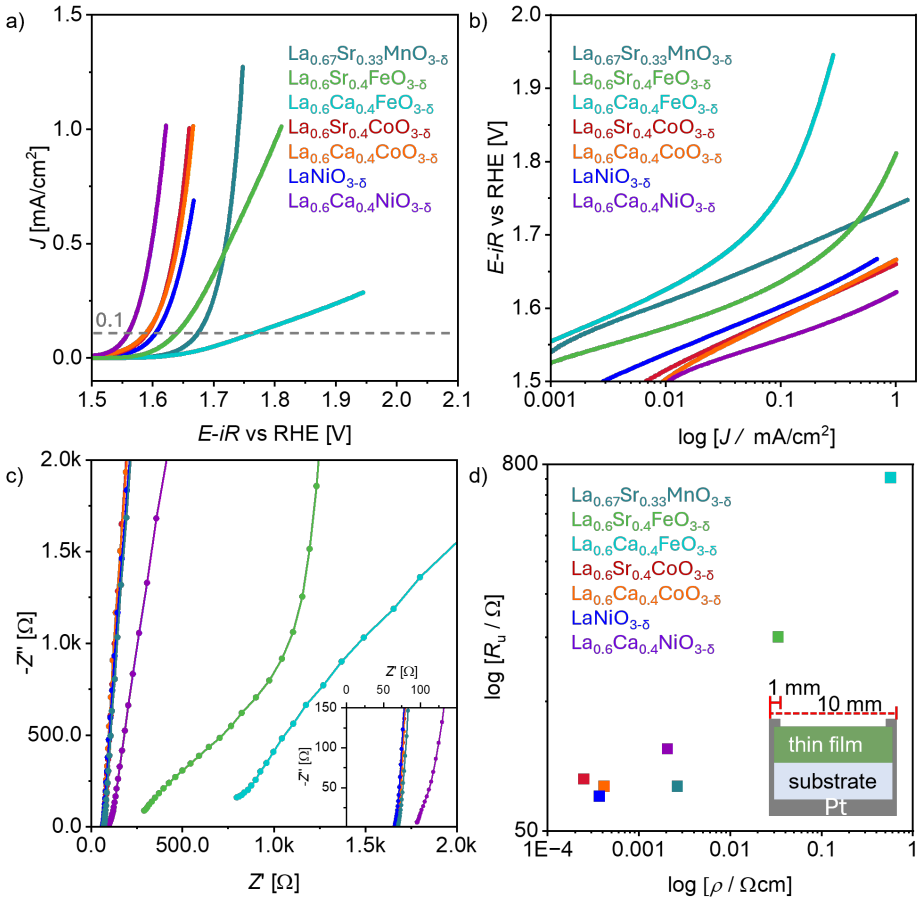

Figure 39: a) OER activity determined by CV of the seven perovskites on insulating substrates. b) Tafel-like plot of the CV scans shown in a). c) Electrochemical impedance in the high frequency range where R_U is determined. d) Scaling of R_U with the resistivity.

features seen, where the latter also represents the catalyst/electrolyte interface.
R_u scales with the resistivity of the perovskites as can be seen in figure 39d (comparing it with figure 29), indicating that a higher resistivity increases the observed R_u in the impedance spectrum. Although the OER CV scan of e.g. $La_{0.6}Ca_{0.4}FeO_{3-\delta}$ was iR_u corrected with the R_u of 724 Ω, this iR_u correction appears to be insufficient to eliminate all ohmic resistances as evident by the linear CV characteristic in figure 39a remaining after the nominal iR_u correction. A possible reason might be that the employed fitting procedure to determine R_u underestimates

Table 14: Overpotential η at 0.1 mA cm^{-2} of the seven perovskites on insulating substrates.

perovskite	η V
$La_{0.6}Sr_{0.4}CoO_{3-\delta}$	0.36
$La_{0.6}Ca_{0.4}CoO_{3-\delta}$	0.36
$LaNiO_{3-\delta}$	0.37
$La_{0.6}Ca_{0.4}NiO_{3-\delta}$	0.33
$La_{0.6}Sr_{0.4}FeO_{3-\delta}$	0.41
$La_{0.6}Ca_{0.4}FeO_{3-\delta}$	0.53
$La_{0.67}Sr_{0.33}MnO_{3-\delta}$	0.44

the true serial resistances in the cell, e.g., due to the large offset from the abscissa. Alternatively, the *Z*'-axis offset as measured in impedance spectroscopy might not include all bulk related resistances, a point to which we will return below.

Kinetic limitations of the OER can be obtained from Tafel slope values. Typical Tafel slope values are obtained between ca. 30 mV dec^{-1} and 120 mV dec^{-1} for the OER [47, 177]. The Tafel slopes which are the first derivative of the Tafel-like plots [178] of figure 39b are displayed in figure 40 over the full current density range (and not cut off at 1 mA cm^{-2}).

For $La_{0.6}Sr_{0.4}CoO_{3-\delta}$, $La_{0.6}Ca_{0.4}CoO_{3-\delta}$, $LaNiO_{3-\delta}$, and $La_{0.67}Sr_{0.33}MnO_{3-\delta}$, the Tafel slope values are in a reasonable range below the reported 120 mV dec^{-1}. In contrast,

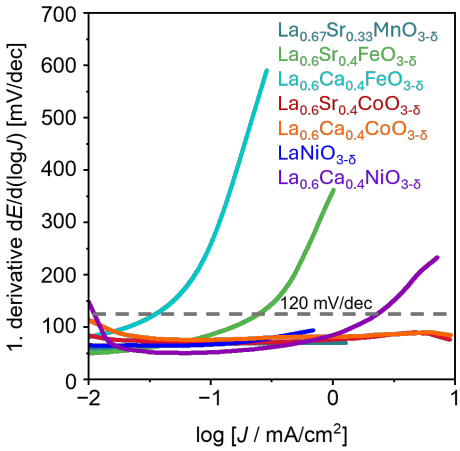

Figure 40: First derivative of the Tafel plots of the averaged CV scans from figure 39b. The first derivative represents the Tafel slope at each point of the increasing current density.

$La_{0.6}Ca_{0.4}FeO_{3-\delta}$ Tafel slopes exceed this value already above 50 µA cm^{-2} reaching extremely high values of about 600 mV dec^{-1}. $La_{0.6}Sr_{0.4}FeO_{3-\delta}$ and $La_{0.6}Ca_{0.4}NiO_{3-\delta}$ graphs start to exceed reasonable Tafel slope values at one and two orders of magnitude higher current density, respectively. This correlates with the one and two orders of magnitude higher resistivity of $La_{0.6}Ca_{0.4}NiO_{3-\delta}$ and $La_{0.6}Sr_{0.4}FeO_{3-\delta}$. $La_{0.67}Sr_{0.33}MnO_{3-\delta}$, which exhibits the same order of magnitude resistivity as $La_{0.6}Ca_{0.4}NiO_{3-\delta}$, was only measured up to 1 mA cm^{-2}. Therefore, it may be expected that the resistivity becomes a limiting factor for $La_{0.67}Sr_{0.33}MnO_{3-\delta}$ in the higher current range as well. In principle, a change in Tafel slope can indicate e.g. a change in rate-determining step or surface coverage [47, 48]. However, these extremely high Tafel slope values of the ferrates and $La_{0.6}Ca_{0.4}NiO_{3-\delta}$ hint at an additional influence of resistances. The lower OER activity may result from either increasingly unfavorable OER kinetics or, as suggested by the correlation between diverging Tafel slope values and resistivity, from a decrease in catalytic activity due to higher resistivity. Hence, it remains unclear if the observed catalytic activity trend is due to intrinsic catalytic performance and/or higher resistances in this sample geometry. As conductivity may be a OER descriptor, it would imply that the ferrates cannot be sufficient catalysts.

5.2 Electrochemical characterization on insluating substrates in hexacyanoferrate(II)/(III) electrolyte

To investigate possible resistance induced limitations in the thin film independent of the sluggish OER kinetics, we employed CV in hexacyanoferrate(II)/(III) containing electrolyte, constituting the outer-sphere reversible redox couple Fe^{2+}/Fe^{3+}. In contrast to inner-sphere electrocatalytic reactions, such as the OER, outer-sphere fast redox couples have no significant material-dependent kinetic charge-transfer challenges but can directly reveal electronic transport limitations. For barrier-free band alignment at all involved interfaces and a low overall resistance, one expects a reversible redox process with symmetric anodic and cathodic peaks and a small peak potential separation. Any decrease in peak height as well as asymmetries can be related to electronic resistances in the electrode stack [23], or in some cases, toward smaller surface areas [179]. The redox potential of hexacyanoferrate(II) to hexacyanoferrate(III) is 1.2 V vs. RHE, which is similar to the thermodynamic OER redox potential, giving the advantage to test electron transport limitations in the relevant potential range [23]. To obtain the typical duck shape of the CV scan, the rotation is turned off for this experiment.

To obtain the influence of possible electrical resistances on the observed potential shift of the hexacyanoferrate(II)/(III) redox reaction, we chose to investigate the behavior of $LaNiO_{3-\delta}$ ($3.7 \times 10^{-4}\,\Omega\,cm$), $La_{0.67}Sr_{0.33}MnO_{3-\delta}$ ($2.7 \times 10^{-3}\,\Omega\,cm$) and $La_{0.6}Ca_{0.4}FeO_{3-\delta}$ ($0.57\,\Omega\,cm$), ranging over three orders of magnitude in resistivity. Note that for this experiment, all three catalyst layers are 25 nm thick to exclude any influence on the resistances from different thicknesses.

Figure 41a compares the CV of the hexacyanoferrate(II)/(III) redox reaction of $LaNiO_{3-\delta}$, $La_{0.67}Sr_{0.33}MnO_{3-\delta}$ (here in orange) and $La_{0.6}Ca_{0.4}FeO_{3-\delta}$ thin films to a 50 nm Pt thin film as ideally metallic reference. The $LaNiO_{3-\delta}$ CV scan strongly overlaps with the Pt CV scan, indicating that the $LaNiO_{3-\delta}$ is not limited by any electrical resistance for the reaction. $La_{0.67}Sr_{0.33}MnO_{3-\delta}$ shows a slightly increased overpotential for the oxidation and reduction of hexacyanoferrate(II)/(III), as indicated by the slight decrease and shift of the current density maximum towards higher and lower potentials, respectively. In contrast, $La_{0.6}Ca_{0.4}FeO_{3-\delta}$ exhibits no clear oxidation and reduction peaks in this potential range, indicating that its high resistivity strongly limits the electron transport. These electron transport limitations are reflected in the correspond-

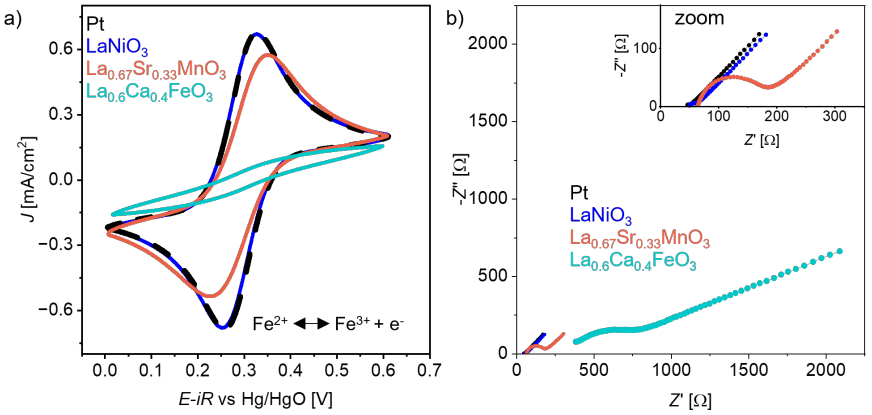

Figure 41: a) CV scans of $LaNiO_{3-\delta}$, $La_{0.67}Sr_{0.33}MnO_{3-\delta}$ and $La_{0.6}Ca_{0.4}FeO_{3-\delta}$ in $K_4[Fe(CN)_6]/K_3[Fe(CN)_6]$ solution. The sweep rate was 30 mV/s. b) Corresponding impedance spectroscopy measured at OCP. The inset shows a zoom to the region of 0-350 Ω in *Z*' direction. The figure was adapted by the color scheme from our publication [176], with the rights of the license CC-BY 4.0.

ing OCP impedance spectra shown in figure 41b. $LaNiO_{3-\delta}$ and Pt exhibit comparable spectra, whereas $La_{0.67}Sr_{0.33}MnO_{3-\delta}$ exhibits a larger semi-circle in the high frequency range. In the low frequency range, the impedance shows a nearly linear increase at an angle close to 45° for the Pt, $LaNiO_{3-\delta}$ and $La_{0.67}Sr_{0.33}MnO_{3-\delta}$ thin films, indicating the presence of a semi-infinite Warburg element [141] in the equivalent circuit. This feature stems from the mass transport limitations of the hexacyanoferrate(II)/(III) species at the solid/liquid interface. The small overpotentials observed for $La_{0.67}Sr_{0.33}MnO_{3-\delta}$ in the CV scan in Figure 41a could stem from a higher resistivity compared to $LaNiO_{3-\delta}$, but the observed semi-circle in the impedance indicates that there could be an interface resistance for the $La_{0.67}Sr_{0.33}MnO_{3-\delta}$ thin film reducing the observed currents as well.

For $La_{0.6}Ca_{0.4}FeO_{3-\delta}$, R_u exhibits a significantly higher value since the higher total resistance

of the thin film might add up to the overall observed x-axis offset, similar to the behavior of the impedance shown in Figure 39c. Moreover, the observed semi-circle in the high frequency range is deformed, a characteristic often represented by a constant phase element in equivalent electrical circuits. The low-frequency region shows a distorted incline with a slope less than 45°, which indicates that the condition for an ideal Warburg element is not fulfilled either. Together, the CV and impedance spectroscopy with the hexacyanoferrate(II)/(III) redox couple confirm that the $La_{0.6}Ca_{0.4}FeO_{3-\delta}$ thin film with a high resistivity exhibits poor electrochemical performance due to impeded electron transport in the film. For $La_{0.67}Sr_{0.33}MnO_{3-\delta}$, it remains an open question, if the higher overpotentials in the hexacyanoferrate(II)/(III) redox reaction stem from the one order of magnitude higher resistivity than $LaNiO_{3-\delta}$ or/and from the interfacial resistance that was observed as a semi-circle in the higher frequency range.
The influence of the resistivity on the observed overpotentials may be rationalized with the sample geometry. The Pt side-contacts imply that electrons released in redox reactions at the center of the 10x10 mm^2 sample must travel up to 4 mm through the bulk of the catalyst layer to reach the metal contact as illustrated in the sketch of figure 39d. This will be investigated in the following section through a simulation of the current density distribution of such thin film catalysts within the electrolyte.

5.3 Simulated current density variation along the perovskite thin film

To investigate and quantify the influence of the thin film resistivity on the local current density along the thin film/electrolyte interface, a COMSOL Multiphysics study was conducted for the $LaNiO_{3-\delta}$, $La_{0.67}Sr_{0.33}MnO_{3-\delta}$ and $La_{0.6}Ca_{0.4}FeO_{3-\delta}$ films, which is illustrated in Figure 42a. The COMSOL study was conducted by Dr. Daan Wielens from the University of Twente. The mesh of the catalyst, Pt contacts, and electrolyte layer was adapted to our model catalyst of a similar geometry as used for the experimental approach. For the simulations, the sample was modeled using an axisymmetric line cut, as illustrated by the dashed line in the sketch in Figure 42a. The thin films are 25 nm thick, contacted with Pt edges that are located in 4 mm distance to the sample center, approximating the real sample geometry in the RDE setup. The thin film is covered by a 50 µm electrolyte layer, which exhibited same total resistance as our electrolyte solution in the experiment. A fixed current of 0.44 mA was applied corresponding to an average current density of 1 mA cm^{-2}, as the exposed geometric surface area is 0.44 cm^2. We simulated the current density distribution $J_z(x)$ across the catalyst surface from the sample center to the boundary of the catalyst, i.e. the location of the O-ring at 3.75 mm distance from the sample center. $J_z(x)$ is the current density perpendicular to the catalyst surface, read out along the sample interface in x-direction (further details of the simulation can be found in the publication [176]).

The resulting current density distribution shows significant differences for the three materials with varying resistivities (figure 42a). For $LaNiO_{3-\delta}$, the current density is almost homogeneously distributed, indicating that the low resistivity does not significantly affect the current pathway

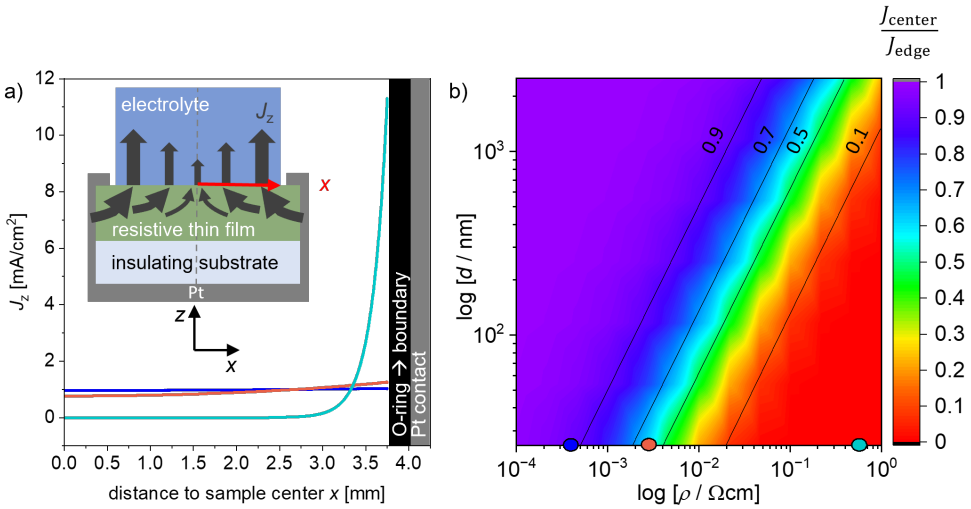

Figure 42: a) Simulated current density distribution of the thin films on insulating substrates. The inset shows a sketch of the radial current density distribution $J_z(x)$ on resistive thin films along the x-axis of the simulation. The dashed line in the center represents the axisymmetric line cut. b) Heat map of the current density variation J_{center}/J_{edge} as a function of catalyst layer resistivity ρ and thickness d. Blue, green, and orange dots are the data points for 25 nm thick $LaNiO_{3-\delta}$, $La_{0.67}Sr_{0.33}MnO_{3-\delta}$ and $La_{0.6}Ca_{0.4}FeO_{3-\delta}$ thin films, respectively. The figure was adapted by the color scheme from our publication [176], with the rights of the license CC-BY 4.0.

through the thin film towards the metallic contacts, and the entire catalyst area contributes similarly to the reaction current. In the sample center, the current density is 0.96 mA cm^{-2} and increases to 1.04 mA cm^{-2} at the catalyst boundary.

To describe the current density variation along the sample profile, we define the ratio J_{center}/J_{edge} which is the current density at the sample center in relation to the catalyst boundary: $(J_{center}/J_{edge} = J_z(x = 0\,\text{mm})/J_z(x = 3.75\,\text{mm})$. For $LaNiO_{3-\delta}$, J_{center}/J_{edge} is about 0.92. For $La_{0.67}Sr_{0.33}MnO_{3-\delta}$, however, the current density in the sample center is 0.76 mA cm^{-2} which is 20% lower than the value obtained for $LaNiO_{3-\delta}$. The current density of the $La_{0.67}Sr_{0.33}MnO_{3-\delta}$ current density profile increases continuously from the sample center towards the catalyst boundary reaching a current density of around 1.25 mA cm^{-2}. Hence, the one order of magnitude higher resistivity in the $La_{0.67}Sr_{0.33}MnO_{3-\delta}$ film leads to a significant change of the current density distribution along the interface, where J_{center}/J_{edge} is only 0.6, and the deviations from the center to the eadge are on a linear scale. This behavior is even more pronounced for $La_{0.6}Ca_{0.4}FeO_{3-\delta}$. Here, the current density is only 3.6 nA cm^{-2} in the sample center and essentially does not contribute to the overall reaction. At 3 mm radial distance, the current density increases to 0.15 mA cm^{-2}. And only towards the edge, the current density increases drastically

to more than 11 mA cm^{-2} leading to an extremely small $J_{\text{center}}/J_{\text{edge}}$ ratio of only 2×10^{-8}.
Due to the high resistance of the $La_{0.6}Ca_{0.4}FeO_{3-\delta}$ thin film, the area close to the metal contacts hence over-proportionally contributes to the current and shows a locally higher current density (as sketched in the inset of Figure 41c). The COMSOL study thus suggests a large effect of the electrode resistivity on the current density distribution in the electrochemical measurement where a highly resistive sample can lead to inhomogenously distributed current scenarios. In principle, electrolyte effects can also lead to inhomogeneous current distributions [180]. Therefore, such inhomogeneities are estimated for our setup in the appendix E, where the variation is only about 10 % in the sample center. However, according to our COMSOL simulations, the inhomogeneities caused by the thin film catalyst resistivity can reach values that are orders of magnitude higher. Hence, inhomogeneities caused by the electrolyte effects have a minor influence.
Thus, the COMSOL study shows that the effective surface area accessible for electrochemical reactions is extremely small for $La_{0.6}Ca_{0.4}FeO_{3-\delta}$ in the chosen sample geometry. Therefore, for samples with higher resistivity, the observed electrochemical currents can effectively not be related to their geometric surface area that is exposed to the electrolyte, making it impossible to reveal their intrinsic catalytic properties in any electrochemical reaction in such sample geometry. The observed low activity of $La_{0.6}Ca_{0.4}FeO_{3-\delta}$ (Figure 39a) thus results from ill-defined normalization of the current density with respect to the total exposed catalyst area. To generalize which resistivity-thickness relations are suitable to reveal the intrinsic properties for this sample geometry, we extended the COMSOL study for the full resistivity range from $1 \times 10^{-4}\,\Omega\,\text{cm}$ to $1\,\Omega\,\text{cm}$ and thin film thicknesses of up to 2.5 µm. The expected current density ratio $J_{\text{center}}/J_{\text{edge}}$ is determined for various combinations of catalyst resistivity and layer thickness, yielding the heat map shown in Figure 42b. The values for 25 nm thick $LaNiO_{3-\delta}$, $La_{0.67}Sr_{0.33}MnO_{3-\delta}$ and $La_{0.6}Ca_{0.4}FeO_{3-\delta}$ thin films are marked as blue, orange and light blue dot, respectively.
We consider the $LaNiO_{3-\delta}$ case with $J_{\text{center}}/J_{\text{edge}} = 0.92$ as an acceptable scenario to extract intrinsic catalytic properties in this geometry, while for $La_{0.67}Sr_{0.33}MnO_{3-\delta}$ with $J_{\text{center}}/J_{\text{edge}} = 0.6$ the current density would already be too inhomogeneous for a proper analysis at the current density of 1 mA cm^{-2}. However, with an exemplary sample thickness of more than 200 nm, $J_{\text{center}}/J_{\text{edge}}$ would be 0.9 or more also for $La_{0.67}Sr_{0.33}MnO_{3-\delta}$, enabling us to principally reveal the intrinsic catalytic properties of $La_{0.67}Sr_{0.33}MnO_{3-\delta}$ in this sample geometry. For $La_{0.6}Ca_{0.4}FeO_{3-\delta}$, however, even a film thickness of 1 µm would only lead to $J_{\text{center}}/J_{\text{edge}} = 0.2$, making it impossible to determine the intrinsic catalytic properties in this sample geometry. Figure E.2 shows the heatmap on a logarithmic scale, highlighting the extremely small $J_{\text{center}}/J_{\text{edge}}$ values for resistivities above $2 \times 10^{-2}\,\Omega\,\text{cm}$.
The previously mentioned ill-defined normalization of the current density in $La_{0.6}Ca_{0.4}FeO_{3-\delta}$ can also explain the deformed impedance features observed in Figure 41b. As the current-potential distribution exhibits a strong radial distribution, the equivalent electric circuit needs to be described as a series of R_u-RC elements that vary along the solid/liquid interface. Such 2D

surface distributions are experimentally observed as a constant phase element in the global impedance [140, 181, 182], thus explaining the suppressed impedance feature in the high and low frequency ranges observed for $La_{0.6}Ca_{0.4}FeO_{3-\delta}$. An additional reason for the non-ideal Warburg element in Figure 41b could be sideward diffusion of ionic species in the electrolyte, which has been observed as an edge effect [183] that can principally also occur on metallic electrodes. The phenomenon of varied radial current-potential distribution could also occur in the catalyst bulk, where not solely Ohmic resistances are present but also capacitive contributions [184, 185] might be present in the lateral dimension. Hence, the catalyst bulk might also be described as 2D distributed *RC* elements along the lateral dimension. Therefore, R_u determined by the x-axis intercept of the impedance at high frequencies does not include all relevant bulk related impedances. In other words, each location on the sample surface exhibits a different 'effective' iR_u value, resulting from increasing series resistances from the edge to the center. This might explain the fact that the linear slope observed for $La_{0.6}Ca_{0.4}FeO_{3-\delta}$ in Figure 39 cannot be compensated by a classic iR_u correction. This outlines the necessary conditions to ensure that performance is not limited by the thin film resistance.

5.4 Electrochemical characterization on conducting Nb:$SrTiO_3$ in hexacyanoferrate(II)/(III) electrolyte

To suppress electron transport limitations and the large radial current density distribution of the resistive thin film electrocatalysts, the chosen OER catalyst layers were deposited on 0.5 wt% Nb-doped $SrTiO_3$ (Nb:$SrTiO_3$), which possesses metallic conductivity in the bulk. As sketched in figure 43a, the electrons can now travel from the solid/liquid interface directly through the only nanometers thick films into the Nb:$SrTiO_3$ substrate, which can act as current collector. The film thickness is 10 nm for $LaNiO_{3-\delta}$, 20 nm for $La_{0.6}Ca_{0.4}FeO_{3-\delta}$ and 25 nm for $La_{0.67}Sr_{0.33}MnO_{3-\delta}$, which is far above the thickness where finite size phenomena occur. The $LaNiO_{3-\delta}$ thickness was decreased because the probability of electrons moving to the sides decreases. In this geometry, Pt is only sputtered on the back side of the substrate as sketched in figure 43a.
With this different sample stack design, $La_{0.6}Ca_{0.4}FeO_{3-\delta}$ and notably also $LaNiO_{3-\delta}$ show largely suppressed current densities and large peak separations in the hexacyanoferrate(II)/(III) redox reaction (Figure 43a). In contrast, the current density of $La_{0.67}Sr_{0.33}MnO_{3-\delta}$ is the closest to the Pt reference, and the peak separation is much smaller compared to $LaNiO_{3-\delta}$ and $La_{0.6}Ca_{0.4}FeO_{3-\delta}$ in this sample geometry. This indicates that although the travelling distance has changed from a few millimeters in lateral dimensions to a few nanometers in vertical dimension in this sample geometry, the charge transport remains limited. This is particularly observed for the OER catalyst with lowest ($La_{0.6}Ca_{0.4}FeO_{3-\delta}$) and largest ($LaNiO_{3-\delta}$) conductivity, indicating a departure from the systematic scaling with electrical conductivity as observed before. Instead, the observed behavior suggests an interfacial contact resistance across the substrate/thin film interface [185–188], resulting from Schottky-type space charge layers.

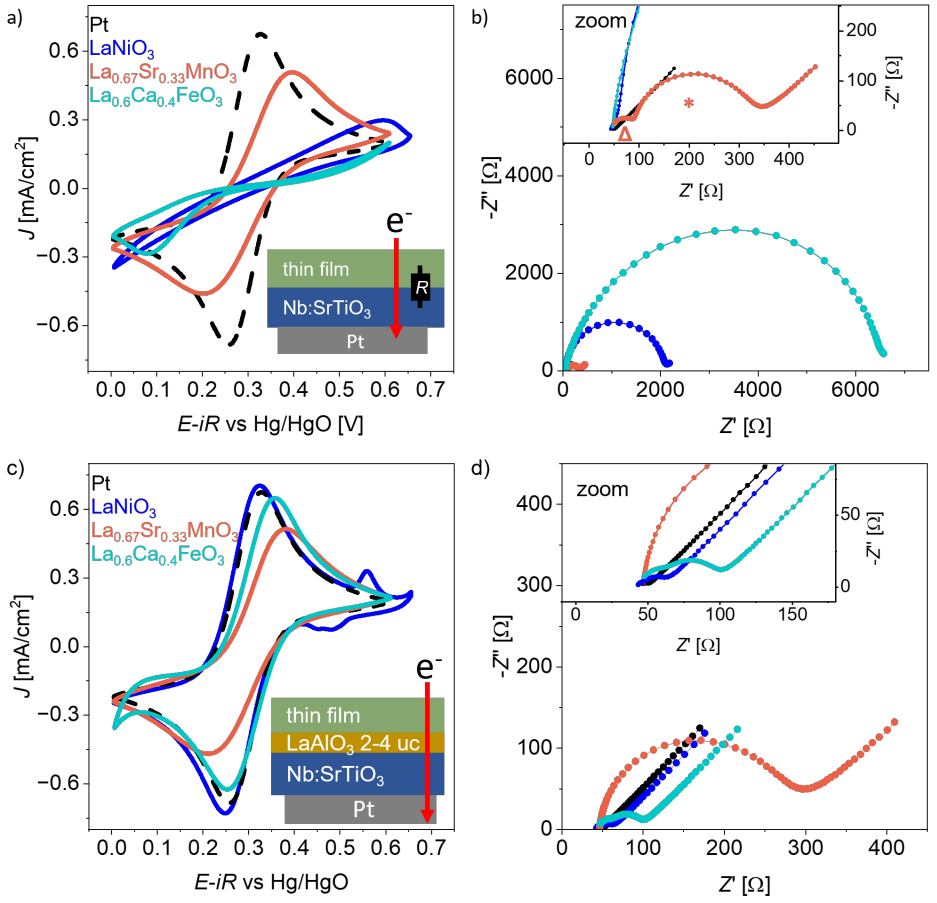

Figure 43: a) CV in hexacyanoferrate(II)/(III) electrolyte for $LaNiO_{3-\delta}$, $La_{0.67}Sr_{0.33}MnO_{3-\delta}$ and $La_{0.6}Ca_{0.4}FeO_{3-\delta}$ thin films grown on Nb:$SrTiO_3$ in comparison to the Pt sample. The sweep rate was 30 mV/s. For $LaNiO_{3-\delta}$ in this case, the sweep window was extended to 0.65 V vs Hg/HgO to obtain a possible contribution from Ni oxidation. b) Corresponding impedance spectra at the OCP. Legend corresponds to a). Inset shows the zoom of the lower impedance values. Δ refers to the semi-circle in the high frequency range of $La_{0.67}Sr_{0.33}MnO_{3-\delta}$ and * refers to the semi-circle toward lower frequencies. c) CV in hexacyanoferrate(II)/(III) electrolyte for Nb:$SrTiO_3$/2 uc $LaAlO_3$/ $LaNiO_{3-\delta}$, Nb:$SrTiO_3$/2 uc $LaAlO_3$/ $La_{0.67}Sr_{0.33}MnO_{3-\delta}$ and Nb:$SrTiO_3$/4 uc $LaAlO_3$/ $La_{0.6}Ca_{0.4}FeO_{3-\delta}$ thin films in comparison to the Pt sample. The sweep rate was 30 mV/s. For $LaNiO_{3-\delta}$, additional oxidation and reduction peaks are seen at 0.55 V and 0.45 V vs Hg/HgO, respectively, representing the Ni^{2+}/Ni^{3+} redox reaction. d) Corresponding impedance spectra at the OCP. Inset shows the zoom to the lower impedance values. The figure was adapted by the color scheme from our publication [176], with the rights of the license CC-BY 4.0. The $LaNiO_{3-\delta}$ experiments were conducted by Iris van den Bosch.

For a Schottky barrier (the catalyst work function is higher than the Nb:$SrTiO_3$ electron affinity), it is expected that the electron transport is more hampered for the oxidation reaction rather than for the reduction reaction [23]. This is due to the rectifying properties of the Schottky barrier.
For $La_{0.6}Ca_{0.4}FeO_{3-\delta}$, the oxidation and reduction peak of hexacyanoferrate(II)/(III) are asymmetric, indicating that the (Schottky barrier-type) contact resistance at the Nb:$SrTiO_3$/thin film interface especially hampers the oxidation from hexacyanoferrate(II) to hexacyanoferrate(III). A similar interface resistance is expected for $LaNiO_{3-\delta}$, which has a work function larger than the Nb:$SrTiO_3$ electron affinity, as described in the references [185, 186, 189]. However, the Ni oxidation takes place in the same measured potential window [19] as the Fe oxidation, therefore the Ni^{3+} and Fe^{3+} formation might lead to additional asymmetric behavior in the anodic sweep compared to the cathodic sweep seen in Figure 43a.
The Nyquist plots in Figure 43b show large semi-circles for $La_{0.6}Ca_{0.4}FeO_{3-\delta}$ and $LaNiO_{3-\delta}$ with a real impedance (Z') of up to several kΩ which may be attributed to the substrate/thin film contact resistance. In contrast, $La_{0.67}Sr_{0.33}MnO_{3-\delta}$ exhibits two semi-circles that are below 400 Ω (marked with an orange * and Δ in the inset of Figure 43b), indicating a significantly lower contact resistance at the substrate/thin film interface, consistent with the smaller peak separation and higher current densities in the hexacyanoferrate(II)/(III) CV compared to $La_{0.6}Ca_{0.4}FeO_{3-\delta}$ and $LaNiO_{3-\delta}$. The semi-circle in the high frequency range (marked with Δ) of $La_{0.67}Sr_{0.33}MnO_{3-\delta}$ could stem from the Nb:$SrTiO_3$/thin film interface impedance and the semi-circle towards lower frequencies (*) could stem from $La_{0.67}Sr_{0.33}MnO_{3-\delta}$ -specific and contact-independent behavior as the same order of magnitude impedance was already observed on the insulating substrate (Figure 41b). This explains the occurrence of two separate impedance features in the high-frequency range.
The Nyquist plots in Figure 43b show that the uncompensated resistance R_u is now in the same range of 40-50 Ω for all three materials, indicating that the additional ohmic resistance of the resistive $La_{0.6}Ca_{0.4}FeO_{3-\delta}$ thin film that was observed in Figure 41b, is circumvented in this geometry. Nevertheless, the large contact resistance to the substrate, especially for $La_{0.6}Ca_{0.4}FeO_{3-\delta}$ and $LaNiO_{3-\delta}$ still affects the electrochemical performance and thus hinders the observation of intrinsic catalytic properties of the OER. As interface resistances depend on the applied potential, the quantification of this resistance only at OCP would be insufficient to determine an R_u, that could include such interface resistance.

5.5 Interface engineering between Nb:$SrTiO_3$ and perovskite thin films

To decrease the contact resistance between the thin film and Nb:$SrTiO_3$, a 2-4 uc thick interlayer of $LaAlO_3$ was introduced (see sketch in Figure 43c). This polar oxide layer induces an electrical dipole which can counteract interfacial space charge layers and Schottky barriers, facilitating the electron transport across the interface [81, 189, 190]. Only one unit cell of the $LaAlO_3$ can already have a strong effect on the compensation of interface barriers as reported

by Hikita et al. [190]. Nonetheless, $LaAlO_3$ is an insulator, and should therefore not be too thick, so that the electron transport through the interlayer itself cannot be hampered. We note that the ideal dipole layer thickness to compensate the built-in potentials is specific to the materials at the interface.

For the $LaNiO_{3-\delta}$ /Nb:$SrTiO_3$ interface, 2 uc of $LaAlO_3$ as interlayer effectively decreased the contact resistance, as evident by the resulting CV scan in the hexacyanoferrate(II)/(III) redox couple (Figure 43c) and the impedance at OCP (Figure 43d), both of which are now similar to the Pt reference (Figure 43c and d). This shows a clear improvement in comparison to the $LaNiO_{3-\delta}$/Nb:$SrTiO_3$ sample without $LaAlO_3$ interlayer (Figure 43a and b).

In the case of $La_{0.67}Sr_{0.33}MnO_{3-\delta}$, introducing 2 uc of $LaAlO_3$ results in a slightly smaller peak separation as can be seen in the hexacyanoferrate(II)/(III) CV scan (comparing Figure 43a and c with 0.2 V and 0.17 V peak separation, respectively) but still exhibits a small remaining overpotential. Comparing the impedance data of $La_{0.67}Sr_{0.33}MnO_{3-\delta}$ with and without $LaAlO_3$ interlayer on Nb:$SrTiO_3$ in Figure 43b and d shows that with the $LaAlO_3$ interlayer, the semi-circle in the high frequency range (Δ) is not visible anymore but the semi-circle marked with a * in Figure 43b remains. The $LaAlO_3$ interlayer might have compensated the smaller interface resistance at the Nb:$SrTiO_3$/$La_{0.67}Sr_{0.33}MnO_{3-\delta}$ interface, but an additional $La_{0.67}Sr_{0.33}MnO_{3-\delta}$-specific impedance behavior remains, which was observed in all contacting geometries.

For $La_{0.6}Ca_{0.4}FeO_{3-\delta}$, a $LaAlO_3$ interlayer thickness of 4 uc was required here to sufficiently decrease the Nb:$SrTiO_3$/$La_{0.6}Ca_{0.4}FeO_{3-\delta}$ contact resistance. Note that especially for $La_{0.6}Ca_{0.4}FeO_{3-\delta}$, the interface resistance was not always reproducible when applying different layer thicknesses of $LaAlO_3$. As the termination of the substrate and possible defect structures can influence the effectiveness of the $LaAlO_3$ dipole layer, this might lead to possible deviations in the final charge compensation across the Nb:$SrTiO_3$/$LaAlO_3$/thin film interface.

For the Nb:$SrTiO_3$/$LaAlO_3$/$La_{0.6}Ca_{0.4}FeO_{3-\delta}$ stack, the reduction peak from hexacyanoferrate(III) to hexacyanoferrate(II) shows now similar behavior as the Pt sample (Figure 43c) and the oxidation peak exhibits only a small overpotential. The total impedance was decreased by two orders of magnitude by the 4 uc thick $LaAlO_3$ interlayer comparing the impedance in Figure 43b and d. Only two small semi-circles remain that are observed in the Nyquist plot in Figure 43d. The small remaining overpotential of the oxidation reaction might stem from a small remaining contact resistance at the Nb:$SrTiO_3$/$LaAlO_3$/ $La_{0.6}Ca_{0.4}FeO_{3-\delta}$ interface and/or from an $La_{0.6}Ca_{0.4}FeO_{3-\delta}$ -specific resistance. As a result, the electrochemical performance in this geometry should not be strongly limited by electronic transport anymore despite the high resistivity of $La_{0.6}Ca_{0.4}FeO_{3-\delta}$. This is evidenced by the high currents obtained with the outer-sphere fast redox couple. This indicates that electronic transport limitations are also negligible for electrocatalytic inner-sphere redox reactions such as OER, implying that the measured electrocatalytic current in this geometry directly scales with the intrinsic ability of $La_{0.6}Ca_{0.4}FeO_{3-\delta}$ to catalyze the reaction of interest, here the OER.

5.6 Substrate/thin film interface resistances under applied voltage toward the OER regime

To obtain the influence and behavior of the interface resistances at higher applied potentials, impedance spectra were recorded at increasing potential steps towards the OER. As observed for $LaNiO_{3-\delta}$ and $La_{0.6}Ca_{0.4}FeO_{3-\delta}$ directly deposited on Nb:$SrTiO_3$ in figure 43a and b, large interface resistances between Nb:$SrTiO_3$ and the catalyst layer lead to large overpotentials already at small current densities. However, even small remaining interface resistances can impact the observed electrochemical performance at higher current densities. Moreover, Schottky barrier-type interfaces are voltage-dependent, and their interface barrier might change towards the OER voltage regime.

Therefore, we made an exemplary staircase impedance spectroscopy measurement to obtain the influence of the applied potential on the interface resistance and observed OER current densities for $La_{0.6}Sr_{0.4}FeO_{3-\delta}$ directly deposited on Nb:$SrTiO_3$ in comparison to a stack with 3 uc $LaAlO_3$ interlayer (Figure 44). Note, that not $La_{0.6}Ca_{0.4}FeO_{3-\delta}$ was chosen here, as this exhibits a reduction reaction close in the OCP regime as can be seen in the appendix figure F.1. $La_{0.6}Sr_{0.4}FeO_{3-\delta}$ did not show such a reduction peak in this regime. From 1-1.5 V vs RHE, the Nb:$SrTiO_3$/ 20 nm $La_{0.6}Sr_{0.4}FeO_{3-\delta}$ sample shows one semi-circle in the high-frequency region, representing the Nb:$SrTiO_3$/$La_{0.6}Sr_{0.4}FeO_{3-\delta}$ interface. Towards the low-frequency region, a steep incline of the imaginary part of the impedance indicates the initial part of a large semi-circle, representing the $La_{0.6}Sr_{0.4}FeO_{3-\delta}$/electrolyte interface [34]. At 1.63 V vs RHE the impedance of the $La_{0.6}Sr_{0.4}FeO_{3-\delta}$/electrolyte interface (marked with *) is strongly decreased, making a clear semi-circle observable. At the lowest frequency of 0.1 Hz, the EIS data now reach the real axis, owing to the non-zero net current (OER) under DC conditions. At this potential, the $La_{0.6}Sr_{0.4}FeO_{3-\delta}$/electrolyte semi-circle is still larger than the one from the substrate/thin film interface. Above these voltages both semi-circles become smaller indicating a decrease in the charge-transfer resistance on both interfaces. Note that faradaic currents from the OER might partly influence the measured impedance in this higher voltage range.

To quantify the values of the charge-transfer resistance at both interfaces, an impedance fit was conducted with an equivalent electric circuit $R_u + R/Q_{\text{substrate/film}} + R/Q_{\text{film/electrolyte}}$ (substrate/film in the index will be abbreviated with sub./film). Further information about the fit and equivalent electric circuit can be found in the methodology section 3.6.2. The fit results are shown in figure 45a and b. $R_{\text{sub./film}}$ is 1273 Ω at 1 V vs RHE and decreases to 590 Ω at 2 V vs RHE. This indicates that with applied potential the resistance of the Nb:$SrTiO_3$/$La_{0.6}Sr_{0.4}FeO_{3-\delta}$ space charge layer gets smaller. However, this barrier is still very high under OER conditions and hence, significantly increases the observed overpotential η, for example, at 0.1 mA cm^{-2} by 90 mV compared to the Nb:$SrTiO_3$/3 uc $LaAlO_3$/ $La_{0.6}Sr_{0.4}FeO_{3-\delta}$ sample. The second semi-circle representing the $La_{0.6}Sr_{0.4}FeO_{3-\delta}$/electrolyte interface $R_{\text{film/electrolyte}}$ exhibits a large interface resistance of 300 kΩ at 1 V vs RHE and drastically decreases to only 165 Ω at 2 V vs RHE.

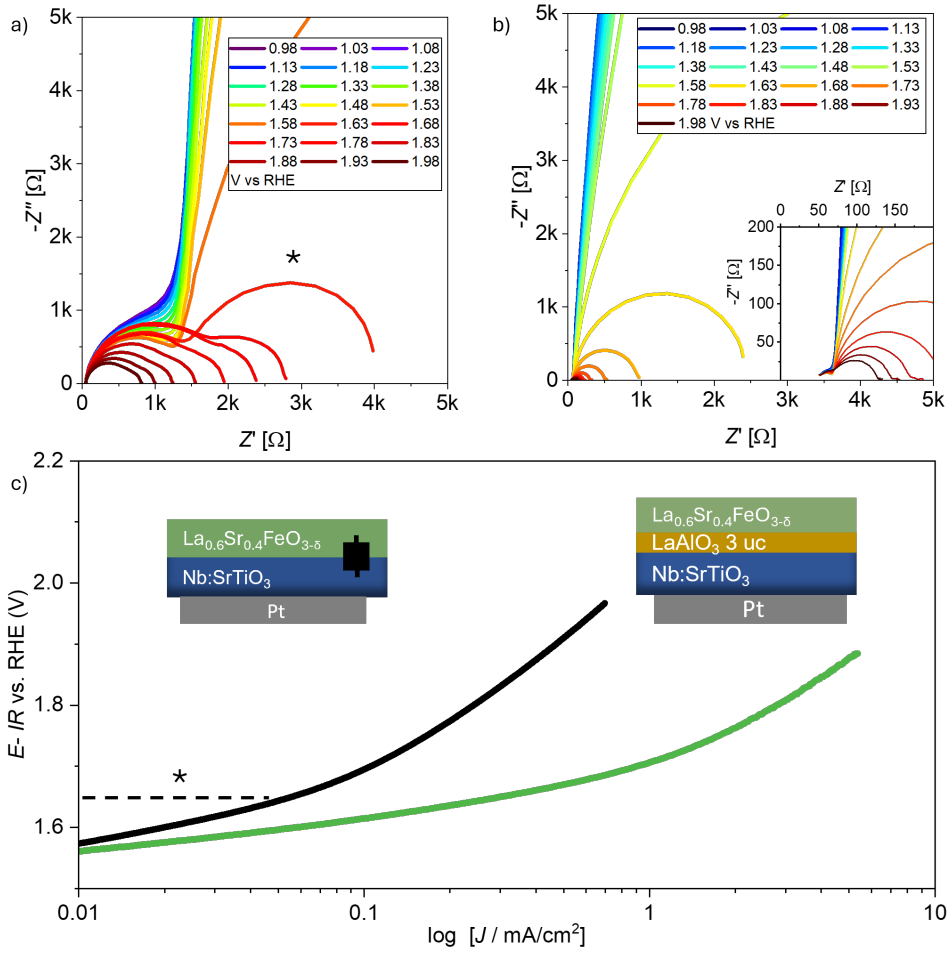

Figure 44: Stair case impedance spectroscopy towards the OER voltage regime in a) for Nb:$SrTiO_3$/ 20 nm $La_{0.6}Sr_{0.4}FeO_{3-\delta}$ and b) Nb:$SrTiO_3$/ 3 uc $LaAlO_3$/ 20 nm $La_{0.6}Sr_{0.4}FeO_{3-\delta}$. As oxygen gas evolves, the RDE rotation is set to 1600 rpm. c) Tafel-like plot of the averaged, second CV scan with and without $LaAlO_3$ interlayer. The * marks where the catalyst/electrolyte interface impedance is still bigger than that of the substrate/thin film interface.

Hence, under higher applied potentials the interfacial resistance $R_{\text{substr./film}}$ dominates the overpotential, as its charge transfer resistance is higher than $R_{\text{film/electrolyte}}$.

For the sample, with a 3 uc thick $LaAlO_3$ interlayer, there is a small semi-circle observed for the substrate/$LaAlO_3$/film interface at high frequencies (inset of figure 44b). This semi-circle is represented by a $QR_{\text{sub./LAO/film}}$ element in the equivalent electric circuit. However, it is not

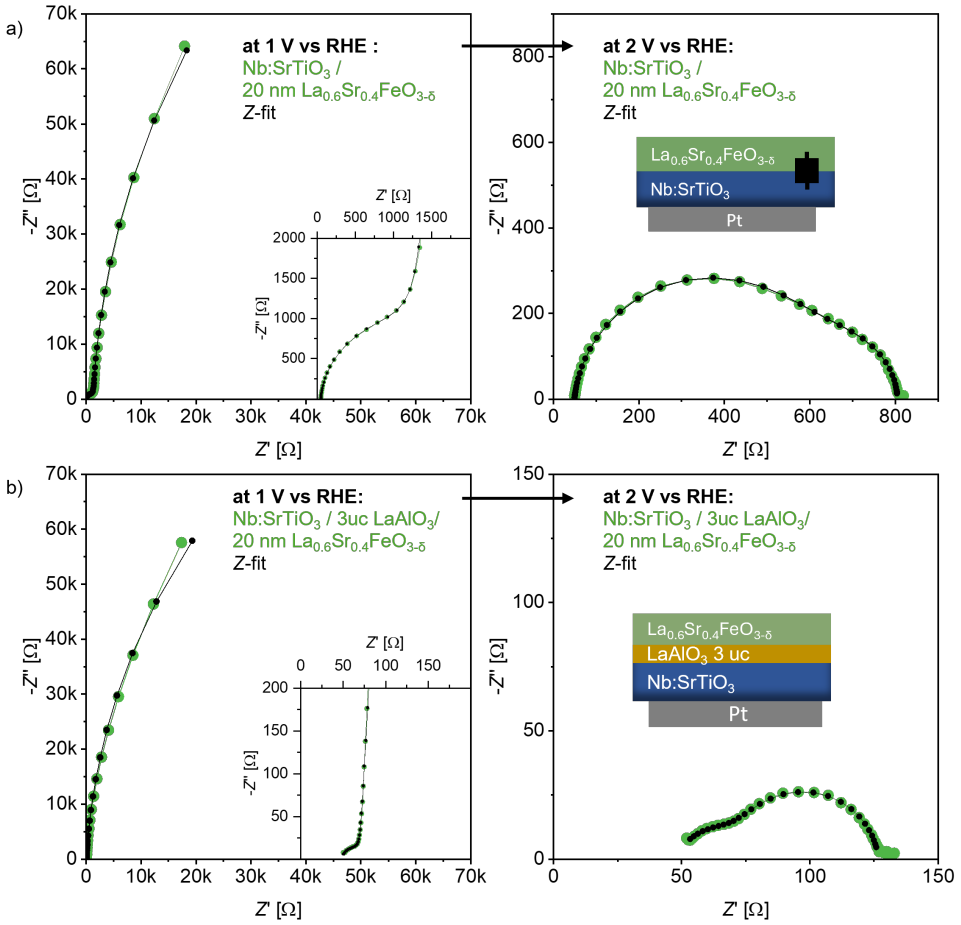

Figure 45: Impedance spectra and corresponding fits at 1 V vs RHE and 2 V vs RHE with the equivalent electric circuit $R_u + R/Q_{\text{substrate/film}} + R/Q_{\text{film/electrolyte}}$ a) for Nb:SrTiO$_3$/ 20 nm $La_{0.6}Sr_{0.4}FeO_{3-\delta}$ and b) Nb:SrTiO$_3$/ 3 uc $LaAlO_3$ 20 nm $La_{0.6}Sr_{0.4}FeO_{3-\delta}$.

significantly affected in the applied voltage range towards the OER. The value of the charge transfer resistance (impedance fits in figure 45c and d) remains similar at 1 and 2 V vs RHE, with 21 Ω and 25 Ω, respectively. Hence, the influence on the OER performance is significantly smaller, leading to an additional overpotential of only 20 mV at 1 mA cm^{-2}. The large semi-circle seen at 1 V vs RHE represents the film/electrolyte interface, and a $QR_{\text{film/electrolyte}}$ element in the equivalent electric circuit. The charge transfer resistance $R_{\text{film/electrolyte}}$ representing the electron transfer of the OER into the catalyst layer, decreases from 230 kΩ to only 54 Ω at 2 V vs RHE. Hence, it is only twice as high as the charge transfer resistance $R_{\text{sub./LAO/film}}$ at the substrate/$LaAlO_3$/film interface. This indicates an effective reduction of the interface resistance by the insertion of the $LaAlO_3$ dipole layer.

The effect of the interfacial resistances is reflected in the OER CV scans. Figure 44c shows their Tafel-like plots. The overpotential is 480 mV at 1 mA cm^{-2} with $LaAlO_3$ interlayer, whereas without a charge compensating layer the current density of 1 mA cm^{-2} is not even reached anymore. The Tafel slope of the Nb:$SrTiO_3$/$La_{0.6}Sr_{0.4}FeO_{3-\delta}$ sample increases significantly above 1.65 V vs RHE (marked with the *). Here, the charge transfer resistance of the $La_{0.6}Sr_{0.4}FeO_{3-\delta}$/electrolyte interface is still larger than the charge transfer resistance of the Nb:$SrTiO_3$/$La_{0.6}Sr_{0.4}FeO_{3-\delta}$ interface. The corresponding impedance spectrum at 1.65 V vs RHE is marked with a *. Above this voltage, the CV scan is dominated by the charge transfer resistance of the Nb:$SrTiO_3$/$La_{0.6}Sr_{0.4}FeO_{3-\delta}$ interface. The Tafel slope increases even more, making a determination of intrinsically driven Tafel slope values impossible. With 3 uc $LaAlO_3$ charge compensating layer, the CV curve is significantly less affected over the whole potential range. However, also for this sample, already at around 0.4 mA cm^{-2} the slope of the Tafel-like plot increases, which can be the effect of the small remaining interface resistance, which has an increasing impact on the observed catalytic activity at increasing current densities.

Therefore, the intrinsic catalytic activity can be obtained at current densities up to around 0.4 mA cm^{-2}, when the interface resistance is sufficiently small. Above this, it cannot be differentiated if the change in slope is only due to the remaining substrate/$LaAlO_3$/film interface resistance $R_{\text{sub./LAO/film}}$ or OER kinetics. Before, the intrinsic activity trend is revealed, possible charge transfer resistance at the catalyst/electrolyte interface are investigated in the following section.

5.7 Catalyst/electrolyte interface resistances under applied voltage toward the OER regime

Narrow space charge barriers and favorable band bending directions facilitate the electron transport at the interface to the substrate, as demonstrated for the Nb:$SrTiO_3$/catalyst stacks in the previous section. While stack-related interface barriers should be minimized for efficient electrode design in electrolyzers, the occurring space charge barrier at the catalyst/electrolyte interface is an unavoidable property of the catalyst material, which can significantly influence the OER performance [15]. For the OER, upward band bending at the catalyst surface is beneficial. This is because holes accumulate at the interface that can easily receive incoming electrons from the oxidation reaction [15, 34].

For $La_{0.67}Sr_{0.33}MnO_{3-\delta}$, we observed in the previous chapter that an interfacial resistance remains visible in the impedance spectra independent of the contacting geometry (figure 41b and 43d). This interface resistance might be attributed to a space charge layer at the $La_{0.67}Sr_{0.33}MnO_{3-\delta}$/electrolyte interface. However, since band alignment depends on voltage, the space charge barrier in the OER voltage regime may differ from that observed in the lower potential window in the hexacyanoferrate (II)/(III) electrolyte. Moreover, the thermodynamic standard potential of the OER and the hexacyanoferrate (II)/(III) is both about 1.2 V vs RHE, but the experimentally observed potentials to drive the OER lie at around 1.5 V vs RHE due to the scaling relations explained in section 2.1. Therefore, the observed interface resistance in hexacyanoferrate (II)/(III) containing electrolyte may have changed toward the OER voltage regime, that is at higher voltages.

Hence, to study the band bending at the catalyst/electrolyte interface under applied potentials, we conducted a MS analysis up to 1.55 V vs RHE, similar to our previous study by Heymann *et al*. [34]. Figure 46a shows the MS plots of $La_{0.6}Sr_{0.4}CoO_{3-\delta}$, $LaNiO_{3-\delta}$, $La_{0.6}Ca_{0.4}NiO_{3-\delta}$, $La_{0.6}Ca_{0.4}FeO_{3-\delta}$, $La_{0.6}Sr_{0.4}FeO_{3-\delta}$ and $La_{0.67}Sr_{0.33}MnO_{3-\delta}$. The maximum of each plot is normalized to one. The MS plot of $La_{0.6}Sr_{0.4}CoO_{3-\delta}$ exhibits a positive slope close to the OCP regime, which indicates for such *p*-type conductors that the bands are strongly bent downward at the catalyst/electrolyte interface, leading to an even inversely charged surface. A sketch of the inversely charged surface is shown in Figure 46b. Toward higher voltages between 1 V and 1.35 V vs RHE, the MS plot slope changes to a negative sign and shows a linear slope. This is attributed to a hole-depleted space charge layer in a *p*-type catalyst. A linear fit of the MS plot in this region yields the flat band potential, which is reached at 1.45 V vs RHE. Above this potential, the bands bend upward and holes accumulate toward the surface (see also sketch of figure 46b bottom). This benefits the OER and ensures that enough hole carriers can recombine with the electrons from the oxidation reaction.

$LaNiO_{3-\delta}$ and $La_{0.6}Ca_{0.4}NiO_{3-\delta}$, and $La_{0.6}Sr_{0.4}FeO_{3-\delta}$, similar to $La_{0.6}Sr_{0.4}CoO_{3-\delta}$, exhibit declining MS plots above 1.0-1.1 V vs RHE resulting in flat band potentials of 1.33 V, 1.44 V and 1.41 V vs RHE, respectively. Their bands are bent upward above the flat band potential in the typical OER regime, hence favorable for the electronic charge transfer. $La_{0.6}Ca_{0.4}FeO_{3-\delta}$ shows

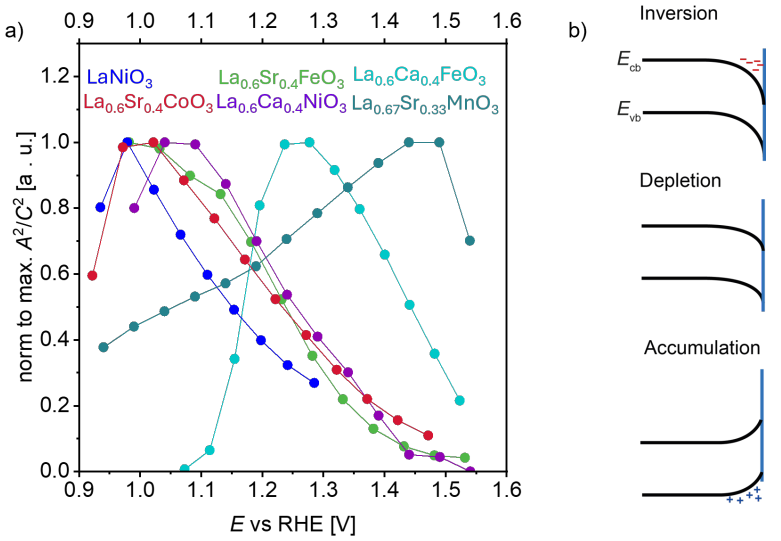

Figure 46: a) Mott-Schottky plots from OCP to near OER conditions normalized to the maximum. The analysis and the $La_{0.6}Sr_{0.4}CoO_{3-\delta}$ plot are adapted from Heymann *et al*. [34], with the rights of the license CC-BY 4.0. b) Sketch of the band bending at the catalyst/electrolyte interface with an inversion (top), hole depleted (middle), and hole accumulated space charge layer (bottom) [34].

a positive slope up to 1.25 V vs RHE, indicating charge inversion in this regime. Then the slope becomes negative, resulting in a flat band potential of 1.59 V vs RHE. $La_{0.67}Sr_{0.33}MnO_{3-\delta}$ however, shows a positive slope even up to almost 1.5 V vs RHE. Only above that potential, the $La_{0.67}Sr_{0.33}MnO_{3-\delta}$ MS plot starts to drop. The turn in slope is hence 250 mV higher than for $La_{0.6}Ca_{0.4}FeO_{3-\delta}$. This indicates that $La_{0.67}Sr_{0.33}MnO_{3-\delta}$ band bending at the electrolyte interface is in a charge inversion even close to the OER voltage regime, which might limit the electron transport across the catalyst/electrolyte interface. This is consistent with the appearance of an additional impedance feature in this sample in the hexacyanoferrate(II)/(III) containing electrolyte.

Intuitively, the high doping concentration in $La_{0.67}Sr_{0.33}MnO_{3-\delta}$ would lead to only a narrow space layer at the interface to the electrolyte. However, if the distance between the Fermi level of $La_{0.67}Sr_{0.33}MnO_{3-\delta}$ and the electrolyte is significantly large, a space charge barrier may form. As $La_{0.67}Sr_{0.33}MnO_{3-\delta}$ showed one order of magnitude lower contact resistance to Nb:$SrTiO_3$ as $LaNiO_{3-\delta}$ or $La_{0.6}Ca_{0.4}FeO_{3-\delta}$ on Nb:$SrTiO_3$, the Fermi level distance might be smaller towards the Nb:$SrTiO_3$ Fermi level than to the one from the electrolyte. In contrast, $LaNiO_{3-\delta}$ and $La_{0.6}Ca_{0.4}FeO_{3-\delta}$ showed only very small remaining interfacial resistances to the electrolyte with

the Nb:$SrTiO_3$/$LaAlO_3$/catalyst stack design, indicating that there is not such a significant space charge barrier limiting the electron transport at the catalyst/electrolyte interface.

5.8 Intrinsically driven OER activity with minimized electron transport pathways and contact resistances

Based on the detailed understanding of the influence of resistivity and interface resistances, the intrinsic OER activity is now determined from the individually optimized Nb:$SrTiO_3$/$LaAlO_3$/perovskite catalyst stack designs. This was determined at low current densities to avoid interfering resistance limitation at higher current densities (cf. section 5.6). Note that in contrast to the experiments in hexacyanoferrate(II)/(III) containing electrolyte (section 5.2), RDE rotation is set to 1600 rpm for OER experiments, to remove evolving oxygen gas from the surface during the CV scan. Figure 47a shows the corresponding low-frequency range impedance in 0.1 M KOH of the Nb:$SrTiO_3$/$LaAlO_3$/catalyst stacks. $LaAlO_3$ layer thicknesses of the displayed samples can be obtained from the legend. The onset of the large semi-circle representing the thin film/ electrolyte interface is seen. $La_{0.6}Ca_{0.4}FeO_{3-\delta}$ shows a smaller semi-circle (inset of the graph) in the low frequency range compared to the other

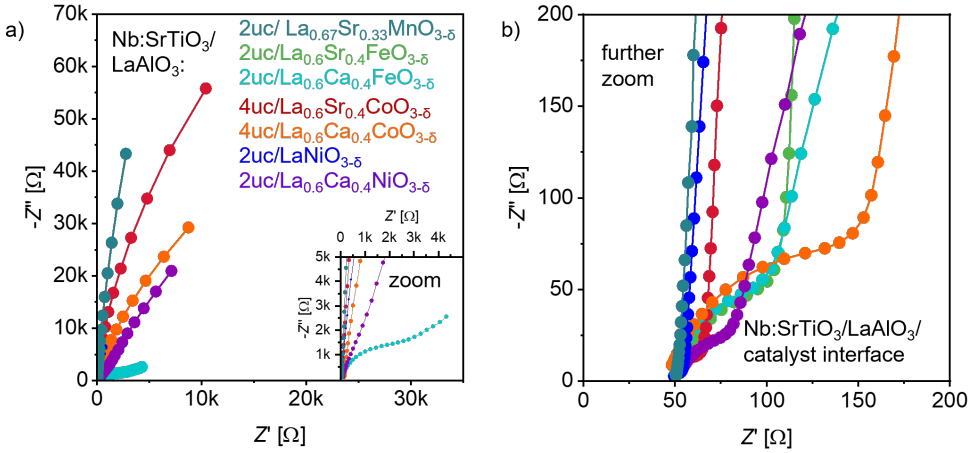

Figure 47: Impedance spectroscopy at OCP of the seven perovskite stacks on Nb:$SrTiO_3$/$LaAlO_3$ stacks in 0.1 M KOH. The uc numbers in the legend represent the $LaAlO_3$ interlayer thickness. a) Shows low-frequency range with the initial part of the large semi-circle of the thin film/electrolyte interface; inset shows the zoom to the $La_{0.6}Ca_{0.4}FeO_{3-\delta}$ impedance. b) Zoom to the high-frequency region, showing the area of the R_u and contact resistance at the Nb:$SrTiO_3$/$LaAlO_3$/catalyst interface. The legend from a) applies also to b).

perovskites. This may be due to the extended charge inversion region of $La_{0.6}Ca_{0.4}FeO_{3-\delta}$ in the OCP regime as determined in the MS analysis (section 5.7). This may facilitate the reduction reaction taking place around OCP, evident in the CV scans in the pre-OER regime shown in figure F.1 of the appendix. As the OCP impedance of $La_{0.6}Ca_{0.4}FeO_{3-\delta}$ on insulating $SrTiO_3$ was distorted due to the high resistivity (section 5.2), this semi-circle and redox behavior could only be revealed in the Nb:$SrTiO_3$/$LaAlO_3$/$La_{0.6}Ca_{0.4}FeO_{3-\delta}$ contacting geometry.
In figure 47b the impedance spectroscopy is zoomed to the high-frequency region. The R_u is small (ca. 40-60 Ω) for all perovskite oxides indicating no significant ohmic losses through bulk resistances are present, which is consistent with the observation of the impedance in the hexacyanoferrate(II)/(III) containing electrolyte. $La_{0.67}Sr_{0.33}MnO_{3-\delta}$ shows no additional semi-circle in the high-frequency range. Nb:$SrTiO_3$/2 uc $LaAlO_3$/$LaNiO_{3-\delta}$ and Nb:$SrTiO_3$/4 uc $LaAlO_3$/$La_{0.6}Sr_{0.4}CoO_{3-\delta}$ stacks exhibit very small contact resistances at the Nb:$SrTiO_3$/$LaAlO_3$/catalyst interface with 8 Ω and 21 Ω, respectively. Nb:$SrTiO_3$/2 uc $LaAlO_3$/$La_{0.6}Ca_{0.4}NiO_{3-\delta}$ shows a bit larger $R_{sub./film}$ of 30 Ω. The two ferates, $La_{0.6}Sr_{0.4}FeO_{3-\delta}$ and $La_{0.6}Ca_{0.4}FeO_{3-\delta}$, show with a 2 uc thick $LaAlO_3$ interlayer a contact resistance of 52 Ω and 61 Ω, respectively. For $La_{0.6}Ca_{0.4}CoO_{3-\delta}$, even a 4 uc thick $LaAlO_3$ interlayer results in a larger contact resistance of 109 Ω. Importantly, as mentioned beforehand, the final values of the substrate/$LaAlO_3$/thin film contact resistance was not always the same and could scatter for different unit cells thicknesses. Overall, however, the R_u and the contact resistances to the substrate show significantly lower absolute values than initially observed on the insulating substrates with Pt side contacts and $LaAlO_3$ free thin film stacks on Nb:$SrTiO_3$, indicating a successful decrease of the OER-performance limiting resistances in the lower current density ranges.

In figure 48a, the CV scans of the seven perovskite Nb:$SrTiO_3$/$LaAlO_3$/thin film stacks are shown up to 1 mA cm^{-2}. At 0.1 mA cm^{-2}, the cobaltates, $La_{0.6}Sr_{0.4}CoO_{3-\delta}$ and $La_{0.6}Ca_{0.4}CoO_{3-\delta}$, the nickelates, $LaNiO_{3-\delta}$ and $La_{0.6}Ca_{0.4}NiO_{3-\delta}$, as well as $La_{0.6}Ca_{0.4}FeO_{3-\delta}$ show very similar catalytic activity. $La_{0.6}Sr_{0.4}FeO_{3-\delta}$ shows a slightly smaller intrinsic OER activity, whereas $La_{0.67}Sr_{0.33}MnO_{3-\delta}$ shows by far the lowest OER activity. Note, that the CV scans of the two ferrates show a crossing of the backward sweep with the forward sweep, leading to an anomalous hysteresis (Appendix F.2). Towards 1 mA cm^{-2}, the CV scans start to spread which might be attributed to the increasing influence of $R_{substr./film}$ or deviating Tafel slopes. The influence of the $R_{substr./film}$ interface resistance gets clearer in figure 48b, where the Tafel-like plots of the CV scans are shown, also in the higher current density range. The slopes significantly increase above 1 mA cm^{-2}. Even for $La_{0.6}Sr_{0.4}CoO_{3-\delta}$ and $La_{0.6}Ca_{0.4}CoO_{3-\delta}$, which are considered semi-metallic perovskites, the Tafel slopes increase significantly. This is because their substrate/$LaAlO_3$/film interface resistance $R_{substr./film}$ is 21 Ω and 109 Ω, respectively.
The Tafel slope plots (as first derivative of figure 48b) are illustrated in figure 48c and show now in this contacting geometry reasonable values below 120 mV dec^{-1} up to about 0.5 mA cm^{-2}

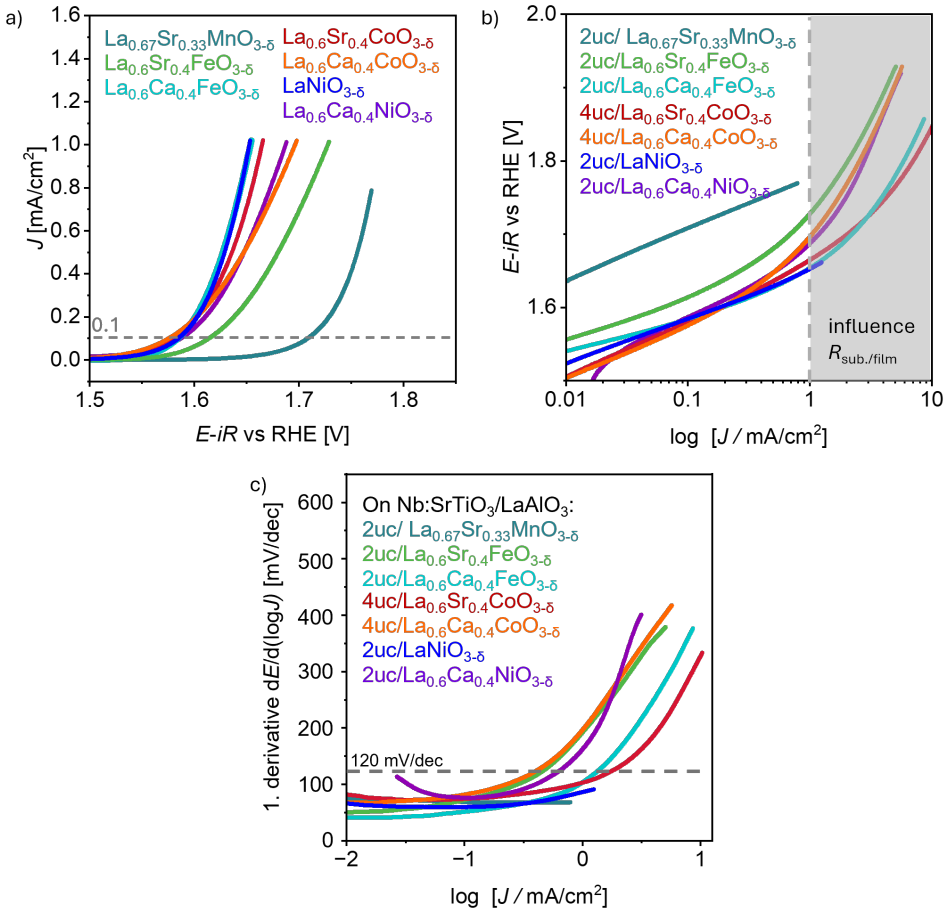

Figure 48: CV up to 1 mA cm^{-2} of the Nb:$SrTiO_3$/$LaAlO_3$/catalyst stacks with only back side contact. b) Corresponding Tafel-like plot shown also in the higher current density range where the $R_{sub./LAO/film}$ interface starts to dominate the slope of the CV curve, c) First derivative of the plots shown in b), which are the Tafel slope values as a function of the current density.

for all perovskites independent of their resistivity. On the insulating substrates with Pt side contacts, $La_{0.6}Ca_{0.4}FeO_{3-\delta}$ Tafel slope values exceeded 120 mV dec^{-1} already at 0.05 mA cm^{-2} (figure 40). However, for the Nb:$SrTiO_3$/$LaAlO_3$/catalyst stacks, the remaining interface resistance leads to extremely high Tafel slope values above 0.5 mA cm^{-2}. Therefore, this contacting geometry allows to determine η and Tafel slope values (b) in the lower current density range for also highly resistive perovskites but does not allow the determination of the

two parameters at higher current densities.
Interestingly, the ferrates with two and three orders of magnitude higher resistivity than the cobaltates and nickelates show similar high intrinsic OER activity. The low OER activity of the two ferrates obtained on the insulating substrates (Figure 39b) is hence dominated by the long electron transport pathway of up to 4 mm to the metallic side contacts as the COMSOL study showed. As a result, the intrinsic OER activity of the perovskite oxides does not scale monotonically with their electronic resistivity. In fact, even a high resistivity perovskite can exhibit high OER performance – a result that could not have been revealed without a dedicated and systematic choice of the sample substrate and interfacial layers.

To test the OER activity of epitaxial thin films with diverging resistivity, it is hence important to differentiate which contacting geometry can reveal the intrinsic catalytic properties. Table 15 lists the contacting geometries used to evaluate the intrinsic activity of each perovskite in dependence of their resistivity ρ. For perovskite thin films with a thickness of about 25 nm and low resistivity of $\rho < 5 \times 10^{-4}\,\Omega\,\text{cm}$, the $J_{\text{center}}/J_{\text{edge}}$ is greater than > 0.9, such as for the cobaltates, and $LaNiO_{3-\delta}$. Thus, the intrinsic OER activity can be determined on insulating substrates and in the smaller current density range on the $Nb:SrTiO_3/LaAlO_3$ stacks. For 25 nm thick thin films with a resistivity of about $1 \times 10^{-3}\,\Omega\,\text{cm}$ such as for $La_{0.6}Ca_{0.4}NiO_{3-\delta}$ and $La_{0.67}Sr_{0.33}MnO_{3-\delta}$, the $J_{\text{center}}/J_{\text{edge}}$ is around 0.7-0.6 at an average current density of $1\,\text{mA}\,\text{cm}^{-2}$. At this current density, the inhomogeneity of the current distribution (referring to $J_{\text{center}}/J_{\text{edge}}$) is still on a linear scale with those sample specifications, but might be too inhomogeneous to reveal the intrinsic catalytic activity. However, as the samples of $La_{0.6}Ca_{0.4}NiO_{3-\delta}$ and $La_{0.67}Sr_{0.33}MnO_{3-\delta}$ showed on the insulating substrates lower overpotentials than on the $Nb:SrTiO_3/LaAlO_3$ stacks in the low current density range of up to $1\,\text{mA}\,\text{cm}^{-2}$ (Appendix F.3 shows the comparison), the inhomogeniety is less relevant in this range. Therefore, it was considered here that perovskites with a resistivity in the range of $1 \times 10^{-3}\,\Omega\,\text{cm}$, intrinsic catalytic activity can be revealed on the

Table 15: $J_{\text{center}}/J_{\text{edge}}$ and considered sample geometries on insulating substrates with Pt side contact and $Nb:SrTiO_3/LaAlO_3$/catalyst stacks to determine the intrinsic catalytic activity of the seven perovskites. The side contacted samples of $La_{0.67}Sr_{0.33}MnO_{3-\delta}$ and $La_{0.6}Ca_{0.4}NiO_{3-\delta}$ is only considered in the low current density range, below $1\,\text{mA}\,\text{cm}^{-2}$.

perovskite	$J_{\text{center}}/J_{\text{edge}}$	side contact substrate, layer thickness	back side contact $LaAlO_3$/thin film thickness
$La_{0.67}Sr_{0.33}MnO_{3-\delta}$	0.6	$SrTiO_3$, 25 nm	2 uc/25 nm
$La_{0.6}Sr_{0.4}FeO_{3-\delta}$	0.04	not considered	2 and 3 uc/20 nm
$La_{0.6}Ca_{0.4}FeO_{3-\delta}$	2×10^{-8}	not considered	2 and 3 uc/20 nm
$La_{0.6}Sr_{0.4}CoO_{3-\delta}$	0.91	$NdGaO_3$ 20 nm	4 uc/20 nm
$La_{0.6}Ca_{0.4}CoO_{3-\delta}$	0.91	$LaAlO_3$ 20 nm	4 uc/20 nm
$LaNiO_{3-\delta}$	0.91	$SrTiO_3$, 10 nm	2 uc/10 nm
$La_{0.6}Ca_{0.4}NiO_{3-\delta}$	0.66	$SrTiO_3$, 20 nm	2 uc/20 nm

Nb:$SrTiO_3$/$LaAlO_3$ stacks, and on insulating substrates in the low current density range. The intrinsic OER activity cannot be revealed at higher current densities above 1 mA cm^{-2}. For $La_{0.6}Sr_{0.4}FeO_{3-\delta}$ and $La_{0.6}Ca_{0.4}FeO_{3-\delta}$, exhibiting a higher resistivity of $3.5 \times 10^{-2}\,\Omega$ cm and $5.7 \times 10^{-1}\,\Omega$ cm, $J_{\text{center}}/J_{\text{edge}}$ is only 0.04 and 2×10^{-8}. Therefore, their intrinsic catalytic activity can only be determined on Nb:$SrTiO_3$/$LaAlO_3$ stacks in the low current density range.
Based on the assessment, the average potential of two samples for each catalyst was calculated to compare the intrinsic catalytic activity of those seven perovskites in the low current density range at 0.05, 0.1, and 0.2 mA cm^{-2} shown in figure 49a. The considered Tafel-like plots are shown in the Appendix F.3.

This simplifies a direct comparison with the literature, where often perovskite oxide OER activity is given at small current densities of 0.05 mA cm^{-2} such as in the seminal paper of Suntivich *et al*. [13]. The OER potential at 0.1 mA cm^{-2} and 0.2 mA cm^{-2} (figure 49a) is surprisingly similar for $La_{0.6}Ca_{0.4}FeO_{3-\delta}$, $La_{0.6}Sr_{0.4}CoO_{3-\delta}$, $La_{0.6}Ca_{0.4}CoO_{3-\delta}$, and $LaNiO_{3-\delta}$, although different transition metal B-sites and even A-sites are present. While $La_{0.6}Ca_{0.4}NiO_{3-\delta}$ has a slightly lower OER potential in this current density range, the difference remains close to the experimental error. $La_{0.6}Sr_{0.4}FeO_{3-\delta}$ shows a slightly increased OER potential compared to the aforementioned perovskites. $La_{0.67}Sr_{0.33}MnO_{3-\delta}$, however, exhibits by far the highest OER overpotentials compared to all the other perovskites. At 0.05 mA cm^{-2}, $La_{0.6}Ca_{0.4}CoO_{3-\delta}$ ($\eta = 0.33$ V) and $La_{0.6}Ca_{0.4}NiO_{3-\delta}$ ($\eta = 0.32$ V) exhibit a slightly lower OER potential compared to $La_{0.6}Sr_{0.4}CoO_{3-\delta}$ and $La_{0.6}Ca_{0.4}FeO_{3-\delta}$ ($\eta = 0.34$ V).
The differences in the overpotential trends at different current densities can be explained by the Tafel slope values shown in figure 49b. The Tafel slope values are extracted from the Tafel slope plots at 0.1 mA cm^{-2} and vary in the range of 52 mV/dec to 80 mV/dec. $La_{0.6}Ca_{0.4}FeO_{3-\delta}$ exhibits the smallest Tafel slope with a value of 52 mV/dec, whereas $La_{0.6}Ca_{0.4}CoO_{3-\delta}$ exhibits the highest Tafel slope with a value of around 80 mV/dec. Therefore, the slight overpotential difference of these two perovskites observed at 0.05 mA cm^{-2} vanishes already at 0.1 mA cm^{-2}. The other Tafel slopes of $La_{0.67}Sr_{0.33}MnO_{3-\delta}$, $La_{0.6}Sr_{0.4}CoO_{3-\delta}$, $LaNiO_{3-\delta}$ and $La_{0.6}Ca_{0.4}NiO_{3-\delta}$ vary between 60-70 mV/dec. The larger error of the $La_{0.6}Ca_{0.4}NiO_{3-\delta}$ Tafel slope and overpotential might be related to the averaged result from the two different contacting geometries on the insulating substrate and Nb:$SrTiO_3$/$LaAlO_3$ stack. However, other phenomena might play a role here, which are discussed in section 5.10. Although the Tafel slope values lead to different overpotential trends at different current densities, one might speculate that the rate-determining step might still be similar for all seven perovskites in this current density range. A Tafel slope of 60 mV/dec can be attributed to the chemical step after the first electron transfer, which can be the deprotonation of the adsorbed species [48, 85]. However, as Tafel slope values can be similar for different rate-determining steps, a final conclusion is difficult to draw [47].
Summarizing, the highest overpotential was observed for $La_{0.67}Sr_{0.33}MnO_{3-\delta}$, which might be explained by the remaining charge transfer resistance at the $La_{0.67}Sr_{0.33}MnO_{3-\delta}$/electrolyte interface in the OER voltage regime, as observed by the MS-analysis and in the hexacyanoferrate

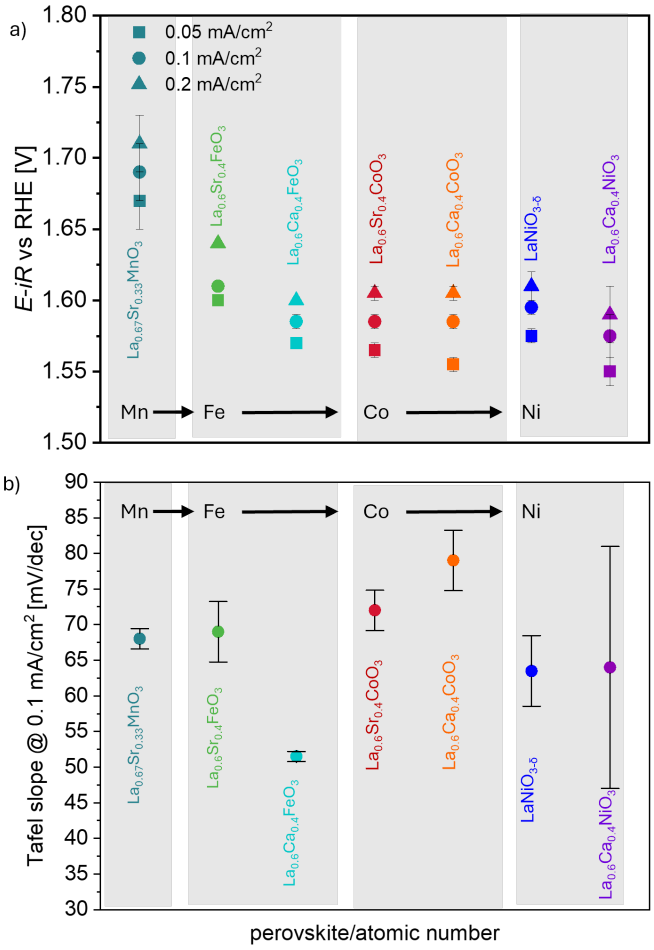

Figure 49: a) OER potential of the seven perovskites at 0.05, 0.1 and 0.2 mA cm^{-2} averaged from 2 samples for each perovskite. The values were taken from the geometries explained in table 15. The error bars stem from the average of those two samples. The CV scans of those can be viewed in the appendix F.3. b) Averaged Tafel slope values at 0.1 mA cm^{-2} of the same samples.

(II/III) redox couple impedance spectroscopy, and CV analysis. In contrast, the OER activity of the ferrates, cobaltates, and nickelates is significantly higher than that of $La_{0.67}Sr_{0.33}MnO_{3-\delta}$, and the OER activity does not differ drastically between them. This is remarkable as the valence band electronic structure is significantly influenced by the B-site substitution from Fe to

Co to Ni (section 4.4.3). A possible influence of the electronic structure on the observed OER activity trend will be further elaborated in section 6.

5.9 OER activity on platinized silicon

To determine whether the observed intrinsic catalytic activity trend is also representative in the high current density regime, $La_{0.6}Sr_{0.4}FeO_{3-\delta}$ $La_{0.6}Ca_{0.4}FeO_{3-\delta}$, $La_{0.6}Sr_{0.4}CoO_{3-\delta}$, and $La_{0.6}Ca_{0.4}CoO_{3-\delta}$ perovskites were deposited on platinized silicon. Higher current densities are closer to industrial conditions, allowing us to determine the power-to-mass ratio for the material sustainability evaluation. While the metallic contact might enable one to determine the overpotential also at high current densities, other factors such as the exposed crystal facet, defect chemistry and surface roughness might influence the OER activity trend, as the deposited layer is now grown as polycrystalline layer on Pt.

In figure 50a the OCP impedance spectra are shown for the perovskites deposited on Pt. The R_u is for all samples similar exhibiting only a value of around 50 Ω. In the low-frequency range, $La_{0.6}Ca_{0.4}FeO_{3-\delta}$ exhibits the smallest impedance, which is in line with the impedance of the thin films on single crystalline substrates. Figure 50b shows the Tafel-like plot of the CV scans. In the low current density range, the two cobaltates exhibit a slightly higher OER activity compared to the ferrates, while above 1 mA cm^{-2} $La_{0.6}Ca_{0.4}FeO_{3-\delta}$ shows very similar catalytic activity. $La_{0.6}Ca_{0.4}FeO_{3-\delta}$, $La_{0.6}Sr_{0.4}CoO_{3-\delta}$ and $La_{0.6}Ca_{0.4}CoO_{3-\delta}$ reach a similar high maximum current density of about 12 mA cm^{-2} at around 1.75 V vs RHE. $La_{0.6}Sr_{0.4}FeO_{3-\delta}$ shows a higher overpotential than the other perovskites, still reaching a maximum current density of 10 mA cm^{-2} at 1.82 V vs RHE.

Figure 50c shows the Tafel slope plots of the ferrates and cobaltates on Pt. The two cobaltates and $La_{0.6}Sr_{0.4}FeO_{3-\delta}$ exhibit similar high Tafel slopes up to 1 mA cm^{-2}, whereas $La_{0.6}Ca_{0.4}FeO_{3-\delta}$ shows the smallest Tafel slopes in this range. This was also the case for the catalysts deposited on single-crystalline substrates. Above 1 mA cm^{-2} the Tafel slopes of the two ferrates start to increase while the ones from the cobaltates remain rather stable. The Tafel slopes of the ferrates reach a bit higher value than 120 mV dec^{-1}, indicating that the rate-determining step might change with the current density. However, compared to the Tafel slope values on the insulating substrates or on the Nb:$SrTiO_3$/$LaAlO_3$/catalyst stacks (figure 48), they are in a reasonable range. Possibly, the 20 nm thick perovskite layer of the resistive ferrates might still increase the OER potential at higher current densities.

Figure 50d shows the OER potential extracted at 1, 5 and 10 mA cm^{-2}. The error bars of $La_{0.6}Sr_{0.4}CoO_{3-\delta}$ and $La_{0.6}Ca_{0.4}FeO_{3-\delta}$ represent the standard deviation of three different samples. The two cobaltates show similar OER potentials at all current densities. $La_{0.6}Ca_{0.4}FeO_{3-\delta}$ OER activity is similar at 1 mA cm^{-2} and starts to deviate slightly more at 5 and 10 mA cm^{-2}. However, the deviations are located within the error of the OER potentials of $La_{0.6}Sr_{0.4}CoO_{3-\delta}$, where the sample-to-sample variation of three $La_{0.6}Sr_{0.4}CoO_{3-\delta}$ thin films on Pt was ±20 mV at 1 mA cm^{-2} and that of $La_{0.6}Ca_{0.4}FeO_{3-\delta}$ only ±10 mV. Possibly, the effects of crystal facet

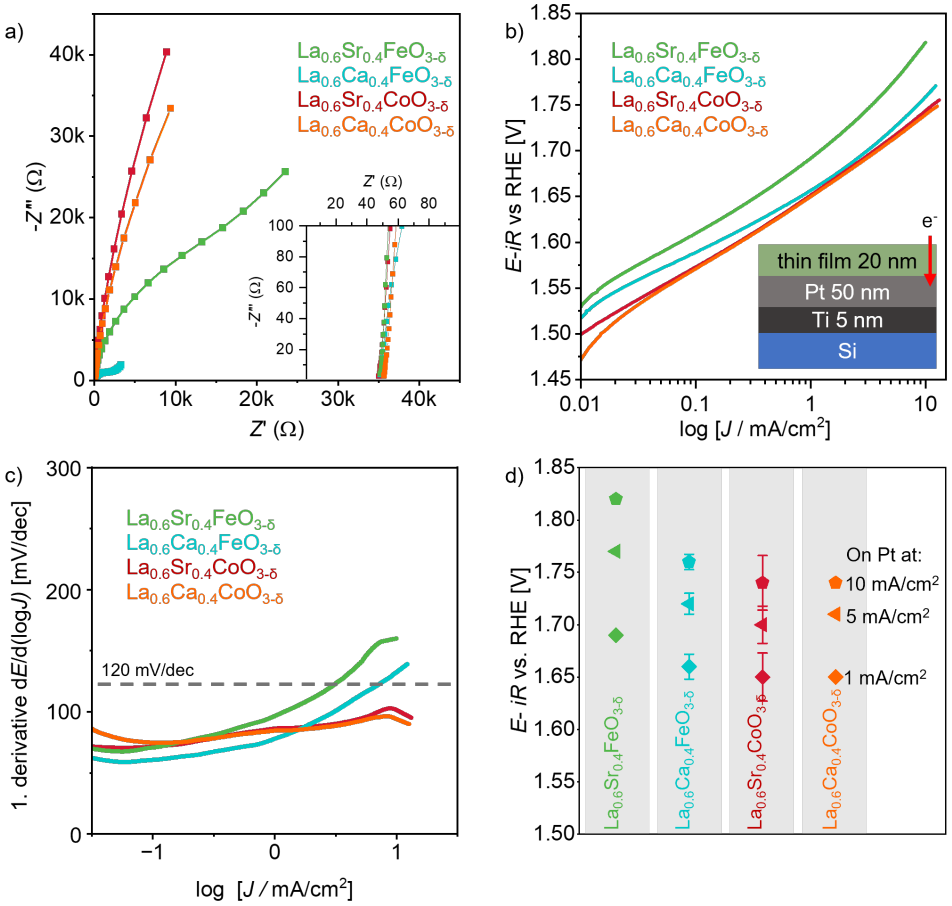

Figure 50: a) OCP impedance of 20 nm thick $La_{0.6}Sr_{0.4}FeO_{3-\delta}$, $La_{0.6}Ca_{0.4}FeO_{3-\delta}$, $La_{0.6}Sr_{0.4}CoO_{3-\delta}$, $La_{0.6}Ca_{0.4}CoO_{3-\delta}$ thin films on Si/Ti 5 nm/Pt 50 nm stacks. b) Tafel-like plots of the thin films. c) Tafel slope plots of the catalysts on Pt. d) OER potenitals of the four perovskites on Pt at 1, 5, and 10 mA cm^{-2}.

and grain boundaries more significantly influence the OER activity for $La_{0.6}Sr_{0.4}CoO_{3-\delta}$ than for $La_{0.6}Ca_{0.4}FeO_{3-\delta}$ grown on Pt. In summary, the OER activity of the ferrates and cobaltates is also comparable at higher current densities, which could be revealed by the use of the Pt contact layer. This was not possible to adress with the thin films grown on the single crystal

substrates. A CV comparison of the thin films on single crystalline substrates and Pt is shown in the appendix figure F.4.

5.10 Intrinsic OER activity comparison to the literature

To obtain, whether the observed intrinsic activity trend of the perovskites is also reflected in previous literature studies on perovskite powders and thin films, we compare literature values in this section. We discuss if possible differences may be influenced by the resistivities of the catalysts and how powder catalyst experiments may diverge from thin film experiments due to the experimental additives and procedure. The OER potential results on the single crystal substrates from figure 49 are compared to the literature values in table 16.

A similar OER activity trend, identifying $La_{0.67}Sr_{0.33}MnO_{3-\delta}$ as least active, and Co-, Ni-, Fe-based perosvkites as similar active was also observed for comparable perovskite compositions by Suntivich *et al*. in RDE electrolysis with powder catalysts (particle size of 0.2-1.0 µm), added conductive carbon and Nafion [13]. The authors compared $La_{0.5}Ca_{0.5}CoO_{3-\delta}$, $LaNiO_{3-\delta}$, $La_{0.75}Ca_{0.25}FeO_{3-\delta}$, $La_{0.5}Ca_{0.5}FeO_{3-\delta}$ and $La_{0.5}Ca_{0.5}MnO_{3-\delta}$ at 50 µA cm^{-2}. In the study of Suntivich *et al*., a lower activity was observed also for the manganate $La_{0.5}Ca_{0.5}MnO_{3-\delta}$ compared to $LaNiO_{3-\delta}$ and the calcium doped ferrates: η ($LaNiO_{3-\delta}$) $\approx$ η ($La_{0.5}Ca_{0.5}FeO_{3-\delta}$) $\approx$ η ($La_{0.5}Ca_{0.5}CoO_{3-\delta}$) $<$ η ($La_{0.5}Ca_{0.5}MnO_{3-\delta}$).

In contrast, another report in the literature by Sankannavar *et al*. observed that especially $La_{0.6}Ca_{0.4}FeO_{3-\delta}$ in the solid solution series of $La_{1-x}Ca_xFeO_{3-\delta}$ has a low catalytic activity [166] with an overpotential (at 50 µA cm^{-2}) comparable to what we observed for $La_{0.6}Ca_{0.4}FeO_{3-\delta}$ on the insulating substrate with a long bulk electron transport pathway. One reason for the higher overpotentials observed (compared to our Nb:$SrTiO_3$/$LaAlO_3$/$La_{0.6}Ca_{0.4}FeO_{3-\delta}$ sample and to the findings of Suntivich *et al*.) could be a larger particle size in the catalyst powder of the highly resistive $La_{0.6}Ca_{0.4}FeO_{3-\delta}$. The particle size is not reported in the study, so this hypothesis can not be verified. The larger particle size could extend the electron transport pathway through the powder bulk significantly even with conductive carbon, so that larger current losses occur. Additionally, conductive carbon can, for example, change the valence state of the B-site or can act as a co-catalyst [191–193], hindering the revelation of intrinsic catalytic properties as well. Different catalyst binders and their loadings may have an influence as well [194, 195].

Shen *et al*. observed that Sr doping in a solid solution series of $La_{1-x}Sr_xFeO_{3-\delta}$ improves OER activity significantly. $La_{0.67}Sr_{0.33}FeO_{3-\delta}$ (La:Sr 0.67:0.33) exhibits slightly lower OER activity compared to $LaNiO_{3-\delta}$, and $La_{0.33}Sr_{0.67}FeO_{3-\delta}$ (La:Sr 0.33:0.67) exhibits even similar high OER activity as $LaNiO_{3-\delta}$ at 0.05 mA cm^{-2}. This trend agrees with our observation that $La_{0.6}Sr_{0.4}FeO_{3-\delta}$ is only slightly less active compared to $LaNiO_{3-\delta}$ (by 20 mV at 0.05 mA cm^{-2}). Shen *et al*. do not add any conductive carbon to the $La_{1-x}Sr_xFeO_{3-\delta}$ powder catalysts but only focus on the OER activity trend of up to 0.3 mA cm^{-2}. In contrast, an older study from Matsumoto *et al*. compares $La_{0.6}Sr_{0.4}FeO_{3-\delta}$ and $La_{0.6}Sr_{0.4}CoO_{3-\delta}$ powder catalysts without carbon additives at high current densities of 60 mA cm^{-2}. In this range, $La_{0.6}Sr_{0.4}FeO_{3-\delta}$ shows 150 mV

Table 16: OER activity comparison of the epitaxial thin film results with the literature at 0.05 mA cm^{-2} if not noted differently.

comparison this work and literature	OER potential at 0.05 mA cm^{-2} [V] vs RHE
$La_{0.67}Sr_{0.33}MnO_{3-\delta}$	1.67
$La_{0.6}Sr_{0.4}FeO_{3-\delta}$	1.6
side contact	1.61
$La_{0.6}Ca_{0.4}FeO_{3-\delta}$ back contact	1.57
$La_{0.6}Ca_{0.4}FeO_{3-\delta}$ side contact	1.70
$La_{0.6}Sr_{0.4}CoO_{3-\delta}$	1.57
$La_{0.6}Ca_{0.4}CoO_{3-\delta}$	1.56
$LaNiO_{3-\delta}$	1.58
$La_{0.6}Ca_{0.4}NiO_{3-\delta}$	1.55
Suntivich *et al*. powder, Nafion, carbon, 0.1 M KOH [13]	
$La_{0.5}Ca_{0.5}MnO_3$	1.60
$La_{0.25}Ca_{0.25}FeO_3$	1.59
$La_{0.5}Ca_{0.5}FeO_3$	1.54
$LaNiO_{3-\delta}$ (Suntivich)	1.55
$La_{0.5}Ca_{0.5}CoO_3$	1.53
Sankannavar *et al*. powder, Nafion, carbon, 0.5 M NaOH [166]	
$La_{0.6}Ca_{0.4}FeO_{3-\delta}$	1.67
Shen *et al*. powder, Nafion, 1 M KOH [35]	
$La_{0.67}Sr_{0.33}FeO_3$	1.59
$La_{0.33}Sr_{0.67}FeO_3$	1.56
$LaNiO_{3-\delta}$ Shen et al	1.56
Matsumoto *et al*. powder 1 M KOH at 60 mA cm^{-2}	
$La_{0.4}Sr_{0.6}FeO_3$	1.92
$La_{0.6}Sr_{0.4}CoO_{3-\delta}$	1.76
Liu *et al*. thin film 0.1 M KOH [69]	
$LaNiO_{3-\delta}$	1.59
$La_{0.25}Sr_{0.25}NiO_3$	1.56
$La_{0.5}Sr_{0.5}NiO_3$	1.52

higher overpotential compared to $La_{0.6}Sr_{0.4}CoO_{3-\delta}$. Intrinsically, we only observe a difference of 30 mV at 0.05 mA cm^{-2}.The discrepancy might be related to the different activities at different current densities, however, a lower conductivity might be the relevant factor. As these results from Matsumoto *et al*. are also used for OER activity trend description in more recent literature [196], there might be a bias that $La_{0.6}Sr_{0.4}FeO_{3-\delta}$ is intrinsically and *per se* a lot less active than $La_{0.6}Sr_{0.4}CoO_{3-\delta}$, in stark contrast to the results on intrinsic activity in this thesis.
Liu *et al*. see that Sr doping in a $La_{1-x}Sr_xNiO_{3-\delta}$ series increases the OER activity significantly

while the resistivity increases. From $LaNiO_{3-\delta}$ to $La_{0.5}Sr_{0.5}NiO_{3-\delta}$ they observe a decrease of about 70 mV in OER overpotential while the resistivity triples [69]. Such a strong increase in activity was not observed in this work from $LaNiO_{3-\delta}$ to $La_{0.6}Ca_{0.4}NiO_{3-\delta}$, where the two averaged values show only a decrease of 30 mV (at 0.05 mA cm^{-2}) with 40 % Ca doping on the A-site, and the conductivity changes by one order of magnitude. The larger standard deviation of the two measured $La_{0.6}Ca_{0.4}NiO_{3-\delta}$ samples might also be related to chemical phase changes on the $La_{0.6}Ca_{0.4}NiO_{3-\delta}$ surface. As described in the thin film characterization section 4.3, $La_{0.6}Ca_{0.4}NiO_{3-\delta}$ surface morphology is less stable upon air exposure, indicating that the surface undergoes possibly also chemical changes in air. E.g. Baeumer *et al*. reported that carbonate species form on the $LaNiO_{3-\delta}$ surface over time decreasing the OER activity [197]. Such deactivation might also occur for the $La_{0.6}Ca_{0.4}NiO_{3-\delta}$ samples leading to a higher variability.
Comparing the $LaNiO_{3-\delta}$ absolute OER potentials vs RHE from the literature in table 16, the activity for the (100) oriented thin films of Liu *et al*. are similar to the one in this work whereas the powder $LaNiO_{3-\delta}$ of Suntivich *et al*. and Shen *et al*. show a slightly higher OER activity. This might be, for example, because $LaNiO_{3-\delta}$ (111) crystal facets, which are catalytically more active than (100) facets [20], may contribute to the activity in powder catalysts. Moreover, different iron incorporation scenarios into the $LaNiO_{3-\delta}$ surface might lead to a discrepancy in absolute values from study to study [76, 198, 199]. Also, variable electrochemically active surface areas, defect sites, edges and kinks might lead to those differences between thin films and powder catalysts. This exemplary discrepancy of absolute OER potential comparison hints that an observed OER trend within one research group is more reliable than a comparison of absolute values in the literature.

Our findings and the comparison to the literature indicate that the establishment of catalyst design rules must be taken with care, especially when materials across large resistivity ranges are tested and/or substrate-to-catalyst contact resistances occur. Therefore, it is crucial not to assume a direct correlation between low conductivity and low OER catalytic activity, which has become obvious from our revelation that metal oxides with low conductivity can exhibit high catalytic activity. Extra steps have to be taken to disentangle intrinsic catalytic activity from conductivity to accurately assess performance. As we have shown, this can be achieved using epitaxial model systems with appropriate current collectors and favorable interface properties. As the OER overpotential trend could be revealed for the seven perovskites, the following chapter investigates which *ex-situ* electronic structure OER descriptors might correlate with the intrinsic OER activity.

6 Electronic structure OER descriptors of the perovskite oxides

In the literature, electronic structure OER descriptors are heavily discussed as they may give rise to catalyst design rules that can support the prediction of highly efficient catalysts. Based on the fact that we could reveal the intrinsic catalytic properties of the perovskites, the electronic structure OER descriptors can now be correlated to the intrinsic activity. Here, we will compare the e_g electron filling, the energy distance of the O 2*p* and TM 3*d* states (ΔTM 3*d*-O 2*p*), the O 2*p* band center, and the charge transfer energy in the valence band (as determined in section 4.4.3) as possible OER descriptors using the intrinsic OER activity parameters determined in section 5.8. The basics and literature background about those are detailed in section 2.3.2.

6.1 e_g filling and OER activity

The e_g states directly overlap with the states of the OH^- adsorbates and form a σ-bond, hence, their reactivity plays a crucial role in the OER. Suntivich *et al*. found that the e_g electron filling close to unity results in the most active perovskite oxide catalysts for the OER. Higher or lower e_g filling leads to lower OER catalytic activity, forming a volcano-shaped OER activity trend with e_g electron filling on the x-axis [13]. A more detailed description can be found in section 2.3.2. To determine if the OER-potential trend correlates with the e_g filling volcano trend of Suntivich *et al*., we calculated the e_g filling based on their study. We assumed that the e_g filling nominally changes when the A-site doping deviates from that of Suntivich *et al*., and that the spin configuration does not change, so we take the spin configuration from figure 5a and b. For example, $La_{0.5}Ca_{0.5}FeO_{3-\delta}$ has an e_g filling of 1.5 determined by Suntivich *et al*., so $La_{0.6}Ca_{0.4}FeO_{3-\delta}$ in this thesis has an e_g filling of 1.6. Note, that Suntivich *et al*. consider for the highly doped cobaltate $La_{0.5}Ca_{0.5}CoO_{3-\delta}$ a high spin configuration, which deviates from the intermediate spin configuration of $LaCoO_{3-\delta}$ in their study. Hence, $La_{0.5}Ca_{0.5}CoO_{3-\delta}$ exhibits an e_g filling of 1.5, and therefore our $La_{0.6}Ca_{0.4}CoO_{3-\delta}$ and $La_{0.6}Sr_{0.4}CoO_{3-\delta}$ are considered with an according e_g filling of 1.6.

The e_g filling is plotted against the OER potential in figure 51 for our single-crystalline samples in comparison to Suntivich *et al*. The OER potential only roughly follows a volcano-shaped trend. The doped ferrates and cobaltates are located on the right side of the volcano plot. However, $La_{0.5}Ca_{0.5}CoO_{3-\delta}$ of Suntivich *et al*. has a similar e_g filling as the $La_{0.6}Sr_{0.4}FeO_{3-\delta}$ of this thesis, but still the OER activity varies significantly. The nickelates and manganates are located on the left side. Here, the two manganates exhibit the smallest e_g filling and the highest overpotential. However, their activity values differ significantly, although the e_g filling is similar. Possibly, the $La_{0.67}Sr_{0.33}MnO_{3-\delta}$/electrolyte interface space charge barrier toward the OER voltage regime increases the overpotential, and has to be considered as an additional factor.

As mentioned above in section 5.10, the $LaNiO_{3-\delta}$ OER activity differences between our and Suntivich *et al*. can result from several reasons, as the authors used powder catalysts and we used epitaxial thin films. $La_{0.6}Ca_{0.4}NiO_{3-\delta}$ should nominally have a smaller e_g filling than

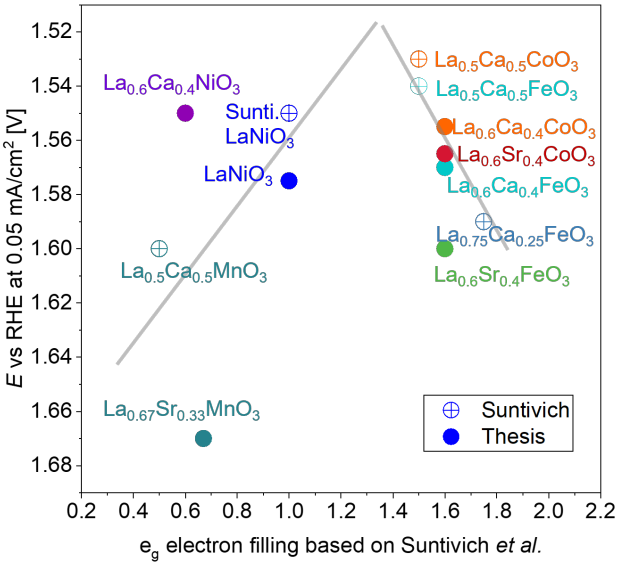

Figure 51: OER potential at 50 µA cm^{-2} in correlation to the e_g filling from Suntivich *et al*. and this thesis.

$LaNiO_{3-\delta}$. Hence, $La_{0.6}Ca_{0.4}NiO_{3-\delta}$ should exhibit lower OER activity. However, the opposite is observed here. Suntivich *et al*. argue that an increased TM-O covalency increases OER performance when the e_g filling is around unity. Sr-doping in the $(La,Sr)NiO_{3-\delta}$ solid solution series increases the higher Ni-O covalency, and also increases OER activity [69]. This might suggest that not only the e_g electron filling can explain the OER activity trend, but other descriptors also need to be considered. The volcano plot suggests that an e_g filling around unity is favorable for the OER, however, the explained discrepancies show that predicting OER activity based on the e_g filling is limited.

6.2 ΔTM 3*d*-O 2*p*, O 2*p* band center and charge transfer energy in the OER

It is known that additional factors aside from e_g filling might play a crucial role for the OER activity, such as the energetic distance between TM 3*d* and O 2*p* states (ΔTM 3*d*-O 2*p*), O 2*p* band center, and charge transfer energy. Figure 52 shows the OER potential at 0.05 mA cm^{-2} and 0.1 mA cm^{-2} in correlation to the ΔTM 3*d*-O 2*p*, O 2*p* band center and charge transfer energy, that were determined from the valence band spectroscopy in section 4.4.3. Those two current densities were chosen for comparison because they are not significantly influenced by interface resistances, and they are directly comparable to several literature studies [13, 35, 52, 69]. Furthermore, as elaborated from the discussion on figure 49, the trend slightly changes from

0.05 mA cm^{-2} to 0.1 mA cm^{-2} due to diverging Tafel slopes of the different catalysts. Therefore, it is important to determine possible OER descriptors in dependence on the two varying OER activity trends.
Figure 52a and b shows the energetic distance **ΔTM 3*d*-O 2*p*** in correlation to the OER potential. Note that the potential scale is flipped here. At both current densities, an increasing ΔTM 3*d*-O 2*p* does not strongly correlate with the OER activity. At 0.05 mA cm^{-2}, a decreasing ΔTM 3*d*-O 2*p* tends to increase the OER potential; however, this trend is close to the error range and scatters. At 0.1 mA cm^{-2}, this slight scaling is not observed anymore; although ΔTM 3*d*-O 2*p* increases, the OER activity is not significantly affected. The $La_{0.67}Sr_{0.33}MnO_{3-\delta}$ covalency is not included here, as the t_{2g} and e_g states have a larger crystal field splitting, challenging the determination of ΔTM 3*d*-O 2*p* (for more details see appendix figure A.2). Possibly, the ΔTM 3*d*-O 2*p* does not play a significant role here or is sufficiently high in these perovskite compositions, and does not lead to significant OER activity differences.

As second OER descriptor, the **O 2*p* band center** is correlated to the OER potential of the seven perovskites in figure 52c and d. At 0.05 mA cm^{-2}, the OER potential and O 2*p* band center form a volcano shape trend. The cobaltates and nickelates are located on the left side of the volcano plot, while the ferrates and the manganate are located on the right side. The volcano-shaped trend suggests that the O 2*p* band center indeed has an influence on the OER activity, especially visible at small current densities where thermodynamic trends of the catalysts may be less influenced by kinetic rate constants. The volcano trend suggests that the O 2*p* band center relates to the oxygen-adsorbate binding strength, following the Sabatier principle [41] where neither too strong nor too weak binding of oxygen based adsorbates leads to the highest OER activity. With increasing O 2*p* band center from 3.6 eV to 4.5 eV the adsorbate binding strength might transit from weaker to stronger binding of the oxygen species, leading to a fairly similar OER activity across this energetic O 2*p* band center range. This trend dilutes only a little at the higher current density of 0.1 mA cm^{-2} as seen in figure 52d. The O 2*p* band center difference between 3.6 eV and 4.5 eV still correlates with the OER potential.

As third OER descriptor, the **charge transfer energy** is correlated to the OER potentials in figure 52e and f. At both current densities, the plots show a scattering of the data and no clear trend. From $La_{0.6}Sr_{0.4}CoO_{3-\delta}$ to $La_{0.6}Sr_{0.4}FeO_{3-\delta}$ the charge transfer energy differs by 2 eV (from 1.9 eV to 3.9 eV). Between these two perovskites the OER potential only differs by 30 mV and 20 mV at 0.05 mA cm^{-2} and 0.1 mA cm^{-2}. Moreover, $La_{0.67}Sr_{0.33}MnO_{3-\delta}$ has a similar high charge transfer energy as $La_{0.6}Sr_{0.4}FeO_{3-\delta}$ and has a 70 mV higher OER potential at 0.05 mA cm^{-2}. The high charge transfer energy of the semiconducting $La_{0.6}Sr_{0.4}FeO_{3-\delta}$ stems here from the band gap of 1 eV, while for $La_{0.67}Sr_{0.33}MnO_{3-\delta}$ the O 2*p* state is further away from the Fermi level (see also in section 4.4.3). Thus, the charge transfer energy does not show a clear trend for the OER activity for the perovskites investigated in this thesis, while the O 2*p* band center does show a volcano trend.

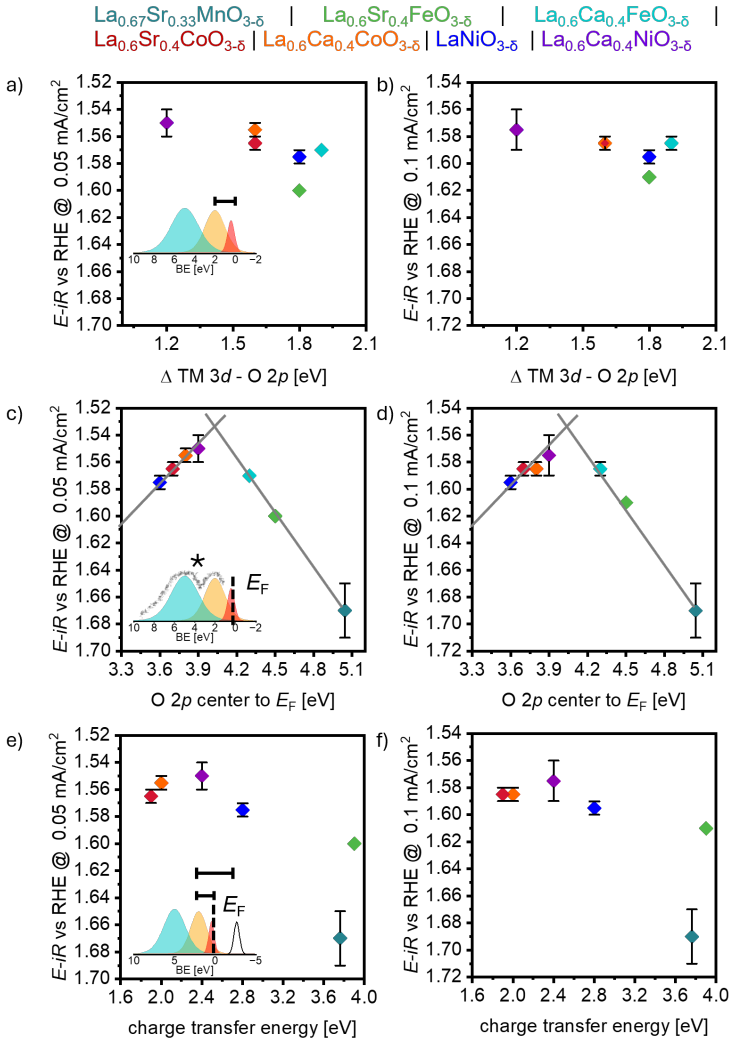

Figure 52: OER potential at 0.05 mA cm^{-2} and 0.1 mA cm^{-2} correlated with a) ΔTM 3*d*-O 2*p*, b) O 2*p* band center as the centroid of the two O 2*p* states, and c) charge transfer energy. The sketches illustrate the quantified parameters from table 11 and figure 48.

6.3 Discussion on OER activity trend and OER descriptors

The here investigated perovskite oxides vary vastly in their electrical conductivity and electronic valence band structure. These two factors can significantly influence the observed catalytic activity. As we designed epitaxial thin film stacks, that enabled us to reveal intrinsic properties independent of the conductivity; the intrinsic catalytic properties could be directly correlated to the electronic valence band structure.

Astonishingly, the OER intrinsic activity was comparably high for the ferrates, cobaltates, and nickelates, spanning a three-order of magnitude resistivity range. Only $La_{0.67}Sr_{0.33}MnO_{3-\delta}$ showed strongly decreased OER activity compared to the others. At 0.05 mA cm^{-2} the trend is that $La_{0.6}Sr_{0.4}FeO_{3-\delta}$ shows slightly lower OER activity than $La_{0.6}Ca_{0.4}FeO_{3-\delta}$, $La_{0.6}Sr_{0.4}CoO_{3-\delta}$, $La_{0.6}Ca_{0.4}CoO_{3-\delta}$ and $LaNiO_{3-\delta}$ whereas $La_{0.6}Ca_{0.4}NiO_{3-\delta}$ shows a slightly higher activity than those. To assess the origin of the observed OER activity trend, we investigated possible space charge barriers at the catalyst/electrolyte interface and the electronic structure, including its e_g electron filling, ΔTM 3*d*-O 2*p*, O 2*p* band center, and charge transfer energy.

The e_g electron filling roughly correlated with the observed OER activity trend, agreeing with Suntivich *et al*. that a filling close to unity increases OER activity. However, certain discrepancies remained. For example, $La_{0.6}Ca_{0.4}NiO_{3-\delta}$ should nominally have an e_g filling of 0.6 which is similar to $La_{0.67}Sr_{0.33}MnO_{3-\delta}$, but their catalytic activity varies drastically. In this case, other descriptors such as the covalency in $La_{0.6}Ca_{0.4}NiO_{3-\delta}$ may play a more crucial role. Furthermore, addressing the true spin state of those mixed valence perovskites is challenging and directly affects the final e_g band filling.

$La_{0.67}Sr_{0.33}MnO_{3-\delta}$, which had by far the lowest OER activity, exhibits in the close-to-OER voltage regime an inversely charged (electron accumulation) space charge barrier at the $La_{0.67}Sr_{0.33}MnO_{3-\delta}$/electrolyte interface, which might increase the overpotential to drive the OER as the incoming electrons need to overcome this barrier. Furthermore, its e_g filling is nominally small, and the quantified charge transfer energy and O 2*p* band center are the smallest among all investigated perovskites here. Hence, the low OER activity of $La_{0.67}Sr_{0.33}MnO_{3-\delta}$ might be the sum of those listed parameters. While the ferrates, cobaltates and nickelates do not show an inversely charged catalyst/electrolyte space charge barrier in the close-to-the-OER voltage regime, the valence band electronic structure shows large differences in the spectral shape as well as in the quantified parameters of the charge transfer energy and O 2*p* band center.

Interestingly, the only correlation between an electronic structure parameter and OER activity was seen for the O 2*p* band center at 0.05 mA cm^{-2} and 0.1 mA cm^{-2}. The trend exhibits a volcano-shape that typically originates from the Sabatier principle. This could hint that for the single B-site perovskites, an O 2*p* band center between 3.6 eV and 4.3 eV is at the peak for the lowest OER potentials. When OH^- binds/adsorbs at the dangling bond of a surface transition metal, its energy might align to the O 2*p* states of the nominally MO_6 octahedra. Hence, the adsorbed oxygen species would align to the O 2*p* bands of the perovskite which influences how strongly or weakly the oxygen species is bound to the catalyst surface, leading to the volcano

trend.

As introduced in section 2.3.2, another study also reports a volcano trend for the O 2*p* band center in the case of double perovskites [83]. The authors observe that a smaller O 2*p* band center is beneficial up to the point where it is so close to the Fermi level that the catalyst amorphizes rapidly, decreasing the OER performance and leading to the volcano trend. Since structural transformations were not the focus of this study, such trends would need to be further investigated.

In contrast, Hong *et al*. suggest that the charge transfer energy is a more suitable and advanced OER descriptor compared to the O 2*p* band center, especially for semiconductors. In study of Hong *et al*., the OER activity correlates well with the charge transfer energy from semi-metals to charge transfer insulators, but not well with the O 2*p* band center of semiconductors and insulators. Such a discrepancy between Hong *et al*. and this thesis might stem from the choice of the perovskites. Hong *et al*. include undoped perovskites $LaMO_3$ with M = Cr, Mn, Fe, Co and Ni, and only A-site doped (and double) cobaltates. In contrast, we compare an A-site doped and B-site varied manganate, ferrate, cobaltate, and nickelate ($La_{0.67}Sr_{0.33}MnO_{3-\delta}$, $La_{0.6}Sr_{0.4}FeO_{3-\delta}$ $La_{0.6}Sr_{0.4}CoO_{3-\delta}$, $La_{0.6}Ca_{0.4}CoO_{3-\delta}$, and $La_{0.6}Ca_{0.4}NiO_{3-\delta}$). The charge transfer energy might play a bigger role for the undoped perovskites with a larger band gap, which were included in the study by Hong *et al*. For example, $LaFeO_3$ (Hong *et al*.) has a wide band gap of 2.2 eV and $La_{0.6}Sr_{0.4}FeO_{3-\delta}$ only 1 eV (this thesis) which may affect the charge transfer energy more than the O 2*p* band center. Furthermore, additional factors, such as a smaller ΔTM 3*d*-O 2*p* as a indicator for higher TM-O covalency in $La_{0.6}Sr_{0.4}FeO_{3-\delta}$ can positively influence the OER activity, as shown by ref. [35]. Moreover, Hong *et al*. use perovskite powder catalysts with conductive carbon. Hence, the influence of the catalyst conductivity and the influence of the conductive carbon itself, especially for the semiconducting perovskites, is not systematically decoupled, which could play an additional role for the observed discrepancies in their and our study.

Summarizing, the ferrates, cobaltates and nickelates, that vary vastly in the conductivity and spectral shape of the valence band, show similar catalytic activity where the O 2*p* band center might hint at a volcano shape trend at low current densities. However, a single factor might not lead to a full conclusion of observed activity trends as e.g. $La_{0.67}Sr_{0.33}MnO_{3-\delta}$ has a larger O 2*p* band center and additionally an inversely charged space charge barrier close-to-the-OER voltage regime where both parameters need to be considered for the OER activity.

7 Sustainability evaluation of $La_{0.6}Sr_{0.4}CoO_{3-\delta}$ and $La_{0.6}Ca_{0.4}FeO_{3-\delta}$ electrocatalysts in early-stage research

Based on previous chapters, it was found that many perovskites, including the ferrates and cobaltates, may be used as comparably active OER catalysts. Besides their electrochemical properties, however, the different chemical compositions of the tested OER catalysts may result in advantageous or disadvantageous economic, environmental, and social impacts associated with the material supply of the selected elements. Such impacts are typically addressed in sustainability and life cycle assessments, but are often neglected in technical performance studies in early-stage research. Therefore, this chapter provides a sustainability evaluation of complex perovskite OER catalysts in the early stages of research based on the OER activity of thin film model catalysts. For the holistic material sustainability evaluation, $La_{0.6}Ca_{0.4}FeO_{3-\delta}$ and $La_{0.6}Sr_{0.4}CoO_{3-\delta}$ are compared as an exemplary case study of electrocatalysts for AWE (alkaline water electrolysis) in early-stage research. $La_{0.6}Sr_{0.4}CoO_{3-\delta}$ was chosen for comparison as a highly active and well-studied catalyst in the literature [15, 16, 21, 34, 85]. However, known Sr and Co reserves might deplete in the next 20-50 years and 50-100 years, respectively. Therefore, $La_{0.6}Ca_{0.4}FeO_{3-\delta}$ was chosen as an alternative perovskite as Ca and Fe are expected to have plentiful supply in the long term [26, 38, 39], and showed similar high OER activity in our study (section 5.8). The expected reserve depletion was hence considered as the first and easy-to-access decision criterion for our material selection before a more detailed analysis of economic, environmental, and social parameters is evaluated and discussed. Parts of this chapter are based on the preprint by Heymann *et al*. [200].

7.1 Catalytic mass activity of $La_{0.6}Sr_{0.4}CoO_{3-\delta}$ and $La_{0.6}Ca_{0.4}FeO_{3-\delta}$

As basis for the material sustainability evaluation the catalytic mass activity of the two perovskites is obtained enabling one to define the FU (section 3.7) for the here considered sustainability parameters and to estimate a projected catalyst material consumption for AWE in the EU in 2050. Here, the CV results are taken from the perovskite catalysts grown on Pt (section 5.9), because they are free of contact resistances to the substrate, and the catalytic mass activity can be obtained at higher current densities than on the single-crystal substrates.
The mass of the thin films was obtained from the total volume of unit cells that is exposed to the electrolyte. That is calculated from the 20 nm thick film and 0.44 cm^2 geometric surface area. $La_{0.6}Sr_{0.4}CoO_{3-\delta}$ has a mass of 5.7 µg in this area, and $La_{0.6}Ca_{0.4}FeO_{3-\delta}$ has a smaller mass of 5.0 µg in this area because the molar mass of Ca is smaller than that of Sr. In figure 53, representative CV scans of $La_{0.6}Sr_{0.4}CoO_{3-\delta}$ and $La_{0.6}Ca_{0.4}FeO_{3-\delta}$ are shown, where the current is normalized to the catalyst mass load of the thin films. The two perovskite catalysts exhibit comparable mass activity in the OER, indicating that the oxygen and hence hydrogen production is comparable with the given catalyst mass of $La_{0.6}Sr_{0.4}CoO_{3-\delta}$ and $La_{0.6}Ca_{0.4}FeO_{3-\delta}$. They reach

a mass activity of about 0.75 mA/µg at an anode voltage of 1.76 V vs RHE. The standard deviation of three CV scans from three different samples is shown in the graph as horizontal bars at 0.1, 0.5, and 0.8 mA/µg. The standard deviation is 9-11 mV for $La_{0.6}Ca_{0.4}FeO_{3-\delta}$ and 20-25 mV for $La_{0.6}Sr_{0.4}CoO_{3-\delta}$ (the standard deviation differences of 9-11 mV and 20-25 mV stem from these three different points along the CV scan). This might result from grain boundary effects, differences in crystal facet activity, and defect structures (see also section 5.9).
Also, the charge produced in a representative CV cycle is comparable for $La_{0.6}Sr_{0.4}CoO_{3-\delta}$ and $La_{0.6}Ca_{0.4}FeO_{3-\delta}$ as shown in figure 53b. Hence, a similar amount of oxygen and respectively hydrogen are produced, implying a comparable mass performance of both materials for their envisioned application as AWE OER catalysts.

To assess how much oxygen (hydrogen) may be produced over the full lifetime of these cata-

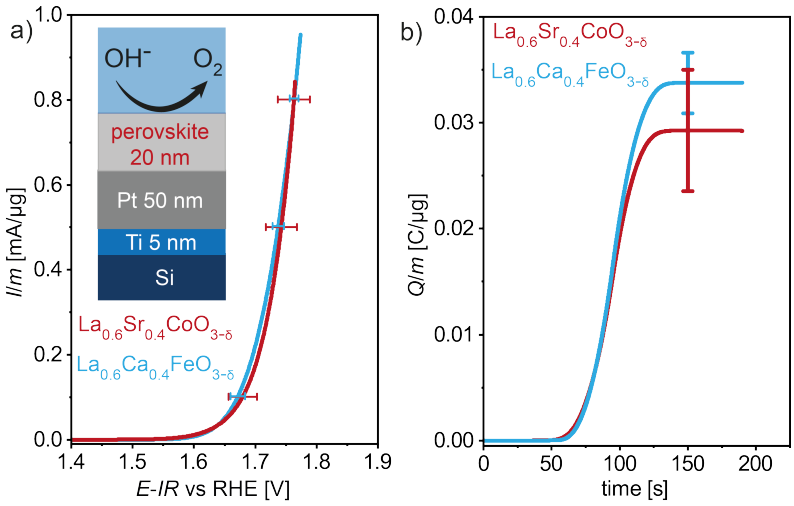

Figure 53: a) OER catalytic mass activity is shown from the averaged CV scan of $La_{0.6}Sr_{0.4}CoO_{3-\delta}$ and $La_{0.6}Ca_{0.4}FeO_{3-\delta}$ thin films deposited on Pt. b) Charge per µg catalyst passed in one CV cycle. Both perovskites generate a comparable charge within one CV scan.

lysts, ideally, the catalyst stability should be considered as a second parameter. However, while these lab-based RDE measurements are ideal for determining relative catalytic activity, they are less ideal for the determination of the catalyst stability in a final application scenario [201, 202]. Particularly, degradation rate and lifetime depend on the system integration of the catalyst layers. For example, enhanced lifetimes were reported for integrated catalysts in membrane-electrode assemblies compared to RDE experiments [201, 202]. While these studies confirmed that accurate stability tests under industrial conditions are inaccessible using a model-system approach and testing setup, various model-system studies of these and similar compounds

have shown that very thin layers of perovskite oxides are sufficiently stable to serve as model systems to assess and compare activity trends [19, 21, 80]. Thus, final stability benchmarks have to be established in a recurring manner at higher integration levels to yield additional and more precise input parameters for the sustainability evaluation towards industrial levels.
Therefore, one relies on the intrinsic activity comparison as a starting point for a comprehensive material evaluation in early-stage catalyst research. The similar mass activity and generated charge in one CV cycle suggests that comparable amounts of $La_{0.6}Sr_{0.4}CoO_{3-\delta}$ and $La_{0.6}Ca_{0.4}FeO_{3-\delta}$ catalysts may be projected to achieve similarly efficient hydrogen production in the final electrolyzer assembly. Hence, the economic and environmental aspects were elaborated based on the FU of 1 kg perovskite, assuming that similar masses of the catalysts will allow one to generate comparable amount of oxygen (hydrogen) in a real application scenario.

7.2 Projected synthesis route of perovskites on large area electrodes

While the determination of the intrinsic catalytic activity of the selected materials is done ideally on laboratory- and model-system level, a quantification of the projected sustainability parameters must consider the projected industrial-scale production route of the respective catalysts. Perovskite oxides for industrial applications are typically synthesized via solid-state or wet-synthesis methods [14, 50]. Since the solid-state route is more susceptible to impurities, requires higher reaction temperatures, and typically forms larger particles which is coupled to a lower specific surface area [14, 50], the wet chemical methods are considered to achieve high-purity nanoparticles for a potential industrial perovskite oxide synthesis.
Figure 54 illustrates the life cycle of an alkaline water electrolyzer with projected synthesis routes for $La_{0.6}Sr_{0.4}CoO_{3-\delta}$ and $La_{0.6}Ca_{0.4}FeO_{3-\delta}$, starting from the raw material input to the finally coated electrode for AWE. In this scenario, La, Sr, and Co containing rocks are extracted and further processed to La_2O_3, $SrCO_3$, and Co_3O_4. For the $La_{0.6}Ca_{0.4}FeO_{3-\delta}$ production, La and Ca containing rocks are extracted from mines and processed to La_2O_3 and $CaCO_3$. In contrast, iron (Fe) can be sourced from the primary market through iron ore or from the secondary market as recycled iron scrap. For the $La_{0.6}Ca_{0.4}FeO_{3-\delta}$ production iron scrap is considered here, because large amounts of iron scrap are available on the market, and iron scrap can be directly converted to iron nitrate [203] or another organic metal salt, and hence generally bypass the mining process. Here, an alloy free [204] and new iron scrap can be chosen and potentially be used for the perovskite oxide synthesis. More details about the option to use recycled materials can be found in the material recycling section 7.7.

In the subsequent production step, the precursor materials are dissolved in acidic solution to form metal nitrates or other metal-organic acid salts. Stoichiometric amounts of the precursor solutions are then mixed, combined with additives, and thermally treated to arrive at fine nanoparticle perovskite powders. Different synthesis options for this have recently been considered in ref. [205]. Note that identified precursors are also suitable for the solid-state route besides iron scrap as that would have to be converted to iron oxide first [146]. The perovskite

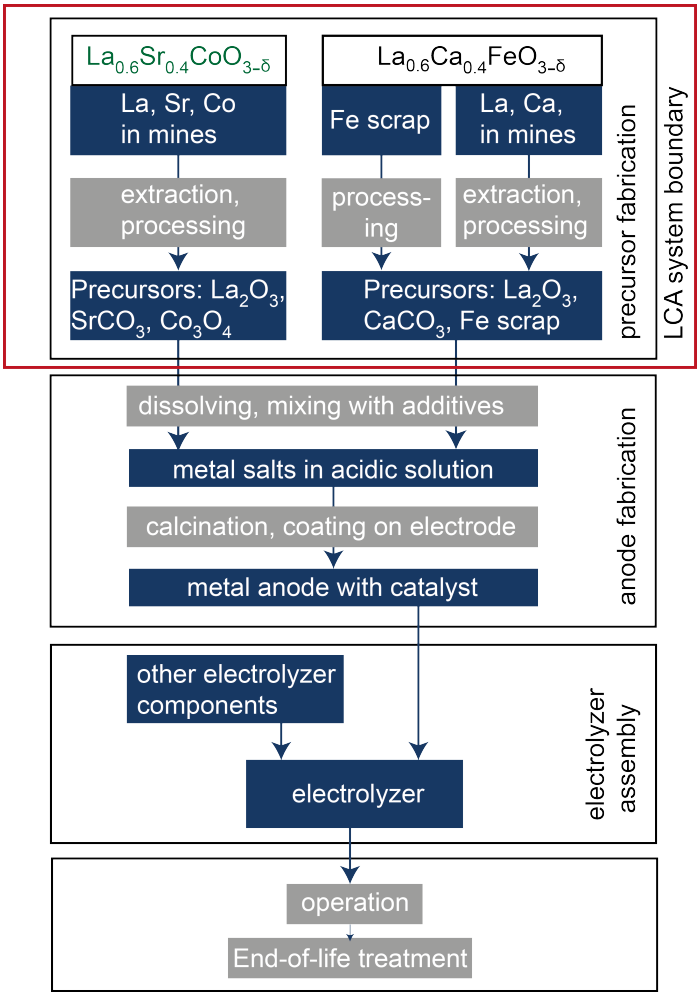

Figure 54: Life cycle of an alkaline water electrolyzer with projected production pathways for perovskite oxides $La_{0.6}Sr_{0.4}CoO_{3-\delta}$ and $La_{0.6}Ca_{0.4}FeO_{3-\delta}$ catalysts for the anode. The LCA system boundary includes material extraction, transportation, and precursor production.

nanoparticles are then deposited on large-area metal electrodes via for example screen printing [206, 207], jet printing, tape casting, or electrochemical deposition (Figure 54 middle) [14, 24, 146].
The latter process steps to arrive at the functional nanoparticles are typically quite similar for the

perovskite family, and for $La_{0.6}Sr_{0.4}CoO_{3-\delta}$ and $La_{0.6}Ca_{0.4}FeO_{3-\delta}$ in particular as can be seen in the refs. [208, 209]. Therefore, for a direct comparison of the two perovskites, one can focus on the production of the precursor materials La_2O_3, $SrCO_3$, $CaCO_3$, Co_3O_4, and iron scrap which is marked in figure 54 with the box “precursor fabrication”. This defines the system boundary of this sustainability evaluation. The subsequent common process steps will similarly add to the full sustainability evaluation, e.g., through the thermal treatment, which requires a high energy input but can be regarded as similar for both materials under test. In the following sections, the material criticality, raw material prices, as well as environmental and social impacts resulting from the precursor masses for 1 kg perovskite (see table 4) are discussed with a focus on the precursor materials.

7.3 Material criticality of $La_{0.6}Sr_{0.4}CoO_{3-\delta}$ and $La_{0.6}Ca_{0.4}FeO_{3-\delta}$

In the current EC-CRM 2023 assessment, a material is considered critical when the supply risk (SR) parameter exceeds a value of 1 and the economic importance (EI) parameter exceeds a value of 2.8 (shaded area in figure 55) [93, 142]. As shown, Sr, Co and La are hence considered as critical in the 2023 EU assessment, whereas limestone (the major source for Ca) and Fe ore are considered as non-critical. Both, limestone and Fe ore have a high economic importance for the EU, but the supply risk is low because of a high diversification level of supplying countries inside and outside the EU [93]. Sr is evaluated as critical, primarily because it is essential to

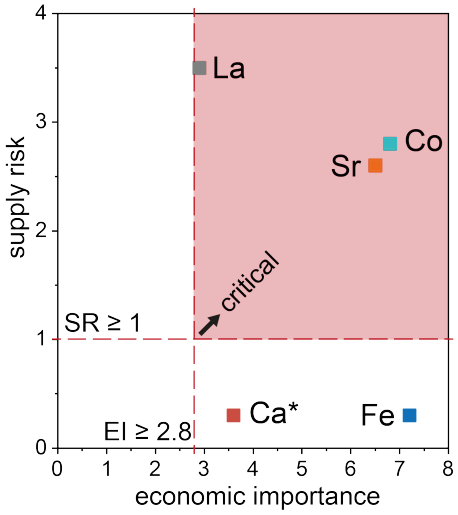

Figure 55: EU criticality assessment for the raw materials used for $La_{0.6}Sr_{0.4}CoO_{3-\delta}$ and $La_{0.6}Ca_{0.4}FeO_{3-\delta}$ adapted from [93]. Ca* is limestone and Fe the iron ore.

produce magnets and pyrotechnics and has only one EU-supplying country (Spain). It is hence affected by both a high economic importance as well as a high supply risk. Co is evaluated as critical primarily because its supply is poorly diversified, and the Democratic Republic of Congo (with 63 % the main global Co supplier) is suffering from high political instability. Furthermore, Co is essential to produce several alloys and hard materials that add high value to the EU economy.
La is a critical raw material due to a high supply risk of 3.5 and a high economic importance of 2.9. This is because 85 % of the global La supply comes from China where La is extracted as well as processed. Since La is not recycled and not easily substituted in relevant applications, the EU relies to a large extent on La import from China. La mainly adds value to the EU economy as component in fluid cracking catalysts and other catalysts [93]. While the depletion of known La reserves is projected to occur within the next 100-500 years [38], the high geopolitical dependencies and low supply chain diversification for La supply can be a significant supply risk in the closer future. Based on this evaluation, exchanging Sr and Co for Ca and Fe can reduce the overall material criticality of our model catalysts. However, La is of immediate concern for both perovskites regarding its high supply risk.

Projected increase in demand for perovskite oxides in the EU based on experimental results

To estimate how many tons of perovskite would be required for AWE in a gigawatt scale in the EU in the future, the power-to-mass ratio was calculated based on the catalyst model systems and compared to an estimated hydrogen demand scenario in 2050 based on ref. [5]. With that, it can be estimated if some of the perovskite precursors would require larger supply chain expansions than others in comparison to today's EU material consumption.
Here, the mass-to-power ratio was calculated at 1.76 V vs RHE with an output of 0.75 mA/µg. At this operating voltage the required perovskite mass-to-power ratio is around 0.76 t/GW under the assumption that the perovskite catalysts form dense 20 nm thick layers on commercial electrode surfaces and are operated in 0.1 M KOH solution at room temperature (as according to our experiments). Note that AWE electrolyzers are typically operated in 5-10 M KOH solution at 40-85°C [40, 210, 211]. This power-to-mass ratio is an upper limit, as under industrial conditions the surface roughness would be significantly higher and the surface coverage would diverge. Hence, the industrial operating conditions have an influence on the final mass-to-power ratio of the perovskites as well as the operational catalyst lifetimes. However, this calculated mass-to-power ratio is comparable to the estimate of Ir catalyst ratio which is 0.75 t/GW in acidic proton exchange membrane electrolysis [12]. The comparability of catalyst loads in AWE is difficult because Ni, as the main catalyst material, is also applied as substrate and as bipolar plate material [12].
To upscale the power-to-mass ratio to the forecasted EU hydrogen consumption in 2050, it is

Table 17: Projected increased precursor demand in 2050. For the high demand scenario in 2050 in the EU, 1073 GW hydrogen electrolyzer capacity are estimated, where 40% i.e. 429 GW stem from AWE (reference [5] and its appendix 3 table 33). In this scenario, it is estimated from these experiments that about 325 t of perovskite are required if all AWE electrolyzers utilize the perovskites as catalysts. The required La, Sr and Co masses (as metal content) for $La_{0.6}Sr_{0.4}CoO_{3-\delta}$ as well as La, Ca, and Fe masses for $La_{0.6}Ca_{0.4}FeO_{3-\delta}$ are listed on the left side of the table. The relative content of the required metals compared to the EU metal consumption is shown in the second column. The corresponding EU material consumption is shown on the right side of the table. The shown mass values correspond to the 2016-2020 EU average consumption [212–216].

	required metal in the calculated scenario t	relative material content to the EU consumption %	element	EU consumption t
$La_{0.6}Sr_{0.4}CoO_{3-\delta}$ -**La**	120	5.38	La	2234
$La_{0.6}Sr_{0.4}CoO_{3-\delta}$ -**Sr**	51	0.09	Sr	53577
$La_{0.6}Sr_{0.4}CoO_{3-\delta}$ -**Co**	85	0.78	Co	10946
$La_{0.6}Ca_{0.4}FeO_{3-\delta}$ -**La**	133	5.97		
$La_{0.6}Ca_{0.4}FeO_{3-\delta}$ -**Ca**	26	2.9×10^{-4}	Ca	8817600
$La_{0.6}Ca_{0.4}FeO_{3-\delta}$ -**Fe**	89	1.2×10^{-4}	Fe	76000000

estimated that 429 GW of AWE power is required in a high demand scenario (HDS) (calculations found in table 17) [5].

To cover this demand, the here investigated perovskite catalyst layers would sum up to around 325 t of perovskite. As not all AWE plants will be operated with perovskite oxides, this number is an upper limit for the experimental results. Such perovskite catalyst loads in AWE correspond to 5-6% of the recent, annual EU lanthanum consumption [216], 0.8% of the average EU Co consumption [212] whereas the other elements Sr, Ca and Fe fall below the average EU consumption of 0.1% [213–215].

As we chose here thin film catalysts that have comparably smooth surface morphologies to obtain a fair comparison of the catalytic performance, the final mass-to-power ratio may be further optimized and influenced by material morphology engineering, catalyst integration, and by the application of industrial operation conditions. However, an estimate of possible material consumption gives an overview of possible supply bottlenecks. The relatively larger supply chain expansion of La compared to the other precursors, as well as lanthanum's high material criticality, might hence lead to a threat for the application of both perovskites. All rare earth elements are classified as critical raw materials in the EC-CRM report [93] and their demand in the energy sector is increasing sharply [4]. Hence, the rather monopolistic supply chain of rare earth elements is alarming for the energy transition.

7.4 Economic impact based on precursor prices

Beyond the critical raw materials classification, the market prices of the required precursor materials directly indicate the economic effects of the material selection. Figure 56 shows the cumulative precursor price per kg perovskite for $La_{0.6}Sr_{0.4}CoO_{3-\delta}$ and $La_{0.6}Ca_{0.4}FeO_{3-\delta}$. De-

tailed price information and sources are summarized in table C.1 of the appendix. The cumulative precursor price for 1 kg perovskite is about 10 times lower for $La_{0.6}Ca_{0.4}FeO_{3-\delta}$ compared to $La_{0.6}Sr_{0.4}CoO_{3-\delta}$. For $La_{0.6}Sr_{0.4}CoO_{3-\delta}$, the cumulative price is dominated by Co_3O_4 while La_2O_3 and $SrCO_3$ share only about 10 % of the precursor costs. For $La_{0.6}Ca_{0.4}FeO_{3-\delta}$, the iron substitution reduces the cumulative price by a factor of 10, where iron scrap makes up only 15 % of the projected $La_{0.6}Ca_{0.4}FeO_{3-\delta}$ price. The rest of the cumulative price is shared by La_2O_3 and $CaCO_3$ with 57 % and 27 %, respectively. Therefore, the significantly lower cumulative precursor prices of $La_{0.6}Ca_{0.4}FeO_{3-\delta}$ compared to $La_{0.6}Sr_{0.4}CoO_{3-\delta}$ suggest that $La_{0.6}Ca_{0.4}FeO_{3-\delta}$ is the more economically favorable catalyst.

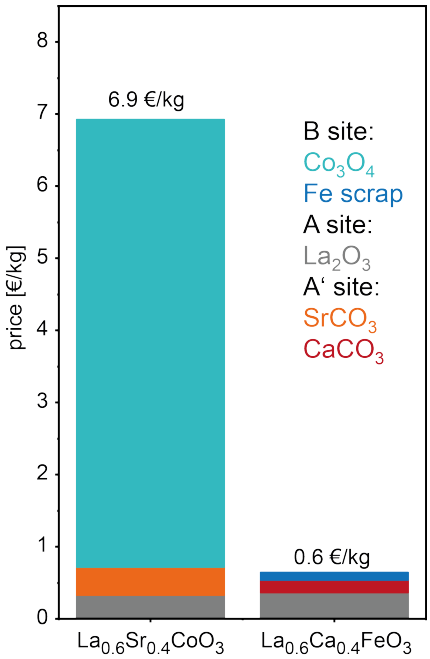

Figure 56: Cumulative precursor prices for $La_{0.6}Sr_{0.4}CoO_{3-\delta}$ and $La_{0.6}Ca_{0.4}FeO_{3-\delta}$ per kg perovskite.

7.5 Environmental impacts of precursor production

Figure 57 shows the environmental impact results of the precursor materials for 1 kg perovskite oxide for the categories climate change, water use, land use, acidification potential, human toxicity ecotoxicity, and more, where all of them are listed and explained in table 6. Detailed definitions of the single impact categories can be found in ref. [117].

The use of Fe from scrap instead of Co from Co_3O_4 for the perovskite oxide B-site significantly

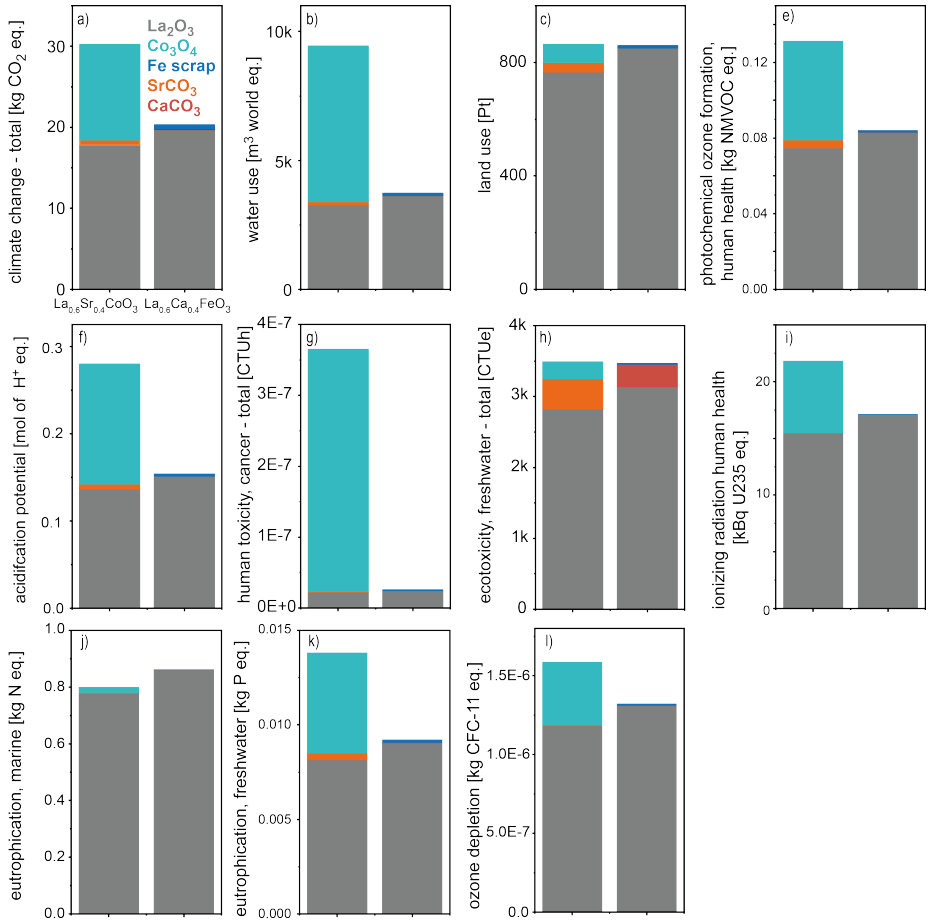

Figure 57: Environmental impact category results of the precursors required to produce 1 kg of $La_{0.6}Sr_{0.4}CoO_{3-\delta}$ and $La_{0.6}Ca_{0.4}FeO_{3-\delta}$.

decreases the environmental impact, particularly for the categories climate change (figure 57a), water use (b), photochemical ozone formation (e), acidification potential (f), human toxicity (g) and eutrophication-freshwater (k). In contrast, $SrCO_3$ and $CaCO_3$ precursors both have almost no environmental impact in all categories. For $La_{0.6}Ca_{0.4}FeO_{3-\delta}$, the La_2O_3 production dominates in all impact categories by at least 90 %. Also, for $La_{0.6}Sr_{0.4}CoO_{3-\delta}$, the La_2O_3 production makes up at least 75 % of the environmental impact in the four categories land use (c), ecotoxicity -freshwater (h), marine eutrophication (j), and ozone depletion (l). This indicates that the

use of La in both catalysts implies severe environmental burdens.

Discussion on environmental impact aspects for the subsequent nanoparticle synthesis: As discussed in section 7.2, different perovskite nanoparticle synthesis routes are possible, where both perovskites can be produced under similar conditions as reported in the references [208, 209]. The further processing of the precursor materials to the final perovskite nanoparticles will add up to the environmental impact assessment of the catalyst production, however, in a similar manner for both. Consistent with the analysis of figure 57, Nandikes *et al*. recently published an LCA study on various $LaFeO_3$ nanoparticle synthesis routes [205] and consistently found that the La precursor production is the predominant factor in several impact categories. Therefore, decreasing the La amount in the perovskite would support the overall environmental footprint of the nanoparticle synthesis. Another LCA study referring to high temperature solid oxide electrolyzers with a $La_{0.6}Sr_{0.4}CoO_{3-\delta}$ air electrode, reported a higher global warming potential per kg of $La_{0.6}Sr_{0.4}CoO_{3-\delta}$ compared to this thesis [217]. Yet, this difference stems presumably from the final synthesis step requiring sintering and firing at high temperatures. However, for perovskites used in low temperature AWE, nanoparticle synthesis routes such as suggested by Nandikes *et al*. would be more suitable and require less extreme temperatures.

In summary, the substitution of Co to Fe in the perovskite decreases the environmental impact in several categories, whereas La has a high environmental impact for both perovskites, and can sometimes dominate the whole impact category. While the system boundary comprised the precursor production, even all fabrication steps for the perovskite nanoparticle synthesis may be significantly influenced by the high environmental impact of the La precursor production.

7.6 Social aspects

A quantitative analysis of the social impacts of the catalyst production process is important for a holistic sustainability assessment. Yet, quantitative estimates are elusive on the level of early-stage research. However, some key aspects are highlighted here that can yield a preliminary assessment of the expected social impacts of raw material extraction. With respect to the Co mining industry, social impact assessments exist mainly for the Democratic Republic of the Congo, as main supplier of Co. While there are regulated working standards for artisanal mining in the Democratic Republic of the Congo, many mining sites do not follow those rules and many artisanal miners do not have the knowledge about these regulations. Hence, mining tunnels are exceeding the allowed tunnel length, and several safety constructions are often not installed [218]. Although child labor is also regulated in the Democratic Republic of the Congo, 29% of the miners were children in 2011, reflecting the high poverty in the country [218]. In contrast, the use of iron scrap is generally acknowledged to have a positive social impact as, for example, the use of iron scrap reduces climate change related socio-economic costs globally, as it reduces CO_2 pollution [219].

The assessment of social impacts in the La industry is less mature [220]. However, it is reported

that the rare earth industry in China causes health problems for the directly involved stakeholders such as increased exposure to radioactive tailings [220–224]. Moreover, it is stated that the environmental burdens of rare earth material processing are so high that it is hard to get a permission for rare earth processing sites in developed countries [220]. Therefore, rare earth material processing takes mainly place in less developed countries [220]. In contrast, with Spain as a major supplier for Sr in the European Union [214], child labor and hazardous working conditions are regulated and can be considered as negligible in the European Union. Likewise, Ca is also locally sourced in Europe [213] and to our knowledge no child labor or hazardous working conditions are reported. Accordingly, the substitution of Co for Fe may decrease the social impact, especially concerning the hazardous working conditions and prevalence of child labor. The La production, however, is linked to hazardous working conditions, which is a disadvantage for both perovskites.

7.7 Material recycling

Environmental, economic, and social impacts as well as the material criticality, can be potentially improved if recycling rates increase and accessible secondary material supply is provided, especially in the case of La and Co, as critical raw materials with high environmental impact in the precursor production. Today, the EOL-RIR of Co is already around 22% [93]. However, the recycled Co is to a large extent embedded in Co-alloys and therefore not directly accessible for Co_3O_4 recovery [225], and may hence not be suitable for the catalyst production. The use of recycled Co from battery cathodes would potentially be suitable for the perovskite production, but it competes with the battery market itself [226, 227]. Therefore, the case study is based on the primary (non-recycled) material supply for Co_3O_4.
In contrast, Fe has a high recycling rate (EOL-RIR 31% [93]), and certain scraps are suitable for the precursor production. Iron scrap can be domestically available and iron scrap contributes to the comparably low Fe market prices and the lowered environmental and social impacts. The EOL-RIR of La is only 1% [93], and hence, for the perovskite production not applicable at this stage. The same holds for limestone with an EOL-RIR smaller than 1% [93]. However, as Ca is a non-critical material, and $CaCO_3$ production from primary sources has a low environmental impact, the need for increased recycling rates is of lower priority. The Sr EOL-RIR is nearly zero [93] and hence not considerable for secondary material input today. Given the material criticality of Sr, Co and La, efficient recycling may reflect a future strategy to mediate the high supply risk for the primary material supply.

7.8 Summary of $La_{0.6}Sr_{0.4}CoO_{3-\delta}$ and $La_{0.6}Ca_{0.4}FeO_{3-\delta}$ sustainability parameter results

All analyzed sustainability parameters of $La_{0.6}Sr_{0.4}CoO_{3-\delta}$ and $La_{0.6}Ca_{0.4}FeO_{3-\delta}$ OER catalysts are summarized and compared in figure 58. While the two perovskites exhibit a comparable

sustainability parameters	**$La_{0.6}Sr_{0.4}CoO_3$**	**$La_{0.6}Ca_{0.4}FeO_3$**
material criticality (EC-CRM 2023)		
supply risk (≥ 1 ●)	La ● Sr ● Co ●	La ● Ca ● Fe ●
economic importance (≥ 2.8 ●)	La ● Sr ● Co ●	La ● Ca ● Fe ●
economical impact		
cumulative precursor price	●	● 90 % lower
environmental impact (LCA EF 3.1 ecoinvent 3.9) similar impact ● | at least 25 % higher ● | at least 25 % lower ●		
climate change (CO_2 equivalents)	●	●
land use	●	●
water use	●	●
acidification potential	●	●
human toxicity	●	●
ecotoxicity	●	●
ozone depletion	●	●
photochemical ozone formation	●	●
eutrophication (freshwater)	●	●
eutrophication (marine)	●	●
ionizing irradiation	●	●
social impact **yes ● no ●**		
child labor	La not known, Sr ● Co ●	La not known, Ca ● Fe ●
hazardous working conditions	La ● Sr ● Co ●	La ● Ca ● Fe ●

Figure 58: Summary of the sustainability parameters of $La_{0.6}Sr_{0.4}CoO_{3-\delta}$ and $La_{0.6}Ca_{0.4}FeO_{3-\delta}$ as alkaline oxygen evolution catalysts.

technical performance in our laboratory-based experiments, several sustainability parameters of $La_{0.6}Ca_{0.4}FeO_{3-\delta}$ have a lower impact compared to $La_{0.6}Sr_{0.4}CoO_{3-\delta}$ (marked in green/red color in figure 58). This includes that the supply risk of Ca and Fe is low compared to Sr and Co. Moreover, the projected cumulative precursor price of $La_{0.6}Ca_{0.4}FeO_{3-\delta}$ is 90 % lower than for $La_{0.6}Sr_{0.4}CoO_{3-\delta}$ because Co is avoided. The environmental impact of $La_{0.6}Ca_{0.4}FeO_{3-\delta}$ is at least 25 % lower compared to $La_{0.6}Sr_{0.4}CoO_{3-\delta}$ in those categories, where cobalt oxide production has a significant impact. However, in the environmental impact categories that are dominated by La_2O_3 production, both $La_{0.6}Sr_{0.4}CoO_{3-\delta}$ and $La_{0.6}Ca_{0.4}FeO_{3-\delta}$ have similarly high environmental impact (marked in black). $La_{0.6}Ca_{0.4}FeO_{3-\delta}$ has potentially a lower social impact than $La_{0.6}Sr_{0.4}CoO_{3-\delta}$ because Co mining often involves child labor and can occur under hazardous working conditions. Nevertheless, La processing can also occur under hazardous working conditions, which is a disadvantage for both. In summary, the exchange of Co to Fe may hence be assessed as generally beneficial for the majority of sustainability parameters.

Similarly, the exchange of Sr by Ca further reduces the overall supply risk of the perovskite. Nevertheless, the presence of La yields a significant challenge for the catalyst usage in larger scales for both perovskites and has to be addressed in the future.
In agreement with these points, the EU 2023 foresight study shows that La, Sr or Co are ranked at the top of the different possible supply risks for an AWE stack whereas commercial alkaline water electrolyzers do not rely on these raw materials today [5]. Regarding the environmental impact of commercialized AWE stacks, Ni, which is used as anode and cathode catalyst, and sometimes also mesh, exhibits high environmental impact in several categories [228]. The usage of perovskite catalysts on the anode instead of Ni can therefore decrease or increase the environmental impact and raw material supply risk of the AWE stack, depending on their final composition, mass load, and technical performance.

7.9 Chances, limitations and future perspectives of early-stage materials research and sustainability evaluation for energy storage technologies

The case study emphasizes that material sustainability evaluation in early-stage research can provide additional criteria for a holistic materials selection next to physical and chemical performances [26]. These criteria might act as an additional driver to test and to optimize materials that have a lower supply risk as well as lower economic, environmental and social impacts in their final application [26–28]. If the results of the sustainability evaluation are not as clear as in this case study (a clearly preferred perovskite), multi-criteria decision analysis (MCDA) can be used to structure decision-making processes. MCDA includes mathematical approaches to cluster many individual results into fewer but more manageable results [229].
At the same time, the case study revealed both the chances and limitations as well as required assumptions to arrive at a quantitative sustainability evaluation. Model catalysts, as employed in this study, are ideal for determining intrinsic catalytic activity as they have comparable surface morphologies and can be independent of additional stack assembly related resistances. Hence, for the comparison of two materials that are supposed to serve the same function (here, the anode electrocatalysts in AWE), the model catalysts can be quantitatively related to sustainability parameters via their mass activity. However, the scaling to industrial applications is limited, as for example, lifetimes and loadings of final electrolyzer stacks are hard to predict, which is indispensable to project and approximate the final electrolyzer production and operation impact. Importantly, the FU of 1 kg perovskite oxide chosen here delivers a fair comparison in such an early stage of research, while in industrial electrocatalyst research, the LCA can be conducted with more commonly used FUs [147]. This enables a comparison to other commercial or prototype AW electrolyzers where realistic lifetimes are considered, catalyst loads are optimized, and the surface roughness is optimized.
Nevertheless, a first evaluation can be made with the model system approach if the assumptions and conditions are well-defined. This can be the basis for material choices in later stages

of materials research. Testing a broad range of materials with catalyst model systems in early-stage research can provide a general basis for preselecting materials in the applied research of energy materials. Implementing a sustainability evaluation already at early stages of materials research can be a strong opportunity to identify less sustainable material compositions and potentially refocus the research.

As found in this study, reducing the La content or even eliminating it could improve the sustainability of the material even more as compared to the sole exchange of Co and Sr to Fe and Ca. However, the replacement of La has to be tested for OER catalyst performance to make a further decision on the necessity of La containing perovskite catalysts.

There is a recent and important study [91] that tests several lanthanide substituted $RBaCuFeO_{5-\delta}$ (with R = lanthanides) perovskite oxides OER catalysts. The motivation of this work was to avoid Co-based perovskites, as Co is suffering from high prices and is competing in the battery market. This approach is crucial for a holistic material choice, yet, considering the e.g. material criticality of the investigated lanthanides can further improve it. This is an example where the materials science community can benefit from knowledge on e.g. precursor environmental footprints and criticality assessments to tackle holistic material choices from the onset. Which alternative perovskite oxide compositions might be suitable is elaborated in the section 7.10.

In further feedback loops, the sustainability of energy materials can be evaluated both in applied research (e.g., testing the catalyst in an actual electrolyzer stack) as well as in industrial research (e.g., long term tests under industrial conditions) as illustrated in figure 59. The latter includes the development of a sustainable material design strategy for final scaling parameters and long-term technical performance. Such a feedback loop between energy materials research and sustainability evaluation would be beneficial at all stages of research to constantly reevaluate and leverage the sustainability of material-intensive technologies. The factors discussed here, such as the use of critical raw materials, precursor price distribution, and the environmental and social footprint of preliminary products (here precursors), also remain relevant in applied and industrial research. There, they are incorporated into social, economic and environmental life cycle assessments over the entire product life cycle, which are already established today. Many industrial companies, including those in the energy sector, are feeling increasing economic pressure and are facing increasing regulatory requirements to reduce their environmental footprint and to avoid possible supply bottlenecks in times of tensioned geopolitics [230]. Thus, materials scientists can consider and even influence the design of materials in the early development phase that meet these needs from the onset. Such evaluation can yield an initial guidance for expected sustainability bottlenecks, also at a higher level of integration and technology.

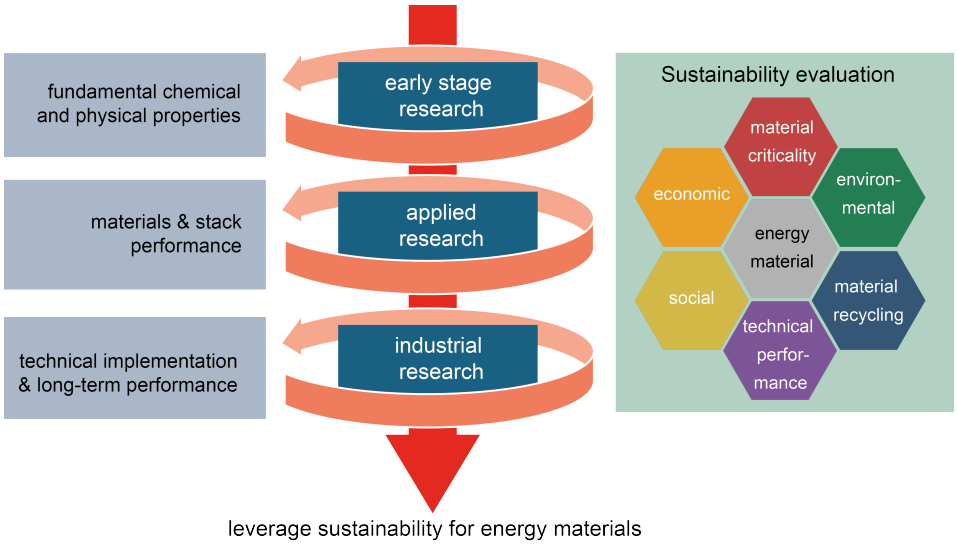

Figure 59: Approach of holistic material choice for electrolyzers, fuel cells and batteries in early-stage, applied, and industrial research. A consecutive feedback loop delivers opportunities for a sustainable material choice from the onset.

7.10 Perovskite material choice and fabrication outlook

Regarding the other perovskites of this thesis, $La_{0.6}Ca_{0.4}CoO_{3-\delta}$ has a reduced supply risk compared to $La_{0.6}Sr_{0.4}CoO_{3-\delta}$, but has no additional advantages at this point, because the catalytic activity of the two cobaltates is similar. $La_{0.6}Sr_{0.4}FeO_{3-\delta}$ has an increased supply risk compared to $La_{0.6}Ca_{0.4}FeO_{3-\delta}$ and has a slightly lower OER activity. Hence, it may not be more desirable than $La_{0.6}Ca_{0.4}FeO_{3-\delta}$. $La_{0.67}Sr_{0.33}MnO_{3-\delta}$ showed the lowest OER activity, and Mn is a critical raw material [93]. Therefore, it may not be considered beneficial. $La_{0.6}Ca_{0.4}NiO_{3-\delta}$ could be more desirable than $LaNiO_{3-\delta}$ as is has a lower La content. Ni, moreover, is a strategic material defined by the European Commission, which means it has a very high economic importance, but the supply risk is small enough so that it is not considered critical [93], which is an advantage compared to Co. However, the NiO price (12.450 €/t [231] 16.06.25) is much higher than that of iron scrap. The Ni EOL-RIR is 16 %, which is lower than those of Fe and Co. Furthermore, recycled NiO also competes with the battery market [231, 232]. An environmental impact assessment would be desired to gain more insights, if Ni may have an advantage compared to Co in this aspect. However, in total, the La content is a concern for all investigated perovskites in this thesis.

One option could be to replace La by other rare earth elements such as dysprosium or neodymium, but these are also critical raw materials [93] and do not have a lower environmental

impact [233, 234]. Hence, they are not necessarily suitable for a La exchange. Another option could be to replace La fully with Ca on the A-site where some studies show that $CaCoO_{3-\delta}$ [235] or $CaFeO3_{3-\delta}$ [166] show high catalytic activity. Nonetheless, it was also reported that the usage of only alkaline earth elements on the A-site might lead to a faster structural transformation, which may accelerate catalyst degradation [236, 237]. Yet, the structural transformation and degradation characteristics of the perovskite oxide depend on the final A- and B-site combination. For example, only 1-2 unit cells of $SrTiO_3$ coverage can stabilize the highly unstable $SrRuO_{3-\delta}$ in the OER [32]. This is because Ti^{4+} has a d^0 configuration and is therefore relatively inert [238] compared to the high *d*-band occupancy of $SrRuO_{3-\delta}$. Thus, combining elements that can stabilize the perovskite alkaline earth elements might be a promising approach to overcome degradation and dissolution effects. Ti metal, in particular, is classified as a critical raw material, whereas TiO_2 is uncritical [93]. As the synthesis of perovskite oxides would require only TiO_2 as precursor material, insertion of Ti on the B-site could be a promising alternative to decrease alkaline earth element dissolution on the A-site. Possibly perovskite compositions of $CaFe_{1-x}Ti_xO_{3-\delta}$ might stabilize the perovskite during catalysis.
The full replacement of La can be even further advantageous, as possible passivation layers of $La(OH)_3$ could be avoided [21]. It is reported that the removal of the passivation layers from A-site elements stabilizes the electrochemical performance over a long period [239]. Moreover, another promising hint for an improved stability of alkaline earth elements on the A-site is given by a recent master thesis conducted by Linda Joseph [240] in our group under my daily supervision. It was found that the electrolyte concentration of 0.1 M KOH with a pH of 13 leads to a more severe degradation of the catalyst than in pH = 14. The higher solubility of the perovskites toward a lower pH, as expected from the Pourbaix diagrams, might induce a more accelerated degradation. Increasing the KOH concentration towards industrial conditions of 6 M KOH in AWE could hence even be beneficial.
Regarding the perovskite synthesis and coating of the electrode, the study by Nandikes *et al*. shows that e.g. hydrothermal synthesis can be more environmentally friendly than e.g., co-precipitation of perovskite oxide nanoparticles. Unfavorable would be the solid-state synthesis route, as typically high calcination temperatures and firing come at the cost of high CO_2 pollution. As mentioned before, several nanoparticle synthesis routes do not need such high temperatures compared to the solid-state route. However, an alternative could be the use of amorphous catalysts [241], which could potentially be deposited at room temperature.

While $La_{0.6}Ca_{0.4}FeO_{3-\delta}$, and iron oxides in general, have a high resistivity, such electrocatalysts are often discarded due to their low catalytic performance [24, 25]. As the ferrates showed indeed a low OER activity on the insulating substrates in this thesis, they could have been discarded here as well. However, the decoupling of the resistivity from the intrinsic catalytic activity by our heterostructure thin film design revealed that ferrates can be highly active OER catalysts similar to the cobaltates and nickelates. This renders the ferrates as potentially competing OER catalysts with the Ni and Co-based catalysts. The epitaxial thin film model sys-

tem approach enabled one to directly assess the intrinsic catalytic activity, which is more difficult on a higher integration level of the catalysts into an electrolyzer stack. Based on this, a fair sustainability evaluation could be built in the early-stages of electrocatalyst research, identifying $La_{0.6}Ca_{0.4}FeO_{3-\delta}$ on a holistic level as a promising OER catalyst. This shows how early-stage research of electrocatalysts can uncover promising ways for a continuous evaluation of holistic material choices, although final process chains and supply chains are not known at this stage.

8 Summary and Conclusion

This thesis advances the understanding of how the perovskite oxide catalyst conductivity and their electronic structure properties influence the OER activity, where the A- and B-site exchanged $La_{0.6}Sr_{0.4}CoO_{3-\delta}$, $La_{0.6}Ca_{0.4}CoO_{3-\delta}$, $LaNiO_{3-\delta}$, $La_{0.6}Ca_{0.4}NiO_{3-\delta}$, $La_{0.6}Sr_{0.4}FeO_{3-\delta}$, $La_{0.6}Ca_{0.4}FeO_{3-\delta}$, and $La_{0.67}Sr_{0.33}MnO_{3-\delta}$ perovskites were investigated. At the same time, it showcases how a sustainability evaluation on the level of early-stage research can advance the holistic material choice for the applied research and industry from the onset. The main findings and sustainability considerations performed in this thesis are summarized in figure 60.

The first goal of this thesis was to investigate the influence of the electrocatalyst conductivity and possible interface resistances on the OER activity, and if this can be decoupled to reveal the intrinsic catalytic activity of perovskites over a large resistivity range. For this, epitaxial thin films were used, as they allow one to actively tune electron transport pathways and interface resistances, which is a clear advantage compared to powder catalysts. The considered perovskites exhibited three orders of magnitude different resistivities, and to systematically investigate the influence of such a large resistivity range, the electron transport pathway through the catalyst layer was actively varied by the sample geometry. For long electron transport pathways through the catalyst layer, the highly resistive ferrates exhibited very low catalytic activity, and at higher current densities, even for the less resistive $La_{0.6}Ca_{0.4}NiO_{3-\delta}$. This resulted from a strongly inhomogenous current distbrution along the catalyst active surface as sketched by the arrows in figure 60 at the stack on the left side. Therefore, to minimize the influence of long electron transport pathways, the thin films were deposited on the conducting Nb:$SrTiO_3$, which decreased the pathway to only nanometer lengths. Occurring interface resistances to the conducting substrate were identified and successfully minimized with a dipole layer of 2-4 unit cells as an interlayer between the substrate and the catalyst layer.

The interface engineering and nanometer-long transport path enabled us to reveal the intrinsic properties of all thin films. Astonishingly, the most resistive perovskite $La_{0.6}Ca_{0.4}FeO_{3-\delta}$ had similar OER activity as the highly conductive cobaltates and $LaNiO_{3-\delta}$ at 0.1 mA cm^{-2}. This is in contrast to the observation where a long transport pathway through the catalyst governed the OER activity. Hence, the electrical conductivity does not necessarily correlate with intrinsic catalytic properties. Thus, it is of high importance to quantify electron pathway-dependent current density losses in chosen sample geometries as well as to distinguish intrinsic properties from resistivity for the establishment of OER catalyst design rules.

The intrinsic OER activity trend showed promising OER activities for the ferrates, nickelates, and cobaltates, while the OER activity of the manganate was significantly lower. This behavior was related to an electronic inversion layer at the surface of $La_{0.67}Sr_{0.33}MnO_{3-\delta}$ to the electrolyte under applied potentials toward the OER voltage regime. In contrast, the ferrates, cobaltates, and nickelates exhibited a hole accumulation layer at the electrolyte interface under applied

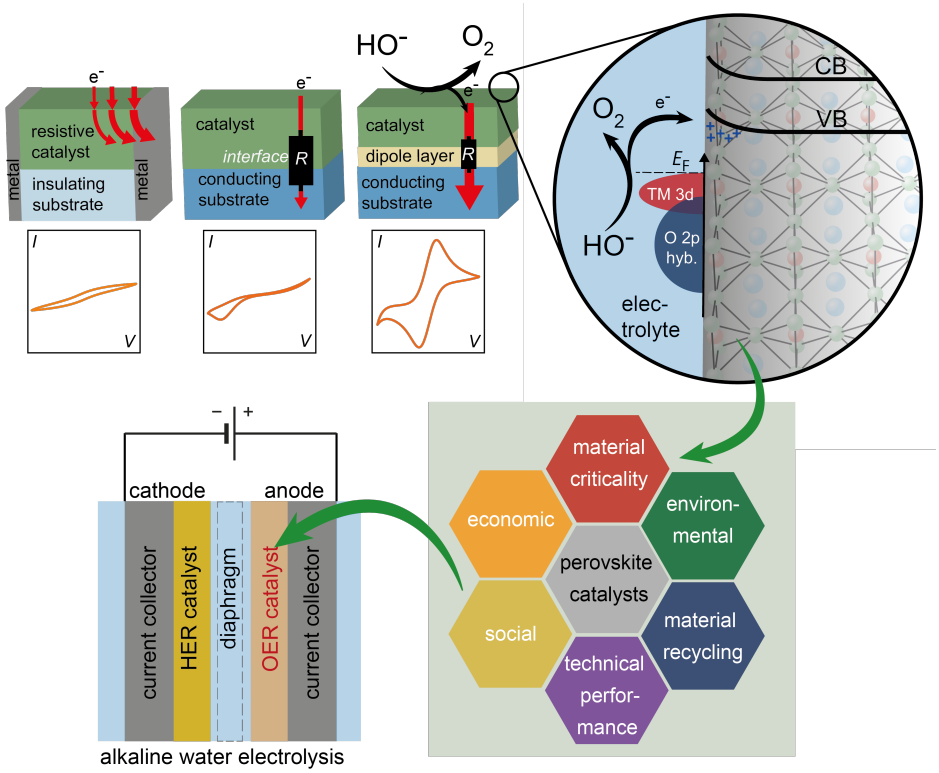

Figure 60: Upper left side: tuning of the epitaxial thin film stack geometry to reveal intrinsic catalytic properties decoupled from catalyst resistivity and contact resistance. Upper right corner: Zoom to the catalyst/electrolyte interface. The valence and conduction band (VB, CB) are sketched with interface band bending to the electrolyte. Oxygen (O 2*p*) and transition metal states (TM 3*d)* are sketched on the Energy scale close to the Fermi level (E_F). The band bending and electronic structure influence the OER activity. The perovskite catalysts were evaluated with the parameters shown in the "sustainability flower" in the bottom right corner. For final application, the sustainable catalyst is sketched in a water electrolyzer stack.

potential, where an access of electron holes is favorable for recombining with the incoming electrons of the OER.

The second goal was to determine electronic structure properties in order to correlate them to their intrinsic OER activity, which may uncover possible OER descriptors and possibly hint at crucial catalyst design rules. The intrinsic OER activity roughly followed a volcano-shaped trend for the e_g electron filling, spiking at an e_g filling around unity. This is in agreement with the guiding literature of Suntivich *et al*. and can deliver a first guidance to identify highly active

OER catalysts. However, certain discrepancies remained. The O 2*p* center is another crucial property that can provide insight into the bonding strength of the oxygen adsorbates of the electrolyte at the catalyst surface. The intrinsic OER activity correlated with the O 2*p* band center in a volcano-shaped trend at a current density of $0.05\,\mathrm{mA\,cm^{-2}}$. This means that an intermediate O 2*p* band center enables high OER activity as it results in neither too strong nor too weak binding of the catalyst adsorbates, decreasing the energetic distance between the reaction intermediates. Hence, the O 2*p* center determined by XPS can offer a good alternative to address the bonding strength of the oxygen adsorbates, which is formally expressed by the Gibbs free energy ΔG but is experimentally hard to access. The valence band O 2*p* band center may hence serve as a design parameter for predicting highly efficient perovskite oxide electrocatalysts for their thermodynamic energies of the reaction intermediates.

The third goal was to showcase to what extent a material sustainability evaluation can be conducted for such model system electrocatalysts in the early stages of materials research, and how this can improve the determination of possible material hotspots of the energy transition. For this, the crucial parameters of the energy transition were evaluated, starting from possible material shortages, and going to economic, environmental, and social impacts of the considered material. For one, material criticality assessments that include the raw material economic importance and their supply risks are a powerful indicator of whether there might be possible material shortages for the economy in the context of geopolitical constraints and monopolistic supply chains. Furthermore, based on projected industrial synthesis routes, economic and environmental parameters of precursor materials of the perovskites can already be related to the mass activity of model catalysts in the lab-scale. Environmental impact categories considered in life cycle assessment can be assigned to the electrocatalyst precursor materials, uncovering possible hotspots. Social impacts can also be considered on a qualitative scale to identify if, for example, poor working conditions exist in raw material extraction. Moreover, secondary material input from recycling presents an attractive parameter if a sufficient supply is offered on the commodity market. Although final industrial synthesis routes and the industrial catalyst performance cannot be determined at the stage of our lab-based tests, the evaluated sustainability impact of the identified precursor materials and possible supply bottlenecks remain highly relevant at the industrial level. Therefore, the broader view of a holistic material choice already in early-stage research can transfer and mitigate those factors to applied research and the industry, where the economic pressures and regulatory requirements grow.
In the exemplary case study, the sustainability of $La_{0.6}Sr_{0.4}CoO_{3-\delta}$ and $La_{0.6}Ca_{0.4}FeO_{3-\delta}$ was compared. The exchange from Sr to Ca is beneficial because Sr is a critical raw material in the EU, as it has only one supplying country. Furthermore, the exchange of Co to Fe is highly advantageous as the high material criticality of Co can be avoided. Co has a very concentrated supply chain where 63% of the Co production stems from the Democratic Republic of Congo, and the raw material extraction can take place under hazardous working conditions, where child labor can be involved. Additionally, the environmental impact categories, such as greenhouse

gas emissions or human toxicity, of the Co precursor production are significantly higher compared to Fe precursor production. However, the La precursor supply is a big disadvantage for all perovskites, as it has a high environmental impact, can take place under hazardous working conditions, and it is a critical raw material where 85 % are provided from China to the EU.

This thesis reveals that electrical resistivity does not imply a poor intrinsic OER activity, and even highly resistive perovskite oxide catalysts can be as active as quasimetallic catalysts. Electrocatalysts of poor conductivity often receive little attention, which may mislead the verification of catalyst design rules. For the perovskites investigated here, the O 2*p* center correlates with OER activity, which can be a promising OER descriptor to predict the structure-property relationships of the catalysts. Without the decoupling of the electrical resistivity, this could not have been verified. As the energy transition requires massive material consumption, and an established hydrogen economy is only one branch of it, early-stage materials research with less critical materials, higher recycling rates, and lower environmental, social, and economic impact can drive a successful and especially feasible energy transition.

A Epitaxial growth and valence band of $LaNiO_{3-\delta}$ and $La_{0.67}Sr_{0.33}MnO_{3-\delta}$

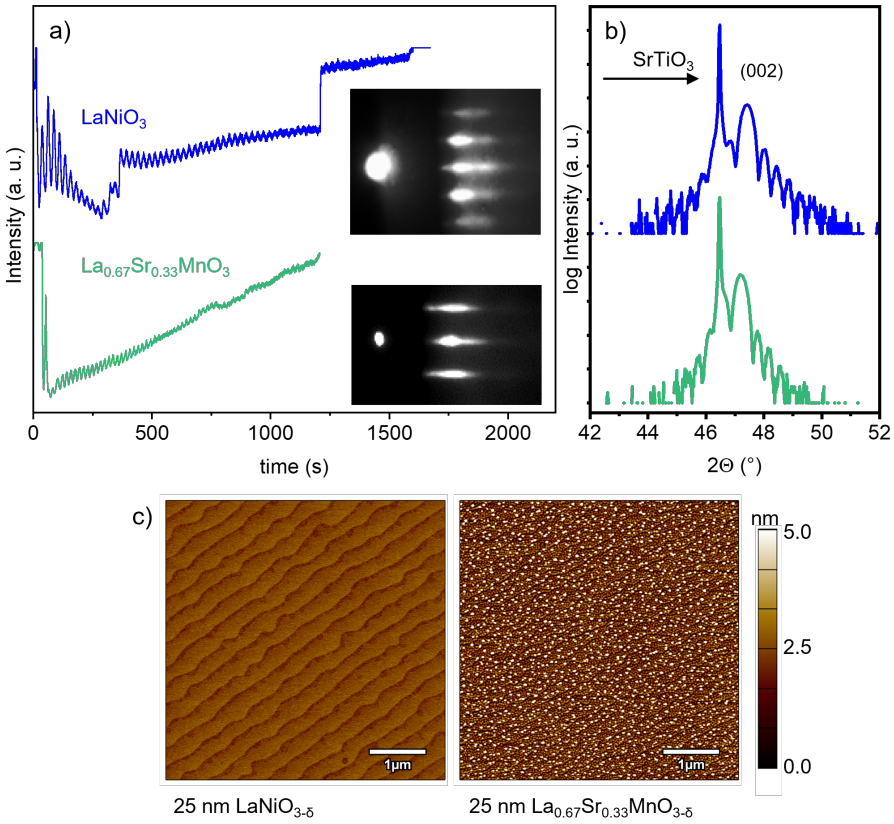

Figure A.1: a) RHEED intensity oscillations of the specular spot for 25 nm thick $LaNiO_{3-\delta}$, $La_{0.67}Sr_{0.33}MnO_{3-\delta}$ thin films deposited on $SrTiO_3$. Inset: final RHEED pattern. b) XRD of the two thin films after electrochemical treatment. c) AFM scans of the corresponding thin films. The thin films were fabricated by Iris van den Bosch, Emma van der Minne and Ellen Kiens at the University of Twente (Netherlands).

The thin films grow in a layer-by-layer mode where in the case of $La_{0.67}Sr_{0.33}MnO_{3-\delta}$, the RHEED oscillations start to fade out after 800 s (figure A.1). The sharp intensity increase seen for the $LaNiO_{3-\delta}$ growth stems from manually increased primary beam intensity at around 360 s and 1210 s. The corresponding RHEED patterns are shown on the right as insets after 25 nm

thin film growth. Figure A.1b shows the X-ray diffraction patterns of the corresponding thin films. The diffractograms were obtained after electrochemical treatment, confirming the high crystalline quality throughout the application. As shown in figure A.1c $LaNiO_{3-\delta}$ exhibits smooth, step-terraced morphology. The $La_{0.67}Sr_{0.33}MnO_{3-\delta}$ surface exhibits small islands of 7 nm height on top of the step-terraces. We find that the islands do not have a major impact on the electrocatalytic properties by comparison to thinner films which do not exhibit such islands [22, 242]. Furthermore, the resulting surface area deviates below 2 % compared to the geometric surface area. Thus, the surface area is very similar for all thin films which cannot significantly influence the catalytic activity.

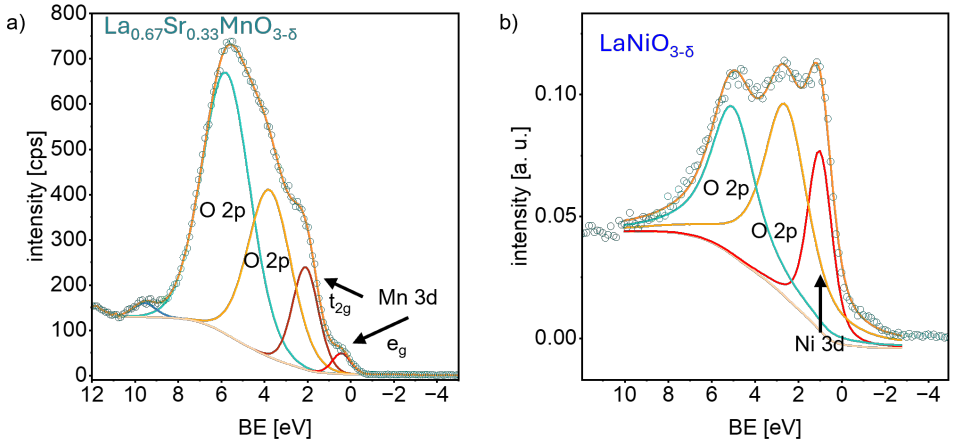

Figure A.2: XPS valence band spectrum with component fits of a) $La_{0.67}Sr_{0.33}MnO_{3-\delta}$ measured by Emma van der Minne. b) XPS valence band spectrum of $LaNiO_{3-\delta}$ which was taken from Kante *et al*. [170], with the CC-BY 4.0 license.
$La_{0.67}Sr_{0.33}MnO_{3-\delta}$ shows a small peak at low binding energies which is attributed to the e_g states. The dark red peak at 2.1 eV is attributed to the Mn 3*d* t_{2g} states. The states above that (here the yellow and blue peak) are attributed to the O 2*p* and hybrid Mn and O 2*p* states [64, 66, 71]. Therefore, these two peaks are considered to determine the O 2*p* centroid. The crystal field splitting is smaller for the ferrates, cobaltates, and nickelates than for the manganate according to ref. [172] as the crystal field splitting reduces with higher *d*-electron number. This might explain why $La_{0.67}Sr_{0.33}MnO_{3-\delta}$ shows distinct Mn 3d t_{2g} and e_g states.

B AFM of thin films on Nb:$SrTiO_3$ with $LaAlO_3$ interlayer

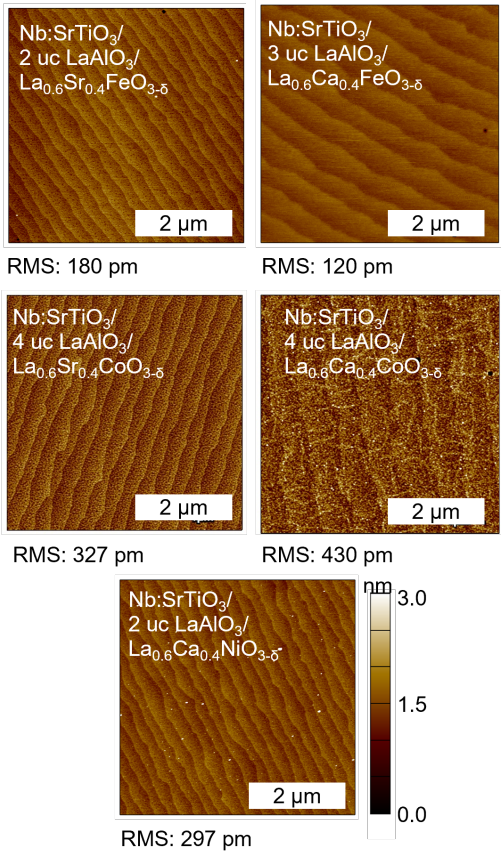

Figure B.1: AFM of the five perovskites grown by PLD on Nb:$SrTiO_3$ with 2-4 unit cell thick $LaAlO_3$ interlayer. The thin films were used for electrochemical characterization.

C price information of perovskite oxide precursors

Table C.1: The table shows the information sources of $La_{0.6}Sr_{0.4}CoO_{3-\delta}$ and $La_{0.6}Ca_{0.4}FeO_{3-\delta}$ precursor material prices and the prices per kg or ton. Moreover, the table shows which price is globally available, which prices were requested or considered domestically, and on which date the price was determined or the price estimate received.

Precursor	Company and website	Global or domestic	Price	Purity	Date (web-site visited)	Date of price
Cobalt oxide	Institut für seltene Erden: https://ise-metal-quotes.com/	global and delivered to EU	17.40 €/kg (warehouse Rotterdam)	72 % min	21.02.2024 13:30	Average price of the last 6 months
Lanthanum oxide	Institut für seltene Erden https://ise-metal-quotes.com/	global	0.76 €/kg (FOB China)	99.9 %	21.02.2023 13:35	Average price of the last 6 months
New Fe scrap: type 2/8	BDSV - Bundesvereinigung Deutscher Stahlrecycling- und Entsorgungsunternehmen e.V. https://www.bdsv.org/unser-service/markt-preise/	Germany	357 €/t	–	21.02.2024 14:05	Average price January 2024
Strontium carbonate	Kandelium: personal request https://www.kandelium.com/	Germany	1500 €/t	98 %	Price estimate sent: 29.01.2024	Price January 2024
Calcium carbonate	BÜFA chemicals: personal request https://buefa-chemicals.de/	Germany	855 €/t	98 %	Price estimate sent: 29.02.2024	Price Februrary 2024

D Material criticality underlying equations

In the EC-CRM 2023 assessment, a raw material is considered critical above a supply risk (SR) of 1 and an economic importance (EI) of 2.8 [93, 142]. The EI represents the relevance of a raw material in an end-use application with its value added to the European economy. The EI of a raw material is determined for each relevant NACE manufacturing sector (s) on a 2-digit level [93, 142] (NACE represents the "statistical classification of economic activities in the European Community"). For example, the relevant sectors for cobalt usage are "Manufacture of fabricated metal products, except machinery and equipment" and "Manufacture of chemicals and chemical products" [93]. The raw material EI is calculated as sum of the share (A_s) of each raw material's end use in a NACE sector multiplied by the value added (Q_s) and corrected by the substitution index (SI_{EI}). To calculate the SI_{EI} the substitution of a raw material to another is related to its technical performance and cost changes in the end-use application.

$$EI = \sum_{s} (A_s * Q_s) * SI_{EI} \tag{D.1}$$

A_s = share of the end use of a raw material in a NACE sector
Q_s = the value added of each NACE sector
SI_{EI} = substitution index related to the economic importance
SR is calculated by the raw material supplier concentration of countries inside (denoted as EU source) and outside the EU (global) and weighted with the import reliance (IR) of raw-material supply from non-EU countries. The supplier concentration is calculated with the Herfindahl-Hirschmann index by the supply share (S_c) of each country (c) in either global supply or EU sourcing of the raw material multiplied with the world governance index (WGI) and country specific export restrictions t_c (export tax, trade agreement, export quota, export prohibition). The factors of end-of-life recycling input rate (EOL-RIR) and substitution index (SI) are risk-reducing factors for the supply risk [93, 142].

$$SR = \left[(HHI_{WGI,t})_{global} \cdot \frac{IR}{2} + (HHI_{WGI,t})_{EU\ source} \cdot \left(1 - \frac{IR}{2}\right) \right] \cdot (1 - EOL\_RIR) \cdot SI_{SR} \tag{D.2}$$

$$HHI_{WGI,t(global;EU)} = \sum_{c} (S_c)^2 \cdot WGI_c \cdot t_c \tag{D.3}$$

SR = supply risk; HHI = Herfindahl-Hirschmann Index including the world governance index (WGI) and t_c export specific restrictions; S_c = share of supply of country c; IR = import reliance; EOL-RIR = end-of-life recycling input rate; SI = substitution index

E Impedance and COMSOL study remarks

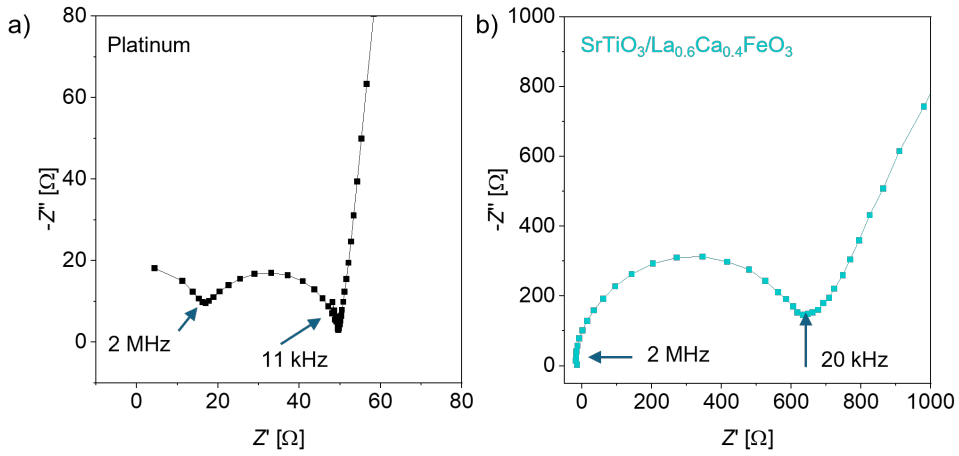

Figure E.1: a) Nyquist plot of a Pt sample in the high frequency range. The sample was placed in 0.1 M KOH and the impedance was measured at OCP. There is a semicircle observed between 2 MHz and 11 kHz. When the reference electrode is equipped with a shunt that consists of a Pt wire and capacitor in parallel, the impedance feature systematically changes with capacitor size (section 3.6.2) Hence, the impedance feature can be attributed to the frit of the reference electrode, as was also described in the literature [138]. At 11 kHz, the imaginary part of the impedance is zero and the x-axis offset represents the uncompensated resistance Ru. At lower frequencies, a large incline is seen which is attributed to the working electrode solid/liquid interface. b) Nyquist plot of 25 nm $La_{0.6}Ca_{0.4}FeO_{3-\delta}$ on $SrTiO_3$ in the high frequency range. The impedance signal from the reference electrode (dominating at high frequencies) overlaps with the impedance signal of the working electrode and therefore -Z'' does not reach zero. This hinders an accurate determination of the R_u.

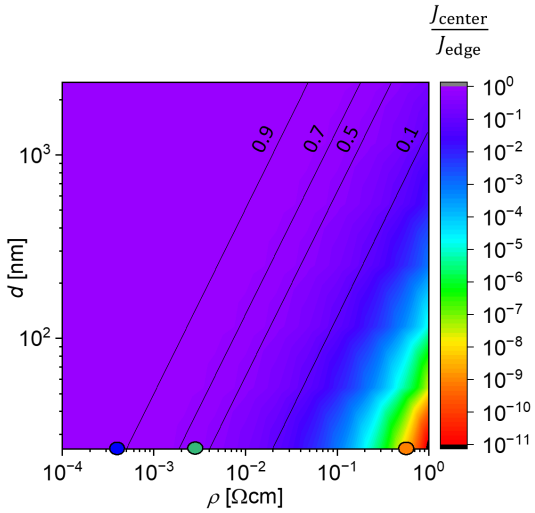

Figure E.2: Heatmap of the $(J_{center})/J_{edge}$ ratio on a logarithmic scale to obtain the rapidly increasing inhomogeneity above a resistivity of $2 \times 10^{-2}\,\Omega\,cm$.

The purpose of the COMSOL simulations is to quantify inhomogeneities in the current distributions caused by the resistivity of the catalyst thin films. Importantly, as addressed in the manuscript, other inhomogeneities can occur from electrolyte effects where Tafel polarization dominates. According to Newman [243] the value of the term:

$$\frac{\beta Z F}{R T} \cdot \frac{r_0 i_{avg}}{\kappa_\infty} \tag{E.4}$$

estimates the extent of the inhomogeneities in this scenario. β denotes the symmetry factor of the reaction, Z is the number of charges of the redox reaction, r_0 the radius of the disk, i_{avg} the average current density and κ_∞ the conductivity of the solution. In our experiment κ_∞ is 0.02 S/cm, r_0 is 0.375 mm and i_{avg} is $1\,mA\,cm^{-2}$, as also taken into account in the COMSOL study. Under the assumption that $\beta = -0.5$, the equation E.4 yields the value 1.3. This corresponds to a rather linear inhomogeneous current density distribution along the electrode with a ratio of $\frac{i}{i_{avg}} \approx 0.9$ in the sample center whereas the inhomogeneity $\frac{i}{i_{avg}}$ caused by the thin film catalyst resistivity can be orders of magnitude higher as in the case for $La_{0.6}Ca_{0.4}FeO_{3-\delta}$ with $\frac{i}{i_{avg}} \approx 3.6 \times 10^{-6}$.

F Electrochemical characterization (pre-) OER sweeps

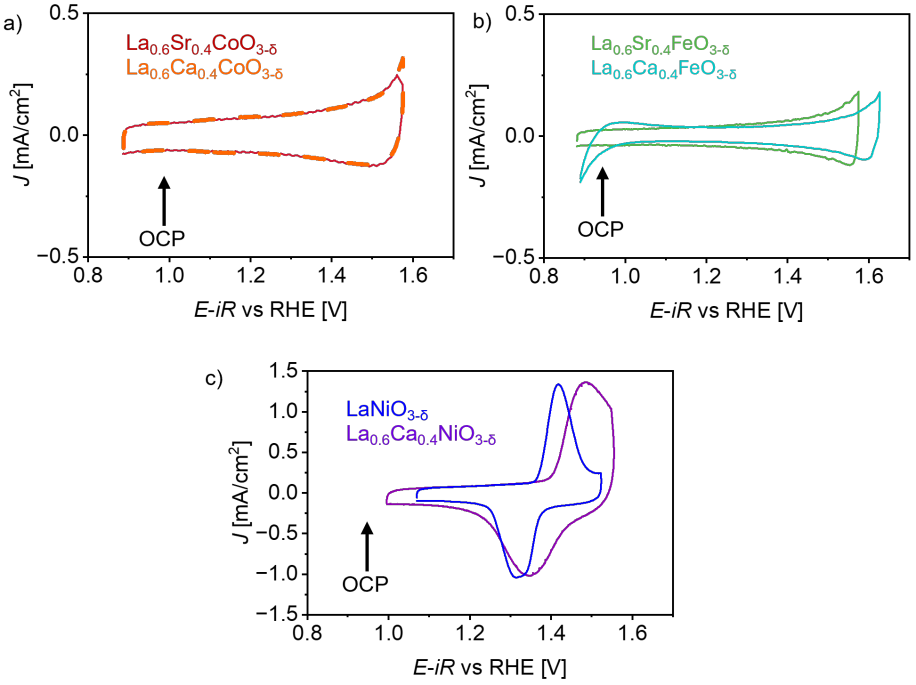

Figure F.1: CV scans of a) $La_{0.6}Sr_{0.4}CoO_{3-\delta}$, $La_{0.6}Ca_{0.4}CoO_{3-\delta}$ b) $La_{0.6}Sr_{0.4}FeO_{3-\delta}$, $La_{0.6}Ca_{0.4}FeO_{3-\delta}$ and c) $LaNiO_{3-\delta}$, $La_{0.6}Ca_{0.4}NiO_{3-\delta}$ from 0.9/1.0 V to about 1.6 V vs RHE with a scan rate of 500 mV s^{-1}. $La_{0.6}Ca_{0.4}FeO_{3-\delta}$ undergoes a redox reaction in the OCP region, causing a lower impedance value at the solid/liquid interface. This is not the case for the other perovskites. Nevertheless, all perovskites show redox reactions towards the OER voltage regime. The two Nickelates exhibit strong redox peaks around 1.4 V vs RHE which is attributed to Ni^{2+}/Ni^{3+} [19].

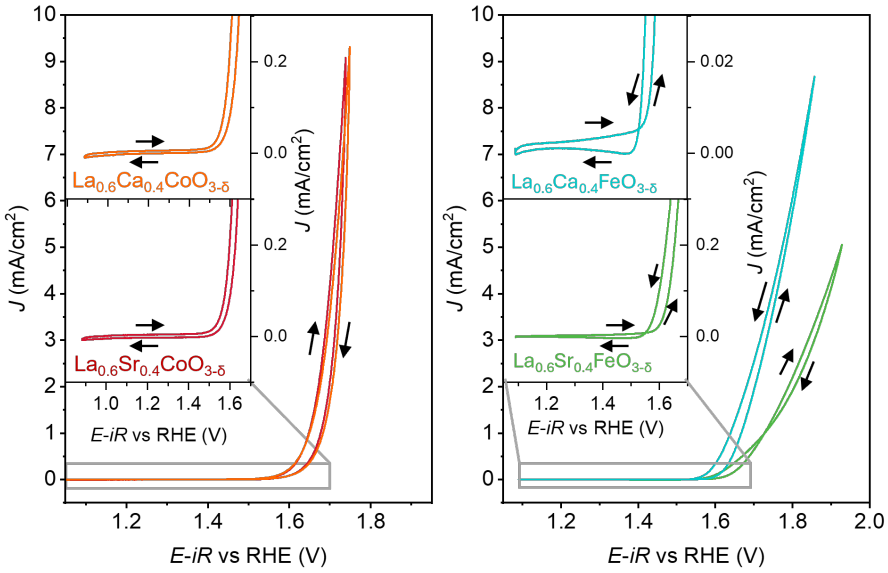

Figure F.2: CV scan from close to OCP to the OER voltage regime. The scan rate was 10 mV/s. a) shows the CV from the two cobaltates grown on insulating substrates $NdGaO_3$ and $LaAlO_3$. The hysteresis is caused by capacitive charging and discharging. b) shows the CV of the two ferrates. The hysteresis is anomalous. The backward sweep shows higher current densities than the forward sweep from the current density maximum to 1.5 V vs RHE. Then it crosses the forward sweep. The backward sweep of $La_{0.6}Sr_{0.4}FeO_{3-\delta}$ crosses at around 1.7 V vs RHE the forward sweep for the first time and at 1.5 V vs RHE for the second time. The reasons could be a change in coverage, rate-determining step or change in oxidation state. However, this remains an open question.

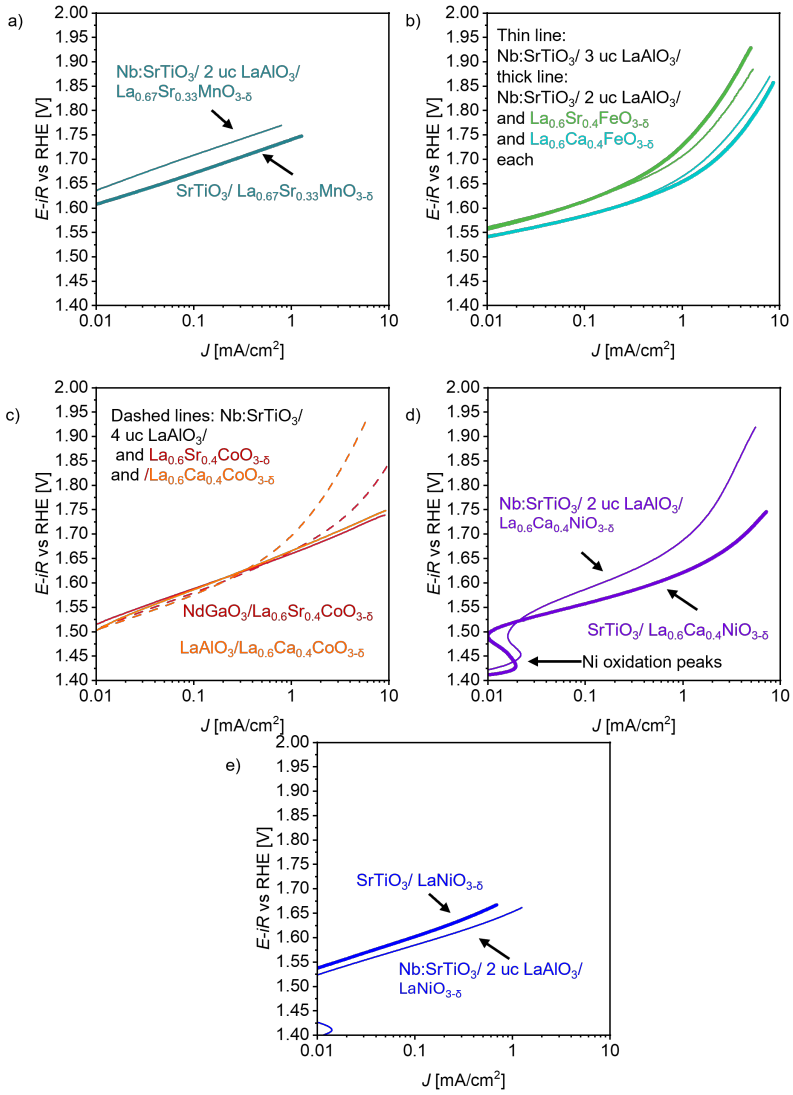

Figure F.3: Tafel-like plots for the seven perovskites. The CV scans were used to define the average overpotential and Tafel slopes in figure 49. For the nickelates, cobaltates and the manganate both contacting geometries were considered in the low current density range of up to 0.2 mA cm^{-2}. For the ferrates, only the back side contacted samples on the Nb:$SrTiO_3$/$LaAlO_3$ stacks are considered.

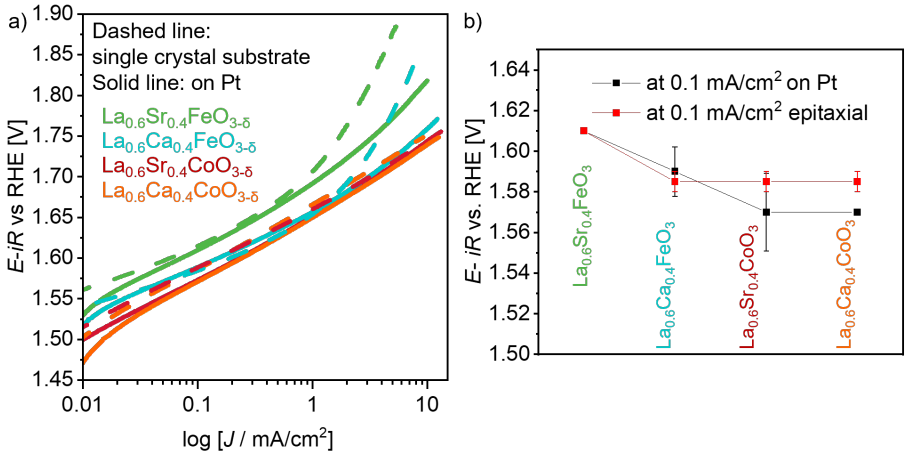

Figure F.4: a) Compares representative CV curves of $La_{0.6}Sr_{0.4}FeO_{3-\delta}$, $La_{0.6}Ca_{0.4}FeO_{3-\delta}$, $La_{0.6}Sr_{0.4}CoO_{3-\delta}$ and $La_{0.6}Ca_{0.4}CoO_{3-\delta}$ grown on single-crystal substrates (the ferrates on Nb:$SrTiO_3$/$LaAlO_3$, $La_{0.6}Sr_{0.4}CoO_{3-\delta}$ on $NdGaO_3$ and $La_{0.6}Ca_{0.4}CoO_{3-\delta}$ on $LaAlO_3$) with the thin films grown on Pt from figure 50b. In the low current density range (0.1-1 mA cm^{-2}), the OER activity of the ferrates grown on single crystalline substrates is very similar to that of the ferrates grown on Pt. Therefore, the influence of the different surface roughnesses, crystal facets, or grain boundaries on the ferrate OER activity seems small. At high current densities, the ferrates grown on Pt remain with high activity, while the ferrates grown on Nb:$SrTiO_3$/$LaAlO_3$/thin film show increasing overpotential due to the remaining substrate/thin film interface resistance. Still, a change in slope is seen for the ferrates grown on Pt, which stems from changes in reaction kinetics or small thin film resistances as seen in figure 50c. The two cobaltates grown on single-crystal substrates show slightly higher overpotentials at low current densities compared to the thin films deposited on Pt, but are similar in the higher current density range. Possibly, crystal facet orientation or grain boundary effects might play a role here. However, the surface roughness seems to have a minor influence, as for example the $La_{0.6}Ca_{0.4}CoO_{3-\delta}$ film on Pt has an RMS of 11 nm while the single crystal has an RMS below 1 nm. b) OER potential at a current density of 0.1 mA cm^{-2} of the epitaxial thin films in comparison to the polycrystalline thin films grown on Pt. The error bar stems from three different samples grown on Pt. The error bars for the epitaxial thin films stem from two averaged samples. The two ferrates show on both substrate types similar OER activity at this current density. The two cobaltates vary slightly. On Pt, the OER potential is lower for the cobaltates, but the standard deviation of $La_{0.6}Sr_{0.4}CoO_{3-\delta}$ is much higher than for the ferrates. This might result from a higher influence of e.g. different crystal facets or grain boundaries. Some $La_{0.6}Ca_{0.4}FeO_{3-\delta}$ thin films grown on Pt had the same catalytic activity as some $La_{0.6}Sr_{0.4}CoO_{3-\delta}$ thin film layers on Pt.

References

1. United Nations / Framework Convention on Climate Change. Adoption of the Paris Agreement, 21st Conference of the Parties, Paris: United Nations. https://unfccc.int/documents/184656 (2018).
2. American Chemical Society. Shifting from a Fuel-Intensive, to a Material-Intensive World. *ACS Industry Matters Newsletter.* https://www.acs.org/industry/industry-matters/mark-e-jones/future-elements.html (2021).
3. International Energy Agency IEA. The Role of Critical Minerals in Clean Energy Transitions. https://www.iea.org/reports/the-role-of-critical-minerals-in-clean-energy-transitions (2021).
4. European Commission. *Critical raw materials for strategic technologies and sectors in the EU - a foresight study* ISBN: 978-92-76-15336-8. doi:10.2873/865242 (2020).
5. Carrara, S., Bobba, S., Blagoeva, D., Alves Dias, P., Cavalli, A., Georgitzikis, K., Grohol, K., Itul, A., Kuzov, T., Latunussa, C., Lyons, L., Malano, G., Maury, T., Prior Arce, A., Somers, J., Telsnig, T., Veeh, C., Wittmer, D., Black, C., Pennington, D. & Christou, M. *Supply chain analysis and material demand forecast in strategic technologies and sectors in the EU – A foresight study* Policy assessment, Anticipation and foresight, Risk assessment KJ-NA-31-437-EN-N (online),KJ-NA-31-437-EN-C (print) (Publications Office of the European Union, Luxembourg (Luxembourg), 2023).
6. Rahimpour, S., El-Wali, M., Makarava, I., Tuomisto, H. L., Lundström, M. & Kraslawski, A. Selected social impact indicators influenced by materials for green energy technologies. *Nature Communications* **15,** 9336. ISSN: 2041-1723. https://doi.org/10.1038/s41467-024-53652-0 (2024).
7. Buttler, A. & Spliethoff, H. Current status of water electrolysis for energy storage, grid balancing and sector coupling via power-to-gas and power-to-liquids: A review. *Renewable and Sustainable Energy Reviews* **82,** 2440–2454. ISSN: 1364-0321. https://www.sciencedirect.com/science/article/pii/S136403211731242X (Feb. 1, 2018).
8. Götz, M., Lefebvre, J., Mörs, F., McDaniel Koch, A., Graf, F., Bajohr, S., Reimert, R. & Kolb, T. Renewable Power-to-Gas: A technological and economic review. *Renewable Energy* **85,** 1371–1390. ISSN: 0960-1481. https://www.sciencedirect.com/science/article/pii/S0960148115301610 (Jan. 1, 2016).
9. Bailera, M., Lisbona, P., Romeo, L. M. & Espatolero, S. Power to Gas projects review: Lab, pilot and demo plants for storing renewable energy and CO2. *Renewable and Sustainable Energy Reviews* **69,** 292–312. ISSN: 1364-0321. https://www.sciencedirect.com/science/article/pii/S1364032116307833 (Mar. 1, 2017).

10. Xie, X., Du, L., Yan, L., Park, S., Qiu, Y., Sokolowski, J., Wang, W. & Shao, Y. Oxygen Evolution Reaction in Alkaline Environment: Material Challenges and Solutions. *Advanced Functional Materials* **32,** 2110036. ISSN: 1616-301X. https://doi.org/10.1002/adfm.202110036 (May 1, 2022).

11. Liu, J., Liu, H., Chen, H., Du, X., Zhang, B., Hong, Z., Sun, S. & Wang, W. Progress and Challenges Toward the Rational Design of Oxygen Electrocatalysts Based on a Descriptor Approach. *Advanced Science* **7,** 1901614. ISSN: 2198-3844. https://doi.org/10.1002/advs.201901614 (Jan. 1, 2020).

12. Eikeng, E., Makhsoos, A. & Pollet, B. G. Critical and strategic raw materials for electrolysers, fuel cells, metal hydrides and hydrogen separation technologies. *International Journal of Hydrogen Energy* **71,** 433–464. ISSN: 0360-3199. https://www.sciencedirect.com/science/article/pii/S036031992401783X (2024).

13. Suntivich, J., May, K. J., Gasteiger, H. A., Goodenough, J. B. & Shao-Horn, Y. A Perovskite Oxide Optimized for Oxygen Evolution Catalysis from Molecular Orbital Principles. *Science* **334,** 1383–1385. https://doi.org/10.1126/science.1212858 (2011).

14. Hong, W. T., Stoerzinger, K. A., Lee, Y.-L., Giordano, L., Grimaud, A., Johnson, A. M., Hwang, J., Crumlin, E. J., Yang, W. & Shao-Horn, Y. Charge-transfer-energy-dependent oxygen evolution reaction mechanisms for perovskite oxides. *Energy & Environmental Science* **10,** 2190–2200. ISSN: 1754-5692. http://dx.doi.org/10.1039/C7EE02052J (2017).

15. Cheng, X., Fabbri, E., Yamashita, Y., Castelli, I. E., Kim, B., Uchida, M., Haumont, R., Puente-Orench, I. & Schmidt, T. J. Oxygen Evolution Reaction on Perovskites: A Multieffect Descriptor Study Combining Experimental and Theoretical Methods. *ACS Catalysis* **8,** 9567–9578. https://doi.org/10.1021/acscatal.8b02022 (2018).

16. Mefford, J. T., Rong, X., Abakumov, A. M., Hardin, W. G., Dai, S., Kolpak, A. M., Johnston, K. P. & Stevenson, K. J. Water electrolysis on $La_{1-x}Sr_xCoO_{3-\delta}$ perovskite electrocatalysts. *Nature Communications* **7,** 11053. ISSN: 2041-1723. https://doi.org/10.1038/ncomms11053 (2016).

17. Zhang, M., Jeerh, G., Zou, P., Lan, R., Wang, M., Wang, H. & Tao, S. Recent development of perovskite oxide-based electrocatalysts and their applications in low to intermediate temperature electrochemical devices. *Materials Today* **49,** 351–377. ISSN: 1369-7021. https://www.sciencedirect.com/science/article/pii/S1369702121001607 (Oct. 1, 2021).

18. Zhao, J.-W., Li, Y., Luan, D. & Lou, X. W. (Structural evolution and catalytic mechanisms of perovskite oxides in electrocatalysis. *Science Advances* **10,** eadq4696. https://doi.org/10.1126/sciadv.adq4696 (2024).

19. Baeumer, C., Li, J., Lu, Q., Liang, A. Y.-L., Jin, L., Martins, H. P., Duchoň, T., Glöß, M., Gericke, S. M., Wohlgemuth, M. A., Giesen, M., Penn, E. E., Dittmann, R., Gunkel, F., Waser, R., Bajdich, M., Nemšák, S., Mefford, J. T. & Chueh, W. C. Tuning electrochemically driven surface transformation in atomically flat $LaNiO_3$ thin films for enhanced water electrolysis. *Nature Materials* **20,** 674–682. ISSN: 1476-4660. https://doi.org/10.1038/s41563-020-00877-1 (2021).

20. Füngerlings, A., Wohlgemuth, M., Antipin, D., van der Minne, E., Kiens, E. M., Villalobos, J., Risch, M., Gunkel, F., Pentcheva, R. & Baeumer, C. Crystal-facet-dependent surface transformation dictates the oxygen evolution reaction activity in lanthanum nickelate. *Nature Communications* **14,** 8284. ISSN: 2041-1723. https://doi.org/10.1038/s41467-023-43901-z (Dec. 13, 2023).

21. Weber, M. L., Lole, G., Kormanyos, A., Schwiers, A., Heymann, L., Speck, F. D., Meyer, T., Dittmann, R., Cherevko, S., Jooss, C., Baeumer, C. & Gunkel, F. Atomistic Insights into Activation and Degradation of $La_{0.6}Sr_{0.4}CoO_{3-\delta}$ Electrocatalysts under Oxygen Evolution Conditions. *Journal of the American Chemical Society* **144,** 17966–17979. ISSN: 0002-7863. https://doi.org/10.1021/jacs.2c07226 (Oct. 5, 2022).

22. Van der Minne, E., Korol, L., Krakers, L. M. A., Verhage, M., Rosário, C. M. M., Roskamp, T. J., Spiteri, R. J., Biz, C., Fianchini, M., Boukamp, B. A., Rijnders, G., Flipse, K., Gracia, J., Mul, G., Hilgenkamp, H., Green, R. J., Koster, G. & Baeumer, C. The effect of intrinsic magnetic order on electrochemical water splitting. *Applied Physics Reviews* **11,** 011420. ISSN: 1931-9401. https://doi.org/10.1063/5.0174662 (Mar. 2024).

23. Antipin, D. & Risch, M. Trends of epitaxial perovskite oxide films catalyzing the oxygen evolution reaction in alkaline media. *Journal of Physics: Energy* **2,** 032003. ISSN: 2515-7655. http://dx.doi.org/10.1088/2515-7655/ab812f (2020).

24. Egelund, S., Caspersen, M., Nikiforov, A. & Møller, P. Manufacturing of a $LaNiO_3$ composite electrode for oxygen evolution in commercial alkaline water electrolysis. *International Journal of Hydrogen Energy* **41,** 10152–10160. ISSN: 0360-3199. https://www.sciencedirect.com/science/article/pii/S0360319916314690 (June 29, 2016).

25. Lakhanlal & Caspary Toroker, M. Filling the gaps on the relation between electronic conductivity and catalysis of electrocatalysts for water splitting using computational modelling. *Current Opinion in Electrochemistry* **40,** 101342. ISSN: 2451-9103. https://www.sciencedirect.com/science/article/pii/S2451910323001357 (Aug. 1, 2023).

26. Klemenz, S., Stegmüller, A., Yoon, S., Felser, C., Tüysüz, H. & Weidenkaff, A. Holistic View on Materials Development: Water Electrolysis as a Case Study. *Angewandte Chemie International Edition* **60,** 20094–20100. ISSN: 1433-7851. https://doi.org/10.1002/anie.202105324 (Sept. 6, 2021).

27. Helbig, C., Kolotzek, C., Thorenz, A., Reller, A., Tuma, A., Schafnitzel, M. & Krohns, S. Benefits of resource strategy for sustainable materials research and development. *Sustainable Materials and Technologies* **12,** 1–8. ISSN: 2214-9937. https://www.sciencedirect.com/science/article/pii/S2214993716300689 (July 1, 2017).

28. Hofmann, M., Hofmann, H., Hagelüken, C. & Hool, A. Critical raw materials: A perspective from the materials science community. *Sustainable Materials and Technologies* **17,** e00074. ISSN: 2214-9937. https://www.sciencedirect.com/science/article/pii/S2214993717300969 (2018).

29. Porzio, J. & Scown, C. D. Life-Cycle Assessment Considerations for Batteries and Battery Materials. *Advanced Energy Materials* **11,** 2100771. https://onlinelibrary.wiley.com/doi/abs/10.1002/aenm.202100771 (2021).

30. Sharma, S. S. & Manthiram, A. Towards more environmentally and socially responsible batteries. *Energy Environ. Sci.* **13,** 4087–4097. http://dx.doi.org/10.1039/D0EE02511A (2020).

31. Seitz, L. C., Dickens, C. F., Nishio, K., Hikita, Y., Montoya, J., Doyle, A., Kirk, C., Vojvodic, A., Hwang, H. Y., Norskov, J. K. & Jaramillo, T. F. A highly active and stable $IrO_x/SrIrO_3$ catalyst for the oxygen evolution reaction. *Science* **353,** 1011–1014. https://www.science.org/doi/abs/10.1126/science.aaf5050 (2016).

32. Akbashev, A. R., Zhang, L., Mefford, J. T., Park, J., Butz, B., Luftman, H., Chueh, W. C. & Vojvodic, A. Activation of ultrathin $SrTiO_3$ with subsurface $SrRuO_3$ for the oxygen evolution reaction. *Energy Environ. Sci.* **11,** 1762–1769. http://dx.doi.org/10.1039/C8EE00210J (2018).

33. Weber, M. L. & Gunkel, F. Epitaxial catalysts for oxygen evolution reaction: model systems and beyond. *Journal of Physics: Energy* **1,** 031001. ISSN: 2515-7655. http://dx.doi.org/10.1088/2515-7655/ab1577 (July 25, 2019).

34. Heymann, L., Weber, M. L., Wohlgemuth, M., Risch, M., Dittmann, R., Baeumer, C. & Gunkel, F. Separating the Effects of Band Bending and Covalency in Hybrid Perovskite Oxide Electrocatalyst Bilayers for Water Electrolysis. *ACS Applied Materials & Interfaces* **14,** 14129–14136. ISSN: 1944-8244. https://doi.org/10.1021/acsami.1c20337 (Mar. 30, 2022).

35. Shen, Z., Zhuang, Y., Li, W., Huang, X., Oropeza, F. E., Hensen, E. J. M., Hofmann, J. P., Cui, M., Tadich, A., Qi, D., Cheng, J., Li, J. & Zhang, K. H. L. Increased activity in the oxygen evolution reaction by Fe4+-induced hole states in perovskite $La_{1-x}Sr_xFeO_3$. *Journal of Materials Chemistry A* **8,** 4407–4415. ISSN: 2050-7488. http://dx.doi.org/10.1039/C9TA13313E (2020).

36. Sun, Y., Liu, Z., Zhang, W., Chu, X., Cong, Y., Huang, K. & Feng, S. Unfolding B-O-B Bonds for an Enhanced ORR Performance in ABO_3-Type Perovskites. *Small* **15,** 1803513. ISSN: 1613-6810. https://doi.org/10.1002/smll.201803513 (July 1, 2019).

37. Gupta, S., Kellogg, W., Xu, H., Liu, X., Cho, J. & Wu, G. Bifunctional Perovskite Oxide Catalysts for Oxygen Reduction and Evolution in Alkaline Media. *Chemistry – An Asian Journal* **11,** 10–21. ISSN: 1861-4728. https://doi.org/10.1002/asia.201500640 (Jan. 1, 2016).

38. Supanchaiyamat, N. & Hunt, A. J. Conservation of Critical Elements of the Periodic Table. *ChemSusChem* **12,** 397–403. ISSN: 1864-5631. https://doi.org/10.1002/cssc.201802556 (2019).

39. Chemical society, E. *The 90 natural elements that make up everything* (2024). https://www.euchems.eu/euchems-periodic-table/.

40. Publications Office of the European Union, Tsotridis, G. & Pilenga, A. *EU harmonised protocols for testing of low temperature water electrolysers* ISBN: 978- 92-76-39266-8. doi:10.2760/58880 (2021).

41. Man, I. C., Su, H.-Y., Calle-Vallejo, F., Hansen, H. A., Martínez, J. I., Inoglu, N. G., Kitchin, J., Jaramillo, T. F., Nørskov, J. K. & Rossmeisl, J. Universality in Oxygen Evolution Electrocatalysis on Oxide Surfaces. *ChemCatChem* **3,** 1159 (2011).

42. Hong, W. T., Risch, M., Stoerzinger, K. A., Grimaud, A., Suntivich, J. & Shao-Horn, Y. Toward the rational design of non-precious transition metal oxides for oxygen electrocatalysis. *Energy & Environmental Science* **8,** 1404–1427. ISSN: 1754-5692. http://dx.doi.org/10.1039/C4EE03869J (2015).

43. Exner, K. S. Is Thermodynamics a Good Descriptor for the Activity? Re-Investigation of Sabatier's Principle by the Free Energy Diagram in Electrocatalysis. *ACS Catalysis* **9,** 5320–5329. https://doi.org/10.1021/acscatal.9b00732 (June 7, 2019).

44. Nørskov, J. K., Bligaard, T., Rossmeisl, J. & Christensen, C. H. Towards the computational design of solid catalysts. *Nature Chemistry* **1,** 37–46. ISSN: 1755-4349. https://doi.org/10.1038/nchem.121 (Apr. 1, 2009).

45. Koper, M. T. Thermodynamic theory of multi-electron transfer reactions: Implications for electrocatalysis. *Physics and Chemistry of Charge Transfer in Condensed Media* **660,** 254–260. ISSN: 1572-6657. https://www.sciencedirect.com/science/article/pii/S1572665710003917 (Sept. 15, 2011).

46. Exner, K. S. On the mechanistic complexity of oxygen evolution: potential-dependent switching of the mechanism at the volcano apex. *Materials Horizons* **10,** 2086–2095. ISSN: 2051-6347. http://dx.doi.org/10.1039/D3MH00047H (2023).

47. Antipin, D. & Risch, M. Calculation of the Tafel slope and reaction order of the oxygen evolution reaction between pH 12 and pH 14 for the adsorbate mechanism. *Electrochemical Science Advances* **3,** e2100213. ISSN: 2698-5977. https://doi.org/10.1002/elsa.202100213 (Dec. 1, 2023).

48. Fletcher, S. Tafel slopes from first principles. *Journal of Solid State Electrochemistry* **13,** 537–549. ISSN: 1433-0768. https://doi.org/10.1007/s10008-008-0670-8 (Apr. 1, 2009).

49. Koper, M. T. M. Analysis of electrocatalytic reaction schemes: distinction between rate-determining and potential-determining steps. *Journal of Solid State Electrochemistry* **17,** 339–344. ISSN: 1433-0768. https://doi.org/10.1007/s10008-012-1918-x (Feb. 1, 2013).

50. Zhu, J., Li, H., Zhong, L., Xiao, P., Xu, X., Yang, X., Zhao, Z. & Li, J. Perovskite Oxides: Preparation, Characterizations, and Applications in Heterogeneous Catalysis. *ACS Catalysis* **4,** 2917–2940. https://doi.org/10.1021/cs500606g (Sept. 5, 2014).

51. George, G., Ede, S. R. & Luo, Z. *Fundamentals of Perovskite Oxides: Synthesis, Structure, Properties and Applications (1st ed.)* ISBN: 978-0-429-35141-9. https://doi.org/10.1201/9780429351419 (CRC Press., 2020).

52. Adiga, P. & Stoerzinger, K. A. Epitaxial oxide thin films for oxygen electrocatalysis: A tutorial review. *Journal of Vacuum Science & Technology A* **40,** 010801. ISSN: 0734-2101, 1520-8559. https://pubs.aip.org/jva/article/40/1/010801/2846223/Epitaxial-oxide-thin-films-for-oxygen (Jan. 1, 2022).

53. Chen, X. & Grande, T. Anisotropic Chemical Expansion of $La_{1-x}Sr_xCoO_{3-\delta}$. *Chemistry of Materials* **25,** 927–934. ISSN: 0897-4756. https://doi.org/10.1021/cm304040p (Mar. 26, 2013).

54. Imada, M., Fujimori, A. & Tokura, Y. Metal-insulator transitions. *Reviews of Modern Physics* **70,** 1039–1263. https://link.aps.org/doi/10.1103/RevModPhys.70.1039 (Oct. 1, 1998).

55. Torrance, J. B., Lacorre, P., Asavaroengchai, C. & Metzger, R. M. Why are some oxides metallic, while most are insulating? *Physica C: Superconductivity* **182,** 351–364. ISSN: 0921-4534. https://www.sciencedirect.com/science/article/pii/0921453491905346 (1991).

56. Zaanen, J., Sawatzky, G. A. & Allen, J. W. Band gaps and electronic structure of transition-metal compounds. *Physical Review Letters* **55,** 418–421. https://link.aps.org/doi/10.1103/PhysRevLett.55.418 (July 22, 1985).

57. Green, R. J. & Sawatzky, G. A. Negative Charge Transfer Energy in Correlated Compounds. *Journal of the Physical Society of Japan* **93,** 121007. ISSN: 0031-9015. https://doi.org/10.7566/JPSJ.93.121007 (Dec. 15, 2024).

58. Arima, T., Tokura, Y. & Torrance, J. B. Variation of optical gaps in perovskite-type 3d transition-metal oxides. *Physical Review B* **48,** 17006–17009. https://link.aps.org/doi/10.1103/PhysRevB.48.17006 (Dec. 15, 1993).

59. Ma, C.-L. & Cang, J. First principles investigation on the band gap of the ground state of $LaCoO_3$. *Solid State Communications* **150,** 1983–1986. ISSN: 0038-1098. https://www.sciencedirect.com/science/article/pii/S0038109810005053 (Nov. 1, 2010).

60. Chainani, A., Mathew, M. & Sarma, D. D. Electron-spectroscopy study of the semiconductor-metal transition in $La_{1-x}Sr_xCoO_{3-\delta}$. *Physical Review B* **46,** 9976–9983. https://link.aps.org/doi/10.1103/PhysRevB.46.9976 (Oct. 15, 1992).

61. Saitoh, T., Mizokawa, T., Fujimori, A., Abbate, M., Takeda, Y. & Takano, M. Electronic structure and magnetic states in $La_{1-x}Sr_xCoO_3$ studied by photoemission and x-ray-absorption spectroscopy. *Physical Review B* **56,** 1290–1295. https://link.aps.org/doi/10.1103/PhysRevB.56.1290 (July 15, 1997).

62. Kozuka, H., Yamada, H., Hishida, T., Yamagiwa, K., Ohbayashi, K. & Koumoto, K. Electronic transport properties of the perovskite-type oxides $La_{1-x}Sr_xCoO_{3-\delta}$. *Journal of Materials Chemistry* **22,** 20217–20222. ISSN: 0959-9428. http://dx.doi.org/10.1039/C2JM34613C (2012).

63. Iwasaki, K., Ito, T., Nagasaki, T., Arita, Y., Yoshino, M. & Matsui, T. Thermoelectric properties of polycrystalline $La_{1-x}Sr_xCoO_3$. *Journal of Solid State Chemistry* **181,** 3145–3150. ISSN: 0022-4596. https://www.sciencedirect.com/science/article/pii/S0022459608004441 (Nov. 1, 2008).

64. Saitoh, T., Bocquet, A. E., Mizokawa, T., Namatame, H., Fujimori, A., Abbate, M., Takeda, Y. & Takano, M. Electronic structure of $La_{1-x}Sr_xMnO_3$ studied by photoemission and x-ray-absorption spectroscopy. *Physical Review B* **51,** 13942–13951. https://link.aps.org/doi/10.1103/PhysRevB.51.13942 (May 15, 1995).

65. Hong, W. T., Stoerzinger, K. A., Moritz, B., Devereaux, T. P., Yang, W. & Shao-Horn, Y. Probing $LaMO_3$ Metal and Oxygen Partial Density of States Using X-ray Emission, Absorption, and Photoelectron Spectroscopy. *The Journal of Physical Chemistry C* **119,** 2063–2072. ISSN: 1932-7447. https://doi.org/10.1021/jp511931y (Jan. 29, 2015).

66. Chaluvadi, S. K., Polewczyk, V., Petrov, A. Y., Vinai, G., Braglia, L., Diez, J. M., Pierron, V., Perna, P., Mechin, L., Torelli, P. & Orgiani, P. Electronic Properties of Fully Strained $La_{1-x}Sr_xMnO_{3-\delta}$ Thin Films Grown by Molecular Beam Epitaxy ($0.15 \leq x \leq 0.45$). *ACS Omega* **7,** 14571–14578. https://doi.org/10.1021/acsomega.1c06529 (May 3, 2022).

67. Wadati, H., Kobayashi, D., Kumigashira, H., Okazaki, K., Mizokawa, T., Fujimori, A., Horiba, K., Oshima, M., Hamada, N., Lippmaa, M., Kawasaki, M. & Koinuma, H. Hole-doping-induced changes in the electronic structure of $La_{1-x}Sr_xFeO_3$: Soft x-ray pho-

toemission and absorption study of epitaxial thin films. *Physical Review B* **71,** 035108. https://link.aps.org/doi/10.1103/PhysRevB.71.035108 (Jan. 20, 2005).

68. Wadati, H., Chikamatsu, A., Takizawa, M., Hashimoto, R., Kumigashira, H., Yoshida, T., Mizokawa, T., Fujimori, A., Oshima, M., Lippmaa, M., Kawasaki, M. & Koinuma, H. Strong localization of doped holes in $La_{1-x}Sr_xFeO_3$ from angle-resolved photoemission spectra. *Physical Review B* **74,** 115114. https://link.aps.org/doi/10.1103/PhysRevB.74.115114 (Sept. 19, 2006).

69. Liu, J., Jia, E., Wang, L., Stoerzinger, K. A., Zhou, H., Tang, C. S., Yin, X., He, X., Bousquet, E., Bowden, M. E., Wee, A. T. S., Chambers, S. A. & Du, Y. Tuning the Electronic Structure of $LaNiO_3$ through Alloying with Strontium to Enhance Oxygen Evolution Activity. *Advanced Science* **6,** 1901073. ISSN: 2198-3844. https://doi.org/10.1002/advs.201901073 (Oct. 1, 2019).

70. Wang, L., Maxisch, T. & Ceder, G. Oxidation Energies of Transition Metal Oxides within the GGA+U Framework. *Phys. Rev. B: Condens. Matter Mater. Phys.* **73,** 195107 (2006).

71. Bertacco, R., Tagliaferri, A., Riva, M., Signorini, L., Cantoni, M., Cattoni, A., Ciccacci, F., Davidson, B. A., Maccherozzi, F., Vobornik, I. & Panaccione, G. Surface electronic and magnetic properties of $La_{2/3}Sr_{1/3}MnO_3$ thin films with extended metallicity above the Curie temperature. *Physical Review B* **78,** 035448. https://link.aps.org/doi/10.1103/PhysRevB.78.035448 (July 31, 2008).

72. Tobe, K., Kimura, T., Okimoto, Y. & Tokura, Y. Anisotropic optical spectra in a detwinned $LaMnO_3$ crystal. *Physical Review B* **64,** 184421. https://link.aps.org/doi/10.1103/PhysRevB.64.184421 (Oct. 19, 2001).

73. Kolchugin, A., Pikalova, E., Bogdanovich, N., Bronin, D., Pikalov, S., Plaksin, S., Ananyev, M. & Eremin, V. Structural, electrical and electrochemical properties of calcium-doped lanthanum nickelate. *Proceedings of the 20th International Conference on Solid State Ionics SSI-20* **288,** 48–53. ISSN: 0167-2738. https://www.sciencedirect.com/science/article/pii/S0167273816000606 (May 1, 2016).

74. Pikalova, E., Sadykov, V., Sadovskaya, E., Yeremeev, N., Kolchugin, A., Shmakov, A., Vinokurov, Z., Mishchenko, D., Filonova, E. & Belyaev, V. Correlation between Structural and Transport Properties of Ca-Doped La Nickelates and Their Electrochemical Performance. *Crystals* **11.** ISSN: 2073-4352 (2021).

75. Zou, S., Burke, M. S., Kast, M. G., Fan, J., Danilovic, N. & Boettcher, S. W. Fe (Oxy)hydroxide Oxygen Evolution Reaction Electrocatalysis: Intrinsic Activity and the Roles of Electrical Conductivity, Substrate, and Dissolution. *Chemistry of Materials* **27,** 8011–8020. ISSN: 0897-4756. https://doi.org/10.1021/acs.chemmater.5b03404 (Dec. 8, 2015).

76. Burke, M. S., Enman, L. J., Batchellor, A. S., Zou, S. & Boettcher, S. W. Oxygen Evolution Reaction Electrocatalysis on Transition Metal Oxides and (Oxy)hydroxides: Activity Trends and Design Principles. *Chemistry of Materials* **27,** 7549–7558. ISSN: 0897-4756. https://doi.org/10.1021/acs.chemmater.5b03148 (Nov. 24, 2015).

77. Fan, L., Rautama, E. L., Lindén, J., Sainio, J., Jiang, H., Sorsa, O., Han, N., Flox, C., Zhao, Y., Li, Y. & Kallio, T. Two orders of magnitude enhancement in oxygen evolution reactivity of $La_{0.7}Sr_{0.3}Fe_{1-x}Ni_xO_{3-\delta}$ by improving the electrical conductivity. *Nano Energy* **93,** 106794. ISSN: 2211-2855. https://www.sciencedirect.com/science/article/pii/S2211285521010430 (Mar. 1, 2022).

78. Stoerzinger, K. A., Choi, W. S., Jeen, H., Lee, H. N. & Shao-Horn, Y. Role of Strain and Conductivity in Oxygen Electrocatalysis on $LaCoO_3$ Thin Films. *The Journal of Physical Chemistry Letters* **6,** 487–492. https://doi.org/10.1021/jz502692a (Feb. 5, 2015).

79. Yun, T. G., Heo, Y., Bin Bae, H. & Chung, S.-Y. Elucidating intrinsic contribution of d-orbital states to oxygen evolution electrocatalysis in oxides. *Nature Communications* **12,** 824. ISSN: 2041-1723. https://doi.org/10.1038/s41467-021-21055-0 (Feb. 5, 2021).

80. Baniecki, J. D., Yamaguchi, H., Harnagea, C., Ricinschi, D., Gu, Z., Spanier, J. E., Yamazaki, T. & Aso, H. Enhanced Stability and Thickness-Independent Oxygen Evolution Electrocatalysis of Heterostructured Anodes with Buried Epitaxial Bilayers. *Advanced Energy Materials* **9,** 1803846. ISSN: 1614-6832. https://doi.org/10.1002/aenm.201803846 (July 1, 2019).

81. Yajima, T., Hikita, Y., Minohara, M., Bell, C., Mundy, J. A., Kourkoutis, L. F., Muller, D. A., Kumigashira, H., Oshima, M. & Hwang, H. Y. Controlling band alignments by artificial interface dipoles at perovskite heterointerfaces. *Nature Communications* **6,** 6759. ISSN: 2041-1723. https://doi.org/10.1038/ncomms7759 (Apr. 7, 2015).

82. Burton, A. R., Paudel, R., Matthews, B., Sassi, M., Spurgeon, S. R., Farnum, B. H. & Comes, R. B. Thickness dependent OER electrocatalysis of epitaxial $LaFeO_3$ thin films. *J. Mater. Chem. A* **10,** 1909–1918. http://dx.doi.org/10.1039/D1TA07142D (2022).

83. Grimaud, A., May, K. J., Carlton, C. E., Lee, Y.-L., Risch, M., Hong, W. T., Zhou, J. & Shao-Horn, Y. Double perovskites as a family of highly active catalysts for oxygen evolution in alkaline solution. *Nature Communications* **4,** 2439. ISSN: 2041-1723. https://doi.org/10.1038/ncomms3439 (Sept. 17, 2013).

84. Suntivich, J., Gasteiger, H. A., Yabuuchi, N., Nakanishi, H., Goodenough, J. B. & Shao-Horn, Y. Design Principles for Oxygen-Reduction Activity on Perovskite Oxide Catalysts for Fuel Cells and Metal–Air Batteries. *Nat. Chem.* **3,** 546 (2011).

85. Grimaud, A., Diaz-Morales, O., Han, B., Hong, W. T., Lee, Y.-L., Giordano, L., Stoerzinger, K. A., Koper, M. T. M. & Shao-Horn, Y. Activating lattice oxygen redox reactions in metal oxides to catalyse oxygen evolution. *Nature Chemistry* **9,** 457–465. ISSN: 1755-4349. https://doi.org/10.1038/nchem.2695 (2017).

86. Krishnan Rajeshwar. in *Encyclopedia of Electrochemistry* (Dec. 15, 2007). ISBN: 978-3-527-61042-6. https://doi.org/10.1002/9783527610426.bard060001.

87. Yu, B., Wang, Y., Li, J., Jin, Y., Liang, Z., Zhou, L. & Chen, M. Recent advances on low-Co and Co-free high entropy layered oxide cathodes for lithium-ion batteries. *Nanotechnology* **34,** 452501. ISSN: 0957-4484. https://dx.doi.org/10.1088/1361-6528/acec4f (Aug. 25, 2023).

88. Wang, X., Ding, Y.-L., Deng, Y.-P. & Chen, Z. Ni-Rich/Co-Poor Layered Cathode for Automotive Li-Ion Batteries: Promises and Challenges. *Advanced Energy Materials* **10,** 1903864. ISSN: 1614-6832. https://doi.org/10.1002/aenm.201903864 (Mar. 1, 2020).

89. Lyu, F., Wang, Q., Choi, S. M. & Yin, Y. Noble-Metal-Free Electrocatalysts for Oxygen Evolution. *Small* **15,** 1804201. ISSN: 1613-6810. https://doi.org/10.1002/smll.201804201 (Jan. 1, 2019).

90. Bergmann, A., Martinez-Moreno, E., Teschner, D., Chernev, P., Gliech, M., de Araújo, J. F., Reier, T., Dau, H. & Strasser, P. Reversible amorphization and the catalytically active state of crystalline Co_3O_4 during oxygen evolution. *Nature Communications* **6,** 8625. ISSN: 2041-1723. https://doi.org/10.1038/ncomms9625 (Oct. 12, 2015).

91. Marelli, E., Lyu, J., Morin, M., Leménager, M., Shang, T., Yüzbasi, N. S., Aegerter, D., Huang, J., Daffé, N. D., Clark, A. H., Sheptyakov, D., Graule, T., Nachtegaal, M., Pomjakushina, E., Schmidt, T. J., Krack, M., Fabbri, E. & Medarde, M. Cobalt free layered perovskites $RBaCuFeO_{5+\delta}$ (R = 4f lanthanide) as electrocatalysts for the oxygen evolution reaction. *EES. Catal.,* 335–350. http://dx.doi.org/10.1039/D3EY00142C (2024).

92. Delmas, C. Sodium and Sodium-Ion Batteries: 50 Years of Research. *Advanced Energy Materials* **8,** 1703137. ISSN: 1614-6832. https://doi.org/10.1002/aenm.201703137 (June 1, 2018).

93. European Commission, Grohol, M. & Veeh, C. Study on the Critical Raw Materials for the EU 2023 - Final Report. ISSN: 978-92-68-00414-2 (2023).

94. International Energy Agency. *The Future of Hydrogen* (International Energy Agency (IEA), 2019). https:%20//www.iea.org/reports/the-future-of-hydrogen.

95. International labour organization. child labor in mining and global supply chains (2019).

96. International Energy Agency IEA. Global Critical Minerals Outlook 2024. https://www.iea.org/reports/global-critical-minerals-outlook-2024 (2024).

97. Fortier, S. M., Nassar, N. T., Lederer, G. W., Brainard, J., Gambogi, J. & McCullough, E. A. *Draft Critical Mineral List-Summary of Methodology and Background Information-U.S. Geological Survey Technical Input Document in Response to Secretarial Order No. 3359* 2021.

98. International Renewable Energy Agency IRENA. World Energy Transitions Outlook 2022: 1.5°C Pathway. ISSN: 978-92-9260-429-5 (2022).

99. Energy Transitions Commission. *Material and Resource Requirements for the Energy Transition* (2023). https://www.energy-transitions.org/publications/material-and-resource-energy-transition/#download-form.

100. Hubert, M. A., King, L. A. & Jaramillo, T. F. Evaluating the Case for Reduced Precious Metal Catalysts in Proton Exchange Membrane Electrolyzers. *ACS Energy Letters* **7,** 17–23. https://doi.org/10.1021/acsenergylett.1c01869 (Jan. 14, 2022).

101. Alves Dias, P., Blagoeva, D., Pavel, C., Arvanitidis, N. & of the European Union, P. O. *Cobalt: demand-supply balances in the transition to electric mobility* ISBN: 978-92-79-94311-9 (2018).

102. *Mineral commodity summaries 2024, Appendix C* Report 2024 (Reston, VA, 2024), 212. https://pubs.usgs.gov/publication/mcs2024.

103. Vesborg, P. C. K. & Jaramillo, T. F. Addressing the terawatt challenge: scalability in the supply of chemical elements for renewable energy. *RSC Advances* **2,** 7933–7947. http://dx.doi.org/10.1039/C2RA20839C (2012).

104. U.S. Geological Survey, Department of the Interior. 2022 Final List of Critical Minerals. https://www.usgs.gov/news/national-news-release/us-geological-survey-releases-2022-list-critical-minerals (2022).

105. Li, W., Li, J., Xie, G., Zhang, X. & Liu, H. Critical minerals in China: Current status, research focus and resource strategic analysis. *Earth Science Frontiers* **29,** 1–13. https://www.earthsciencefrontiers.net.cn/EN/10.13745/j.esf.sf.2022.1.25 (2022).

106. Hatayama, H. & Tahara, K. Criticality Assessment of Metals for Japan's Resource Strategy. *MATERIALS TRANSACTIONS* **56,** 229–235 (2015).

107. Su, Y. & Hu, D. Global Dynamics and Reflections on Critical Minerals. *E3S Web Conf.* **352.** https://doi.org/10.1051/e3sconf/202235203045 (2022).

108. Proost, J. State-of-the art CAPEX data for water electrolysers, and their impact on renewable hydrogen price settings. *European Fuel Cell Conference & Exhibition 2017* **44,** 4406–4413. ISSN: 0360-3199. https://www.sciencedirect.com/science/article/pii/S0360319918324157 (Feb. 15, 2019).

109. Hemauer, J., Rehfeldt, S., Klein, H. & Peschel, A. Performance and cost modelling taking into account the uncertainties and sensitivities of current and next-generation PEM water electrolysis technology. *International Journal of Hydrogen Energy* **48,** 25619–25634. ISSN: 0360-3199. https://www.sciencedirect.com/science/article/pii/S0360319923010650 (Aug. 1, 2023).

110. Ishimoto, Y., Wulf, C., Schonhoff, A. & Kuckshinrichs, W. Life cycle costing approaches of fuel cell and hydrogen systems: A literature review. *International Journal of Hydrogen Energy* **54,** 361–374. ISSN: 0360-3199. https://www.sciencedirect.com/science/article/pii/S0360319923017433 (Feb. 7, 2024).

111. Carvalho, F. P. Mining industry and sustainable development: time for change. *Food and Energy Security* **6,** 61–77. https://onlinelibrary.wiley.com/doi/abs/10.1002/fes3.109 (2017).

112. European Commission, Directorate-General for Internal Market Entrepreneurship and SMEs, I., Bobba, S., Claudiu, P., Huygens, D., Alves Dias, P., Gawlik, B., Tzimas, E., Wittmer, D., Nuss, P., Grohol, M., Saveyn, H., Buraoui, F., Orveillon, G., Hámor, T., Slavko, S., Mathieux, F., Gislev, M., Torres De Matos, C., Blengini, G., Ardente, F., Blagoeva, D. & Garbarino, E. *Report on critical raw materials and the circular economy* (Publications Office, 2018).

113. Rebitzer, G., Ekvall, T., Frischknecht, R., Hunkeler, D., Norris, G., Rydberg, T., Schmidt, W.-P., Suh, S., Weidema, B. & Pennington, D. Life cycle assessment: Part 1: Framework, goal and scope definition, inventory analysis, and applications. *Environment International* **30,** 701–720. ISSN: 0160-4120. https://www.sciencedirect.com/science/article/pii/S0160412003002459 (July 1, 2004).

114. ISO 40. *ISO 14040:2006 Environmental management - Life cycle assessment - Principles and framework* 2006. https://www.iso.org/obp/ui/en/#iso:std:iso:14040:ed-2:v1:en.

115. ISO. *ISO 14044:2006 Environmental management - Life cycle assessment - Requirements and guidelines* 2006. https://www.iso.org/standard/38498.html.

116. European Commission: The Directorate-General for Environment (DG ENV). *Recommendation on the use of Environmental Footprint methods* 2021. https://environment.ec.europa.eu/publications/recommendation-use-environmental-footprint-methods_en.

117. European Commission: The Directorate-General for Environment (DG ENV). *Annex I. Product Environmental Footprint Method* (2021).

118. Owen, J. R., Kemp, D., Lechner, A. M., Harris, J., Zhang, R. & Lèbre, É. Energy transition minerals and their intersection with land-connected peoples. *Nature Sustainability* **6,** 203–211. ISSN: 2398-9629. https://doi.org/10.1038/s41893-022-00994-6 (Feb. 1, 2023).

119. Rights office of the high commissioner, U. N. H. *Guiding Principles on Business and Human Rights: Implementing the United Nations 'Protect, Respect and Remedy' Framework* 2011. https://www.ohchr.org/sites/default/files/Documents/Publications/GuidingPrinciplesBusinessHR_EN.pdf.

120. Sartor, M., Orzes, G., Di Mauro, C., Ebrahimpour, M. & Nassimbeni, G. The SA8000 social certification standard: Literature review and theory-based research agenda. *International Journal of Production Economics* **175,** 164–181. ISSN: 0925-5273. https://www.sciencedirect.com/science/article/pii/S0925527316000621 (May 1, 2016).

121. Nations, U. *Global indicator framework for the Sustainable development Goals and targets of the 2030 Agenda for Sustainable Development* 2017.

122. Federal Ministry of Labour and Social Affairs & CSR division – Corporate Social Responsibility. *EU supply chain law initiative* EU supply chain law initiative. https://www.csr-in-deutschland.de/EN/Business-Human-Rights/Europe/EU-supply-chain-law-initiative/eu-supply-chain-law-initiative.html.

123. Herman, M. A., Richter, W. & Sitter, H. in *Epitaxy: Physical Principles and Technical Implementation* (eds Herman, M. A., Richter, W. & Sitter, H.) 81–129 (Springer Berlin Heidelberg, Berlin, Heidelberg, 2004). ISBN: 978-3-662-07064-2. https://doi.org/10.1007/978-3-662-07064-2_6.

124. Dittmann, R. *Epitaxial Growth of Complex Metal Oxides* 231–261. ISBN: 978-1-78242-245-7 (Elsevier Ltd, 2015).

125. Willmott, P. R. & Huber, J. R. Pulsed laser vaporization and deposition. *Reviews of Modern Physics* **72,** 315–328. https://link.aps.org/doi/10.1103/RevModPhys.72.315 (Jan. 1, 2000).

126. Pe´rez Casero, R., Go´mez San Roma´n, R., Mare´chal, C., Enard, J. & Perrie're, J. Laser ablation of oxides: study of the oxygen incorporation by18O isotopic tracing techniques. *Applied Surface Science* **96-98,** 697–702. ISSN: 0169-4332. https://www.sciencedirect.com/science/article/pii/0169433295005471 (Apr. 2, 1996).

127. Dittmann, R. in *Epitaxial Growth of Complex Metal Oxides* 231–261 (Elsevier Ltd, 2015). ISBN: 978-1-78242-245-7.

128. He, S. *Topotactic phase transition in $La_{0.6}Sr_{0.4}CoO_{3-\delta}$ thin films: oxygen content, dynamics and reversibility* PhD thesis (RWTH Aachen, Aachen, 2025).

129. Weber, M. L., Baeumer, C., Mueller, D. N., Jin, L., Jia, C.-L., Bick, D. S., Waser, R., Dittmann, R., Valov, I. & Gunkel, F. Electrolysis of Water at Atomically Tailored Epitaxial Cobaltite Surfaces. *Chemistry of Materials* **31,** 2337–2346. ISSN: 0897-4756. https://doi.org/10.1021/acs.chemmater.8b04577 (Apr. 9, 2019).

130. Rijnders, G. *The initial growth of complex oxides: Study and Manipulation.* PhD thesis (University of Twente, 2001).

131. Birkholz, M. *Thin Film Analysis by X-Ray Scattering* ISBN: 978-3-527-60759-4. DOI: 10.1002/3527607595 (Wiley-VCH, Oct. 26, 2005).

132. Harrington, G. F. & Santiso, J. Back-to-Basics tutorial: X-ray diffraction of thin films. *Journal of Electroceramics* **47,** 141–163. ISSN: 1573-8663. https://doi.org/10.1007/s10832-021-00263-6 (Dec. 1, 2021).

133. Miller, A. M., Lemon, M., Choffel, M. A., Rich, S. R., Harvel, F. & Johnson, D. C. Extracting information from X-ray diffraction patterns containing Laue oscillations. *Zeitschrift für Naturforschung B* **77,** 313–322. https://doi.org/10.1515/znb-2022-0020 (2022).

134. Birkholz, M. in *Thin Film Analysis by X-Ray Scattering* 143–182 (Wiley-VCH, Oct. 26, 2005). ISBN: 978-3-527-60759-4. https://doi.org/10.1002/3527607595.ch4.

135. Stevie, F. A. & Donley, C. L. Introduction to x-ray photoelectron spectroscopy. *Journal of Vacuum Science & Technology A* **38,** 063204. ISSN: 0734-2101. https://doi.org/10.1116/6.0000412 (Sept. 24, 2020).

136. Van der Pauw, L. J. A method of measuring the resistivity and Hall coefficient on lamellae of arbitrary shape. *Philips technical review* **20,** 220–224 (1958).

137. Ramadan, A., Gould, R. & Ashour, A. On the Van der Pauw method of resistivity measurements. *Thin Solid Films* **239,** 272–275. ISSN: 0040-6090. https://www.sciencedirect.com/science/article/pii/004060909490863X (Mar. 1, 1994).

138. Tran, A.-T., Huet, F., Ngo, K. & Rousseau, P. Artefacts in electrochemical impedance measurement in electrolytic solutions due to the reference electrode. *ELECTROCHEMICAL IMPEDANCE SPECTROSCOPY* **56,** 8034–8039. ISSN: 0013-4686. https://www.sciencedirect.com/science/article/pii/S0013468611000090 (Sept. 30, 2011).

139. Jorcin, J.-B., Orazem, M. E., Pébère, N. & Tribollet, B. CPE analysis by local electrochemical impedance spectroscopy. *Electrochemical Impedance Spectroscopy* **51,** 1473–1479. ISSN: 0013-4686. https://www.sciencedirect.com/science/article/pii/S0013468605008285 (Jan. 20, 2006).

140. Huang, V. M.-W., Vivier, V., Orazem, M. E., Pébère, N. & Tribollet, B. The Apparent Constant-Phase-Element Behavior of a Disk Electrode with Faradaic Reactions: A Global and Local Impedance Analysis. *Journal of The Electrochemical Society* **154,** C99. ISSN: 1945-7111. https://dx.doi.org/10.1149/1.2398894 (Dec. 15, 2006).

141. Muralidharan, V. B. Warburg impedance - basics revisited. *Anti-Corrosion Methods and Materials* **44,** 26–29. ISSN: 0003-5599 (1997).

142. European Commission, Pennington, D., Tzimas, E. & Baranzelli. *Methodology for establishing the EU list of critical raw materials - Guidelines* 2017. https://data.europa.eu/doi/10.2873/769526.

143. Zampori, L. & Pant, R. Suggestions for updating the organisation environmental footprint (OEF) method. ISSN: 1831-9424 (online),1018-5593 (print) (KJ-NA-29681-EN-N (online),KJ-NA-29681-EN-C (print) 2019).

144. Zampori, L. & Pant, R. Suggestions for updating the product environmental footprint (PEF) method. ISSN: 1831-9424 (online),1018-5593 (print) (KJ-NA-29682-EN-N (online),KJ-NA-29682-EN-C (print) 2019).

145. ecoinvent. *ecoinvent database* https://ecoinvent.org/database/.

146. Schreiber, A., Marx, J. & Zapp, P. Environmental assessment of a membrane-based air separation for a coal-fired oxyfuel power plant. *Journal of Membrane Science* **440,** 122–133. ISSN: 0376-7388. https://www.sciencedirect.com/science/article/pii/S0376738813002214 (Aug. 1, 2013).

147. Krishnan, S., Corona, B., Kramer, G. J., Junginger, M. & Koning, V. Prospective LCA of alkaline and PEM electrolyser systems. *International Journal of Hydrogen Energy* **55,** 26–41. ISSN: 0360-3199. https://www.sciencedirect.com/science/article/pii/S0360319923053405 (Feb. 15, 2024).

148. Mori, M., Stropnik, R., Sekavčnik, M. & Lotrič, A. Criticality and Life-Cycle Assessment of Materials Used in Fuel-Cell and Hydrogen Technologies. *Sustainability* **13.** ISSN: 2071-1050 (2021).

149. United Nations Environment Programme (UNEP), Traverso, M., Valdivia, S., Luthin, A., Roche, L., Arcese, G., Neugebauer, S., Petti, L., D'Eusanio, M., Tragonne, B., Hanafi, R., Benoit Norris, C. & Zamagni, A. *Methodological Sheets for Subcategories in Social Life Cycle Assessment (S-LCA)* 2021.

150. Van Haaster, B., Ciroth, A., Fontes, J., Wood, R. & Ramirez, A. Development of a methodological framework for social life-cycle assessment of novel technologies. *The International Journal of Life Cycle Assessment* **22,** 423–440. ISSN: 1614-7502. https://doi.org/10.1007/s11367-016-1162-1 (Mar. 1, 2017).

151. Thies, C., Kieckhäfer, K., Spengler, T. S. & Sodhi, M. S. Assessment of social sustainability hotspots in the supply chain of lithium-ion batteries. *26th CIRP Conference on Life Cycle Engineering (LCE) Purdue University, West Lafayette, IN, USA May 7-9, 2019* **80,** 292–297. ISSN: 2212-8271. https://www.sciencedirect.com/science/article/pii/S2212827118312885 (Jan. 1, 2019).

152. Bargiacchi, E., Campos-Carriedo, F., Iribarren, D. & Dufour, J. Social Life Cycle Assessment of a Proton Exchange Membrane Fuel Cell stack. *E3S Web Conf.* **334.** https://doi.org/10.1051/e3sconf/202233409001 (2022).

153. Schlör, H., Koj, J., Zapp, P., Schreiber, A. & Hake, J.-F. The Social Footprint of Hydrogen Production - A Social Life Cycle Assessment (S-LCA) of Alkaline Water Electrolysis. *8th International Conference on Applied Energy, ICAE2016, 8-11 October 2016, Beijing, China* **105,** 3038–3044. ISSN: 1876-6102. https://www.sciencedirect.com/science/article/pii/S187661021730680X (May 1, 2017).

154. Talens Peiro, L., Nuss, P., Mathieux, F. & Blengini, G. *Towards Recycling Indicators based on EU flows and Raw Materials system Analysis data* ISBN: 978-92-79-97247-8. doi:10.2760/092885 (2018).

155. Weidenkaff, A., Ebbinghaus, S. G. & Lippert, T. $Ln_{1-x}A_xCoO_3$ (Ln = Er, La; A = Ca, Sr)/Carbon Nanotube Composite Materials Applied for Rechargeable Zn/Air Batteries. *Chemistry of Materials* **14,** 1797–1805. ISSN: 0897-4756. https://doi.org/10.1021/cm011305v (Apr. 1, 2002).

156. Montenegro, M. J., Döbeli, M., Lippert, T., Müller, S., Schnyder, B., Weidenkaff, A., Willmott, P. R. & Wokaun, A. Pulsed laser deposition of $La_{0.6}Ca_{0.4}CoO_3$ (LCCO) films. A promising metal-oxide catalyst for air based batteries. *Physical Chemistry Chemical Physics* **4,** 2799–2805. http://dx.doi.org/10.1039/B200120A (2002).

157. He, S., Petracic, O., Lauter, V., Cao, L., Zhou, Y., Weber, M. L., Schubert, J., Concepción, O., Dittmann, R., Waser, R., Brückel, T. & Gunkel, F. $La_{0.6}Sr_{0.4}CoO_{3-\delta}$ Films Under Deoxygenation: Magnetic And Electronic Transitions Are Apart from The Structural Phase Transition. *Advanced Functional Materials* **34,** 2313208. ISSN: 1616-301X. https://doi.org/10.1002/adfm.202313208 (June 1, 2024).

158. Lee, W. & Yildiz, B. Factors that Influence Cation Segregation at the Surfaces of Perovskite Oxides. *ECS Transactions* **57,** 2115. ISSN: 1938-5862. https://dx.doi.org/10.1149/05701.2115ecst (Oct. 6, 2013).

159. Han, J. W., Jalili, H., Kuru, Y., Cai, Z. & Yildiz, B. Strain Effects on the Surface Chemistry of La0.7Sr0.3MnO3. *ECS Transactions* **35,** 2097. ISSN: 1938-5862. https://dx.doi.org/10.1149/1.3570200 (Apr. 25, 2011).

160. Huijben, M., Koster, G., Liao, Z. L. & Rijnders, G. Interface-engineered oxygen octahedral coupling in manganite heterostructures. *Applied Physics Reviews* **4,** 041103. ISSN: 1931-9401. https://doi.org/10.1063/1.4985770 (Oct. 20, 2017).

161. Park, J.-C., Kim, D.-K., Byeon, S.-H. & Kim, D. XANES study on ruddlesden-popper phase, $la_{n+1}Ni_nO_{3n+1}$ (n = 1, 2, and infinity). *Journal of Synchrotron Radiation* **8,** 704–706. https://doi.org/10.1107/S0909049500015983 (Mar. 2001).

162. Hu, Q., Li, W., Zhang, B., Sun, W., Lin, R., Jiang, H. & He, G. Uniform NiO nanoparticles used as anodes in Li-ion batteries. *IOP Conference Series: Materials Science and Engineering* **490,** 022063. ISSN: 1757-899X. https://dx.doi.org/10.1088/1757-899X/490/2/022063 (Apr. 1, 2019).

163. Liu, R., Liang, F., Zhou, W., Yang, Y. & Zhu, Z. Calcium-doped lanthanum nickelate layered perovskite and nickel oxide nano-hybrid for highly efficient water oxidation. *Nano Energy* **12,** 115–122. ISSN: 2211-2855. https://www.sciencedirect.com/science/article/pii/S2211285514002948 (Mar. 1, 2015).

164. Khine, E. E., Koncz-Horvath, D., Kristaly, F., Ferenczi, T., Karacs, G., Baumli, P. & Kaptay, G. Synthesis and characterization of calcium oxide nanoparticles for CO_2 capture. *Journal of Nanoparticle Research* **24,** 139. ISSN: 1572-896X. https://doi.org/10.1007/s11051-022-05518-z (July 1, 2022).

165. Song, J., Ning, D. & Bouwmeester, H. J. M. Influence of alkaline-earth metal substitution on structure, electrical conductivity and oxygen transport properties of perovskite-type oxides $La_{0.6}Ca_{0.4}FeO_{3-\delta}$ (A = Ca, Sr and Ba). *Physical Chemistry Chemical Physics* **22,** 11984–11995. ISSN: 1463-9076. http://dx.doi.org/10.1039/D0CP00247J (2020).

166. Sankannavar, R. & Sarkar, A. The electrocatalysis of oxygen evolution reaction on $La_{1-x}Ca_xFeO_{3-\delta}$ perovskites in alkaline solution. *International Journal of Hydrogen Energy* **43,** 4682–4690. ISSN: 0360-3199. https://www.sciencedirect.com/science/article/pii/S0360319917333384 (2018).

167. Kahoul, A., Hammouche, A., Nâamoune, F., Chartier, P., Poillerat, G. & Koenig, J. Solvent effect on synthesis of perovskite-type $La_{1-x}Ca_xCoO_3$ and their electrochemical properties for oxygen reactions. *Materials Research Bulletin* **35,** 1955–1966. ISSN: 0025-5408. https://www.sciencedirect.com/science/article/pii/S0025540800003950 (Sept. 1, 2000).

168. Boschker, H., Huijben, M., Vailionis, A., Verbeeck, J., Aert, S. v., Luysberg, M., Bals, S., Tendeloo, G. v., Houwman, E. P., Koster, G., Blank, D. H. A. & Rijnders, G. Optimized fabrication of high-quality $La_{0.67}Sr_{0.33}MnO_3$ thin films considering all essential characteristics. *Journal of Physics D: Applied Physics* **44,** 205001. https://dx.doi.org/10.1088/0022-3727/44/20/205001 (Apr. 2011).

169. Irmak, A. E. Structural and Electrical Properties of Ca^{2+} Doped $LaFeO_3$: The Effect of A-site Cation Size Mismatch. *Engineering, Technology & Applied Science Research* **Vol. 10,** 5538–5546. https://pdfs.semanticscholar.org/4127/ca913444c392fcaaf3eca11f4cd6794944dd.pdf (No. 2 2020).

170. Kante, M. V., Weber, M. L., Ni, S., van den Bosch, I. C. G., van der Minne, E., Heymann, L., Falling, L. J., Gauquelin, N., Tsvetanova, M., Cunha, D. M., Koster, G., Gunkel, F., Nemšák, S., Hahn, H., Velasco Estrada, L. & Baeumer, C. A High-Entropy Oxide as High-

Activity Electrocatalyst for Water Oxidation. *ACS Nano* **17,** 5329–5339. ISSN: 1936-0851. https://doi.org/10.1021/acsnano.2c08096 (Mar. 28, 2023).

171. Takegami, D., Nicolaï, L., Koethe, T. C., Kasinathan, D., Kuo, C. Y., Liao, Y. F., Tsuei, K. D., Panaccione, G., Offi, F., Monaco, G., Brookes, N. B., Minár, J. & Tjeng, L. H. Valence band hard x-ray photoelectron spectroscopy on 3d transition-metal oxides containing rare-earth elements. *Physical Review B* **99,** 165101. https://link.aps.org/doi/10.1103/PhysRevB.99.165101 (Apr. 2, 2019).

172. Scaramucci, A., Ammann, J., Spaldin, N. A. & Ederer, C. Separating different contributions to the crystal-field parameters using Wannier functions. *Journal of Physics: Condensed Matter* **27,** 175503. ISSN: 0953-8984. https://dx.doi.org/10.1088/0953-8984/27/17/175503 (Apr. 15, 2015).

173. Weinen, J., Koethe, T., Chang, C., Agrestini, S., Kasinathan, D., Liao, Y., Fujiwara, H., Schüßler-Langeheine, C., Strigari, F., Haupricht, T., Panaccione, G., Offi, F., Monaco, G., Huotari, S., Tsuei, K.-D. & Tjeng, L. Polarization dependent hard X-ray photoemission experiments for solids: Efficiency and limits for unraveling the orbital character of the valence band. *Journal of Electron Spectroscopy and Related Phenomena* **198,** 6–11. ISSN: 0368-2048. https://www.sciencedirect.com/science/article/pii/S0368204814002370 (Jan. 1, 2015).

174. Ahvenniemi, E., Matvejeff, M. & Karppinen, M. Atomic layer deposition of quaternary oxide (La,Sr)$CoO_{3-\delta}$ thin films. *Dalton Transactions* **44,** 8001–8006. ISSN: 1477-9226. http://dx.doi.org/10.1039/C5DT00436E (2015).

175. Trinh, B. N. Q. & Horita, S. Control of Preferential Orientation of Platinum Films on RuO_2/SiO_2/Si Substrates by Sputtering. *Japanese Journal of Applied Physics* **45,** 8810. ISSN: 1347-4065. https://dx.doi.org/10.1143/JJAP.45.8810 (Nov. 8, 2006).

176. Heymann, L., van den Bosch, I. C. G., Wielens, D. H., Kurbjeweit, O., van der Minne, E., Kiens, E. M., Kaus, A., Schön, D., Menzel, S., Boukamp, B., Gunkel, F. & Baeumer, C. Revealing the Intrinsic Oxygen Evolution Reaction Activity of Perovskite Oxides across Conductivity Ranges Using Thin Film Model Systems. *ACS Applied Materials & Interfaces* **17,** 21110–21121. ISSN: 1944-8244. https://doi.org/10.1021/acsami.4c20141 (Apr. 9, 2025).

177. Suen, N.-T., Hung, S.-F., Quan, Q., Zhang, N., Xu, Y.-J. & Chen, H. M. Electrocatalysis for the oxygen evolution reaction: recent development and future perspectives. *Chem. Soc. Rev.* **46,** 337–365. http://dx.doi.org/10.1039/C6CS00328A (2017).

178. Van der Heijden, O., Park, S., Vos, R. E., Eggebeen, J. J. J. & Koper, M. T. M. Tafel Slope Plot as a Tool to Analyze Electrocatalytic Reactions. *ACS Energy Letters* **9,** 1871–1879. https://doi.org/10.1021/acsenergylett.4c00266 (Apr. 12, 2024).

179. Davies, T. J., Banks, C. E. & Compton, R. G. Voltammetry at spatially heterogeneous electrodes. *Journal of Solid State Electrochemistry* **9,** 797–808. ISSN: 1433-0768. https://doi.org/10.1007/s10008-005-0699-x (Dec. 1, 2005).

180. Newman, J. in *Electrochemical systems* 4th ed. (John Wiley & Sons, 2021). ISBN: 978-1-119-51460-2.

181. Hirschorn, B., Orazem, M. E., Tribollet, B., Vivier, V., Frateur, I. & Musiani, M. Determination of effective capacitance and film thickness from constant-phase-element parameters. *IMPEDANCE SPECTROSCOPY AND TRANSFER FUNCTIONS* **55,** 6218–6227. ISSN: 0013-4686. https://www.sciencedirect.com/science/article/pii/S0013468609013413 (Aug. 30, 2010).

182. Pospisil, J., Marackova, L., Zmeskal, O. & Kovalenko, A. Universal approach for diffusion quantification applied to lead halide perovskite single crystals. *Applied Physics A* **129,** 129. ISSN: 1432-0630. https://doi.org/10.1007/s00339-023-06398-3 (Jan. 19, 2023).

183. Oldham, K. B. Edge effects in semiinfinite diffusion. *Journal of Electroanalytical Chemistry and Interfacial Electrochemistry* **122,** 1–17. ISSN: 0022-0728. https://www.sciencedirect.com/science/article/pii/S0022072881801362 (1981).

184. Menke, T., Meuffels, P., Dittmann, R., Szot, K. & Waser, R. Separation of bulk and interface contributions to electroforming and resistive switching behavior of epitaxial Fe-doped $SrTiO_3$. *Journal of Applied Physics* **105,** 066104. ISSN: 0021-8979. https://doi.org/10.1063/1.3100209 (Mar. 26, 2009).

185. Chien, T., Liu, J., Yost, A. J., Chakhalian, J., Freeland, J. W. & Guisinger, N. P. Built-in Electric Field Induced Mechanical Property Change at the Lanthanum Nickelate/Nb-doped Strontium Titanate Interfaces. *Scientific Reports* **6,** 19017. ISSN: 2045-2322. https://doi.org/10.1038/srep19017 (Jan. 8, 2016).

186. Yoo, H. K., Chang, Y. J., Moreschini, L., Kim, H.-D., Sohn, C. H., Sinn, S., Oh, J. S., Kuo, C.-T., Bostwick, A., Rotenberg, E. & Noh, T. W. Insulating-layer formation of metallic $LaNiO_3$ on Nb-doped $SrTiO_3$ substrate. *Applied Physics Letters* **106,** 121601. ISSN: 0003-6951. https://doi.org/10.1063/1.4916225 (Mar. 2015).

187. Lu, H. X., Zhang, J., Zhang, H. R., Li, Y., Chen, Y. S., Shen, B. G. & Sun, J. R. A conductive scanning study of $La_{0.67}Sr_{0.33}MnO_3$/Nb:$SrTiO_3$ hetero-junction. *Applied Physics Letters* **108,** 051608. ISSN: 0003-6951. https://doi.org/10.1063/1.4941419 (Feb. 4, 2016).

188. Zhan, J. M., Li, P. G., Liu, H., Tao, S. L., Ma, H., Shen, J. Q., Pan, M. J., Zhang, Z. J., Wang, S. L. & Yuan, G. L. Carrier tuning the metal-insulator transition of epitaxial $La_{0.67}Sr_{0.33}MnO_3$ thin film on Nb doped $SrTiO_3$ substrate. *AIP Advances* **6,** 045001. ISSN: 2158-3226. https://doi.org/10.1063/1.4945694 (Apr. 4, 2016).

189. Nishio, K., Shirasawa, T., Shimizu, K., Nakamura, N., Watanabe, S., Shimizu, R. & Hitosugi, T. Tuning the Schottky Barrier Height at the Interfaces of Metals and Mixed Conductors. *ACS Applied Materials & Interfaces* **13,** 15746–15754. ISSN: 1944-8244. https://doi.org/10.1021/acsami.0c18656 (Apr. 7, 2021).

190. Hikita, Y., Nishio, K., Seitz, L. C., Chakthranont, P., Tachikawa, T., Jaramillo, T. F. & Hwang, H. Y. Band Edge Engineering of Oxide Photoanodes for Photoelectrochemical Water Splitting: Integration of Subsurface Dipoles with Atomic-Scale Control. *Advanced Energy Materials* **6,** 1502154. ISSN: 1614-6832. https://doi.org/10.1002/aenm.201502154 (Apr. 1, 2016).

191. Liu, L.-B., Yi, C., Mi, H.-C., Zhang, S. L., Fu, X.-Z., Luo, J.-L. & Liu, S. Perovskite Oxides Toward Oxygen Evolution Reaction: Intellectual Design Strategies, Properties and Perspectives. *Electrochemical Energy Reviews* **7,** 14. ISSN: 2520-8136. https://doi.org/10.1007/s41918-023-00209-2 (Apr. 4, 2024).

192. Mohamed, R., Cheng, X., Fabbri, E., Levecque, P., Kötz, R., Conrad, O. & Schmidt, T. J. Electrocatalysis of Perovskites: The Influence of Carbon on the Oxygen Evolution Activity. *Journal of The Electrochemical Society* **162,** F579. https://dx.doi.org/10.1149/2.0861506jes (Mar. 2015).

193. Zhu, Y., Zhou, W. & Shao, Z. Perovskite/Carbon Composites: Applications in Oxygen Electrocatalysis. *Small* **13,** 1603793. ISSN: 1613-6810. https://doi.org/10.1002/smll.201603793 (Mar. 1, 2017).

194. Bhandari, S., Narangoda, P. V., Mogensen, S. O., Tesch, M. F. & Mechler, A. K. Effect of Experimental Parameters on the Electrocatalytic Performance in Rotating Disc Electrode Measurements: Case Study of Oxygen Evolution on Ni−Co-Oxide in Alkaline Media. *ChemElectroChem* **9,** e202200479. ISSN: 2196-0216. https://doi.org/10.1002/celc.202200479 (Sept. 13, 2022).

195. Daems, N., Breugelmans, T., Vankelecom, I. F. J. & Pescarmona, P. P. Influence of the Composition and Preparation of the Rotating Disk Electrode on the Performance of Mesoporous Electrocatalysts in the Alkaline Oxygen Reduction Reaction. *ChemElectroChem* **5,** 119–128. ISSN: 2196-0216. https://doi.org/10.1002/celc.201700907 (Jan. 2, 2018).

196. Hong, W. T., Welsch, R. E. & Shao-Horn, Y. Descriptors of Oxygen-Evolution Activity for Oxides: A Statistical Evaluation. *The Journal of Physical Chemistry C* **120,** 78–86. ISSN: 1932-7447. https://doi.org/10.1021/acs.jpcc.5b10071 (Jan. 14, 2016).

197. Baeumer, C., Liang, A. Y.-L., Trstenjak, U., Lu, Q., Waser, R., Mefford, J. T., Gunkel, F., Nemšák, S. & Chueh, W. C. Carbonate formation lowers the electrocatalytic activity of perovskite oxides for water electrolysis. *Journal of Materials Chemistry A: Materials for*

Energy and Sustainability **9,** 19940–19948. http://dx.doi.org/10.1039/D1TA03205D (2021).

198. Twight, L., Tonsberg, A., Samira, S., Velinkar, K., Dumpert, K., Ou, Y., Wang, L., Nikolla, E. & Boettcher, S. W. Trace Fe activates perovskite nickelate OER catalysts in alkaline media via redox-active surface Ni species formed during electrocatalysis. *Journal of Catalysis* **432,** 115443. ISSN: 0021-9517. https://www.sciencedirect.com/science/article/pii/S0021951724001568 (Apr. 1, 2024).

199. Trotochaud, L., Young, S. L., Ranney, J. K. & Boettcher, S. W. Nickel–Iron Oxyhydroxide Oxygen-Evolution Electrocatalysts: The Role of Intentional and Incidental Iron Incorporation. *Journal of the American Chemical Society* **136,** 6744–6753. ISSN: 0002-7863. https://doi.org/10.1021/ja502379c (May 7, 2014).

200. Heymann, L., Schreiber, A., Pithan, C., Baeumer, C. & Gunkel, F. Material sustainability evaluation of electrocatalysts in early-stage development. *pre-print.* https://chemrxiv.org/engage/chemrxiv/article-details/674337c37be152b1d09b87dd (2024).

201. Cherevko, S. Stabilization of non-noble metal electrocatalysts for acidic oxygen evolution reaction. *Current Opinion in Electrochemistry* **38,** 101213. ISSN: 2451-9103. https://www.sciencedirect.com/science/article/pii/S2451910323000066 (Apr. 1, 2023).

202. Bernt, M., Hartig-Weiß, A., Tovini, M. F., El-Sayed, H. A., Schramm, C., Schröter, J., Gebauer, C. & Gasteiger, H. A. Current Challenges in Catalyst Development for PEM Water Electrolyzers. *Chemie Ingenieur Technik* **92,** 31–39. ISSN: 0009-286X. https://doi.org/10.1002/cite.201900101 (Jan. 1, 2020).

203. C. Charles Lewchalermwong & Charlotte, N.C. *pat.* 4,808,393 (1989).

204. European Ferrous Recovery and Recycling Federation. *EU-27 Steel Scrap Specification* (2007). https://www.mgg-recycling.com/wp-content/uploads/2013/06/EFR_EU27_steel_scrap_specification.pdf.

205. Nandikes, G., Pandey, N., Pathak, P. & Singh, L. Sustainable Synthesis Strategies: A Comparative Life Cycle Perspective on $LaFeO_3$ Nanoparticles. *ACS Sustainable Chemistry & Engineering* **12,** 7603–7615. https://doi.org/10.1021/acssuschemeng.4c01930 (May 13, 2024).

206. Boulfrad, S., Cassidy, M., Djurado, E., Irvine, J. T. & Jabbour, G. Pre-coating of LSCM perovskite with metal catalyst for scalable high performance anodes. *International Journal of Hydrogen Energy* **38,** 9519–9524. ISSN: 0360-3199. https://www.sciencedirect.com/science/article/pii/S0360319912026390 (July 26, 2013).

207. Fekete, M., Hocking, R. K., Chang, S. L. Y., Italiano, C., Patti, A. F., Arena, F. & Spiccia, L. Highly active screen-printed electrocatalysts for water oxidation based on β-manganese oxide. *Energy & Environmental Science* **6,** 2222–2232. ISSN: 1754-5692. http://dx.doi.org/10.1039/C3EE40429C (2013).

208. Barbero, B. P., Cadús, L. E. & Marchetti, S. G. Determination of Fe(IV) species in partially substituted perovskite $La_{0.6}Ca_{0.4}FeO_3$. *Hyperfine Interactions* **194,** 367–379. ISSN: 1572-9540. https://doi.org/10.1007/s10751-009-9988-6 (Nov. 1, 2009).

209. Wang, J., Johnson, C., McGraw, A. & Wu, N. N. Sol-gel Synthesis and Characterization of $La_{0.6}Sr_{0.4}CoO_3$ Nanoparticles, Nanotubes, and Thin Films. *ECS Transactions* **6,** 1. ISSN: 1938-5862. https://dx.doi.org/10.1149/1.2790409 (Sept. 28, 2007).

210. Koj, J. C., Schreiber, A., Zapp, P. & Marcuello, P. Life Cycle Assessment of Improved High Pressure Alkaline Electrolysis. *Clean, Efficient and Affordable Energy for a Sustainable Future: The 7th International Conference on Applied Energy (ICAE2015)* **75,** 2871–2877. ISSN: 1876-6102. https://www.sciencedirect.com/science/article/pii/S1876610215013442 (Aug. 1, 2015).

211. Schmidt, O., Gambhir, A., Staffell, I., Hawkes, A., Nelson, J. & Few, S. Future cost and performance of water electrolysis: An expert elicitation study. *International Journal of Hydrogen Energy* **42,** 30470–30492. ISSN: 0360-3199. https://www.sciencedirect.com/science/article/pii/S0360319917339435 (2017).

212. For critical raw materials - a european expert network SCRREEN, C.-S. *FACTSHEETS UPDATES BASED ON THE EU FACTSHEETS 2020 COBALT* (2020). https://scrreen.eu/crms-2023/.

213. For critical raw materials - a european expert network SCRREEN, L.-S. *FACTSHEETS UPDATES BASED ON THE EU FACTSHEETS 2020 LIMESTONE* (2020). https://scrreen.eu/crms-2023/.

214. For critical raw materials - a european expert network SCRREEN, S.-S. *FACTSHEETS UPDATES BASED ON THE EU FACTSHEETS 2020 STRONTIUM* (2020). https://scrreen.eu/crms-2023/.

215. Ore-Solution for critical raw materials - a european expert network SCRREEN, I. *FACTSHEETS UPDATES BASED ON THE EU FACTSHEETS 2020 IRON ORE* (2020). https://scrreen.eu/crms-2023/.

216. Earth elements-Solution for critical raw materials - a european expert network SCRREEN, R. *FACTSHEETS UPDATES BASED ON THE EU FACTSHEETS 2020 RARE EARTH ELEMENTS* (2020). https://scrreen.eu/crms-2023/.

217. Häfele, S., Hauck, M. & Dailly, J. Life cycle assessment of the manufacture and operation of solid oxide electrolyser components and stacks. *International Journal of Hydrogen Energy* **41,** 13786–13796. ISSN: 0360-3199. https://www.sciencedirect.com/science/article/pii/S036031991631535X (Aug. 17, 2016).

218. Tsurukawa, N., Prakash, S., Manhart, A. & e.V., Ö. I. Social impacts of artisanal cobalt mining in Katanga, Democratic Republic of Congo (2011).

219. Fraunhofer IMWS, Pothen, F., Growitsch, C., Engelhardt, J., Reif, C. & Brock, L. V. *SCRAP BONUS External Costs and Fair Competition in the Global Value Chains of Steelmaking* (2020). https://www.bdsv.org/fileadmin/user_upload/Study_Scrap_Bonus.pdf.

220. McLellan, B., Corder, G., Golev, A. & Ali, S. Sustainability of the Rare Earths Industry. *The 4th International Conference on Sustainable Future for Human Security SUSTAIN 2013* **20,** 280–287. ISSN: 1878-0296. https://www.sciencedirect.com/science/article/pii/S187802961400036X (Jan. 1, 2014).

221. IAEA. *Radiation Protection and NORM Residue Management in the Production of Rare Earths from Thorium Containing Minerals Safety Reports Series* **68.** ISBN: 978-92-0-115710-2. https://www.iaea.org/publications/8650/radiation-protection-and-norm-residue-management-in-the-production-of-rare-earths-from-thorium-containing-minerals (INTERNATIONAL ATOMIC ENERGY AGENCY, Vienna, 2011).

222. Wulf, C., Zapp, P., Schreiber, A., Marx, J. & Schlör, H. Lessons Learned from a Life Cycle Sustainability Assessment of Rare Earth Permanent Magnets. *Journal of Industrial Ecology* **21,** 1578–1590. https://onlinelibrary.wiley.com/doi/abs/10.1111/jiec.12575 (2017).

223. Geological Survey of Finland, Institute of Geology & Mineral Exploration & Fen Minerals A/S. *Health and safety issues in REE mining and processing An internal EURARE guidance report* (2014). https://www.eurare.org/docs/internalGuidanceReport.pdf.

224. Yang, X. J., Lin, A., Li, X.-L., Wu, Y., Zhou, W. & Chen, Z. China's ion-adsorption rare earth resources, mining consequences and preservation. *Environmental Development* **8,** 131–136. ISSN: 2211-4645. https://www.sciencedirect.com/science/article/pii/S2211464513000316 (2013).

225. Zeng, A., Chen, W., Rasmussen, K. D., Zhu, X., Lundhaug, M., Müller, D. B., Tan, J., Keiding, J. K., Liu, L., Dai, T., Wang, A. & Liu, G. Battery technology and recycling alone will not save the electric mobility transition from future cobalt shortages. *Nature Communications* **13,** 1341. ISSN: 2041-1723. https://doi.org/10.1038/s41467-022-29022-z (Mar. 15, 2022).

226. Rajaeifar, M. A., Raugei, M., Steubing, B., Hartwell, A., Anderson, P. A. & Heidrich, O. Life cycle assessment of lithium-ion battery recycling using pyrometallurgical technologies. *Journal of Industrial Ecology* **25,** 1560–1571. ISSN: 1088-1980. https://doi.org/10.1111/jiec.13157 (Dec. 1, 2021).

227. Wesselkämper, J., Dahrendorf, L., Mauler, L., Lux, S. & von Delft, S. A battery value chain independent of primary raw materials: Towards circularity in China, Europe and the US. *Resources, Conservation and Recycling* **201,** 107218. ISSN: 0921-3449. https://www.sciencedirect.com/science/article/pii/S092134492300352X (Feb. 1, 2024).

228. Ajeeb, W., Baptista, P. & Neto, R. C. Life cycle analysis of hydrogen production by different alkaline electrolyser technologies sourced with renewable energy. *Energy Conversion and Management* **316,** 118840. ISSN: 0196-8904. https://www.sciencedirect.com/science/article/pii/S0196890424007817 (Sept. 15, 2024).

229. Wulf, C., Zapp, P., Schreiber, A. & Kuckshinrichs, W. Setting Thresholds to Define Indifferences and Preferences in PROMETHEE for Life Cycle Sustainability Assessment of European Hydrogen Production. *Sustainability* **13.** ISSN: 2071-1050. https://www.mdpi.com/2071-1050/13/13/7009 (2021).

230. European Union. Regulation (EU) 2024/1252 of the European Parliament and of the Council of 11 April 2024 establishing a framework for ensuring a secure and sustainable supply of critical raw materials and amending Regulations (EU). http://data.europa.eu/eli/reg/2024/1252/oj (2024).

231. MineralPrices.com. *NiO price* June 16, 2025. https://mineralprices.com/battery-metals/.

232. Shafique, M., Akbar, A., Rafiq, M., Azam, A. & Luo, X. Global material flow analysis of end-of-life of lithium nickel manganese cobalt oxide batteries from battery electric vehicles. *Waste Management & Research* **41,** 376–388. ISSN: 0734-242X. https://doi.org/10.1177/0734242X221127175 (Feb. 1, 2023).

233. Zaimes, G. G., Hubler, B. J., Wang, S. & Khanna, V. Environmental Life Cycle Perspective on Rare Earth Oxide Production. *ACS Sustainable Chemistry & Engineering* **3,** 237–244. https://doi.org/10.1021/sc500573b (Feb. 2, 2015).

234. Zapp, P., Schreiber, A., Marx, J. & Kuckshinrichs, W. Environmental impacts of rare earth production. *MRS Bulletin* **47,** 267–275. ISSN: 1938-1425. https://doi.org/10.1557/s43577-022-00286-6 (Mar. 1, 2022).

235. Li, X., Wang, H., Cui, Z., Li, Y., Xin, S., Zhou, J., Long, Y., Jin, C. & Goodenough, J. B. Exceptional oxygen evolution reactivities on $CaCoO_3$ and $SrCoO_3$. *Science Advances* **5,** eaav6262. https://www.science.org/doi/abs/10.1126/sciadv.aav6262 (2019).

236. Liu, F., Wu, X., Guo, R., Miao, H., Wang, F., Yang, C. & Yuan, J. Suppressing the Surface Amorphization of $Ba_{0.5}Sr_{0.5}Co_{0.8}Fe_{0.2}O_{3-\delta}$ Perovskite toward Oxygen Catalytic Reactions by Introducing the Compressive Stress. *Inorganic Chemistry* **62,** 4373–4384. https://doi.org/10.1021/acs.inorgchem.3c00158 (2023).

237. May, K. J., Carlton, C. E., Stoerzinger, K. A., Risch, M., Suntivich, J., Lee, Y.-L., Grimaud, A. & Shao-Horn, Y. Influence of Oxygen Evolution during Water Oxidation on the Surface of Perovskite Oxide Catalysts. *The Journal of Physical Chemistry Letters* **3,** 3264–3270. https://doi.org/10.1021/jz301414z (Nov. 15, 2012).

238. Betley, T. A., Wu, Q., Van Voorhis, T. & Nocera, D. G. Electronic Design Criteria for O−O Bond Formation via Metal−Oxo Complexes. *Inorganic Chemistry* **47,** 1849–1861. ISSN: 0020-1669. https://doi.org/10.1021/ic701972n (Mar. 1, 2008).

239. Cao, X., Chen, R., Wang, Z., Feng, H., Zhang, Q. & Yan, N. In Situ Reactivating Perovskite Oxide Catalysts in Alkaline Water Electrolyzers: A Generalized Approach Based on Selective Cation Leaching. *ACS Sustainable Chemistry & Engineering* **11,** 16693–16702. https://doi.org/10.1021/acssuschemeng.3c05791 (Nov. 20, 2023).

240. Joseph, L. *Epitaxial Perovskite Thin Films as Sustainable Electrocatalysts for the Oxygen Evolution Reaction* Master Thesis (Universität Hamburg, Nov. 2023).

241. Guo, T., Li, L. & Wang, Z. Recent Development and Future Perspectives of Amorphous Transition Metal-Based Electrocatalysts for Oxygen Evolution Reaction. *Advanced Energy Materials* **12,** 2200827. ISSN: 1614-6832. https://doi.org/10.1002/aenm.202200827 (June 1, 2022).

242. Verhage, M., van der Minne, E., Kiens, E. M., Korol, L., Spiteri, R. J., Koster, G., Green, R. J., Baeumer, C. & Flipse, C. F. J. Electronic and Structural Disorder of the Epitaxial $La_{0.67}Sr_{0.33}MnO_3$ Surface. *ACS Applied Materials & Interfaces* **16,** 21273–21282. ISSN: 1944-8244. https://doi.org/10.1021/acsami.3c17639 (Apr. 24, 2024).

243. Newman, J. Current Distribution on a Rotating Disk below the Limiting Current. *Journal of The Electrochemical Society* **113,** 1235. ISSN: 1945-7111. https://dx.doi.org/10.1149/1.2423795 (Dec. 1, 1966).

Band / Volume 675
Scaling Methods for the Production of Tungsten Fiber-Reinforced Composites via Chemical Vapor Deposition
A. Lau (2025), untersch. Pag.
ISBN: 978-3-95806-851-3

Band / Volume 676
Nanoscale analysis of high-temperature oxidation mechanisms of Cr_2AlC MAX phase and W-Cr-Y self-passivating tungsten alloy
A.J. S. Reuban (2025), ix, 142 pp
ISBN: 978-3-95806-855-1

Band / Volume 677
First principles simulations of high-entropy materials for energy storage
Y. Ting (2025), xviii, 169 pp
ISBN: 978-3-95806-858-2

Band / Volume 678
Deployment of Fuel Cell Vehicles in Road Transport and the Expansion of the Hydrogen Refueling Station Network
T. Grube, M. Sander (2025), iv, 61 pp
ISBN: 978-3-95806-859-9

Band / Volume 679
Entwicklung von nickelbasierten katalysatorbeschichteten Diaphragmen für die alkalische Wasserelektrolyse
C. B. Karacan (2025), 146 pp
ISBN: 978-3-95806-860-5

Band / Volume 680
Bewertung lokaler Eigenspannungsverteilungen bei der lokalen Bauteilreparatur durch Kaltgasspritzen
J.-C. Schmitt (2025), 154, xxvii pp
ISBN: 978-3-95806-861-2

Band / Volume 681
First principles study of the effect of substitution\doping on the performance of layered oxide cathode materials for secondary batteries
N. Yaqoob (2025), iii, 126 pp
ISBN: 978-3-95806-864-3

Band / Volume 682
Field assisted sintering technology/spark plasma sintering in the direct recycling of hot-deformed Nd-Fe-B scrap and PM T15 steel swarf
M. T. M. Keszler (2025), viii, 173 pp
ISBN: 978-3-95806-866-7

Band / Volume 683
Assessment of erosion in recessed areas of fusion devices using multi-scale computer simulations
S. W. Rode (2025), viii, 196 pp
ISBN: 978-3-95806-867-4

Band / Volume 684
Europäische Energiewende – Deutschland im Herzen Europas
T. Klütz, P. Dunkel, T. Busch, J. Linssen, D. Stolten (2025), IV, 56 pp
ISBN: 978-3-95806-870-4

Band / Volume 685
Performance and stability of solar cells and modules: From laboratory characterization to field data analysis
T. S. Vaas (2025), xvii, 146 pp
ISBN: 978-3-95806-871-1

Band / Volume 686
From Soil Legacy to Wheat Yield Decline: Studying the Plant-Soil Feedback Mechanisms in Wheat Rotations
N. Kaloterakis (2025), XXIX, 188 pp
ISBN: 978-3-95806-874-2

Band / Volume 687
Entwicklung von Beschichtungsverfahren für die Herstellung von Wärmedämmschichten auf additiv gefertigten Komponenten
M. Rüßmann (2026), ix, 188 pp
ISBN: 978-3-95806-877-3

Band / Volume 688
Model Perovskite Oxide Electrocatalysts for the Oxygen Evolution Reaction and their Material Sustainability Evaluation
L. Heymann (2026), vi, 174 pp
ISBN: 978-3-95806-878-0

Energie & Umwelt / Energy & Environment
Band / Volume 688
ISBN 978-3-95806-878-0

Mitglied der Helmholtz-Gemeinschaft

JÜLICH
Forschungszentrum